AD-A269 027

DCUMENTATION PAGE

Form Approved
OMB No. 0704-0188

ormation is estimated to average 1 hour per response, including the time for reviewing instructions, searching existing data sources,
completing and reviewing the collection of information. Send comments regarding this burden estimate or any other aspect of this
collection of information, including suggestions for reducing this burden, to Washington Headquarters Services, Directorate for information Operations and Reports, 1215 Jefferson
Davis Highway, Suite 1204, Arlington, VA 22202-4302, and to the Office of Management and Budget, Paperwork Reduction Project (0704-0188), Washington, DC 20503.

1. AGENCY USE ONLY (Leave blank)	2. REPORT DATE	3. REPORT TYPE AND DATES COVERED
		Final Report 15 Feb 93 - 14 Jan 94

4. TITLE AND SUBTITLE

Optical design for photonics

Organization of the 1993 Photonics Science topical Meetings

5. FUNDING NUMBERS

F49620-93-1-0181

6. AUTHOR(S)

Dr Jarus W Quinn

7. PERFORMING ORGANIZATION NAME(S) AND ADDRESS(ES)

Optical Society of America
2010 Massachusetts Avenue NW
Washington DC 20036

8. PERFORMING ORGANIZATION REPORT NUMBER

AFOSR-TR- 93 0644

9. SPONSORING/MONITORING AGENCY NAME(S) AND ADDRESS(ES)

AFOSR/NE
110 Duncan Avenue Suite B115
Bolling AFB DC 20332-0001

10. SPONSORING/MONITORING AGENCY REPORT NUMBER

2301/DS

11. SUPPLEMENTARY NOTES

DTIC
ELECTE
AUG 3 1 1993
S A D

12a. DISTRIBUTION/AVAILABILITY STATEMENT

This document has been approved
for public release and sale; its
distribution is unlimited.

UNLIMITED

b. DISTRIBUTION CODE

13. ABSTRACT (Maximum 200 words)

The following symposium was held

Advanced Solid State Lasers
Compact Blue-Green Lasers
Integrated Photonics Research
Nonlinear Guide-Wave Optics
Optical Amplifiers & Their Applications
Optical Design for Photonics
Photonics in Switching
Quantum Optoelectronics
Shortwavelength: Physics With Intense Laser Pulses
Soft X-Ray Protection Lithography
Ultrafast Electronics & Optoelectronics
Optical Computing
Spatial Light Modulators

14. SUBJECT TERMS

93 8 30 031

15. NUMBER OF PAGES

16. PRICE CODE

17. SECURITY CLASSIFICATION OF REPORT	18. SECURITY CLASSIFICATION OF THIS PAGE	19. SECURITY CLASSIFICATION OF ABSTRACT	20. LIMITATION OF ABSTRACT
UNCLASS	UNCLASS	UNCLASS	UL

NSN 7540-01-280-5500

Standard Form 298 (Rev. 2-89)
Prescribed by ANSI Std 239-18

OPTICAL DESIGN FOR PHOTONICS

POSTCONFERENCE EDITION

Optical Design for Photonics

Summaries of papers presented at the Optical Design for Photonics Topical Meeting

March 22-24, 1993
Palm Springs, California

1993 Technical Digest Series
Volume 9

POSTCONFERENCE EDITION

Sponsored by
Optical Society of America

Optical Society of America
2010 Massachusetts Avenue, NW
Washington, DC 20036-1023

CONTENTS

OPTICAL DESIGN FOR PHOTONICS
PROGRAM COMMITTEE

MONDAY, MARCH 22, 1993

OLEANDER

8:20 am–8:30 am
Introductory Remarks
Douglas Sinclair, *Sinclair Optics;*
W. J. Tomlinson, *Bellcore*

8:30 am–10:00 am
OMA, Design of Diffractive Optical Elements
G. Michael Morris, *University of Rochester, Presider*

8:30 am—OMA1 (Invited)
Applications of diffractive optics to semiconductor laser arrays, J. R. Leger, *Univ. Minnesota.* The design and application of several unique diffractive elements to diode laser arrays are described. Fractional Talbot lenses for array collimation are shown to require reduced lithographic precision. Mode selecting diffractive mirrors establish desired fundamental laser cavity modes while discriminating against modes of higher order. **(p. 2)**

9:00 am—OMA2 (Invited)
Diffractive optical elements in the real world, Peter P. Clark, Carmiña Londoño, William T. Plummer, *Polaroid Corp.* This paper is a review of surface-relief diffractive optical elements. We cover applications in hybrid diffractive/bulk systems, including achromatizing, athermalizing and field flattening. We will also address the performance effects of inherent efficiency limitations as well as those caused by the characteristics of various fabrication technologies. **(p. 6)**

9:30 am—OMA3 (Invited)
Practical considerations for optical design using diffractive optics, T. Heydenburg, D. A. Zweig, *Hughes Danbury Optical Systems, Inc.* This paper examines a number of issues which are taken for granted with conventional optics but which must be more carefully considered when utilizing diffractive optics. **(p. 7)**

GRAND BALLROOM

10:00 am–10:30 am
COFFEE BREAK

OLEANDER

10:30 am–12:00 m
OMB, Design Methods in Free Space Physical Optics
James M. Zavislan, *Lucid Technologies Inc., Presider*

10:30 am—OMB1 (Invited)
Design and modeling of optical systems involving electro-optical and photorefractive materials, Lambertus Hesselink, *Stanford Univ.* Abstract not available at press time. **(p. 10)**

11:00 am—OMB2 (Invited)
Back-of-the-envelope diffraction analysis for optimizing the depth of focus of scanning beams, G. W. Forbes, *Univ. Rochester.* The Fresnel approximation leads to a simple closed-form expression for the width of a focused beam passed by a circular aperture. The beam of smallest maximum width over a fixed scanning depth is investigated. **(p. 11)**

11:30 am—OMB3 (Invited)
Using rules of thumb in the design of physical optics systems, George N. Lawrence, *Applied Optics Research.* While physical optics is difficult both analytically and numerically, there are many useful rules of thumb which can give the intuitive understanding needed for design. **(p. 12)**

12:00 m—1:30 pm
LUNCH (on your own)

OLEANDER

1:30 pm–3:00 pm
OMC, Integrated Optics Design: 1
Zdislaw J. Jakubczyk, *National Optics Institute, Canada, Presider*

1:30 pm—OMC1 (Invited)
CAD tools for integrated optical design, Terry Young, *GEC-Marconi, UK.* Some numerical techniques for integrated opto-electronics are reviewed, emphasizing the beam propagation method as a design tool and illustrating its uses in new application areas. **(p. 16)**

2:00—OMC2 (Invited)
Design of passive waveguide components, N. Fabricius, B. Wolf, *Integrierte Optik-Technologie, Germany;* W. Foss, *Carl Zeiss, Germany.* Integrated optical components made by ion exchange in glass are now used in German telecommunication networks and industrial sensor applications. Therefore the production yield and the reliability under hard environmental conditions have to be optimized during the design procedure. Examples are given in the talk. **(p. 20)**

2:30 pm—OMC3 (Invited)
Design of multilayer cladding waveguides and their applications, Yasuo Kokubun, *Yokohama National Univ., Japan.* Multilayer cladding waveguides have possibility of novel functions such as polarizers, wavelength filters, mode filters, etc., and are promising to the integrated photonics. Design techniques and some applications of the multilayer cladding waveguide are presented. **(p. 21)**

GRAND BALLROOM

3:00 pm–3:30 pm
COFFEE BREAK

OLEANDER

3:30 pm–5:00 pm
OMD, Integrated Optics Design: 2
Laura A. Weller-Brophy, *3M Research Laboratories, Presider*

3:30 pm—OMD1 (Invited)
Design and fabrication of efficient fiber microlenses, Herman M. Presby, *AT&T Bell Laboratories.* The design and fabrication of ideal microlenses which can theoretically couple all of the radiated energy of a circularly-symmetric laser source into a single-mode optical fiber are presented. **(p. 26)**

4:00 pm—OMD2 (Invited)
Design and fabrication of integrated-optic sensors, M. Haruna, *Osaka Univ., Japan.* This paper presents design and fabrication of IO heterodyne interferometers as well as key waveguide components in Ti-diffused Z-propagating $LiNbO_3$. **(p. 29)**

4:30 pm—OMD3 (Invited)
Current issues in free-space digital optical systems, H. Scott Hinton, *McGill Univ., Canada.* This paper will review some of the current issues associated with the design of systems based on free-space digital optics. It will also include a discussion of potential applications of this technology. **(p. 33)**

OLEANDER

9:00 am–10:30 am
OTuA, Diffractive Optics
Contributed Paper Preview
Douglas C. Sinclair, *Sinclair Optics, Presider*

9:00 am—OTuA1
Hybrid diffractive elements for planar optics, Raymond K. Kostuk, Charles W. Haggans, Gene Campbell, *Univ. Arizona;* James M. Battiato, *USAF Rome Laboratory.* Surface relief gratings (binary optics) and volume holograms are evaluated for use in planar optic systems. Analysis and experimental results for fiber array tap are given. **(p. 38)**

9:04 am—OTuA2
Diffractive optical elements within a Matrix–Matrix crossbar, P. Blair, M. R. Taghizadeh, J. Turunen, B. Robertson, *Heriot-Watt Univ., U.K.* Free-space optical interconnection components based on binary and multilevel surface-relief structures have been designed, fabricated, and utilized to implement a matrix–matrix crossbar. **(p. 42)**

9:08 am—OTuA3
Applications of diffractive optics with only a zero order, Robert J. Noll, *Hughes Danbury Optical Systems.* Aside from conventional applications such as antireflection aids and polarizers, Wood's resonant anomaly can be exploited in devices like the surface emitting distributed feedback laser and grating waveguide couplers. **(p. 46)**

9:12 am—OTuA4
HOE for wavelength stabilization and selection for wavelength-division-multiplexing (WDM) in lightwave communications, Haixian Zhou, Charles S. Ih, Rongsheng Tian, Xiaoqing Xia, *Univ. Delaware.* The design and fabrication of a HOE for WDM for lightwave communication systems are described and demonstrated. The advantages of using HOE are illustrated. **(p. 50)**

9:16 am—OTuA5
Fresnel ping-pong algorithm for two-plane CGH display, Rainer G. Dorsch, Adolf W. Lohmann, Stefan Sinzinger, *Physikalisches Institut der Univ., Germany.* Two different image intensities (I_1, I_2) at two depth locations can be generated by a single computer hologram. The phases related to I_1 and I_2 provide design freedom. **(p. 53)**

9:20 am—OTuA6
Design of diffractive optical elements with rigorous diffraction theory, Erkin Sidick, Andre Knoesen, *UC–Davis.* A computer aided approach to design diffractive optical elements is presented that progressively incorporates increasingly more rigorous diffraction theories as the design is optimized. **(p. 57)**

9:24 am—OTuA7
Holographic focusing doublet for polychromatic sources, A. Aharoni, J. W. Goodman, *Stanford Univ.;* Y. Amitai, *Weizmann Institute of Science, Israel.* We consider the design tradeoff between focal-to-background intensity ratio and focal depth-of-field in nearly achromatic holographic doublets for focusing polychromatic sources. **(p. 61)**

9:28 am—OTuA8
Fidelity of postScript-generated masks for diffractive optics fabrication, Donald C. O'Shea, Thomas J. Suleski, *Georgia Institute of Technology.* Masks generated using high-resolution graphics output contain dimensional errors that must be corrected. A description of the errors and compensatory strategies are discussed. **(p. 65)**

9:32 am—OTuA9
Color correction in athermalized hybrid lenses, Gregory P. Behrmann, *U.S. Army Research Laboratory.* Previously published athermalized hybrid lenses suffer from severe chromatic aberration. We examine the requirements for simultaneous athermalization and achromatization of lenses operating in the 8–12 µm band. Comparisons of optical, thermal, and physical properties are discussed. **(p. 67)**

9:36 am—OTuA10
Phase grating optimization using genetic algorithms, Eric G. Johnson, Alan Kathman, *Teledyne Brown Engineering;* Mustafa Abushagar, *Univ. Alabama in Huntsville.* In this paper, a simple genetic algorithm is proposed as an optimization strategy for fanout phase gratings and other diffractive optic components. **(p. 71)**

9:40 am—OTuA11
Optical optimization of binary phase diffractive optical elements, K. J. Weible, H. P. Herzig, *Univ. Neuchâtel, Switzerland.* A liquid crystal television is used to modulate phase in an optical parallel processor which optimizes binary phase diffractive optical elements using simulated annealing. **(p. 74)**

9:44 am—OTuA12
Binary optic beam steering techniques, Michael W. Farn, *MIT Lincoln Laboratory.* We describe and compare two methods of agile beam steering using binary optics: one based on phased array principles and one based on the translation of microlenses. **(p. 78)**

9:48 am—OTuA13
Multibeam grating structures, A. D. Kathman, E. G. Johnson, M. L. Scott, *Teledyne Brown Engineering.* In this paper, we demonstrate optimization of a fanout grating in an n-dimensional solution space using a simulated annealing algorithm. The algorithm provides a successful first-order design which is further optimized using wave optics design software. A three-beam grating is fabricated and tested; diffraction efficiencies will be reported. **(p. 82)**

9:52 am—OTuA14
Multiplexed substrate-mode holographic interconnects, Y. Amitai, *Weizmann Institute of Science, Israel.* A method for designing and recording a compact system based on multiplexed substrate-mode holographic elements is presented. The system can be used for a wavelength-division-multiplexing or for multichannel optical interconnects. **(p. 84)**

9:56 am—OTuA15
Efficient, broad-band holographic axilens doublets for ir sources, Y. Amitai, *Weizmann Institute of Science, Israel;* A. Aharoni, J. W. Goodman, *Stanford Univ.* We present a method for designing and recording holographic doublets for focusing ir laser diodes; the doublets offer high diffraction efficiencies, an extended focal depth, and low aberrations over a comparatively wide spectral range. **(p. 88)**

10:00 am—OTuA16
Designing continuous contour phase plates for beam smoothing, S. N. Dixit, J. K. Lawson, K. Manes, H. T. Powell, *Lawrence Livermore National Laboratory;* K. A. Nugent, *Univ. Melbourne, Australia.* We present an iterative algorithm for constructing continuous contour phase screens (kinoforms) for tailoring the focal plane intensity distribution. **(p. 92)**

10:04 am—OTuA17
Production of high damage threshold diffractive optics for beam smoothing, J. K. Lawson, S. N. Dixit, A. Morgan, I. M. Thomas, B. W. Woods, H. T. Powell, *Lawrence Livermore National Laboratory.* We describe techniques for producing damage resistant, continuous phase patterns (kinoforms) with improved focal plane irradiance control over that reported for binary phase patterns. **(p. 95)**

10:08 am—OTuA18
Optimization of brightness and magnification in holographic image combiner systems, Hirokazu Aritake, Masayuki Kato, Masato Nakashima, *Fujitsu Laboratories Ltd., Japan.* Optimization of image brightness and magnification in holographic image combiner systems is presented, and possible magnification for clear image is given. **(p. 98)**

GRAND BALLROOM

10:30 am–11:00 am
COFFEE BREAK

TUESDAY, MARCH 23, 1993—*Continued*

GRAND BALLROOM

10:30 am–12:00 m
OTuB, Diffractive Optics
Contributed Papers in Poster
Format

(This session includes papers
previewed in OTua.)

12:00 m–1:30 pm
LUNCH (on your own)

OLEANDER

1:30 pm–3:00 pm
OTuC, Plenary Session
Susan N. Houde-Walter,
University of Rochester, Presider

1:30 pm—OTuC1 (Invited)
Optical system design with diffrac-
tive elements, G. Michael Morris, *Univ.*
Rochester. Optimization of optical
system performance and novel optical
components based on diffractive optics
technology will be described. Both
monochromatic and broadband ap-
plications will be discussed. **(p. 106)**

2:15 pm—OTuC2 (Invited)
Design issues in monolithic wave-
guide integration, R. J. Deri, *Bellcore.*
This paper shows how advanced design
techniques have been applied to solve
many problems in photonic integration.
(p. 107)

GRAND BALLROOM

3:00 pm–3:30 pm
COFFEE BREAK

OLEANDER

3:30 pm–5:00 pm
OTuD, Tutorial
Laura Weller-Brophy, *3M*
Research Laboratories, Presider

3:30 pm—OTuD1 (Tutorial)
The applicability of conventional
design notions to integrated optics,
Lambertus Hesselink, *Stanford Univ.*
The objective of this tutorial is to explore
similarities and differences between the
design of conventional and integrated
optical elements. The approach we take
is to briefly review design notions devel-
oped for diffractive elements using bulk
optics. Particular emphasis is placed on
fundamental issues underlying the per-
formance of these devices, usually ex-
pressed in terms of aberrations, diffrac-
tion efficiency and polarization charac-
teristics computed using raytracing and
wavefront analysis. for evaluation of per-
formance in integrated optics, mode
characteristics for the various polariza-
tion states need to be incorporated into
device analysis. We consider examples
such as holographic optical elements,
grating couplers and beam steering
elements to illustrate commonly used
design strategies and approaches.
Throughout the discussion we explore
how knowledge of and rules developed
for the design of conventional diffractive
elements can be applied to the area of
integrated optics. Notions such as
Brewster's angle and k-vector diagrams
for thin and thick diffraction gratings
having equivalent counterparts in the
design and evaluation of integrated op-
tical structures will be highlighted and
studied. **(p. 113)**

WEDNESDAY, MARCH 24, 1993

GRAND BALLROOM

9:00 am–10:20 am
OWA, Design Methods for
Photonics Technology, Paper
Preview
W. J. Tomlinson, *Bellcore,*
Presider

9:00 am—OWA1
Use of Fourier methods to analyze
the effects of birefringence in optical
disk substrates, Bruce E. Bernacki, M.
Mansuripur, *Univ. Arizona.* DIFFRACT,
a scalar/quasi-vectorial diffraction
modeling program is used to analyze
the effects of birefringence due to
injection-molded polycarbonate optical
disk substrates. **(p. 116)**

9:04 am—OWA2
Technique for reducing the spectral
width of an LED, Michael M. O'Toole,
Hewlett-Packard. Insertion into the op-
tical path of an absorbing dye reduces
the spectral width of an LED and allows
longer distances and/or higher data
rates in optical communication systems.
(p. 120)

9:08 am—OWA3
Design and fabrication of astigmatic
GRIN elements for laser diode col-
limation, K.-H. Brenner, S. Sinzinger, T.
Spick, M. Testorf, *Univ. Erlangen-*
Nürnberg, Germany. Design and fab-
ication of collimators for astigmatic laser
diodes by ion exchange in glass is
presented. Such elements offer advan-
tages with respect to compactness,
packaging, and uniformity. **(p. 124)**

9:12 am—OWA4
Focal plane pixel energy redistribu-
tion and concentration using micro-
lens arrays, William H. Southwell,
Rockwell International Science Center.
A physical optics calculation has been
performed to determine the propagation
and potential concentration of pixel light
distribution through focal plane micro-
ens arrays. **(p. 128)**

9:16 am—OWA5
Birefringent polarization ray tracing,
Stephen C. McClain, Russell A. Chip-
man, *Univ. Alabama in Huntsville.* Pro-
cedues for performing polarization ray
tracing through birefringent media are
presented in a form compatible with the
standard methods of geometric ray trac-
ing. **(p. 132)**

9:20 am—OWA6
Complexities of image formation
through liquid crystal televisions, J.
Larry Pezzaniti, Russell A. Chipman,
Univ. Alabama in Huntsville. Imaging
through a liquid crystal television has
been studied using an imaging
polarimeter. Polarization of the PSF
shows spatial polarization variations
resulting from polarization defects in the
television. **(p. 136)**

9:24 am—OWA7
Analysis of coupling efficiency in single-mode fiber components as an optical design problem, Stanislaw Szapiel, *National Optics Institute, Canada;* Jasmin Côte, *Univ. Arizona.* Properly weighted-aberrational wavefront variance is identified as an optical design tool to analyze coupling losses in single-mode fiber components. **(p. 140)**

9:28 am—OWA8
Effective medium theory approach to guided-mode resonances, Scott M. Norton, Daniel H. Raguin, G. Michael Morris, *Univ. Rochester.* Rigorous vector analysis of embedded grating structures is presented. Effective medium theory is used to predict the wavelength which excites resonant behavior. **(p. 143)**

9:32 am—OWA9
The migration of bound and leaky solutions to the waveguide dispersion relation, R. E. Smith, S. N. Houde-Walter, *Univ. Rochester.* Paths followed by solutions to a single-valued open dispersion relation are shown to offer insight into device functionality. Examples include a resonant-tunneling waveguide polarizer. **(p. 147)**

9:36 am—OWA10
Design of optical devices through the finite element method, M. Zoboli, S. Selleri, F. Di Pasquale, *Univ. Parma, Italy.* Design of optical devices through a full vectorial finite element method is presented. Examples of nonlinear optical fibers, analysis of the induced refractive index changes, and comparisons with the gaussian approximation are reported. **(p. 151)**

9:40 am—OWA11
BPM-CAD—waveguide optics modeling software system, Zdzislaw Jakubczyk, *National Optics Institute, Canada.* A comprehensive software package which provides a system for integrated and fiber optics devices modeling and design is presented. Examples of operation and use are shown. **(p. 155)**

9:44 am—OWA12
Integrated optical two-dimensional time-integrating correlator, Triston J. Tayag, Brian M. Sadler, John M. Pellegrino, *U.S. Army Research Laboratory.* An integrated optical architecture is proposed that uses the technique of coherent interferometric time-integration to perform a 2-D, multiproduct correlation. The requirements of the surface acoustic wave transducers, integrated lenses, and waveguide outcoupling gratings are discussed. **(p. 159)**

9:48 am—OWA13
Alignability versus signal density in integrated planar-optical interconnect packages, Anjan K. Ghosh, Russell S. Beech, *Univ. Iowa.* The efficiency of power transfer and the alignability of an integrated, planar-optics, holographic optical backplane for board-to-board interconnections are analyzed with attention to the signal density. From the analyses, optimum design guidelines on packaging of integrated planar-optic interconnects are developed. **(p. 163)**

9:52 am—OWA14
Frequency control, modulation, and packaging of an SDL (100 mW) laser diode for a free-space photonic switching fabric, Jose M. Sasian, Rick L. Morrison, Thomas J. Cloonan, Martin G. Beckman, Michael J. Wojcik, Stephen J. Hinterlong, *AT&T Bell Laboratories.* A built laser system delivers 75 mW of diffraction limited power at 840 nm, and an external grating cavity permits tuning the lasing wavelength within a range of 20 nm. **(p. 167)**

9:56 am—OWA15
Multiple-plane optical interconnections using through-wafer hollow dielectric waveguide vias, A. D. Norte, A. E. Willner, W. Shieh, A. R. Tanguay, Jr., *Univ. Southern California.* We investigate lossy hollow-waveguide vias in a dense optical interconnection system as a means by which many 2-D processor planes can communicate simultaneously with minimal attenuation. Analytical expressions and system design guidelines are derived and compared to unguided interconnections. **(p. 171)**

GRAND BALLROOM

10:20 am–12:00 m
OWB, Design Methods for Photonics Technology, Contributed Papers in Poster Format

(This session includes papers previewed in OWA.)

GRAND BALLROOM

10:30 am–11:00 am
COFFEE BREAK

12:00 m–1:30 pm
LUNCH (on your own)

OLEANDER

1:30 pm–3:00 pm
OWC, Optoelectronic Packaging Design
Bulent Nihat Kurdi, *IBM, Presider*

1:30 pm—OWC1 (Invited)
OEIC packaging for fiber optic computer interconnects, Kenneth P. Jackson, *IBM Applications Business Systems.* The challenges facing optoelectronic packaging for fiber-optic computer interconnects will be discussed with emphasis on parallel, array implementations. **(p. 178)**

2:00 pm—OWC2 (Invited)
Photonic subsystem design based on hybrid optoelectronic integration on silicon substrates, Craig A. Armiento, *GTE Laboratories.* This talk will describe efforts to develop silicon as an integration platform for optoelectronic, optical, and electronic components to achieve low-cost, compact and highly functional optical subsystems. **(p. 179)**

2:30 pm—OWC3 (Invited)
Design and fabrication/packaging of low-loss passive optical devices, Hirochika Nakajima, *Fujitsu Laboratories Ltd., Japan.* Low-loss microoptic/guide-wave passive optical devices, such as magneto-optical switch, in-line isolator, LN switch/modulator, and polymeric spot-size converter etc., are reviewed accompanied with design and fabrication/packaging methods. **(p. 182)**

GRAND BALLROOM

3:00 pm–3:30 pm
COFFEE BREAK

OLEANDER

3:30 pm–5:00 pm
OWD, Packaging Techniques for Guided Wave Optical Systems
Joseph W. Goodman, *Stanford University, Presider*

3:30 pm—OWD1 (Invited)
Optical device packaging technology for fiber-optic communications, Yuji Abe, *NEC Corp., Japan.* Optical devices using micro-optics and active alignment techniques are widely utilized in commercial fiber-optic communication systems. Such current optical device packaging technology are reviewed. Some advanced work in this field, as optical array modules, passive alignment techniques are also discussed. **(p. 184)**

4:00 pm—OWD2
Holographic optical module integrated with chip elements for optical disk pickups, Yuzo Ono, *NEC Corp., Japan.* A new packaging for thin optical pickups utilizing a photodiode substrate as an opto-base, on which chip optical elements are hybrid integrated, has been developed applying flip-chip bonding technique for packaging the substrate. **(p. 186)**

4:30 pm—OWD3
Modeling and design of integrated micro-optical systems, Jürgen Jahns, *AT&T Bell Laboratories.* The concept of planar optics requires folding the optical path in a zigzag fashion between the two surfaces of a substrate. We analyze various means of implementing parallel interconnections using planar optics in terms of the achievable interconnection densities. **(p. 187)**

Design of Diffractive Optical Elements

OMA 8:30am-10:00am
Oleander Room

G. Michael Morris, *Presider*
University of Rochester

Applications of Diffractive Optics to Semiconductor Laser Arrays

J. R. Leger
Dept. of Electrical Engineering
University of Minnesota
Minneapolis, Minnesota 55455
(612) 625-0838

Optical interfacing to modern photonic devices presents several complex design challenges. Semiconductor arrays, for example, require optics that have high numerical apertures, low aberrations, and are efficient. In addition, when the design requires separate optical elements for each laser or group of lasers in the array, these optics must be small (10 − 100 μm diameter), close packed, held on a common substrate, and spaced in an accurate array. Advanced designs may even call for correcting existing aberrations and performing more complex optical functions. Some of these functions include optical interconnections, spatial filtering, establishing coherence, beam collimation and control, and optical geometric transformations. Diffractive optics has been shown to satisfy many of these requirements. In this presentation, we describe the design of some unique diffractive optical structures with applications to semiconductor laser arrays.

The first optical structure converts an array of coherent apertures into a single uniform beam by means of the fractional-Talbot effect. It is well known that a periodic array of coherent apertures will form self-images at periodic intervals spaced by $Z_t = 2D^2/\lambda$, where D is the period of the array and λ is the wavelength[1]. At rational fractions of this distance, more complex images are formed[2]. For example, the original apertures are replicated twice in each direction at $Z_t/4$, three times at $Z_t/6$, four times at $Z_t/8$, etc. Thus, if the original array has a fill factor of $1/N$, a fractional-Talbot image at $Z_t/2N$ will form an intensity image that has a fill factor close to unity (unity is achieved for square apertures only). An examination of the phase in this plane reveals that each newly created aperture has a constant phase, but that the phase ϕ changes abruptly from aperture to aperture according to

$$\phi = \frac{\pi(I^2 + J^2)}{N},$$

where I and J are integers for even N and half-integers for odd N ranging from $-N/2$ to $(N/2 - 1)$[3]. This step-wise parabolic phase distribution is repeated with the periodicity of the original apertures. By fabricating a diffractive optical element with the complex conjugate of the above phase, the light distribution can be converted into a planar phase front with quasi-uniform fill factor. An optical element for $N = 4$ was fabricated and used to collimate an array of square apertures with a two-dimensional fill factor of 1/16. Since the amount of light coupled into the on-axis plane wave is directly proportional to this fill factor, such a diffractive optic can be used to improve the on-axis power from a coherent diode laser array[4, 5]. A demonstration of this is shown in fig. 1. An array of coherent sources (fill factor = 1/4 in each direction) was simulated by illuminating a square aperture array with an expanded HeNe beam. Light in the far field is spread out over many grating lobes in fig. 1a, and the power contained in the main lobe is approximately 1/16 the total array power. By placing the diffractive optics corrector at $Z_t/8$, the far-field was transformed into the pattern shown in fig. 1b. Almost all of the light has been coupled into the on-axis plane wave.

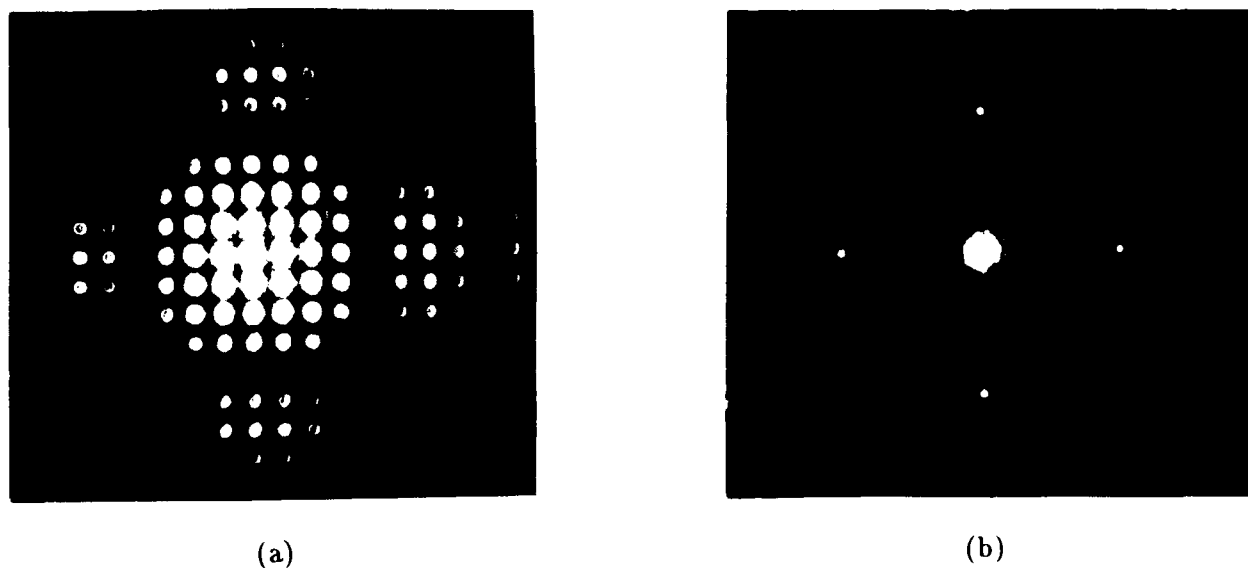(a)　　　　　　　　　　　　　　　　(b)

Figure 1: Far-field pattern of periodic array. (a) is the far-field pattern with no phase-correcting optics. (b) is the far-field pattern using a fractional-Talbot phase corrector.

2-LEVEL FRESNEL ZONE PLATE　　　　FRACTIONAL TALBOT ILLUMINATOR
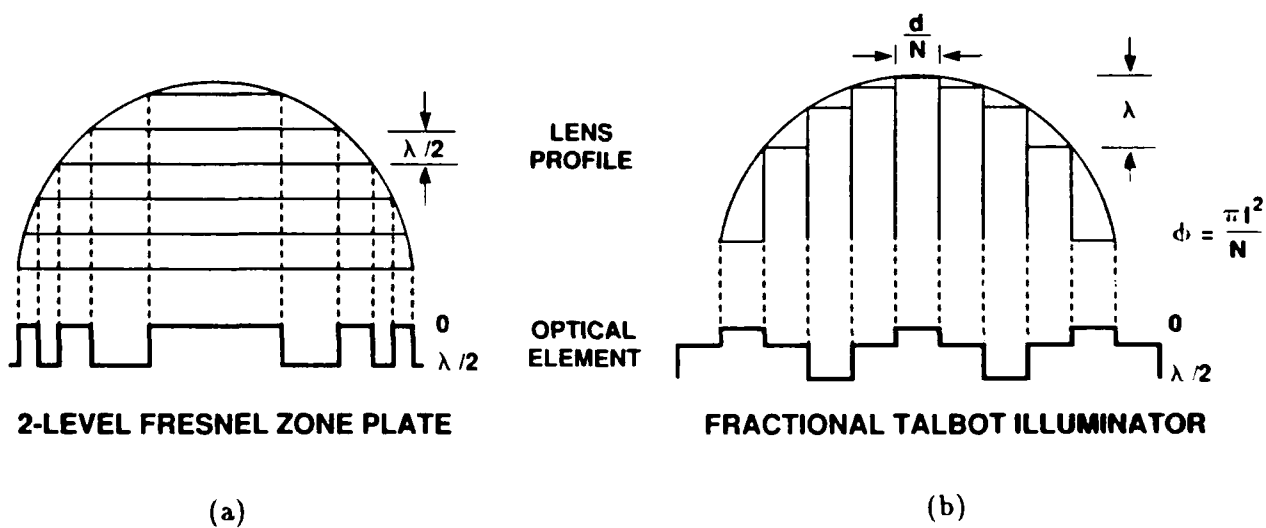
(a)　　　　　　　　　　　　　　　　(b)

Figure 2: Comparison between conventional 2-level diffractive lens and a fractional-Talbot phase corrector.
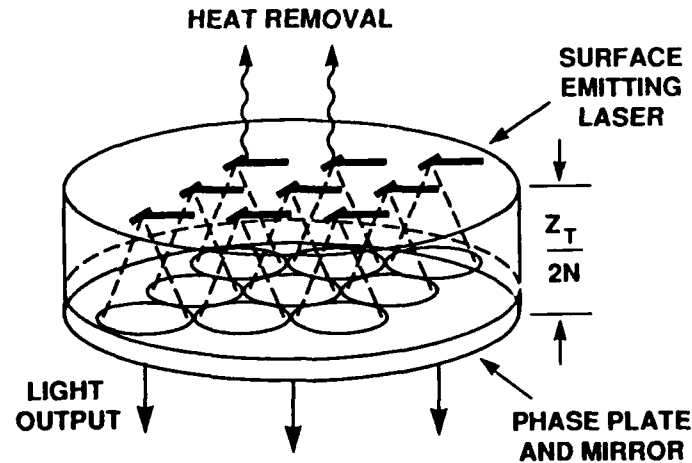
Figure 3: Fractional Talbot resonator

Diffractive elements based on the fractional-Talbot effect are very similar in appearance to multi-level lenslet arrays (see fig. 2). One obvious difference is that each constant phase zone is of identical width (fig. 2b) , whereas a conventional diffractive optical lens usually contains zones with progressively smaller widths (fig. 2a). The smallest feature size required by the fractional-Talbot plate is $\lambda(f/\#)$, where $(f/\#)$ is the focal ratio of the equivalent lens. This feature size is identical to the requirement for a binary (two-level) diffractive lens. However, the diffraction efficiency of the two-level diffractive lens is only 40.5%, whereas for the fractional-Talbot plate, it can theoretically be 100%. Multilevel etching increases the diffraction efficiency of diffractive lenses, but only at the expense of finer linewidths (typically eight to sixteen times smaller).

The fractional-Talbot method is able to achieve high efficiency using large features because of the periodic nature of the source. We can see this by observing the operation of the plate in reverse: a plane wave is converted into an array of square apertures with a fill factor of 1/4 (in each direction). However, a single element of the array can be shown to contain many higher order foci. These higher-order terms contribute coherently to adjacent apertures in such a way that no light is wasted.

A unique optical resonator can be constructed using a fractional-Talbot plate to both combine and redistribute the light from a two-dimensional diode laser array (fig. 3). The lasers are fabricated with integral turning mirrors to send the light through the substrate, and a fractional-Talbot phase plate and output mirror are placed a distance $Z_t/2N = Dd/\lambda$ behind the array, where D is the spacing between the lasers, and d is the size of the laser apertures. This distance completely fills the aperture via the fractional-Talbot effect. It is apparent that the overall length of the cavity can be made much smaller than a conventional Talbot cavity resonator[6, 7] for laser arrays with small fill factors.

The final diffractive optical element described in this presentation is a laser mirror designed to establish a desired fundamental spatial mode and discriminate against all higher-order modes. We have designed and fabricated these diffractive mode selecting mirrors to establish coherence across diode laser arrays. Alternative optical structures have been used with other laser systems[8]. The design proceeds as follows: (1) The amplitude and phase of the desired fundamental array mode are chosen. In our case, it is desirable to have this mode consist of a finite number of equal amplitude Gaussian distributions with uniform phase. The Gaussian shapes are chosen to correspond to the modes of the individual lasers in the array; the equal amplitudes help prevent spatial hole burning which otherwise can contribute to a breakdown of coherence at high powers. The uniform phase is desirable for good far-field performance. (2) The complex amplitude distribution is propagated to
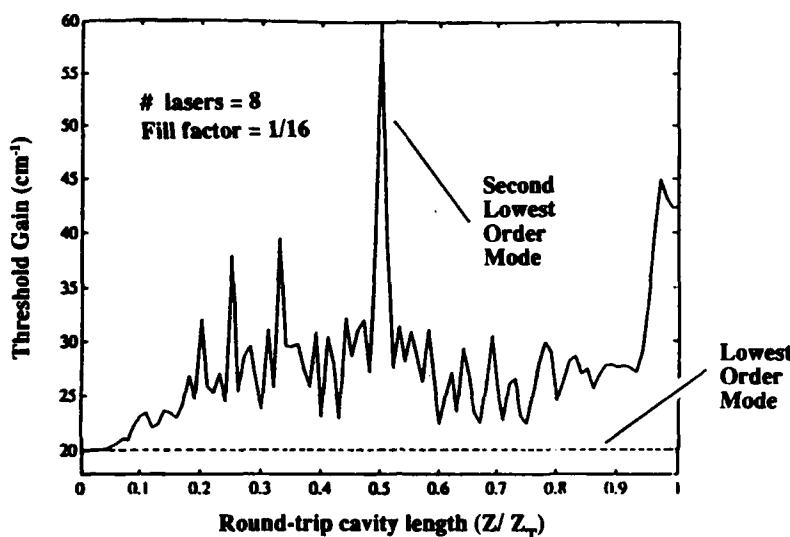
Figure 4: Lasing thresholds of the first two modes as a function of cavity length for the diffractive mode-selecting mirror.

the mirror plane using standard scalar diffraction theory. (3) The optical phase is extracted and the phase reflectance of the mirror calculated to return the complex conjugate of this wavefront. (4) The mirror phase is converted into a multilevel diffractive optical element.

In addition to establishing the proper mode, it is desirable to separate the lasing threshold of the fundamental mode from all other higher-order modes. A coupled mode analysis is used to study the higher-order modes allowed by the cavity. Fig. 4 shows that the cavity length can be used to maximize the separation between mode thresholds. For each cavity length, a new diffractive mode selecting mirror was designed and its modal properties calculated. It is clear from the figure that the fundamental mode losses are unchanged by cavity length (dashed line). The next higher-order mode, however, is greatly affected by cavity length; the optimum round-trip cavity length is given by D^2/λ, where D is the spacing between laser apertures in the array and λ is the wavelength of the light. This corresponds to a propagation length of one-half of a Talbot distance. We describe a mode-selecting mirror design for an eight-element laser array. The modal threshold separation is optimized, and the effects of fill-factor, mirror size, and alignment errors are calculated.

References

[1] W.H.F. Talbot, *Philos. Mag.* **9**, 401-407 (1836).

[2] J.T. Winthrop and C.R. Worthington, *JOSA* **55**, 373-381 (1965).

[3] J.R. Leger and G.J. Swanson, *Opt. Lett.* **15**, 288-290 (1990).

[4] O.R. Kachurin, F.V. Lebedev, M.A. Napartovich, and M.E. Khlynov, *Sov. J. Quantum Electron.* **21**, 351-354 (1991).

[5] W. Cassarly and J.M. Finlan, Paper PD3, OSA Annual Meeting, Orlando (1989).

[6] J.R. Leger, M.L. Scott and W.B. Veldkamp, *Appl. Phys. Lett.* **52**, 1771-1773 (1988).

[7] A.A. Golubentsev, V.V. Likhanskii, and A.P. Napartovich, *Sov. Phys. JETP* **66**, 676-682 (1987).

[8] C. Paré and P.A. Bélanger, *IEEE J. Quantum Electron.* **28**, 355-362 (1992).

Diffractive Optical Elements in the Real World

Peter Clark, Carmina Londono, William Plummer
Polaroid Corporation
Optical Engineering
38 Henry Street
Cambridge, MA 02139

This paper is a review of surface-relief diffractive optical elements. We cover applications in hybrid diffractive/bulk systems, including achromatizing, athermalizing and field flattening. We will also address the performance effects of inherent efficiency limitations as well as those caused by the characteristics of various fabrication technologies.

Practical Considerations for Optical Design Using Diffractive Optics

T. Heydenburg, D.A. Zweig

Hughes Danbury Optical Systems, Inc.

100 Wooster Heights Road, MS 826

Danbury, CT 06810

(203) 797-5202 / (203) 797-5409

This paper examines a number of issues which are taken for granted with conventional optics but which must be more carefully considered when utilizing diffractive optics.

Design Methods in
Free Space Physical Optics

OMB 10:30am-12:00pm
Oleander Room

James M. Zavislan, *Presider*
Lucid Technologies Inc.

Design and Modeling of Optical Systems Involving Electro-Optical and Photorefractive Materials

Lambertus Hesselink
Stanford University
3598 Durand Building
Stanford, CA 94305-4035

Summary not available at time of printing.

Back-of-the-envelope diffraction analysis
for optimizing the depth of focus of scanning beams

G.W. Forbes
The Institute of Optics
University of Rochester
Rochester, NY 14627

Simple models are most effective for feasibility studies and in the preliminary stages of design.   A particularly simple, but accurate, model is presented for analyzing certain diffraction problems and it is applied to the optimization of scanning beam. By using the scalar wave equation and the Fresnel approximation, it is straightforward to arrive at a useful model for the diffracted field in the case of a normally incident monochromatic collimated beam passing through a circular aperture. The half-width-at-half-maximum (HWHM) of the intensity distribution as a function of distance from the diffracting screen takes a well known and simple form. This is a useful result because the diffracted field for the case of an incident beam focused on the axis of the aperture can be shown to be coupled by a simple relationship to the collimated case and this result provides a simple closed form for the HWHM of a diffracted focused field. Among other things, simple expressions for the well known apparent focal shift for low NA beams, the focal spot size, and depth of field are all easily accessible. Further, the depth of focus can be traded off against beam size to determine the aperture size and focal position that ensure the smallest maximum beam spot over any fixed scanning region. The resulting beam profiles are compared to those for other fields including optimal Gaussian beams.

Using rules of thumb in the design of physical optics systems

George N. Lawrence
Applied Optics Research
4455 N. Osage Dr.
Tucson, AZ 85711
tel: 602 299 1933, fax: 602 299 1375

Design is primarily a creative process. Theory provides us the knowledge we need and numerical modeling allows us to visualize a system and to optimize construction parameters, but neither is sufficient to perform design except in the simplest cases where a solution may be derived. We need rules of thumb to aid us in visualizing the process to begin the design process. Rules of thumb are also needed as a sanity check on numerical calculations. This is as true in the optical design of laser optics as in any other field.

The subject of this paper derives from many years of work to develop a general purpose numerical model. The goal of this project is, ultimately, to be able to model all types of laser systems. The availability of fast computers and good modeling capability greatly facilitates the development of intuitive concepts.

In this paper, principles drawn from detailed diffraction analysis are applied to a variety of applications including waveguide grating couplers, high numerical aperture images, diffraction propagation in GRIN media, and illumination of a laser fusion target. The paper shows how intuitive rules may be used using numerical modeling to illustrate provide a detailed treatment.

We can design optical systems using Snell's Law for refractive elements and the Bragg Condition for diffractive optics. Ray optics enable us to calculate and correct the optical path differences. However, from ray optics we have no means of determining the efficiency and polarization state, but a simple dipole projection model gives good information with little effort. A waveguide focusing grating input-output coupler illustrates dramatic differences between TE and TM polarization that are easily understood from the simple dipole projection model. The dipole projection model also explains much of the vector diffraction effects in high numerical aperture imaging.

GRIN is an attractive technology in waveguide devices. Some years ago during investigations of optical design for optical data storage, it became apparent that diffraction propagation in GRIN media was not sufficiently well understood to be able to make accurate numerical calculations. Diffraction propagation in GRIN optics serves as an example to illustrate how what would appear to be a complex problem can be readily treated by well-known paraxial optics. Paraxial optics tell us a great deal about the diffraction performance of an optical system. Collapsing a system into its paraxial equivalent can simplify the analysis and improve the accuracy of the calculations.

The limits of accuracy in applying Fourier optics to thick optical elements can be understood by a generalization of the reduced distance -- a paraxial concept used in describing the equivalent air thickness of a glass plate or prism. Fresnel diffraction is governed by a generalized form of the reduced distance, which determines the local size of the diffraction point spread function. For thick elements and tilted apertures, the diffraction properties vary across the aperture, making Fourier optics not strictly valid.

The susceptibility of such optical systems to non-Fourier diffraction behavior, can be determined from simple elementary optical principles.

The ripples in light diffracted from a circular aperture are easily explained by visualizing the Fresnel zones in the aperture. Characteristic spatial frequencies in the diffraction pattern are straightforward to determine. The theory of Talbot imaging gives a simple explanation of the effect of aberration and irradiance fluctuations on diffraction propagation. To illustrate these principles, the problem of providing highly uniform illumination on a small sphere, such as a laser fusion target, is discussed. In this highly simplified discussion, it will be shown that it is easy to understand the nature of the diffraction effects and that there are a variety of mechanisms (from intentional design and serendipitous) which smooth out the Fresnel diffraction ripples.

Integrated Optics Design 1

OMC 1:30pm-3:00pm
Oleander Room

Zdislaw J. Jakubczyk, *Presider*
National Optics Institute, Canada

CAD tools for integrated optical design

Terry Young

GEC-Marconi Research Centre
Chelmsford, Essex
CM2 8HN

Fax: +44 245 75244

1. Introduction

Design tools based on advanced numerical techniques have been making an increasing impact on electromagnetic design for the past two decades. The impact of such methods in structural and solid modelling are, of course, well known. The aim of this paper it to summarise what is available by way of numerical techniques, to describe the type of interfaces required to make them accessible, and to address the practical matter of applying such tools in earnest. By way of example, the beam propagation method has been selected for closer discussion, since its treatment of propagation is fairly intuitive and the results are therefore readily understood.

It is almost impossible to do justice to the variety of numerical methods which have been developed for analysing whole integrated optical circuits, components, or sections of waveguide. A typical technique is the finite element method (FEM [1-5]) which has been applied in a variety of forms, handling 2D and 3D situations, lossy media, modal and propagating situations, using full vectorial and scalar methods. FEM is generally derived in the frequency domain, although at least one commercial electromagnetic package is available in the time domain [6]. Time domain solutions are attractive because a single run simulating the pulse response can be used to generate a spectrum of frequency domain information. Following this line, the transmission line method (TLM) [7,8] and a range of finite-difference-time-domain techniques (FDTD) [9] have been developed and are widely reported. Various other approaches have been suggested for discretising Maxwell's equations and solving directly [10,11].

The other major family of methods in widespread use today includes beam propagation methods (BPM) [12-18] in which a starting field is propagated through a dielectric structure. The exact form of the propagation algorithm varies, as does the degree of approximation invoked to make the solution tractable on a given machine. The most basic algorithm, described here, uses a 2D scalar solution with a simple FFT propagation algorithm in which phase corrections for each propagation step are accounted for firstly in 'real space' (for refractive index perturbations) and then in 'k-space' (to account for diffraction). Reflections are ignored and paraxial propagation is implicit [19]. A feature of this technique is its extreme stability, yielding plausible results, even when the basic approximations have been wildly violated. Care must therefore be exercised in interpreting results.

The purpose of this paper is not to discuss the relative merits of such algorithms. In fact the author would caution against excessive examination of accuracy since, in many cases, the physical parameters such as differential refractive indices and waveguide size are uncertain at the 1% to 10% level. Given an algorithm which is well understood and which has been shown to be sufficiently general to tackle a range of design problems, the first question is how to make it accessible to those versed in the technology.

Before exploring the interface requirements, it is important to recognise that other solvers may be used in order to simulate the way in which, for instance, applied electrostatic fields may be used to tune or switch an integrated optical device. This merely adds complexity to the question of interfaces and in most cases can be solved using a set of interpolation and interface routines by which a set of results from one solver may be reconditioned for presentation to another. This approach is very powerful and makes modelling methods which are common to a range of engineering disciplines more attractive in consequence.

2. Interface requirements

The key aim is to find a set of packages which enable the physical system to be broken down into a mathematical description (pre-processing), the numerical solution to be reconstructed into a meaningful graphical description (post-viewing) and the results to be manipulated to derive other useful design information (post-processing). Some techniques, such as finite differences or finite elements can use or modify off-the-shelf software, since the techniques have been applied in other fields. However, one must be aware that such packages may embody approximations or meshing routines which relate very directly to the solver for which they were originally intended. For instance, semiconductor and optical FEM solvers required meshes which have been refined in different regions to deliver the best results. An automatic meshing algorithm for one solver will not deliver the best results for another.

The author has used an in-house set of packages for FEM which allows the user freedom to define and refine the mesh to suit the solver [20]. For BPM, a user-friendly environment offering the functions just described has been designed and routinely used. Much of this has been reported elsewhere [21,22]. While the importance of interactive access has long been understood, the accent now lies on developing programmable interfaces, since much of the design process is repetitive and overnight runs can rarely be stored in their entirety.

The MRC BPM pre-processor can also be used as a layout editor, although more functions are typically required. However, an in-house interface has been written which accepts a BPM file and translates it into a format used by a commercial layout editor. This introduces some flexibility to the design process and provides a ready means of generating E-beam mask code for mask procurement.

3. Hardware considerations

Although initially developed for a network of Apollo workstations, the software has been ported to a cluster of SUN SparcStation2's where it operates in a UNIX environment using OpenWindows. An interface exists for X-windows and the code is strict Fortran '77. On the SUNs in recent studies, an 1866 node vector FEM problem took 128 seconds of CPU time. On the same system, a fully programmed BPM cycle (remote generation, solving, and interrogation of results) took 6 minutes, 48 seconds for a problem which was 6000 slices long with 512 nodes per slice. Clearly, dedicated FFT cards could be used to enhance performance further. While this has not yet been done, the solver has been run for a complex problem on a CRAY XMP machine, an operation which required only minimal modification to the data transfer statements.

4. Applications and Examples

The tutorial presentation will focus on the practical aspects of using such software, covering the selection and processing of real world measurements to provide useful input data, and the interpretation of results. The accent will also be laid on deriving useful design results, interpretation of output data and ways of applying such tools most usefully. The role of such software in designing opto-hybrid modules will also be discussed.

The absolute and relative accuracy of these tools will be discussed by example and the route from design to delivery of prototype hardware will be highlighted. The role of such software as a 'design filter' to direct research towards the more promising designs and in providing a visual appreciation of device operation will also be covered.

5. Conclusions

A variety of advanced numerical tools for designing a range of integrated optical and opto-hybrid circuits exists. Interactive and programmable interfaces are presented as the key requirement in making them accessible and versatile. The issue of interfacing to commercial mask generation is discussed and a number of practical examples will be presented to explore the application of such software and highlight the advantages which it brings to design.

Acknowledgements

References

1. A. KONRAD, "Vector Variational Formulation of Electromagnetic Fields in Anisotropic Media" IEEE Trans. Mic. Theory Tech. MTT-24 (9) pp 553-559 (1976).

2. B.M.A. RAHMAN, F.A. FERNANDEZ and J.B. DAVIES, "Review of finite element methods for microwave and optical waveguides", Proc. IEEE 79 (10) pp 1442-1448 (1991).

3. H. KUMAGAMI and M. KOSHIBA, "Finite-element method using Hermitian line elements for planar diffused optical waveguides", IEE Proc. J, 138, (3) pp 218-220 (1991).

4. N. MABAYA, P.E. LAGASSE and P. VANDENBULCKE, "Finite Element Analysis of Optical Waveguides", IEEE Trans. Mic. Theory Tech. MTT-29 (6) pp 660-605 (1981).

5. J.P. WEBB, G.L. MAILE and R.L. FERRARI, "Finite Element Solution of Three-Dimensional Electromagnetic Problems", IEE Proc. 130 pt.H. (2) pp 153-158, (1983).

6. MacNeal-Schwendler Corporation: EMAS. .

7.   D.P. JOHNS, J. WLODARCYZK and A. MALLIK, "New TLM Models for Thin Structures" IEE International Conf. on computation in electromagnetics (Conf. Pub. 350) pp 335-338 (1991).

8.   W.J.R. HOEFER, "The Transmission Line Matrix Method - Theory & Applications", IEEE Trans. Mic. Theory Tech., MTT-33, 1985.

9.   S.T. CHU, W.P. HUANG and S.K. CHAUDHURI, "Simulation and analysis of waveguide based optical integrated circuits", Computer Physics Commun. 68 (1-3) pp 451-483 (1991).

10. J.M. VAN SPLUNTER, H. BLOK, N.H.G. BAKEN and M.F. DANE, "Computational analysis of propagation properties of integrated optical waveguides using a Domain Integral Equation", URSI Int. Symp. Electromagnetic Theory, Budapest, pp 321-323 (1986).

11. T. WEILAND, "Computer Modelling of Two and Three-dimensional Cavities", IEEE J. Nuclear Sci. NS-32, pp 2738-2741.

12. M.D. FEIT and J.A. FLECK Jr., "Light propagation in Graded-index Optical Fibres", Appl. Opt. 17 (24) pp 3990-3998 (1978).

13. J. Van ROEY, J. van der DONK and P.E. Lagasse, "Beam-propagation Method: Analysis and Assessment", J. Opt. Soc. Am. 71 (7) pp 803-810 (1981).

14. L. THYLEN "Beam-propagation Method Analysis of a Nonlinear Directional Coupler", Opt. Lett. 11, (11) pp 739-741 (1986).

15. T.B. KOCH, R. MARZ and J.B. DAVIES, "Beam propagation method using z-transient variational principle", 16th European Conference on Optical Communications, Amsterdam. Proc ECOC '90 1, pp 163-6 (1990).

16. D. YEVICK and B. HERMANSSON, "Efficient Beam Propagation Techniques", IEEE J. Quantum Electron. 26 (1) pp 109-112 (1990).

17. A. SPLETT, M. MAJD and K. PETERMANN, "A Novel Beam Propagation Method for Large Refractive Index Steps and Large Propagation Distances", IEEE Photon. Tech. Lett. 3 (5) pp 466-468 (1991).

18. Z. JAKUBCZYK, "Waveguide Devices Modelling with a BPM-CAD Software System", Tech. Digest OSA Annual Meeting. Paper MPP4 (1991).

19. T.P. YOUNG, S.N. RADCLIFFE, A.J. DAVIES and P. SMITH, "BEAMER - A Design Tool for Integrated Optics", GEC J. Res 6 (3) pp 152-161 (1988).

20. T.P. YOUNG, "Design of Integrated Optical Circuits Using Finite Elements", Proc. IEE 135 pt. A (3) pp 135-144 (1988).

21. T.P. YOUNG "Computer Aided Design of Integrated Optical Components", Proc 7th International Conference on Integrated Optics and Optical Communication, IOOC '89, Kobe, Japan, 18-21 July (1989). Paper 19D2-1.

22. T.P. YOUNG, Computer aided design of integrated optics: closing the synthesis loop", Proc. Topical Meeting on Integrated Photonics Research, 26-28 March, Hilton Head Island, SC, USA. Paper MA4 (1990).

Design of Passive Waveguide Components

N. Fabricius, B. Wolf
Integrierte Optik-Technologie
Bruchsalerstr.22
Waghausel, Germany D-6833

W. Foss
Carl Zeiss, Inc.
Postfach 1380
Oberkochen, Germany 7082

Integrated optical components made by ion exchange in glass are now used in German telecommunication networks and industrial sensor applications. Therefore the production yield and the reliability under hard environmental conditions have to be optimized during the design procedure. Examples are given in the talk.

Design of multilayer cladding waveguides and their applications

Yasuo Kokubun

Yokohama National University

Division of Electrical and Computer Engineering

156 Tokiwadai, Hodogayaku, Yokohama, 240 JAPAN

[General concept of multilayer cladding waveguides]

Multilayer thin films can produce various states of complex reflection coefficient by regulating the thickness and refractive index of each layer and the angle of incidence. When the multilayer is utilized as the cladding of waveguide as shown in Fig. 1, the propagation angle θ of guided and quasi-guided modes is determined by

$$k_0 n_c \sin \theta + \phi_1 + \phi_2 = 2N\pi \tag{1}$$

where k_0 is the propagation constant in a vacuum, n_c is the refractive index of the core, N is
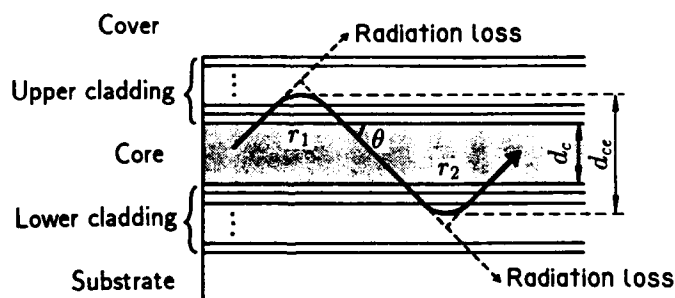
Fig. 1. Generalized structure of multilayer cladding waveguide.

the mode number, and ϕ_1 and ϕ_2 are the phase shifts of complex reflection coefficients upper and under the core, respectively. The phase shift and power reflection coefficient are obtained from the complex reflection coefficient r as $\phi = -\arg(r)$ and $R = |r|^2$, respectively. When both power reflection coefficients upper and under the core are equal to 1, the waveguide supports guided modes and is not so functional. On the other hand, when $R \leq 1$ at least upper or under the core, the waveguide supports leaky (quasi-guided) modes. The radiation loss α_N of Nth leaky mode is given by

$$\alpha_N = 2.17(2 - R_1 - R_2) \frac{\tan \theta_N}{d_{ce}} \quad [dB/m] \tag{2}$$

where R_1 and R_2 are the power reflection coefficients upper and under the core, respectively, and d_{ce} is the equivalent thickness of core involving the penetration of the field into the cladding[2]. In this case, the radiation loss depends on the polarization, wavelength, and the

mode number (propagation angle). By utilizing these dependencies, we can construct some functional waveguide devices such as polarizers, wavelenth filters, polarization splitters, and mode filters as shown in Fig. 2.

[Analysis and intuitive design]

Analysis of multilayer cladding waveguides is possible by the transfer matrix method[1, 4, 12], the system interference matrix method[2, 7, 21], the equivalent network method[10], the transverse resonant method[22] (these are almost equivalent to each other), bounded Finite Element Method[15] and a numerical method using the analyticity of the dispersion relation[18].
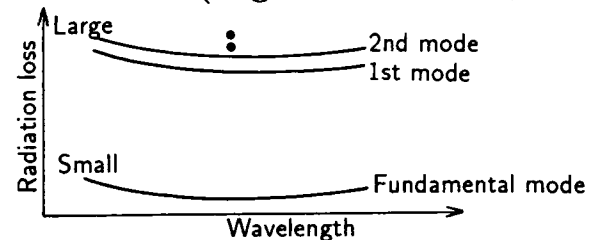
ARROW (Anti-resonant reflecting optical waveguide)[1, 2, 3] and ARROW-B[9, 13] are functional waveguides utilizing multilayer claddings. Since the cladding of ARROW waveguides consists of two layers, its modal characteristics can be calculated analytically[7, 21]. Thus the intuitive design of functional device is also possible from these explicit representations of modal characteristics, and a polarizer utilizing Form birefringence in the first cladding[19], compact integrated structure of ARROW and photodetector[14], wavelength filters using resonance [11] and grating coupling[5, 6], remote switch[20] and optical interconnects by the vertical stacked

• **Low loss single mode waveguide**
(Higher mode filter)

• **Polarizer**
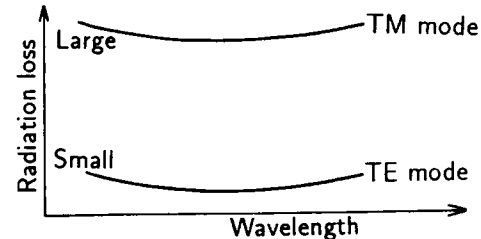
(Suitable for polarization diversity detection)

• **Wavelength filter**
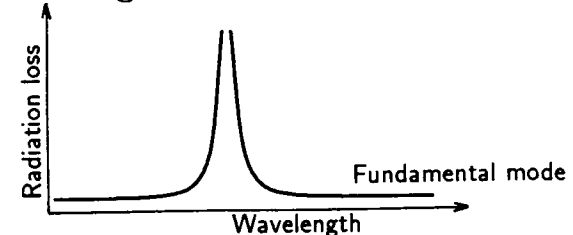
(Suitable for integration with photodetector)

Fig. 2. Functions achievable by multilayer cladding waveguides.

configuration[7, 23] have been proposed. The vertical stacking of ARROW's is advantageous to integrated photonics because of its ease of control of coupling characteristics[17].

[Design by numerial synthesis]

On the other hand, in the case of multilayer cladding involving more than 3 layers, the intuitive design is no longer so easy and some optimization techniques are needed to achieve required characteristics. However, these techniques sometimes end in failure to reach an optimum solution when the number of parameters is somewhat large and/or the objective function involves some singular points or local minimums in the space of parameters.

To discover some multilayer structures satisfying the required characteristics, we developed a novel numerical synthesis method of optical waveguide named random sampling method[16]. The block diagram of this method is shown in Fig.3.

Fig. 3. Block diagram of random sampling method for discovering novel waveguide structure.
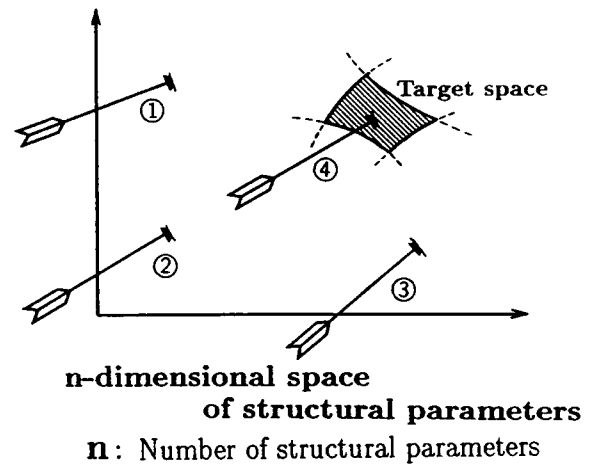
Fig. 4. Similarity of random sampling method to the shooting of arrows.

This method is similar to the randam shooting of arrows in the space of structual parameters, as shown in Fig.4. When this method is applied to multilayer cladding waveguides, the refractive index and the thickness of each cladding layer are set automatically based on the random number series generated from an initially given seed number, and the propagation constant and the propagation loss of modes are analyzed by using some analysis method like the interference matrix method[2, 7, 21]. The resu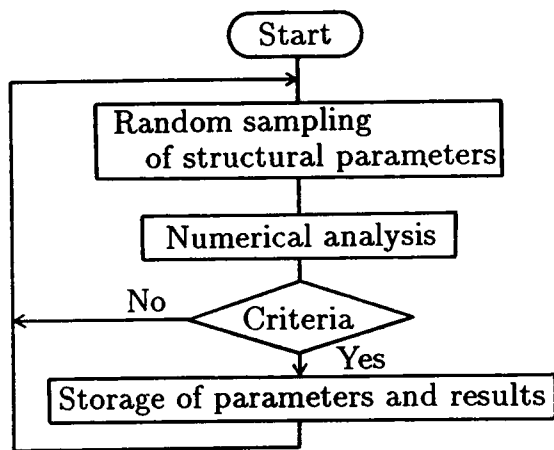lts are compared with the criteria, and if the criteria are satisfied, the parameters and the calculated characteristics are stored in a memory. As for the criteria, we can set any kinds of conditions appropriate to the desired characteristics, e.g., the condition that the propagation loss of TE fundamental mode is smaller than 0.1 dB/cm and that of all TM modes are larger than several tens dB/cm for polarizers with high extinction ratio. The same routine is repeated by setting the next series of random numbers generated from the seed number. By using this method, a narrow band wavelenth filter[16] and some polarizers with high extinction ratio were discovered.

The purpose of this method is not to optimize a well known structure but to discover unknown and novel structures. In addition, our method can reach a solution within reasonable time even when there are some singular points in the space of parameters.

Multilayer cladding waveguides have possiblity for achiving many kinds of functional divices, and are suitable for vertical integration based on the stacked configuration[7, 23]. This configuration will enable us the 3-dimensiosnal integrated photonics.

References

[1] M. A. Duguay, Y. Kokubun, T. L. Koch and L. Pfeiffer : *Appl. Phys. Lett.*, vol. 49, p. 13, 1986.

[2] Y. Kokubun, T. Baba, T. Sakaki and K. Iga : *Electron. Lett.*, vol. 22, p. 892, 1986.

[3] T. L. Koch, U. Koren, G. D. Boyd and P. J. Corvini, M. A. Duguay: *Electron. Lett.*, vol. 23, p. 244, 1987.

[4] A. Ghatak, K. Thyagarajan and M. R. Shenoy: *J. Lightwave Tech.*, vol. 5, p. 660, 1987.

[5] T. L. Koch, P. J. Corvani, W. T. Tsang, U. Koren and B. I. Miller: *Appl. Phys. Lett.*, vol. 51, p. 1060, 1987.

[6] T. L. Koch, E. G. Burkhardt, F. G. Storz, T. J. Bridges and T. Sizer, II: *J. Quantum Electron.*, vol. 23, p. 889, 1987.

[7] T. Baba, Y. Kokubun, T. Sakaki and K. Iga: *J. Lightwave Tech.*, vol. 6, p. 1440, 1988.

[8] T. Baba, Y. Kokubun and Y. Mera: *Top. Meet. Integrated and Guided-Wave Optics (IGWO'89)*, Houston, TuBB5, 1989.

[9] T. Baba and Y. Kokubun: *Photo. Tech. Lett.*, vol. 1, p. 232 1989.

[10] W. Jiang, J. Chrostowski and M. Fontaine: *Optics Commun.*, vol. 72, p. 180, 1989.

[11] T. Baba, Y. Kokubun and H. Watanabe: *J. Lightwave Tech.*, vol. 8, p. 99, 1990.

[12] J. Kubica, D. Uttamchandani and B. Culshaw: *Opt. Commun.*, vol. 78, p. 133, 1990.

[13] R. A. Solef and K. J. Ritter: *Opt. Lett.*, vol. 15, p. 792, 1990.

[14] T. Baba and Y. Kokubun: *Appl. Opt.*, vol. 29, p. 2781, 1990.

[15] J. C. Grant, J. C. Beal and N. J. P. Grenette: *Photo. Tech. Lett.*, vol. 2, p. 890, 1990.

[16] S. Asakawa and Y. Kokubun: *2nd Top. Meet. Integrated Photonics Research (IPR'91)*, Monterey, ThG2, 1991.

[17] M. Mann, U. Trutschel, C. Wächter, L. Leine and F. Lederer: *Opt. Lett.*, vol. 16, p. 805, 1991.

[18] R. E. Smith, S. N. Houde-Walter and G. W. Forbes: *Opt. Lett.*, vol. 16, p. 1316, 1991.

[19] Y. Kokubun and S. Asakawa: *3rd Microoptics Conference (MOC'91)*, Yokohama, E2, 1991.

[20] M. Cantin, C. Carignan, R. Côté, M. A. Duguay, R. Larose, P. LeBel and F. Ouellette: *Opt. Lett.*, vol. 16, p. 1738, 1991.

[21] T. Baba and Y. Kokubun: *J. Quantum Electron.*, vol. 28, p. 1689 1992.

[22] W. Huang, R. M. Shubair, A. Nathan and Y. L. Chow: *J. Lightwave Tech.*, vol. 10, p. 1015, 1992.

[23] S. Asakawa, Y. Kokubun, T. Baba and M. Ohyama: submitted to *Top. Meet. Integrated Photonics Research (IPR'93)*, Palm Springs, 1993.

Integrated Optics Design 2

OMD 3:30pm-5:00pm
Oleander Room

Laura A. Weller-Brophy, *Presider*
3M Research Laboratories

Design and Fabrication of Efficient Fiber Microlenses

Herman M. Presby

AT&T Bell Laboratories

Crawford Hill Laboratory

Holmdel , N. J. 07733-0400

(908) 888-7150

INTRODUCTION

Microlenses, fabricated directly on the ends of optical fiber, are used to improve the coupling of light from semiconductor lasers into the fiber. They achieve this by matching the very much smaller mode of the laser to that of the fiber. The microlenses are generally fabricated by tapering the fiber down to a point and melting the end. The resultant lenses are hemispherical in shape and typically collect less than 50%, and at best 55% of the available laser radiation.

A substantially better microlens can be designed with coupling efficiency approaching 100% when a hyperboloid of revolution replaces the hemispherical shape. We have fabricated such hyperbolic microlenses which demonstrate near optimal performance [1].

HEMISPHERICAL MICROLENSES

In order to design the ideal microlens it is important to understand the limitations of the common hemispherical microlens.

It is well known that the major limiting feature of macroscopic spherical lenses in many applications is spherical aberration. Hemispherical microlenses suffer an additional penalty however, called truncation loss, that results from their small size relative to the width of the light beam. Consider the Hemisperical microlens shown in Figure 1a. and in schematic form in Figure 1b. Geometrical optics shows that a maximum acceptance angle exists beyond which incident rays are rejected. This effect is quantified in the curve marked truncation loss in Figure 2. Note, of course, that the smaller the lens radius, the smaller the aperture and the greater the truncation loss. This loss is small for relatively large lenses, i.e., on the order of 20 um in radius, but such large

lenses are incompatible with matching the modes of the laser and the fiber.

Mode mismatch is also strongly dependent on lens radius. Maximum coupling occurs when the center of curvature of the laser wavefront is located at the focal point of the spherical lens. This source of loss is quantified in Figure 2 by the curve labelled mode-mismatch. There is an optimum lens radius (6.25 um) at which the two modes match perfectly and the loss is zero. For lenses of larger radii the loss increases rapidly. For the large lens radii necessary to avoid fiber truncation , mode-mismatch loss becomes prohibitive.

Two other sources of loss to be considered in the lens design are spherical aberration and Fresnel reflections at the lens surface. These losses are also shown in Figure 2 and amount to about 0.3 dB and 0.2 dB respectively.

HYPERBOLIC LENSES

The three sources of loss affecting hemispherical microlenses: fiber truncation, mode-mismatch, and spherical aberration can be eliminated in an appropriately designed lens. The ideal lens should be free of spherical aberration, have a large aperture to collect all of the laser radiation, and have a focal length that perfectly matches the laser and fiber modes. This lens shape can be shown to be a hyperbola [2], which essentially suffers only from Fresnel reflection loss which can be eliminated however, by appropriately coating the lens.

A hyperbolic microlens , fabricated by a laser micromachining technique [3], is shown in Figure 3a. and in schematic form in Figure 3b for matching laser mode radius of 1 um to a fiber mode radius of 5 um. Also shown are two rays and the hyperbolic asymptotes. The acceptance cone of the hyperbolic lens, while much larger than that of the hemispherical lens, does of course have a limit being just smaller than than the cone traced out by the asymptotes. This is generally not a loss factor for most semiconductor light sources.

REFERENCES

1. H. M. Presby and C. A. Edwards, 'Near 100% efficient fibre microlenses', Electronics Letters 1992 vol.28 No.6, pp. 582-584.

2. C. A. Edwards, H. M. Presby and C. Dragone, 'Ideal microlenses for laser to fiber coupling', to be published in Journal of Lightwave Tech.

3. H. M. Presby, A. F. Benner, and C. A. Edwards, 'Laser micromachining of efficient fibre microlenses', Appl. Opt., 1990, 29,(18),pp.2692-2695.
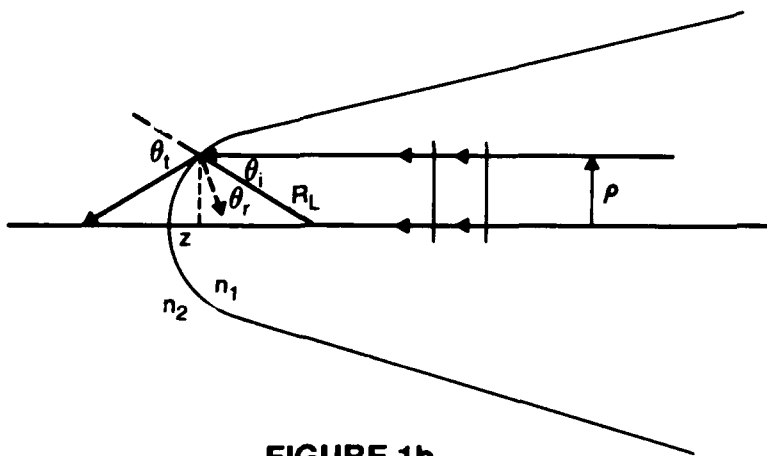
HEMISPHERICAL LENS

HYPERBOLIC LENS

FIGURE 1a

FIGURE 3a
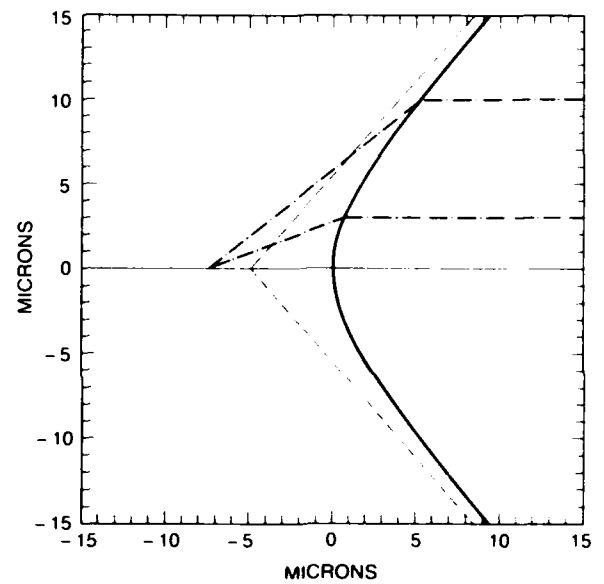

FIGURE 1b

FIGURE 3b

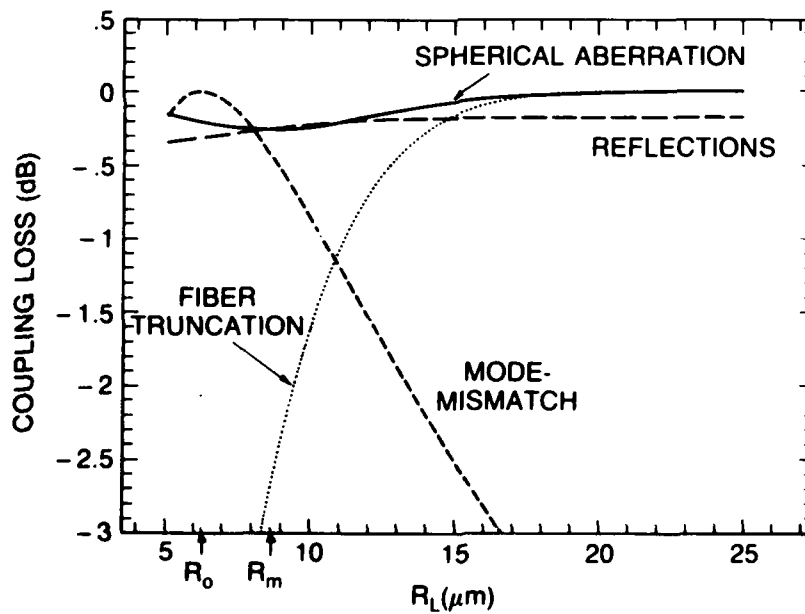## SOURCES OF LOSS FOR HEMISPHERICAL LENS

FIGURE 2

Design and Fabrication of Integrated-Optic Sensors

M. Haruna

Department of Electronic Engineering,
Faculty of Engineering, Osaka University
2-1 Yamada-Oka, Suita, Osaka 565, Japan
TEL +81-6-877-5111   ext 5007

1. Introduction

In the past more than ten years, a variety of optical waveguide sensors have been reported so far, i.e, temperature, pressure and humidity sensors [1]. In contrast to fiber-optic sensors, however, high sensitivity is not attained in such waveguide sensors because a thin-film waveguide used as a sensing transducer is less than a few tens millimeters. On the other hand, an important role of integrated optics in the sensing use is that a rugged and compact sensing system is realized by integration of all optical components used for signal processing where a fiber butt-coupled to a waveguide is often used as a sensing probe. In this sense, our effort has been focused on optical integration of the heterodyne interferometer that is commonly used for velocity and displacement/position with high accuracy. This paper describes design and fabrication of the integrated-optic (IO) heterodyne interferometers in $LiNbO_3$.

2. Key waveguide components in Ti-diffused Z-propagating $LiNbO_3$

A typical bulk-optic interferometer consists of a Bragg cell (frequency shifter), half-wave plate and polarization beam splitter. These functional bulk-optic components are replaced by the waveguide counterparts via the electrooptic effect of $LiNbO_3$. In an IO heterodyne interferometer, the $LiNbO_3$ waveguide should meet the following requirements: (1) high resistance to the optical damage at the visible or near infrared; (2) support of both TE and TM modes in the waveguide; and (3) a sufficiently small modal birefringence of the waveguide for stable detection of phase difference between two modes without any specific temperature stabilization. These requirements are satisfied only by the use of Ti-diffused waveguides in Z-propagating $LiNbO_3$, although the guided modes are controlled via the small electrooptic coefficient r_{22} (=$-r_{61}$). Since there had been few reports on waveguide components/devices in Z-propagating $LiNbO_3$, however, key waveguide components were fabricated and characterized before design of IO heterodyne interferometers.

2.1 Frequency shifters First, optical frequency shift of a reference guided wave is easily attained by a serrodyne single-side band (SSB) modulator. The image-side band suppression ratio of -30dB was obtained at $0.633\mu m$ in a 10-mm long SSB modulator having the half-wave voltage of 14V. In the SSB modulator, however, the frequency shift is usually limited below a few MHz due to the flyback time of a sawtooth-wave voltage applied to the SSB modulator. In contrast, a wideband frequency shifter up to 1.6GHz in Z-propagating $LiNbO_3$ was proposed in which two polarization interferometers were combined, as shown in Fig. 1 [2].

2.2 TE-TM mode converter A TE-TM mode converter corresponding to a wave plate is required for polarization rotation in a heterodyne-detection scheme. An efficient mode conversion can be achieved easily by three planar electrodes placed on a channel waveguide in Z-propagating $LiNbO_3$, as shown in Fig. 2, because a modal birefringence of the order of 10^{-5} is canceled out by an applied voltage without any periodic electrodes; accordingly, the mode conversion is almost independent of the wavelength [3]. The tested mode converter with 10-mm long electrodes exhibited the mode conversion efficiency of >98% with a drive voltage of 5.2V when the applied voltage for phase matching was 23V.

2.3 TE-TM mode splitter Unlike the mode converter, as discussed above, a remarkable

modal birefringence is required for a mode splitter which acts as a polarization beam splitter. A modal birefringence of the order of 10^{-4} is produced by direct metal cladding on a Ti-diffused waveguide even in an isotropic substrate of Z-propagating LiNbO3. Fig. 3 is a possible configuration of the mode splitter consisting of an asymmetric directional waveguide coupler with partial aluminum cladding [4]. The guide B (WB) is slightly wider than the guide A (WA) so that complete power transfer between two guides is attained only for the TE mode. Actually, the difference of the guide width is $0.2\mu m$ at $0.633\mu m$ when WA=$3\mu m$. Under this situation, the incident TM mode on the guide A transmits with no power transfer because of significant phase mismatch due to the aluminum cladding. TE and TM mode are thus split at the output end. In the fabricated mode splitter, the mode splitting ratio was 11 and 15 dB for the TE and TM modes, respectively.

3. Fabrication of waveguide interferometers

An IO heterodyne interferometer is formed by placing three functional components, as mentioned above, along an optical path which consists of Y-junction, crossed and bent waveguides. The interferometer becomes usually above 30mm in the visible and near infrared. A key technology in fabricating the IO interferometer is smooth patterning of 3 to 4 μm wide channel waveguides on the entire substrate surface. To do this, we developed the laser-beam (LB) writing system which could provide very smooth patterning of 3 to 8 μm wide channel waveguide in photoresist coated on a substrate in air with an accuracy of nearly $0.1\mu m$ over 10 $\times 10cm^2$ [5]. The system configuration is shown in Fig. 4. The waveguide patterning for IO interferometers takes typically within several minutes. In contrast, the LB direct writing of TiO2 channels on LiNbO3 allows us to fabricate Ti-diffused waveguides without photoresist [6].

4. Integrated-optic heterodyne interferometers

4-1 Laser Doppler velocimeters (LDVs) The reference-beam type of LDV with a fiber probe was fully integrated on a LiNbO3 chip, as shown in Fig. 5 [7]. A $0.84-\mu m$ LD was used as a light source. Since the coherent length of the LD was <30cm, a dummy fiber ended with aluminum-film coating was butt-coupled to the reference-arm waveguide in order to form an equal-path-length interferometer. Hybrid integration was performed by connecting the LiNbO3 chip, LD and APD via polarization-maintaining fibers; as a result, very stable velocity measurement could be achieved in freedom from an optical bench. In the device testing, the output light from the probing fiber illuminated a moving mirror through a quarter-wave plate. When the frequency shift fR of the reference light was 300kHz, the Doppler-shifted frequency fs was detected with the signal-to-noise ratio of >20dB. Time-division 2-D velocity measurement was also demonstrated by integration of a serrodyne SSB modulator and a high-speed switch on a chip pigtailed with two probing fibers [8]. On the basis of the LDVs described here, a miniature laser vibrometer in proton-exchanged LiNbO3 was reported [9].

4-2 Highly accurate displacement sensors In comparison with the LDVs, a more sophisticated heterodyne interferometer is used for measurement of displacement/position with an accuracy of the order of nanometer. This specific optics is the so-called two-frequency polarization interferometer in which a Zeeman laser is used as a light source to generate two mutually orthogonal linearly polarized light with a frequency separation of a few hundred kHz (=2fR). In the optical integration, a key waveguide component is the two-frequency shifter consisting of a TE-TM mode converter and a serrodyne SSB modulator, as shown in Fig. 6. This component can convert a linearly polarized input light into two orthogonal linear polarizations with a frequency separation of 2fR. The configuration of a LiNbO3 chip for displacement measurement is shown in Fig. 7, where either TE or TM mode is excited at the input end [4]. Because of the use of Z-propagating LiNbO3 as the substrate, our theoretical results indicate that the measurement error is only 1nm with respect to the substrate temperature

change of 1 °C at 0.633 μm although the chip length is as long as 47mm. In the experiment, the displacement of PZT was measured by detection of the reference and signal beats from the LiNbO3 chip, resulting in an error of ±3nm without temperature stabilization of the substrate.

5. Conclusion

The IO heterodyne interferometers in Ti-diffused Z-propagating LiNbO3 have been described briefly as well as design concepts of key waveguide components. The present IO interferometers have almost the same function as the conventional interferometers consisting of discrete bulk-optic components, except their compactness and ruggedness. At the next stage, novel functional IO sensing devices should be developed taking the advantage of inherent features of the guided-wave technology such as high-speed modulation, low-voltage drive, easy control of polarization, sharp wavelength filtering, and so on. Waveguide lasers/amplifiers and nonlinear-optic waveguide devices will also be key components in the IO sensing devices.

References

1. for example, L.M. Johnson, F.J. Leonberger and G.W. Pratt: Appl. Phys. Lett. 41, p.134 (1982).
2. M. Haruna, T. Yamasaki, H. Hirata, H. Toda and H. Nishihara: OFS'90, Proc. p.113, Sydney, Dec. 1990.
3. M. Haruna, J. Shimada and H. Nishihara: Trans. IEICE of Japan, E69, p.418 (1986).
4. H. Toda, M. Haruna and H. Nishihara: J. Lightwave Technol. 9, p.683 (1991).
5. M. Haruna, S. Yoshida, H. Toda and H. Nishihara: Appl. Opt. 26, p.4587 (1987).
6. M. Haruna, Y. Murata and H. Nishihara: Jpn. J. Appl. Phys. 31, Part 1, p.1593 (1992).
7. H. Toda, M. Haruna and H. Nishihara: J. Lightwave Technol. LT-5, p.901 (1987).
8. H. Toda, K. Kasazumi, M. Haruna and H. Nishihara: ibid. LT-7, p.364 (1989).
9. P.G. Suchoski, J.P. Waters and M.R. Fernald: IEEE Photo. Technol. Lett. 2, p.81 (1990).
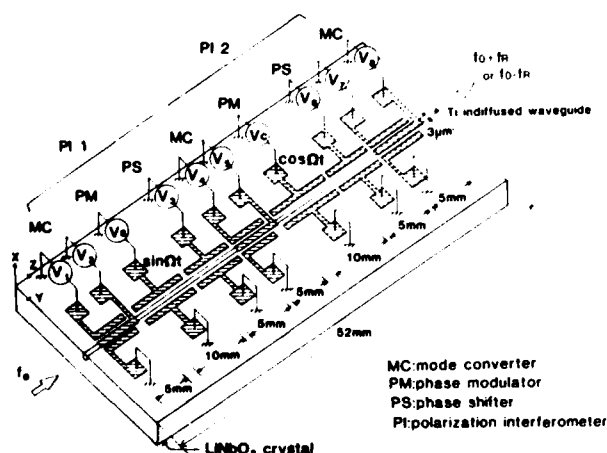
Fig. 1 1.6-GHz bandwidth frequency shifter consisting of two polarization interferometers.
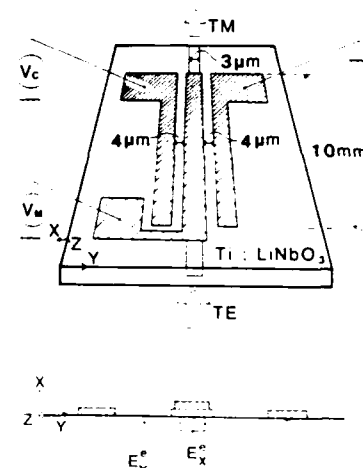
Fig. 2 TE-TM mode converter with three planar electrodes.

Fig. 3 TE-TM mode splitter consisting of an asymmetric directional coupler with partial aluminum cladding.
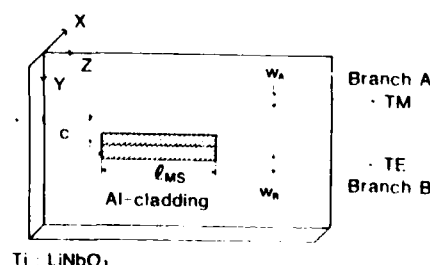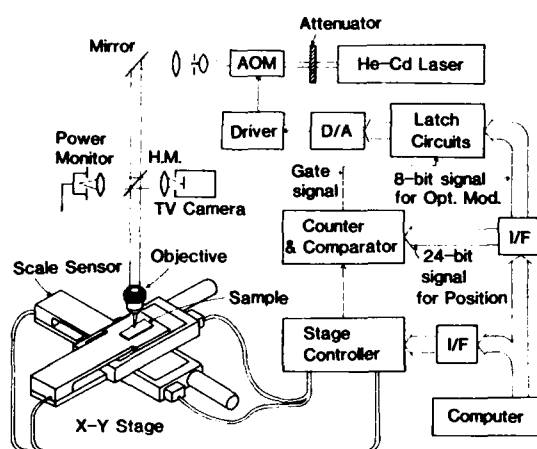
Fig. 4 Laser-beam writing system for channel waveguide patterning.
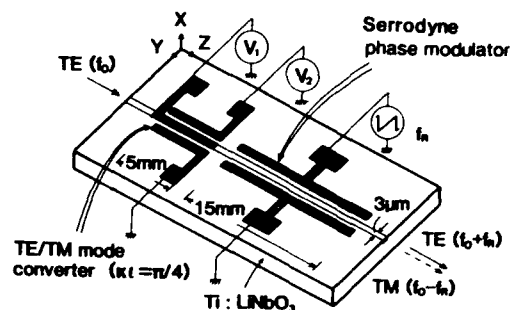
Fig. 6 Two-frequency shifter to convert a linearly polarized input light into TE and TM modes with a frequency separation of 2fR at the output end.
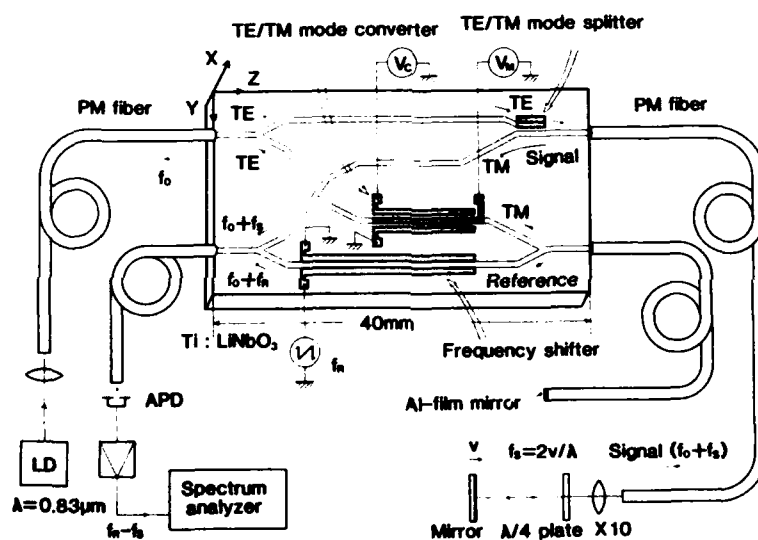
Fig. 5 IO laser Doppler velocimeter with a fiber probe.
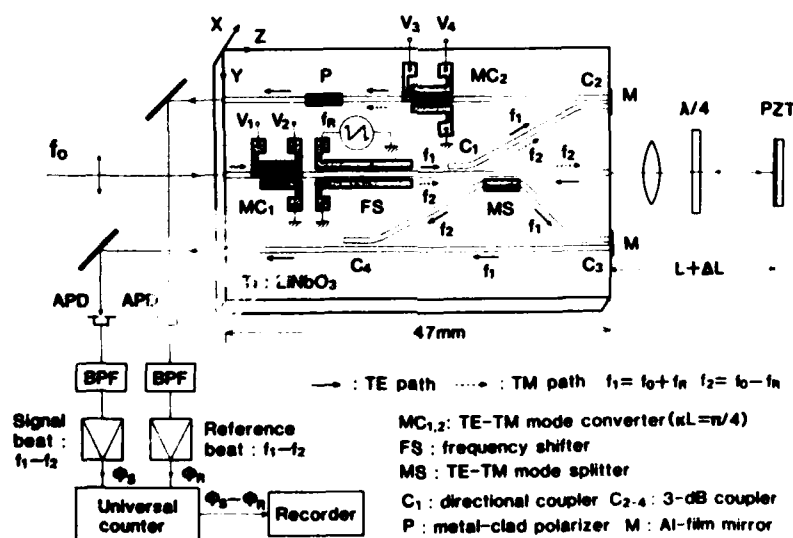
Fig. 7 IO heterodyne interferometer for highly accurate displacement measurement.

CURRENT ISSUES IN
FREE-SPACE DIGITAL OPTICAL SYSTEMS

H. S. Hinton
*AT&T Bell Laboratories**
Naperville, Illinois

1 Introduction

Over the past 9 years there has been an increasing interest in digital optical systems, both computing and switching. It began in 1984 with a demonstration by USC of an optical master-slave flip-flop based on Hughes liquid crystal light valves as optical logic gates and holographic interconnects between the gates.[1] Since then there have been numerous demonstrations of free-space digital optical systems including an simple optical computing system (1990)[2] and several switching fabrics $System_1$ (1988),[3] $System_2$ (1989),[4] $System_3$ (1990),[5] $System_4$ (1991),[6] and $System_5$ (1993)[7] demonstrated by AT&T. Although there has been tremendous progress in these optical systems as a result of advances in the S-SEED[8] device technology and the optical interconnection hardware, the maximum bit-rate through any of these systems is on the order of 1 Mb/s. This limitation in speed is the result of the inability to obtain sufficiently high power, single frequency, diffraction-limited optical sources, the large interconnect losses between active devices, and the large amount of switching energy required by the S-SEED devices. To reduce the switching energy of the devices, in addition to adding more functionality, the SEED technology has evolved to FET-SEEDs[9] which integrate FET structures with SEED modulators and detectors. This new technology yields switching energies that are less than 100 fJ compared to the 4 pJ required by standard SEED devices with demonstrated speeds greater than 100 Mb/s.[10]

2 Free-Space Digital Optical Hardware

To pursue connection-intensive architectures with large chip-to-chip connectivity, most of the proposed and demonstrated photonic interconnection networks and optical pipeline processors have been multi-stage systems. A general purpose, modular, optical hardware module (OHM) is used to package the components required for each stage. A complete system would then be composed of a number of concatenated OHMs. Figure 1 illustrates the OHMs used by $System_3$[6] and $System_4$.[7] These OHMs are composed of four basic components;[11] 1) S-SEED array, 2) spot array generator, 3) optical interconnect, and 4) beam combiner.

Another area of research concerns the packaging of these free-space systems so that they will be stable over both time and temperature. Figure 2 schematically illustrates the collection of optical components (77 surfaces) that must be traversed by every signal going from one OHM to another in $System_4$.

This system has a maximum defocus limit per stage of 10 µm for each of the spots moving through the system. This maximum defocus is a function of variations in the tilt of the device array about the x- and y-axes, image tilt due to lens fabrication and mounting, misalignment of the array on the z-axis, and field curvature of the optical system. These OHMs also require a lateral shift per spot of no more than 2 µm. This offset is the result of misalignment of the device array with respect to the x- and y-axis, non-telecentricity and distortion of the optical system, variation
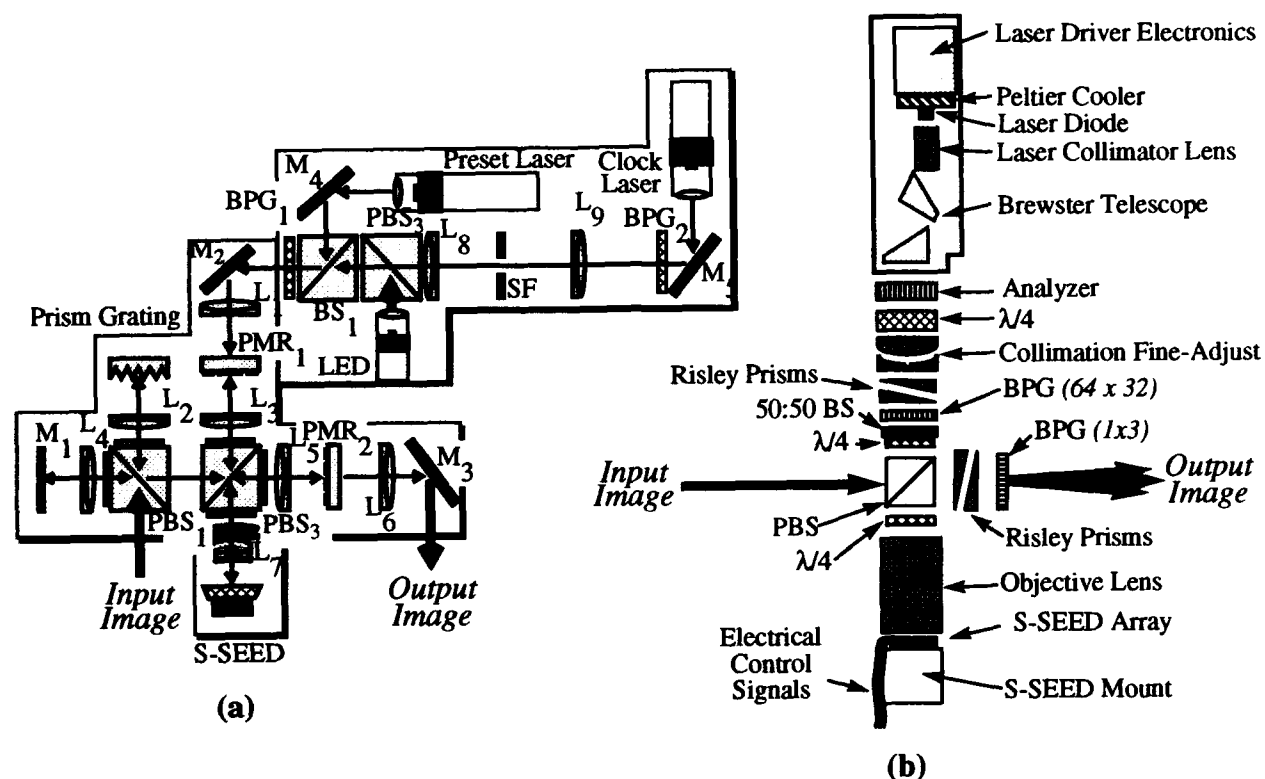
Figure 1. Optical hardware modules: (a) *System₃*: OHM based on image plane interconnects and lossless space multiplexed beam combination, (b) *System₄*: OHM based on pupil-plane interconnects and lossy space multiplexed beam combination.

in the focal length of the lenses, wavelength variation, and mechanical roll about the z-axis. Also, the optical system required to move an image from one device array to another can be rather complex. This complexity implies the need for the control of accumulated aberrations. As an example, the described system required the system distortion to be better than 0.1% (good microscopes are ~1%) with a field flatness of less than 1 μm.[7]

Although there has been significant progress in the development of optical hardware for free-space systems, design rules and

Figure 2. Optical Path Through OHM: AT&T *System₄*

techniques must be identified that will lead to optomechanically stable diffraction limited optical systems. In addition, test equipment and procedures must be developed to verify that the hardware meets the system requirements.

3 System Demonstrators

The evolution of the AT&T switching fabric demonstrators is shown in Figure 3. In this fabric the

fabric topology is shown for each of the demonstrators. Table 1 lists the attributes of each of these system experiments.

Table 1: AT&T Free-Space Photonic Switching System Specifications.

	$System_1$ (1988)	$System_2$ (1989)	$System_3$ (1990)	$System_4$ (1991)	$System_5$ (1993)
Supported Channels	2	32	64	1024	32
System Bit-Rate	10 Kb/s	30 Kb/s	100 Kb/s	1 Mb/s	50 Mb/s
Flat Field Angle	1°	1.6°	3.2°	6.7°	4.5°
Chip/System Pin-outs	12 / 20	256 / 1,024	1,024 / 3,072	10,240 / 61,440	192 / 960
Optics	Catalog	Catalog	Catalog	Custom	Custom
Mechanics	Catalog	Catalog & Custom	Custom	Custom	Custom
System Area	32 ft^2	16 ft^2	6 ft^2	0.78 ft^2	1.16 ft^2
Control	Optical	Optical	Optical	Electrical	Optical
Assembly & Alignment Time	Days	Days	8 Hours	3 Hours	3 Hours
Lifetime	< 8 Hours	< 24 Hours	< 6 Days	> 5 Weeks	??

4 Discussion

In order for this connection-based hardware to become a reality in the marketplace, a packaging technology is required that is stable, reliable, inexpensive, and manufacturable. Although AT&T and others have made significant advances with their free-space system demonstrators, most of these objectives have not been fully realized. More focus is needed on the design and testing issues associated with building stable, reliable optical hardware. As with the existing high speed electronic technology, the development of hardware design rules, testing tools, and verification procedures will be required for the eventual deployment of this free-space digital optical technology.

REFERENCES

[1] A. A. Sawchuk and T. C. Strand, "Digital Optical Computing," *Proceedings of the IEEE*, Vol. 72, No. 7, July 1984, pp. 758-779.

[2] M. E. Prise, N. C. Craft, M. M. Downs, R. E. LaMarche, L. A. D'Asaro, L. M. F. Chirovsky, and M. J. Murdocca, "Optical digital processor using arrays of symmetric self-electro-optic effect devices," *Applied Optics*, Vol. 30, No. 17, June 10, 1991, pp. 2287-2296.

[3] E. Kerbis, T. J. Cloonan, and F. B. McCormick, "An all-optical realization of a 2x1 free-space switching node," *Photonics Technology Letters*, Vol. 2, No. 8, August 1990, pp. 600-602.

[4] T. J. Cloonan, M. J. Herron, F. A. P. Tooley, G. W. Richards, F. B. McCormick, E. Kerbis, J. L. Brubaker, and A. L. Lentine, "An all-optical implementation of a 3D crossover switching network," *IEEE Photonics Technology Letters*, Vol. 2, 1990, pp. 438-440.

[5] F. B. McCormick, F. A. P. Tooley, T. J. Cloonan, J. L. Brubaker, A. L. Lentine, R. L. Morrison, S. J. Hinterlong, M. J. Herron, S. L. Walker, and J. M. Sasian, "Experimental investigation of a free-space optical switching network by using symmetric self-electro-optic-effect devices," *Applied Optics*, vol. 31, no. 26, September 10, 1992, pp. 5431-5446.
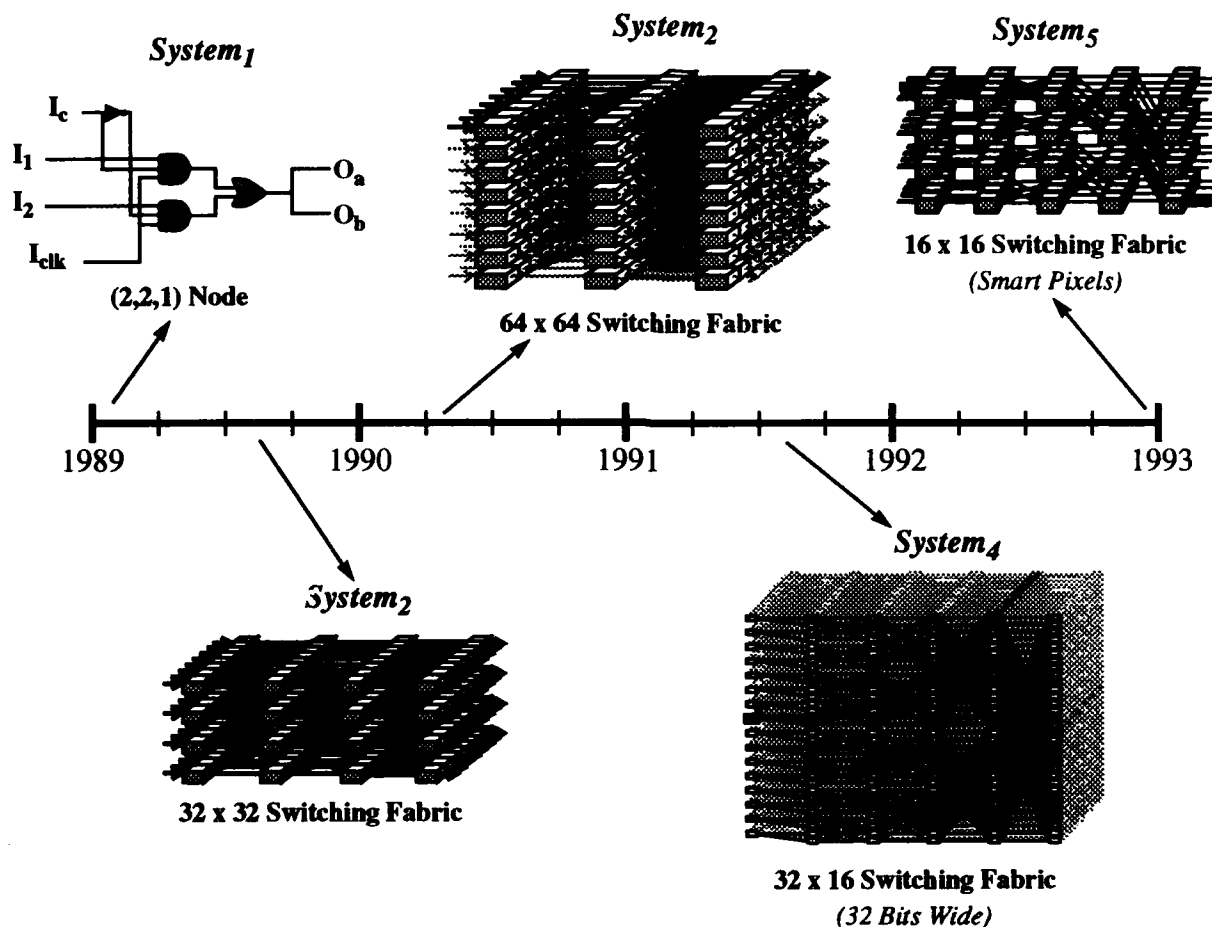
Figure 3. Evolution of AT&T free-space switching fabric demonstrators.

[6] F. B. McCormick, T. J. Cloonan, F. A. P. Tooley, A. L. Lentine, J. M. Sasian, J. L. Brubaker, R. L. Morrison, S. L. Walker, R. J. Crisci, R. A. Novotny, S. J. Hinterlong, H. S. Hinton, and E. Kerbis, "A six-stage digital free-space optical switching network using S-SEEDs," *Accepted for publication in Applied Optics.*

[7] F. B. McCormick et al, *Submitted as postdeadline paper to the 1993 Topical Meeting on Photonics in Switching, Palm Springs, CA.*

[8] H. S. Hinton and A. L. Lentine, "The SEED Technology," *IEEE Circuits & Devices,* To be published.

[9] D. A. B. Miller, M. D. Feuer, T. Y. Chang, S. C. Chunk, J. E. Henry, D. J. Burrows, and D. S. Chemla, "Field-Effect Transistor Self-Electro-optic Effect Device: Integrated Photodiode, Quantum Well Modulator and Transistor," *IEEE Photonics Technology Letters,* Vol. 1, No. 3, March 1989, pp. 62-64.

[10] A. L. Lentine et al, "4x4 arrays of FET-SEED embedded control 2x1 switching nodes," *Topical Meeting on Smart Pixels,* Santa Barbara, CA, August 1992, Postdeadline paper.

[11] H. S. Hinton, "Photonic Switching Fabrics,", *IEEE Communications Magazine,* Vol. 28, No. 4, April 1990, pp. 71-89.

Diffractive Optics
Contributed Paper Preview

OTuA 9:00am-10:30am
Oleander Room

Douglas C. Sinclair, *Presider*
Sinclair Optics

Hybrid Diffractive Elements for Planar Optics

Raymond K. Kostuk, James M. Battiato*, Charles W. Haggans, and Gene Campbell

Electrical and Computer Engineering Department, and
Optical Sciences Center,
University of Arizona
Tucson, AZ. 85721, USA
(602) 621-6172

Planar free-space optical components offer many advantages for compact micro optical systems. This configuration combines the 2 dimensional properties of free-space optics with a guiding substrate. The guiding substrate folds the optical system reducing its size and serves as a platform for cascading several optical elements in series. These components have been discussed for use in optical interconnects[1], and have other potential applications in fiber communication and sensor systems, and optical data storage heads. These systems must incorporate several optical functions including beam focusing, splitting, and input and output coupling to the substrate. These tasks can be accomplished using lithographic binary gratings or interferometrically generated holographic volume elements. Each grating type has distinct advantages and disadvantages for planar optics. In this presentation these factors are considered in the design of a fiber optic array tap.

Planar Optic Functional Requirements

Optical interconnects is a potential application area for planar optical systems. At the board connection level in an electronic processor system several planes must be connected. When these planes are separated over considerable distances alignment of free-space components becomes a problem, and the optical signals must be guided using fibers or other types of waveguides. Distributing optical signals from the guide can be difficult. One solution is to use a planar optical system to tap signals from a fiber or fiber array and

distribute them in a plane (illustrated in Figure 1). This element can be used to broadcast a high speed clock or other types of synchronous signals between several processing boards or between different computers.

In this device light from a fiber (or fiber array) is collimated by an on-axis lens (or lenslet array), and then coupled into the substrate through grating G1. This is a multiplexed grating which splits the incident collimated beam into several diffracted beams and a non-diffracted component. The collimated zero-order component is refocused by an on-axis lens back into a fiber, and transmitted to a subsequent plane in the system. If the spatial frequency of the input coupler is large enough, the diffracted beams will exceed the critical angle of the substrate, and propagate in a TIR mode. This allows the thickness (d) of the substrate to be reduced relative to that needed with smaller spatial frequency input couplers which require reflective surfaces on the substrate[1]. At each detector location an off-axis beam illuminates a lens which focuses light on-axis to a detector. The efficiencies of these lenses must be varied in order to provide equal power to each detector. In summary the different optical functions required for this device are: 1) on-axis beam focusing or collimation, 2) substrate input coupling, 3) multiple beam splitting, and 4) off-axis output coupling with variable efficiency.

A number of trade-offs must be considered when attempting to realize these functions with either volume or surface relief gratings. For example, consider the on-axis focusing element used in the system illustrated in Figure 1. If the element is formed interferometrically the grating period will be infinite at the aperture center and decrease at the edge. This causes a variation in diffraction efficiency across the lens aperture as shown in Figure 2. These values were computed using rigorous coupled wave theory[2] for a 10 μm thick emulsion with a refractive index of 1.51 at a wavelength of 780 nm. The lens has an on-axis focus which is 1.0 mm from the film plane and a 500 μm diameter. Several diffraction orders exist near the center of the lens, and then decrease in strength with the +1 order dominating near the aperture edge.

A better technique for making an on-axis lens is with binary optics. Using approximate scalar theory the efficiency (η) is a function of the number of etch levels (N), and can be expressed as $\eta = \left[\frac{\sin(\pi/N)}{\pi/N}\right]^2$. However, this relation is only true for gratings with a period to wavelength ratio (Λ/λ) which is greater than about 5. Below that level resonance effects change the diffraction process and decreases the efficiency[3]. This limits the useful NA to about 0.2 which is suitable for single mode fibers. Another type of lens used in this system is an output coupling element which is illuminated with an off-axis beam from within the substrate and focuses light on-axis. In this case the required grating periods and step feature sizes exceed the limit of conventional binary lens fabrication methods. Fortunately these large spatial frequencies can be realized with volume holograms, and complement the characteristics of binary optics for realizing systems like the fiber array tap.

The trade-offs between binary optics and volume holograms for the other components in the fiber array tap and its experimental performance will be examined in this presentation.

References

1. J. Jahns and A. Huang, " Optical interconnects using top-surface-emitting microlasers and planar optics," Appl. Opt., **31**, 592-597 (1992).

2. M. G. Moharam and T. K. Gaylord, "Three-dimensional vector coupled-wave analysis of planar grating diffraction," J. Opt. Soc. Am., **73**, 1105-1112 (1983).

3. T. Shiono, M. Kitagawa, K. Setsune, and T. Mitsuyu, "Reflection micro-Fresnel lenses and their use in an integrated focus sensor," Appl. Opt., **28**, 3434-3442 (1989).
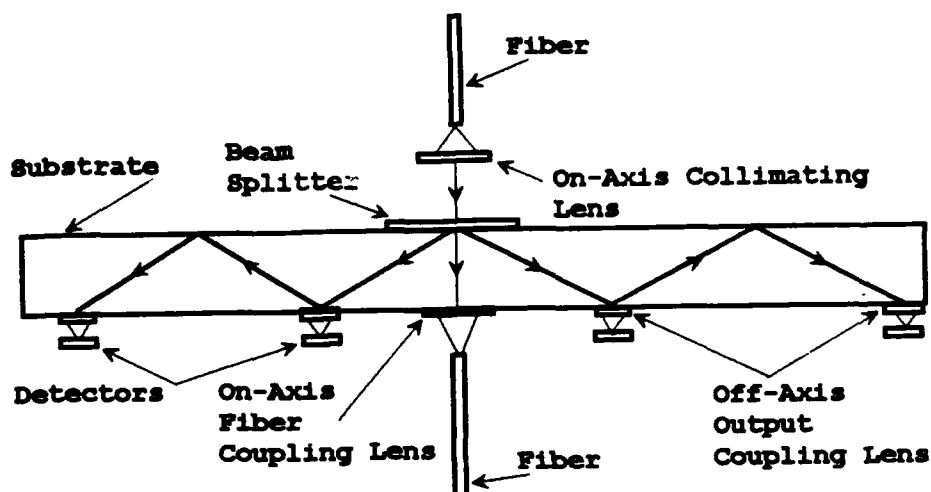
Figure 1. Schematic of fiber optic tap using a hybrid binary and volume hologram micro optic system.

DE Across F/2 Lens Aperture
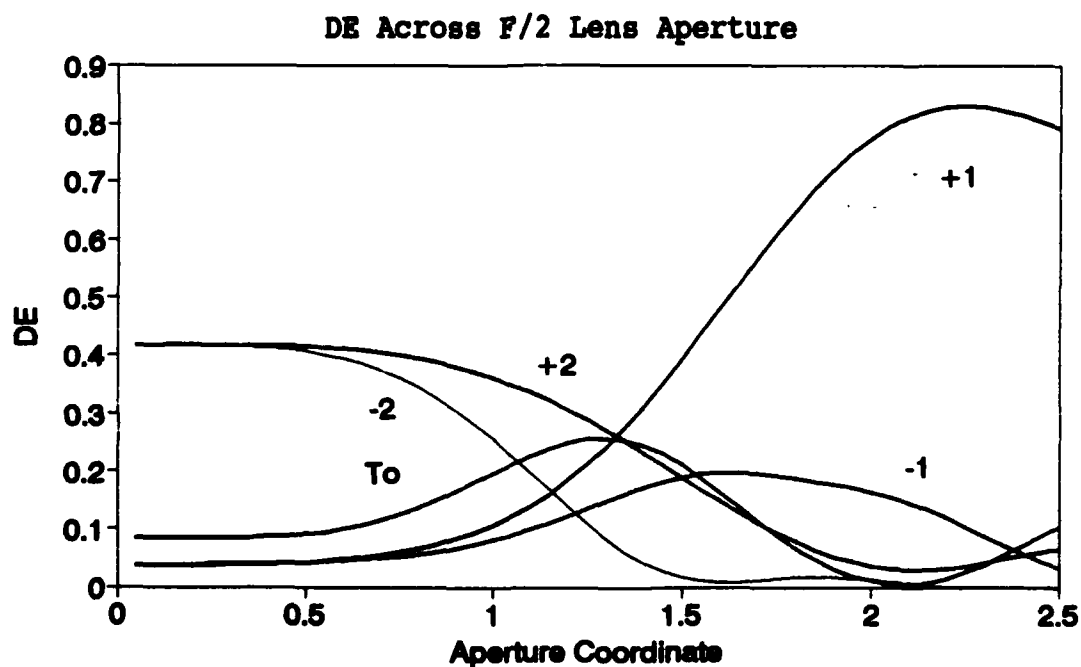
Figure 2. Diffraction efficiency across the aperture of an on-axis f/2 lens calculated using rigorous coupled wave theory.

Diffractive Optical Elements within a Matrix-Matrix Crossbar

P. Blair, M.R. Taghizadeh, J. Turunen and B. Robertson

Department of Physics,

Heriot-Watt University,

Edinburgh

EH14 4AS, UK

Tel: +44−31−449−5111

Fax: +44−31−451−3136

E-mail: PHYPB1@UK.AC.HW.CLUST

The Optically Connected Parallel Machine (OCPM) is a matrix-matrix crossbar interconnect designed to provide high speed links between electronic processors. This is achieved using an electrically addressed spatial light modulator (SLM) in a free-space optical system. At the current stage of development OCPM has a capacity for interconnecting 16 processors, although the ultimate aim is the connection of 64 processors at a bandwidth of 640 Mbit s^{-1} per processor. Input and output is via two 4×4 bundles of optical fibres. The matrix-matrix crossbar interconnection scheme requires, for the 16 channels to be fully interconnected, the input array to be fanned out (replicated) in two-dimensions over a 16×16 array of SLM pixels. After the SLM plane each of the 16 replicated images of the input array must be fanned in to form a 4×4 output array, so providing connection between any of the 16 input channels to 16 output channels. Figure 1 shows a simplified crossbar for a 2×2 array. It is in the fan-out/fan-in stage that diffractive elements have been utilized.

Fan-out of the input array is achieved using a synthetic binary surface-relief grating with a two-dimensional optimized periodic structure. The binary grating structure follows that used by Vasara *et al* [1]; it is a non-separable stripe-geometry
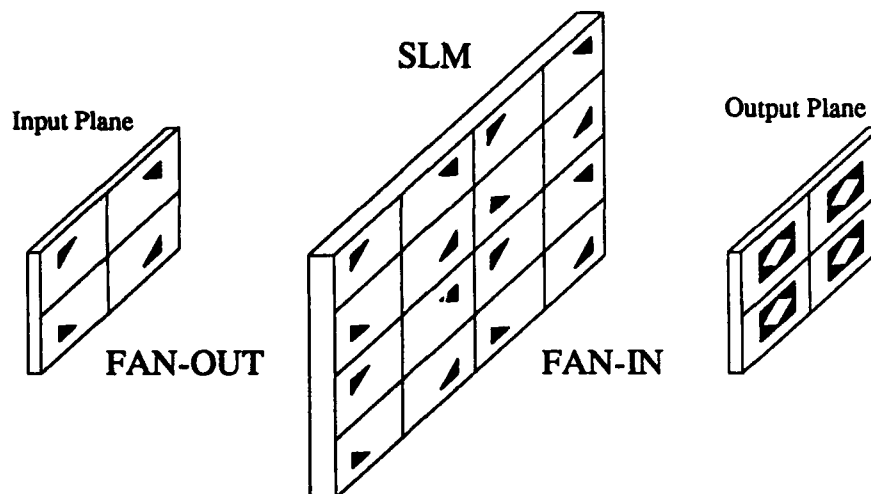
Fig. 1 : 2×2 Matrix-Matrix Crossbar.

design with trapezoidal features. Figure 2 shows one period of the optimized grating and diffraction orders in the Fourier plane. The theoretical diffraction efficiency and array uniformity of the fan-out grating are 77.5% and 0.4% respectively. Electro-beam lithography was used to plot the amplitude pattern in chrome on a quartz mask. This was then used as a mask to transfer the design to a fused silica substrate,

Fig. 2: Left, one period of the fan-out grating. Right, the diffraction orders in the Fourier plane.

the surface-relief profile created using reactive ion etching. The etch depth accuracy achieved was 1nm. The measured diffraction efficiency and uniformity of the fan-out array with reflection losses was 69% and 3% respectively. The decrease in uniformity is due to the error in patterning the chrome mask and during contact copying. Higher efficiencies can be obtained using multi-level designs, however, the introduction of alignment errors during fabrication increases the non-uniformity to an unacceptable level for this application [2].

In order to fan-in the 16 4×4 sets of data channels into the 16 output fibres two planes of diffractive 4-level micro-Fresnel lenses are used. In the first plane a 16×16 array of F/4 lenses, focal length $f_1 = 0.8$mm, collimates the 256 beams from the last lens. The second plane consists of a 4x4 array of F/4 micro-lenses of focal length $f_1 = 3.2$mm. Each micro-lens takes one of the 16 replicated images of the input array and launches it into one of the output fibres as a single beam. The theoretical efficiency of a single 4-level micro-Fresnel lens with reflection losses is 75%. The overall efficiency of the fan-in element is, therefore, 56%. The real efficiency of fan-in was found to be 46%. As little aberration as possible should be introduced by the fan-in micro-lenses to ensure good coupling into the fibre. Spot profiles taken in the output plane show that the output spot sizes were diffraction limited, Fig.3.
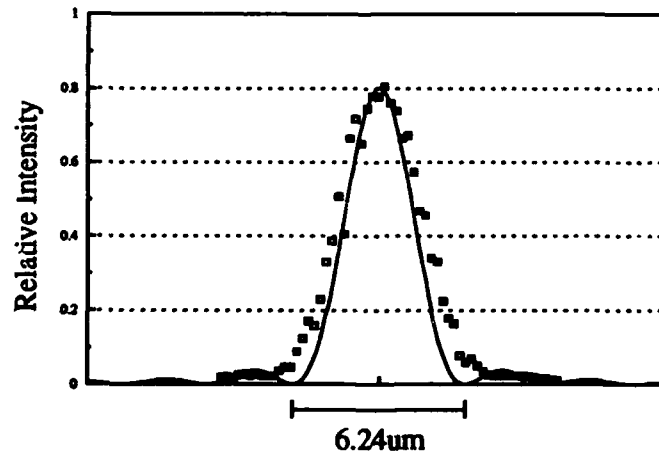
Fig. 3: Spot produced in output fibre plane by fan-in element.

Construction of the fan-in element and positioning within the system called for strict alignment tolerances. To overcome this a single diffractive fan-in element was designed and fabricated that collimates and couples the output array to output fibres. One period of this element consists of a two-dimensional array of 16 off-axis micro-lenses. The output array is focused to a single spot about the period centre where the output fibre is positioned. At present the surface-relief profile design is binary due to difficulties in fabricating the smaller fringes ($\leq 1.5\mu$m) at the edge of the design. The theoretical efficiency of the grating (taking into account reflection losses) is then only 41%.

References

[1] A. Vasara, M.R. Taghizadeh, J. Turunen, J. Westerholm, E. Noponen, H. Ichikawa, J. M. Miller, T. Jaakkola, and S. Kuisma, "Binary surface relief gratings for array illumination in digital optics", *Applied Optics.* **31**, 3320–3336 (1992).

[2] J. Michael Miller, Mohammad R. Taghizadeh, Jari Turunen, and Neil Ross, "Multi-level array illuminators in fused silica: fabrication error analysis and experiment", *Applied Optics* (1992 (in press)).

APPLICATIONS OF DIFFRACTIVE OPTICS WITH ONLY A ZERO ORDER

Robert J. Noll

Hughes Danbury Optical Systems

100 Wooster Heights Rd.

Danbury, Ct. 06810

Gratings whose spacing is short compared to the wavelength of incident radiation have no diffracted orders as can be seen from the grating equation for normal incidence

$$m\lambda = d \sin \theta \tag{1}$$

Only $m = 0$ will have a nonevanescent diffractive order, the reflected wave. The physical properties of such non-classical gratings have been studied by many researchers and can be the source of many different kinds of applications. Some of these applications depend upon the unique properties of this grating region and sometimes produce different results from a classical grating or fourier optics perspective. The simplest applications are antireflection gratings and polarizers[1]. One can greatly reduce the reflectivity of a metal with a grating and even define a condition of zero reflectivity where all of the incident light is absorbed in the metal. This condition can be simply modeled by what is called the long wave approximation. In this approximation all the coupling terms from the Floquet orders in the wave equation are dropped and only the DC term is retained. In this limit the wave equation reduces to that for planar media with an effective index of the grating determined by the duty (fill) factor of the grating and is independent of the absolute grating spacing. In addition different long wave limits exist for TE and TM polarizations. This allows these long wave structures to behave as polarizers.

Wire Grids

Wire grids on dielectric windows for EMI shielding provide another application. In the microwave literature[2,3] the analysis of such structures is carried forward through the use of a method-of-moment code. Simple formulae have been developed to approximate these code calculations, which usually apply to infinite conductors. Comparison of these

results with that produced by the coupled wave method of Moharam & Gaylord[4] show good agreement. Furthermore, the high conductivity wire structures cannot be effectively modeled with a long wave approximation because for this case there is a slight reflectivity dependence on grating spacing even when $d << \lambda$. This dependence is conductivity dependent and can be removed by suitably lowering the metal conductivity of the wire structure thus recovering the long wave limit behavior. In particular using the notation of ref (2) the amplitude transmission of a grid is written as

$$\tau = \frac{1}{1 + \cfrac{1}{R_0 - iZ_0(d/\lambda - \lambda/d)^{-1}}} \tag{2}$$

where R_0 is the normalized resistance of the metal in the grid and Z_0 is a function of the grid duty factor. In the limit as R_0 goes to zero eq. (2) shows that there is a dependence on the spacing d no matter how large λ gets. The long wave limit discussed above can be recovered when the resistance is increased.

Zero Reflectivity

The zero reflectivity mentioned above arises strictly from an appropriate impedance match of a grating/substrate to the incident medium, usually air, and it can occur for both polarizations. It is primarily the result of destructive interference between waves reflected from the top and bottom of the grating. There is another way in which a metal grating can exhibit zero reflectivity and that is through resonant coupling. Metals have excitations known as surface plasmons which can couple to a near 90 degree diffracted wave of TM polarization. The coupling to this resonance is sometimes[5] called a resonant Wood anomaly. For a bare metal grating this effect only occurs for TM polarization and is manifested by a drastic decrease in reflectivity in the incident order.

Waveguide Couplers

If the grating is coated with a thin dielectric layer, it can form a waveguide into which the near 90 degree diffraction order may couple. In this case it is well known[6] that both TE and TM incident light can couple through the grating to the waveguide. The coupled light drastically reduces the reflectivity of the incident order as the grating transfers incident energy to the waveguide. This mechanism is the basis upon which grating waveguide couplers and Bragg reflectors are based. Light can be coupled into or out of the waveguide through the grating and the efficiency of the process is determined by the Floquet mode coupling of the grating orders which can be calculated with

rigorous grating codes. The grating surface emitting laser[7] is an application which uses two grating waveguide couplers integrated on a chip at either end of a gain loaded waveguide. As Bragg reflectors the gratings provide feedback to the gain loaded section allowing laser action in the active guide and outcoupling of the light through the face of the grating at a slight angle.

SEDFB Laser

The surface emitting distributed feedback laser[8] is another more complex application. In this device the waveguide under the tuned second order grating is active. Two waveguide modes, left and right traveling waves in the guide, are set in resonance by grating coupling. Each mode has a full compliment of grating orders. If the right going wave in the guide is denoted as the zero order then its -2 order is coincident with the left going wave at resonance and vice versa. This produces the back-and-forth reflection required for laser oscillation. The -1 order of both waveguide modes coincide, coherently add, and are normal to the grating surface to define the output of the laser.

As might be be expected the waveguide eigenfunctions for this two wave resonance consist of symmetric and antisymmetric combinations of the left and right going waves, each combination having wavenumber eigenvalues of k^+ and k^- respectively. The difference $k^+ - k^-$ is related to the "stop-band" of the device spectrum. An interesting feature of this device is that the lowest gain mode is associated with the antisymmetric mode and this mode suffers destructive interference in the -1 output order from the two sets of waves implying a zero output. This arises because the two wave spectrum is a consequence of an infinite length grating. Real devices have finite length and have a spectrum of more than two modes. It has been shown[8] that the two modes of the infinite length grating are in fact two degenerate bands and the degeneracy is lifted for finite length devices. This fact is of prime importance because it allows the device to have a practical output. It is easily shown[8] that the output laser mode is antisymmetric and its outcoupling coefficient is determined by the infinite length symmetric mode outcoupling coefficient which can be computed from rigorous grating codes.

Thus, gratings with $\lambda/d > 1$ can have a wide variety of applications which exploit the unique physics of gratings in this region. The applications discussed here show the importance of this grating region to the field of integrated optics.

References

1. T.K.Gaylord et al., Appl. Opt. **26**, 3123, (1987)

2. R.Ulrich et al., Appl. Opt. **9**, 2511 (1970)

3. S.W.Lee et al., IEEE tarns Antenna Propagate., **AP-30,** 904 (1982)

4. M.G.Moharam and T.K.Gaylord, JOSE A, **3**, 1780 (1986)

5. R.C.McPhedran and M.D.Waterworth, OPTICA ACTA, **19**, 877 (1972)

6. M.Neviere, Electromagnetic Theory of Gratings, ed. R.Petit, Chap 5, Topics in Current Physics viol 22. Springer-Verlag (1980)

7. A.Hardy et al., IEEE J. Quantum El., **26**, 50 (1990)

8. R.J.Noll and S.H.Macomber, IEEE J. Quantum El., **26**, 456, (1990)

HOE For Wavelength Stabilization and Selection for WDM in Lightwave Communications

Haixian Zhou, Charles S. Ih
Rongsheng Tian, and Xiaoqing Xia

Dept. of Electrical Engineering
University of Delaware
Newark, DE 19716

The use of WDM (Wavelength-Division-Multiplexing) is an attractive alternative to increase the information capacity of an optical communication system. In WDM, the wavelength of the laser diode needs to be stabilized and/or switched to many pre-assigned values. In some high density WDM systems, these wavelengths may be spaced one to several nanometers apart and cover a wavelength range of 40 nm. The required linearity and accuracy of these wavelength is on the order of 0.1 nm. The wavelength stabilizer/selector must be simple, compact and low cost. Also eventually they need to be integrated with the lasers themselves. We believe the HOE is a good candidate for this application[1] [2] [3]. We describe in this paper the design and fabrication of the HOE which is the sole optical element needed for the stabilizer/selector.

Using computer simulations, we have found that a reflective focusing HOE on a concave surface can easily meet the requirements in linearity and accuracy while that on a flat surface cannot. Without using a lens, the wavelength stabilizer/selector will be very simple and can be easily reduced to one dimension and adapted for integrated optics. We have developed computer software to optimize the design and made designs for these wavelengths, 780nm, 830nm , 1300nm and 1500nm. The operating range of wavelength selector is 40 nm, the selectable spacings 1 nm and the accuracy better than 0.1 nm for all the wavelengths listed above.

Since a high spatial frequency HOE on a curved surface is still difficult to make using e-beam machine, the HOE was made optically using an intermediate CGH (Computer-Generated-Hologram) [5], [6]. The HOE is recorded with visible light (for instance, 442 nm of the HeCd laser) and can be reconstructed with diffraction limited performance at the infrared. The advantage of this approach is that HOE's with very high spatial frequencies, of large size and on almost any shapes of surface can be made. It is also possible to make infrared volume holograms by this technique. Basically we make a CGH (Computer-Generated-Hologram) which generates a pre-distorted objective wave at the visible wavelength. This distorted wave is identical to the one when the original IR HOE

is reconstructed at that visible wavelength. Therefore we can use it to make the HOE at a visible wavelength. The HOE so made is identical to the original and therefore can be reconstruct at the IR wavelength without aberrations [5].

A HOE design that could be used with a laser diode as a package for the wavelength stabilization/selection is shown in Fig. 1. The parameters describing their characteristics are as follows.

Range of wavelengths: 760nm-800 nm; Object distance: 6 mm; Object beam angle: 15 deg. (w.r.t. normal); Image distance: 6.23 mm; Image beam angle: 30 deg.; Hologram size : 2mm; Theoretical spot size (Airy disc) : $\leq 6\mu m$; Reconstruction spot size (rms, by computer simulation): $\leq 3\mu m$; Centroid accuracy (simulation): ≤ 0.1 nm in wavelength; Beam separation for 1 nm: $\sim 7\mu m$; Detector array size: $7\mu m \times 280\mu m$, 40 WDM divisions; and Size of system: 3 mm$\times$ 7 mm$\times$ 3 mm.

To facilitate a laboratory demonstration, we designed a HOE which is similar to that mentioned above and which has following parameters.

Range of wavelengths: 760 nm-794nm; Object distance: 50mm; Object beam angle: 15 deg.(w.r.t. normal); Image distance: 50mm; Image beam angle: 30 deg.; Hologram size: 2mm; Theoretical spot size (Airy disc):$\leq 50\mu m$; Reconstruction spot size (rms, by computer simulation): $\leq 7\mu m$; Centroid accuracy (simulation): $\leq 0.1 nm$ in wavelength; Beam separation for 1nm; $\sim 56\mu m$; Detector array size: $56\mu m \times 1960\mu m$.

The following parameters, more or less optimized, are used in recording the HOE.

Recording wavelength: 442 nm; Reference beam distance: 50 mm; Reference beam angle: 25.1 deg.; Object distance: 37.67 mm; Object beam angle: 0.35 deg.. The "object" is reconstructed from and pre-distorted by the CGH (see Fig. 2).

The computer generated hologram is characterized by the following parameters.

Wavelength: 442nm; Object distance: 20.33 mm; Reference distance: 20.41 mm; Angle between object and reference beams: 5 deg.; Average spatial frequency: 394 lines/mm.

The recording arrangement of the final HOE using the computer-generated hologram is shown in Fig 2. Computer simulations and experimental results are in general agreement and thus confirm the viability of this approach.

Reference:

1. K. A. Winick and J. R. Fienup. "Optimum holographic elements recorded with aspherical wavefronts". J. Opt. Soc. Am. 73, p208-217. (1983).

2. Y. Amitai, A. A. Friesem, and V. Weiss. "Designing holographic lenses with different recording and readout wavelengths". J. Opt. Soc. Am. Vol.7, No.1, p80-86, 1990.

3. R. J. Collier, et al.,"Optical holography". Academic press,Inc. 1971.

4. Making an IR HOE using a CGH, C. S. Ih, L. Q. Xiang, and C. W. Yang, The International Congress on Optical Science and Engineering, Proceedings of Topical Conference on Holographic Optics: Principles and Applications, April 24 - 28, 1989, Palais des Congres, Porte Maillot Paris - France.

5. C. S. Ih, L. Q. Xiang, B. H. Zhuang, C. Y. Yang, K. Q. Lu, R. S. Tian and Z. M. Wang, Optical Head Design Using HOE's, SPIE Vol. 1052, p. 177 -184, Holographic Optics: Optically and Computer Generated (1989).
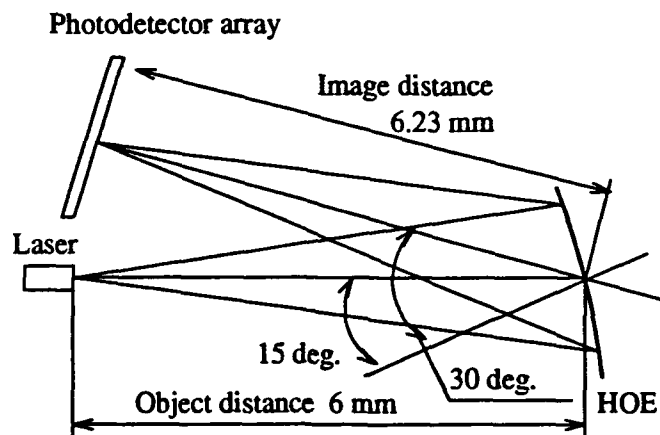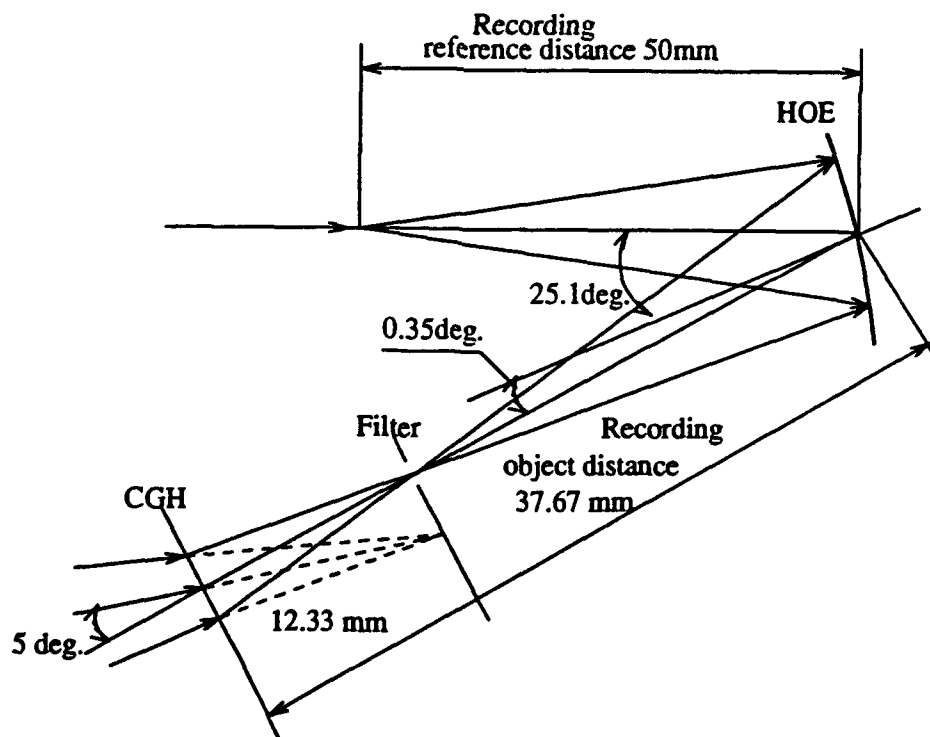

Figure 1. A HOE wavelength stabilizer/selector.

Figure 2. Recording geometry for the experimental IR HOE.

(Recording wavelength is 442 nm)

Fresnel Ping-Pong Algorithm for Two-Plane CGH Display

Rainer G. Dorsch, Adolf W. Lohmann, Stefan Sinzinger
Physikalisches Institut der Universität
Staudtstrasse 7/B2, 8520 Erlangen, Germany
phone: 49-9131-858371, fax: 49-9131-13508

1. Motivation

A breakthrough in 3D display was expected when computer generated hologams were invented about 25 years ago. The special problem of producing the intensity distributions $I_1(x,y)$ in plane z_1 and I_2 in plane z_2 seemed to be a fairly simple special case of 3D display. Setup and examples of I_1 and I_2 are shown in fig. 1 and 2.

However, this seemingly simple display experiment has quite noticeable upper bounds in terms of performance [1]. Here we want to explore those upper bounds. Our attempt makes use of a so-called ping-pong algorithm. The name "ping-pong" implies that the computation bounces back and forth between the two planes z_1 and z_2. We will briefly review three other projects which are also based on the ping-pong algorithm. This context helps to appreciate the problems associated with our own project, which will be described in chapter 3, 4 and 5.

2. Context

We consider four projects which rely on a ping-pong algorithm. They have in common that two intensity distributions I_1 and I_2 in planes z_1 and z_2 are known and one phase distribution α has to be computed:

$$I_1 = |u_1(x)|^2 \quad ; \quad u_1 = A \exp(i\alpha) \tag{1}$$

$$I_2 = |u_2(x)|^2 \quad ; \quad u_2 = B \exp(i\beta) \tag{2}$$

If $\alpha(x)$ is known , β can be computed easily, and vice vera. The complex amplitudes u_1 and u_2 are related either by Fraunhofer diffraction or by Fresnel diffraction. In mathematical terms, u_2 may be the Fourier transform or the Fresnel transform [2] of u_1.

The intensity distributions I_1 and I_2 may be known from measurements. For example in electron microscopy the image intensity I_1 and the diffraction intensity I_2 are easy to observe. The object phase $\alpha(x)$ is the aim of analysis. In a display application the two intensities I_1 and I_2 are specified arbitrarily, regardless of the possibility to actually synthesize a wave field $u(x,z)$ that exhibits those intensities in planes z_1 and z_2. Apparently, the display synthesis problem is more risky than the image analysis project. The two wanted intensity distributions $I_1(x)$ and $I_2(x)$ may not be compatible with the physical process of Fraunhofer or Fresnel diffraction which ties the two complex amplitudes $u(x, z_1)$ and $u(x, z_2)$ together. If, for example $u(x, z_1)$ has sharp edges, it is unlikely that $u(x, z_2)$ may have sharp edges also, because of Fresnel diffraction blur. This coupling problem of I_1 and I_2 is probably more severe for the Fresnel case (as in fig. 1), especially if the distance $z_o = z_2 - z_1$ is only a few depth of focus units long. In table I we categorized the four related methods, identified by the names of the principal investigators Gerchberg and Saxton [3], Fienup [4] and Ferwerda [5]. Based on our remarks above, our own project is

probably the most difficult one among the four in table I:

JOB: TRANSFORM:	ANALYSIS	SYNTHESIS
FOURIER	SAXTON-GERCHBERG	FIENUP
FRESNEL	FERWERDA	√

Table I: Four projects with two specified intensities $I_1(x)$ and $I_2(x)$ in planes z_1 and z_2.

3. Analytic Solutions

For some cases of $I_1(x, y)$ and $I_2(x, y)$ an analytic solution can be found. For example, if I_1 consists of a thin vertical line and I_2 is supposed to be a thin horizontal line, appearing at a distance z_0 the proper complex amplitudes are:

$$u_1(x, y) = \delta(x) \exp(-i\pi y^2 / \lambda z_0) \tag{3}$$

$$u_2(x, y) = \delta(x) \exp(+i\pi x^2 / \lambda z_0) \tag{4}$$

The focal power expressed by the exponential function in eq. (3) causes the concentration of the light into the line $y = 0$ in the second plane at a distance z_0.

Another example of a soluable problem is similar to what is shown in fig. 2. There, I_1 and I_2 are Ronchi ruling distributions, but in orthogonal orientations. Without going here into detail we simply state what is needed for this case. The complex amplitude $u_1(x, y)$ in the first plane ought to consist of the product of two orthogonal Ronchi pattern, one of them an amplitude Ronchi ($u_1 = 0$ or 1) and the other one a phase Ronchi ($U_1 = i$ or 1). The grating period is d.

$$u_1(x, y) = R_A(x) R_P(y) \tag{5}$$

The distance z_0 has to be one quarter of the Talbot distance:

$$z_T = 2d^2 / \lambda \tag{6}$$

Three quarters, five quarters etc. would be alright as well. In other words the distance between the two planes for I_1 and I_2 should be:

$$z_0 = d^2/2\lambda \quad , \quad 3d^2/2\lambda \quad \ldots \tag{7}$$

These two solvable cases are not the result of a general analytic approach. They were found by inspection. It is not trivial to generalize these examples towards non-orthogonal on non-separable cases.

4. Solutions by Iteration

When analytic solutions are not known, an iterative approach is often helpful, although at the expense of computer time. Another reason for employing an iterative approach might occur if no rigorous solution exists, but an approximate solution is useful nevertheless. In all four cases discussed in chapter 2 and listed in table I the following ping-pong algorithm is adequate:

$$U_1(x) = A\exp(i\alpha)$$

$$U_2(x) = B\exp(i\beta)$$
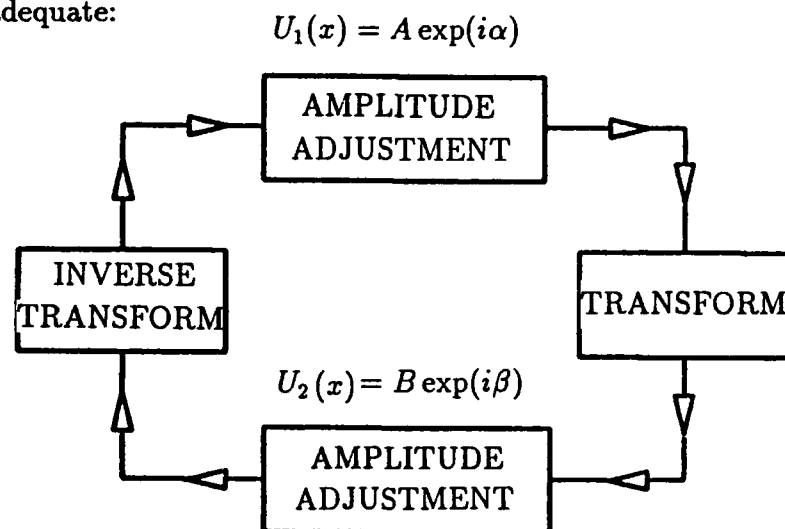
The amplitudes A and B are the roots of the well-defined intensities I_1 and I_2. The phases α and β are the aim of this analysis. The term "transform" stands for forward light propagation and "inverse transform" for backwards propagation from plane z_2 to z_1. The usefulness of this algorithm has been explored quite thouroughly, especially by Fienup and co-workers for the case "Fourier/Analysis" (as defined in table I).

5. The Case of "Fresnel/Synthesis"

That is the case we are interested in. Based on arguments in previous chapters this is probably the most difficult one among the four, listed in table I.
The experiment we are studying is shown in fig. 3. We prefer this image-plane CGH approach over the Fourier-plane CGH setup (fig. 1) because of experimental convenience. The spatial and spectral coherence of the illuminating wave is less critical.

References

1. A. W. Lohmann, "3D properties of wavefields", OPTIK 51 (1978) 105-117
2. L. Mertz, "Transformations in Optics", J. Wiley, New York 1965
3. R. W. Gerchberg, W. O. Saxton, "A practical algorithm for the determination of phase from image and diffraction plane figures", OPTIK 35 (1972) 237-246
4. J. R. Fienup, "Iterative method applied to image reconstruction and to computer generated holograms", Opt. Eng. 19 (1980) 297-305
5. P. van Toorn, H. A. Ferwerda, "The problem of phase retrieval in light and electron microscopy of strong objects", Opt. Acta 23 (1976) 469-481. -See also D. L. Misell, J. Phys. D 6 (1973) 2200, 2217.
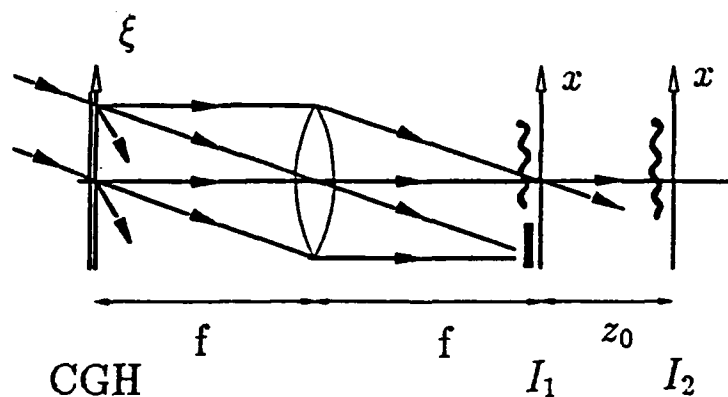
Fig. 1. A hologram CGH, that produces intensity distributions I_1, I_2 in two
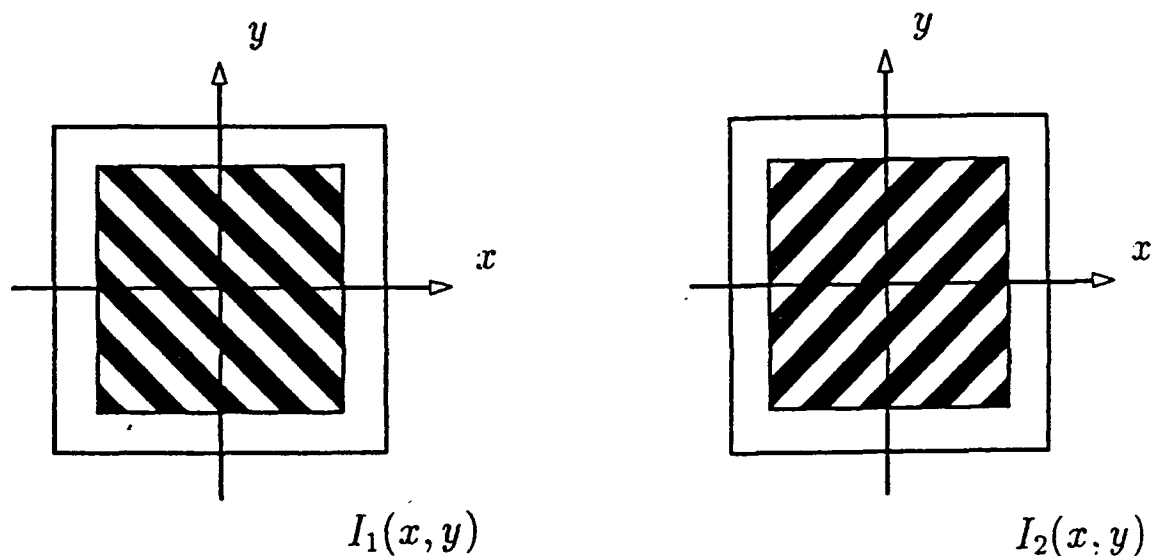
planes z_1, z_2, apart by z_0.

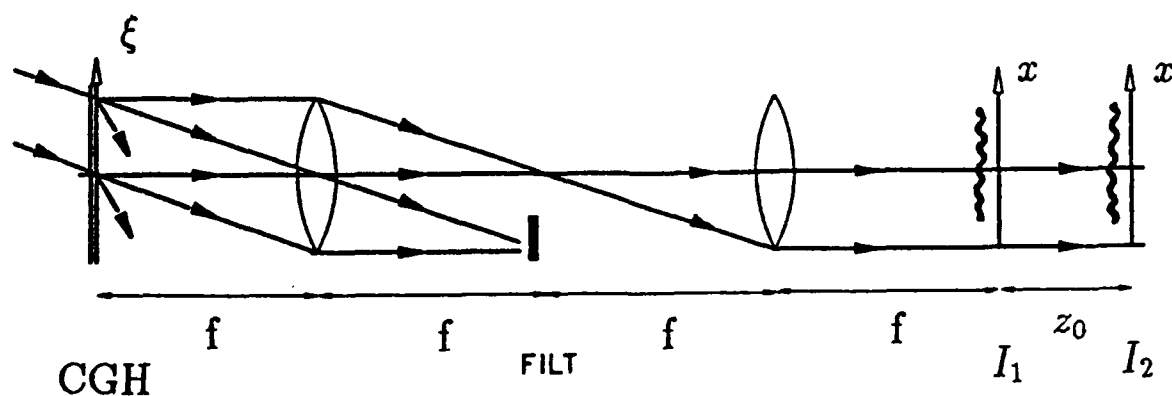Fig. 2. Example of two intensity distributions I_1 and I_2.

Fig. 3. Two-plane display with an image-plane CGH. The filter FILT eli-

minates unwanted diffraction orders.

Design of Diffractive Optical Elements with Rigorous Diffraction Theory

Erkin Sidick and André Knoesen

Department of Electrical Engineering and Computer Science
University of California, Davis
Davis, CA 95616
Phone: (915) 752-8023

Introduction

Diffractive optical elements (DOE's), such as array generators[1] and coherent laser combiners,[2] are designed with scalar diffraction theory (SDT). SDT is computationally very efficient, ideally lending itself to intensive numerical optimization calculations. However, SDT is an approximate theory. For example, it fails to accurately predict the optical performance of periodic surface-relief DOE's with either small period-to-wavelength ratios or large relief depth-to-wavelength ratios. Existing rigorous diffraction theory (RDT) is very accurate in predicting the optical performance of DOE and its use in the DOE analysis is becoming widespread. Incorporating RDT into the optimization process of a design procedure is challenging because of the prohibitively large numerical calculations that are required. To solve i) problem we present an alternative method. In this method, the optimization process starts with SDT, and as the design is refined, progressively more rigorous diffraction theories are used. This design concept is illustrated by designing kinoform array generators.

Array generator splits a single optical beam into a finite number of beams with equal intensities. It can be realized by using periodic surface-relief gratings with either continuous relief modulations over one grating period,[3,4] i.e. continuous surface-relief (CSR) gratings, or with discrete modulation cross sections, i.e. kinoforms[1]. In our design approach we based the initial array generator on a CSR grating. We discretize the CSR designs to obtain the discrete phase levels and the corresponding phase transition points of kinoforms. Then, while keeping the phase levels of kinoforms as fixed parameters, we optimize the phase transition points in two steps. At the beginning, SDT is used in simulated annealing[1] (SA) optimization to calculate the diffraction order intensities, but as soon as the algorithm converges, SA switches over to RDT. Our design examples include eight 1-dimensional array generators with spot numbers $N_s \in \{3, 4, 5, 6, 7, 8, 9, 13\}$. In these designs the surface-relief gratings have relief depths equal to several multiples of wavelength. In this range of relief depth-to-wavelength ratio SDT is not accurate.

Design of Continuous Surface-Relief Grating Array Generators

The CSR grating array generators are designed by using the method of virtual sources[3,4] in combination with SA.[1] The designs are optimized such that the diffraction efficiency η (i.e. the amount of transmitted power distributed among the desired N_S central beams) is maximized and the reconstruction error ΔR (i.e. the maximum deviation of a signal beam power from the average power) is minimized. Table 1 summarizes the values of η and ΔR of the designed CSR grating array generators. All array generators have relatively high efficiency and almost perfect uniformity when their performance is evaluated with Fourier-optics theory (FOT).

Optimization of Discretized Gratings Based on Scalar Diffraction Theory

The CSR grating designs are discretized and the phase transition points of the resulted kinoforms are optimized with a constrained SA algorithm that calculates the diffraction order intensities with FOT. This is referred to the SA-FOT optimization stage. An additional constraint is imposed in SA that restricts the minimum feature size Δ_{min} to values $\geq 0.01\lambda$, where λ is the free space wavelength. As an example, we chose to produce from each CSR grating a kinoform with 32 phase levels and with 32 cells within a period. The CSR grating is discretized by: (i) dividing each grating period into 32 uniform cells; (ii) rounding the space-average value of the continuous phase within the kth cell to the closest value of $L_k(2\pi/32)$, where L_k is an integer satisfying $0 \leq L_k \leq 31$, and assigning that value to ϕ_k, the phase in the kth cell. The subsequent SA-FOT stage takes these ϕ_k as fixed parameters and only optimizes the phase transition points. Table 2 shows the values of η and ΔR of the discretized grating array generators *designed* with FOT and then *analyzed* with RDT. In RDT calculations, we model the gratings as lossless dielectric surface-relief gratings with $\Lambda = 100\lambda$ (Λ is the grating period) etched into an optically thick glass substrate. In all RDT analyses we retain 51 diffraction orders. The discrepancy between FOT and RDT indicates that a further optimization using RDT might be possible.

Optimization of Kinoforms Based on a Rigorous Diffraction Theory

The final design stage is the optimization of the phase transition points with constrained SA that calculates the diffraction order intensities with RDT. This is referred to the SA-RDT optimization stage. This stage is required to correct for the approximation inherent to the SA-FOT stage. The SA-RDT optimization was performed for TE polarization at normal incidence by retaining 25~35 diffraction orders. Table 3 shows the results of η and ΔR obtained by analyzing the array generators for both states of polarization after the

SA-RDT optimization. As is seen from the table, the array generators have high efficiency (*85%~95%*) and small reconstruction error (≤*3%*) when evaluated with RDT.

Conclusion

A new method was presented to design diffractive optical elements. In this method, approximate scalar diffraction theory is used during the initial stage of the design. In the final stage rigorous diffraction theory is used. Although design examples iwere given for only kinoform array generators, a similar design methodology should be applicable to the design of other diffractive optical elements.

References

1) J. N. Mait, J. Opt. Soc. Am. A 7, 1514-1528 (1990).
2) J. R. Leger, G. J. Swanson, and W. B. Veldkamp, Appl. Opt. 26, 4391-4399 (1987).
3) D. Prongué, H. P. Herzig, R. Dändliker, and M. T. Gale, Appl. Opt. 31, 5706-5711 (1992).
4) E. Sidick, A. Knoesen, and J. N. Mait, Appl. Opt., to be published.

Table 1   Diffraction efficiency η and reconstruction error ΔR of continuos surface-relief grating array generators that generate N_s spots.

N_s	3	4	5	6	7	8	9	13
η (%)	92.6	91.9	92.1	88.3	96.8	95.9	99.3	97.6
ΔR (%)	<0.1	0.31	<0.1	1.78	<0.1	0.26	<0.1	<0.1

Table 2   Diffraction efficiency η and reconstruction error ΔR of the kinoform array
generators. The designs were obtained by optimizing the phase transition points
of the kinoforms using Fourier-optics diffraction theory.

	FOT		TE Polarization		TM Polarization	
N_S	η (%)	ΔR (%)	η (%)	ΔR (%)	η (%)	ΔR (%)
3	92.3	0.02	89.0	1.36	89.0	1.38
4	91.4	0.04	88.2	2.32	88.2	2.46
5	88.1	0.34	84.9	4.37	84.9	4.70
6	87.3	0.25	84.8	3.84	84.8	3.84
7	91.1	0.36	88.9	4.03	88.8	4.15
8	94.2	0.32	92.2	4.99	92.2	5.26
9	96.0	0.24	94.6	2.04	94.7	2.08
13	87.3	0.81	87.5	16.35	87.7	17.35

Table 3   Diffraction efficiency η and reconstruction error ΔR of the kinoform array
generators. The designs were obtained by optimizing the phase transition points
of the kinoforms using rigorous diffraction theory for TE polarization.

	TE Polarization		TM Polarization	
N_S	η (%)	ΔR (%)	η (%)	ΔR (%)
3	88.9	0.33	88.9	0.36
4	88.2	0.94	88.2	1.08
5	84.6	0.81	84.6	0.57
6	84.5	1.02	84.5	0.91
7	88.7	0.81	88.7	0.69
8	92.1	2.03	92.1	1.77
9	94.6	1.19	94.6	1.16
13	86.8	3.33	86.9	3.33

A holographic focusing doublet for polychromatic sources

A. Aharoni and J.W. Goodman
Department of Electrical Engineering,
Stanford University, Stanford, CA 94305,

Y. Amitai
Department of Electronics,
The Weizmann Institute of Science, Rehovot 76100, Israel.

We present and analyze a diffractive system for focusing polychromatic sources to near–diffraction-limited $1/e^2$ spot widths. We use two holographic optical elements (HOEs) fabricated and aligned to alleviate lateral chromatic effects and compensate for wavelength induced spot-size variation. Consequently our HOE doublet generates focal spots that are essentially unaffected by the presence of a wide wavelength band. This approach is potentially suitable for many applications that can incorporate partial coherence to reduce the system's cost and improve its environmental immunity.

Diffractive elements typically show strong chromatic dispersion. For example, when implemented independently, each of the two HOEs comprising our doublet[1,2] displays a lateral focal position shift of 85 μm for a 1 nm variation in the incident wavelength. Furthermore, had these been spherically focusing elements, the combined effects of the focal divergence and their inherent longitudinal color would have induced a spot size increase of 50% for the same shift off the nominal design wavelength. To alleviate the lateral color we employ the anti-symmetric arrangement of Figure 1, where any variation in the diffraction angle in the first HOE is automatically compensated by the identical second element which diffracts in the opposite sense. We also partially compensate for the spot-size variation by incorporating an axicon or axilens aberration[2] into both elements to reduce the beam's divergence at the focus. The result is a nearly-achromatic holographic focusing system; the focal axis is maintained over a spectral

Laser Diode

HOE 1

HOE 2

R_c β_i
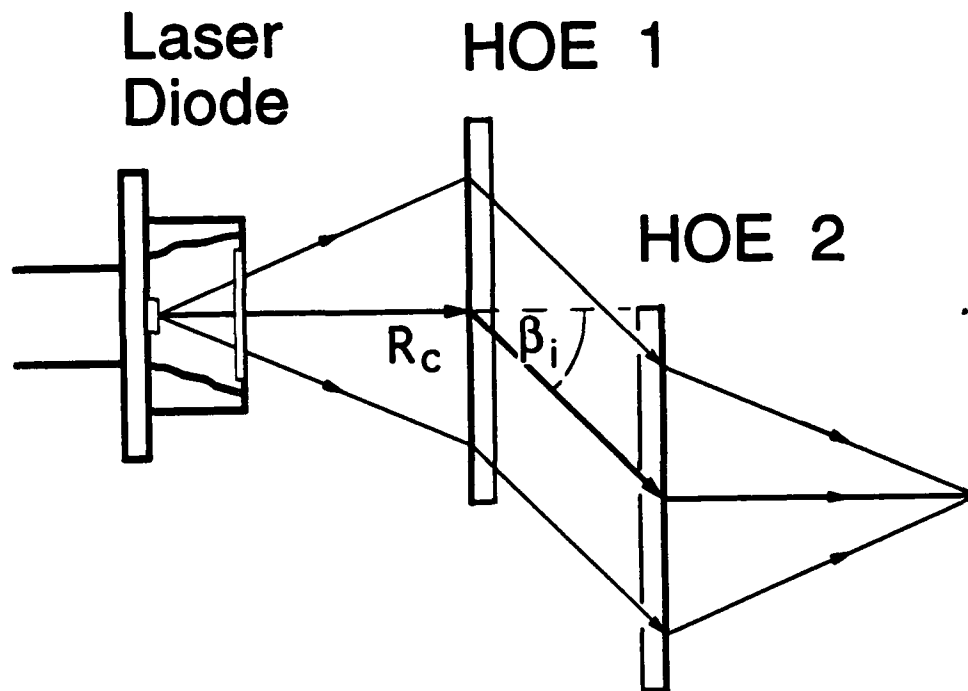
Figure 1: Schematic representation of the holographic focusing doublet. Both elements are designed for operation at 820 nm with a focal length of $R_c = 40$ mm and a diffraction angle of $\beta_i = 50°$.

band of 100 nm, and the spot size remains essentially fixed over 4 nm. Despite the residual longitudinal color of the doublet, it achieves a near–diffraction-limited $1/e^2$ spot size with polychromatic sources.

We demonstrate the polychromatic capability of the doublet with a multimode laser diode. The resulting $1/e^2$ focal spot size in this case is marginally larger ($\sim 8\,\mu$m) than the theoretical diffraction limit ($\sim 6\,\mu$m) but the effective focal depth is extended from approximately 60 μm for the diffraction limited case to nearly 1 mm. Although over thirty longitudinal diode modes are active in this setup, the peak-to-background intensity ratio is better than 20:1, and the cross-section is essentially Gaussian.

These results are confirmed by modeling the source as an incoherent superposition of modes at different wavelengths. Using the diode's empirical intensity and spectral mode distribution, the model replicates the experimental beam section. We demonstrate that only fractional portions of the source's spectral range focus at a given axial location. The strong intensity of the focused wavelengths dominate at this location, so that the overall beam has a near-diffraction-limited $1/e^2$ spot size and suffers only relatively weak background illumination from the unfocused spectral components. This is borne by the variation of the intensity half-width curves with increasing source spectral band [Figure 2(a)]. The lower intensity portions of the polychromatic beam (5 and 10%), which can be associated with the background of the unfocused components, diverge rapidly. In contrast the high intensity portions of the beam are virtually constant. Interestingly, the cross-sectional distribution of the combined modes is nearly independent of the number of wavelengths present. We find that the effective profile is determined by the overall spectral bandwidth of the source, the degree of the residual longitudinal color of the doublet, and the axilens value of the HOEs. Figure 2 compares the focal-spot broadening for a doublet with spherical HOEs [Figure 2(a)] to the broadening expected from our axilens doublet [Figure 2(b)]. Evidently the doublet can be designed to optimize the inherent tradeoff between the focal-to-background ratio and the overall focal depth for a given application.

In conclusion, we have fabricated a laterally achromatic HOE doublet which successfully focuses a polychromatic source to a near-diffraction-limited $1/e^2$ spot with significantly extended focal depths. This device is potentially useful for several application where the partial coherent light is advantageous, and can be designed to optimized the tradeoff between focal-to-background intensity ratio and overall focal depth.

REFERENCES

1. "Efficient, beam-correcting holographic collimator for laser diodes," A. Aharoni, Y. Amitai and J. W. Goodman, Opt. Lett. **17**, pp. 1310-1312 (1992).

2 "A beam-correcting holographic doublet for focusing multimode laser diodes," A. Aharoni, Y. Amitai and J. W. Goodman, Opt. Lett., in press.
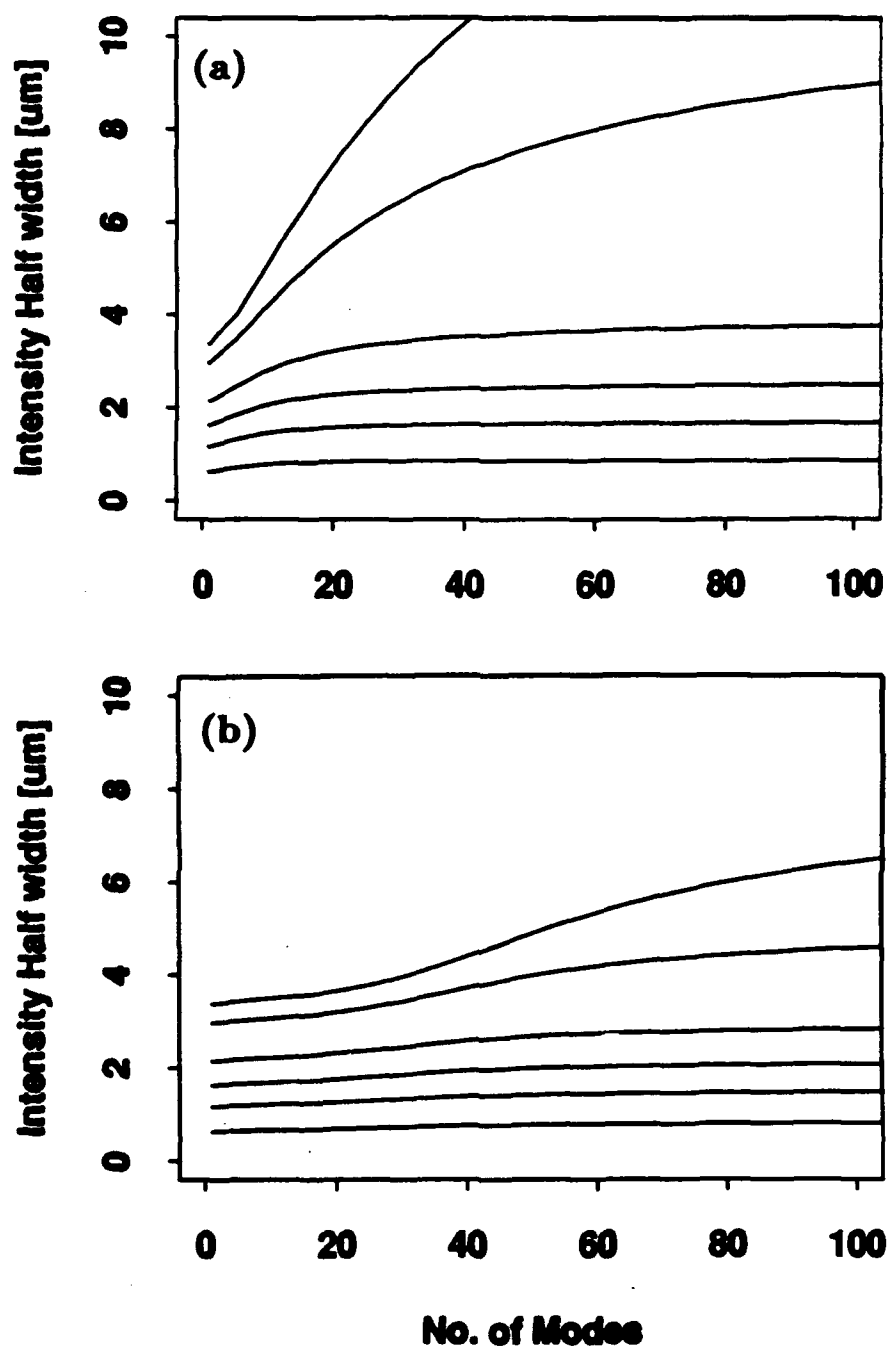
Figure 2: Variation of the 90, 70, 50, 30, 10, and 5% intensity half-widths at the nominal device focus as a function of the incident spectral band. The spectral width is presented as the number of modes present where the mode spectral spacing is 0.125 nm. (a) A spherical HOE doublet. (b) An axilens HOE doublet.

Fidelity of PostScript™-Generated Masks for Diffractive Optics Fabrication

Donald C. O'Shea
Thomas J. Suleski
Center for Optical Science and Engineering
School of Physics
Georgia Institute of Technology
Atlanta, GA 30332-0430

I. Introduction

There is a technique for generating binary masks for the fabrication of diffractive optical elements that uses commercially available desktop publishing hardware and software in conjunction with a standard photoreduction camera[1]. Although it is somewhat limited to details of five to ten micrometers, it is much faster and less expensive than the conventional methods. The short turnaround time and low cost should give researchers a much greater degree of flexibility in the field of binary optics and enable wider application of the technology.

Although graphic artists need sharp transitions and faithful reproduction of type and relative spacing of letters, the dimensional precision required to produce diffractive optics components is greater than this. Work on a number of different diffractive elements, particularly Dammann gratings, has shown that the transparencies output on high resolution graphics imagesetters, while faithful to the repeat dimensions for any periodic pattern, do not produce the dimensions of opaque and transparent regions as specified by the user. That is to say, the transitions specified for a Dammann grating in the illustration program and resulting pattern from the imagesetter do not agree. In all cases examined to date, the opaque regions are too large and the transparent regions correspondingly smaller. The purpose of this paper is to describe the amount and types of errors and to demonstrate strategies for reducing them.

The patterns were generated using Aldus Freehand 3.1 on a Macintosh IIx microcomputer with a built-in floating point processor[2]. This program provides the control over placement and size of details necessary for generating the binary patterns. Other programs, Canvas[3] and Adobe Illustrator[4] are used for comparing the fidelity of patterns between applications. The patterns are output on a Linotronic 330 printer (2540 and 3386 dpi), manufactured by Linotronic AG, Germany. Granted there are possible errors after the transparency is generated, but any effort to reduce errors in the initial steps will make it easier to generate reliable patterns in the final etched profile.

II. Measurements

A series of patterns of opaque bars on a transparent field consisting of either equally spaced multiple lines or rectangles (Ronchi rulings) and Dammann gratings were generated using Freehand and output to the Linotronic 330 at its highest resolution. The resulting transparencies were measured on a Gaertner comparator with 1 μm resolution. In the case of Ronchi rulings constructed from opaque lines of different pen widths, measurements were made of the coordinates of 10 line pairs and the results were averaged to find the line thicknesses of the opaque bars. Standard deviations for these measurements were 2 μm or less. This was done for 10 different line widths ranging from 10 to 1000 μm. It was found that the gratings had the correct periodicity, but the widths of the opaque bars were 14 μm larger than the specified line widths.

When the Ronchi rulings were generated from a set of filled black and white rectangles with no bounding outline (Freehand Attribute Menu: Line and Fill Dialog Box (Fill: Basic, Color: Black or White; Line: None)), the widths of the opaque bars averaged 8 ± 1 μm larger than specified and the transparent spaces were correspondingly smaller than intended. When the pattern was a Dammann grating, which has varying spacing and bar widths, similar line errors

were found. This indicates that the errors were not due to proximity effects (i.e., bar widths were not a function of the separation between bars).

We also found that objects rotated through angles other than multiples of 90° will not maintain the same coordinates when the object dimensions are interrogated within the program. The change in values between interrogation can be as much as 0.01 of a PostScript point (3.5 μm). This value is about one tenth of the smallest feature size that can be generated by our current output devices, but this program bug represents a possible source of error in generating some structures. Thus users should be aware of this problem. Attempts to freeze the coordinates of these rotated objects by entering new values in the Dimension dialog box failed. We feel this is another flaw in the program.

Using the information gained from these measurements, we revised a set of Dammann grating patterns generated using filled rectangles. We reduced the widths of the opaque bars by 8 μm and increased the widths of the transparent regions by the same amount. Our current measurements indicate that the resulting transparency contained Dammann grating patterns with the correct transition distances to within our ability to measure the widths ($\pm 1 \mu$m).

III. Conclusions and Strategies

The ability to generate precision patterns rapidly with commercial software is a compelling reason to use these techniques for diffractive optics fabrication. The problems we have described are of concern but are not impediments to producing reliable patterns. In the experiments we have been able to perform, the corrections have been subtractions or additions of a constant value to the desired dimensions. Whether this strategy will work for other geometrical patterns, we have yet to determine.

We have not determined whether this infidelity is due to hardware or software error, but it is one of the concerns during our investigation of this technique for producing diffractive optical elements.

IV. References

[1] D. C. O'Shea, J. W. Beletic, and M. P. Poutous, "Binary Mask Generation for Diffractive Optical Elements Using Microcomputers," Topical Meeting on Diffractive Optics: Design, Fabrication, and Applications, 1992 Technical Digest Series Volume 9, Paper TuD8, New Orleans, LA, April 13-15, 1992. A revised version has been accepted for publication in the Diffractive Optics Special Issue of *Applied Optics*.

[2] Freehand is a trademark of Aldus Corporation.

[3] Canvas is a trademark of Deneba Systems.

[4] Adobe Illustrator is a trademark of Adobe Systems.

Color Correction in Athermalized Hybrid Lenses

Gregory P. Behrmann
Army Research Laboratory
AMSRL-SS-SF
2800 Powder Mill Road
Adelphi, MD 20783
(301) 394-3800

Recently, it has been shown that it is possible to design athermalized hybrid lenses by combining the thermal properties of refractive and diffractive lenses.[1,2,3] The procedure is similiar to that developed for all refractive athermalization.[4] Hybrid athermalization allows one to reduce the size, weight, and required number of materials for a given design. In fact, it is possible to design athermalized lenses of one material since refractive and diffractive lenses behave differently with temperature.

To date, only single-material solutions have been published. In most cases, athermalized single-material solutions require negative power in the refractive surface and positive power in the diffractive surface. This creates a hybrid element that is highly dispersive and therefore only appropriate for monochromatic applications. In addition, for hybrid lenses of moderate f-number, the diffractive power is usually quite large and thus more difficult to manufacture.

In this work, we examine the requirements for the design of lenses that operate over the entire 8 to 12 micron band. In general, refractive lens designs that simultaneously achromatize and athermalize require three materials.[5] Here, we compare the thermal behavior, secondary spectrum, volume, and mass of four different achromats. They are the achromatic doublet, a hybrid achromat of one material, an achromat consisting of two materials and one diffractive surface, and an achromatic triplet (see Fig. 1).

The opto-thermal expansion coefficient for a refractive lens, $x_{f,r}$, as defined by Jamieson,[4] relates the change in focal length to changes in temperature. For a single thin lens, $x_{f,r}$ is given by

$$x_{f,r} = \frac{1}{f}\frac{df}{dT} = \alpha_g - \frac{1}{n - n_{air}}\left(\frac{dn}{dT} - n\frac{dn_{air}}{dT}\right), \tag{1}$$

where α_g is the coefficient of thermal expansion of the lens material $[^\circ C^{-1}]$, n is its refractive index, and n_{air} is the refractive index of air. Since $x_{f,r}$ is normalized by f it can easily be used to calculate the change in focal length by

$$\Delta f = f x_{f,r} \Delta T. \tag{2}$$

For a diffractive lens, the opto-thermal expansion coefficient, $x_{f,d}$, can be expressed as

$$x_{f,d} = 2\alpha_g + \frac{1}{n_{air}}\frac{dn_{air}}{dT}. \tag{3}$$

A complete derivation of $x_{f,d}$ can be found in Reference 3.

The total power of a k-element lens with a focal length of f_t, is the the sum of individual powers. This can be expressed as

$$\phi_t = \frac{1}{f_t} = \phi_1 + \phi_2 + \dots + \phi_k. \tag{4}$$

Recall that for a thin refractive lens, $\phi(\lambda) = [n(\lambda)-1]C$. C is lens curvature. For a diffractive lens, $\phi(\lambda) = \frac{\lambda}{f\lambda_o}$.[6] λ_o is the design wavelength and λ is the wavelength of illumination.

Eqs. 1, 3, and 4 can be used to calculate the opto-thermal expansion coefficient for a k-element lens, $x_{f,t}$,

$$x_{f,t} = f_t\phi_1 x_{f1} + f_t\phi_2 x_{f2} + \dots + f_t\phi_k x_{fk}. \tag{5}$$

Note that $x_{f,t}$ is dependent on the distribution of power and the thermal characteristics of the individual elements.

In achromatization, power is distributed in the individual elements based on the relative dispersions of the lens materials. In refractive lens design, dispersion is related to the variation of index with wavelength. A diffractive lens has unique dispersive properties. This has been discussed by Stone and George.[6] For the achromats in this work, it is required that the 8 and 12 micron wavelengths have a common focus. That is,

$$f(8) = f(12). \tag{6}$$

However, the wavelength between them - in this case 10 microns - will have a different focal length. The distance between $f(10)$ and $f(8)$ is known as the secondary spectrum. It is desirable to keep this distance to a minimum.

For triplet solutions, Eqs. 4-6 can be used to solve for the individual powers that yield both achromatization and athermalization. As previously stated, this is usually accomplished with three different lens materials. In the following, due to the unique dispersive and thermal behavior of the diffractive lens, we examine the possibility of replacing one of the three materials with a diffractive surface.

For the achromatic doublet and the achromatic hybrid lens, there is insufficient design freedom to correct for both color and thermal performance. Generally only one can be corrected. In this paper, the achromatized condition is imposed and the resulting thermal behavior analyzed.

The materials under consideration are ZnS, ZnSe, and Ge. All three are common materials for use in the 8 to 12 micron range but are certainly not the only ones available. Table 1 lists the material properties for substitution into Eqs. 4-6. The list includes the index of refraction at 8, 10, and 12 microns, $x_{f,r}$, and $x_{f,d}$ for each material.

Table 2 lists the resultant powers, secondary spectrum, and opto-thermal expansion coefficient for all possible material combinations. In each case, the net focal length has been normalized to one. Note that solutions containing two materials with one diffractive surface and the three material solution have an opto-thermal expansion coefficient of zero. Further, the achromatic doublets and achromatic hybrids have large negative opto-thermal expansion coefficients which indicates the difficulty in using such lenses in athermalized systems. Recall

from Eq. 5 that, for a triplet, it is possible to attain any value of the opto-thermal expansion coefficient, for example, the coefficient of expansion of the lens mounting material.

In examining secondary spectrum, note that most lenses containing diffractive surfaces have higher levels of secondary spectrum. There are exceptions. For example, the germanium hybrid achromat has less secondary spectrum than any of the achromatic doublets. Reviewing the athermalized solutions, it is seen that the best two-material solution, ZnSe, Ge, and a diffractive surface, has twice as much secondary spectrum as the triplet. Despite this fact, the level of secondary spectrum in this solution can be tolerated in most systems.

In order to make comparisions of size and weight, one solution of each type was optimized at $f/3$ and a focal length of 100 mm. Third-order aberrations were minimized. Table 3 lists the solution type, materials, volume, and mass. It is obvious that the single material hybrid offers the greatest savings in size and weight. However the negative opto-thermal expansion coefficient could make it undesirable for use in systems that operate over a wide temperature range. If the achromatic doublet and the two material hybrid are compared, only a 5 percent difference in volume and mass is seen. The advantage of the hybrid solution is that it is corrected for both color and thermal behavior. A comparison of the two-material hybrid and the triplet reveals that the hybrid occupies 43 percent less volume and weighs 40 percent less. This is a significant savings when one considers that both solutions offer similiar levels of color correction and thermal control.

In conclusion, for IR lenses operating in the 8 to 12 micron band, it was shown that a triplet solution is necessary for lenses that are both athermal and achromatic. There are not enough variables to adjust the thermal properties in either the achromatic doublet or single material hybrid. The unique properties of a diffractive surface allow it to replace the third element in the triplet solution. This offers significant savings in weight and volume. In addition, the required diffractive power is weak which implies that the feature sizes are large and the surface is easier to fabricate.

1.C. Londono, W. T. Plummer, and P. P. Clark, "Athermalization with Diffractive Optics," Diffractive Optics, Technical Digest Series 9 (OSA, Washington D.C., 1992), p. 7.

2. G. Behrmann and J. Bowen,"Thermal Effects in Diffractive Lenses," Diffractive Optics, Technical Digest Series 9 (OSA, Washington D.C., 1992), pp. 8-10.

3. G. Behrmann and J. Bowen, "The Influence of Temperature on Diffractive Lens Performance," accepted for publication in Appl. Opt.

4. T. H. Jamieson, "Thermal Effects In Optical Systems," Opt. Engr. 20 (1981) pp. 156-160.

5. W. Smith, *Modern Optical Engineering*, 2nd ed., New York, McGraw-Hill, Inc., 1990.

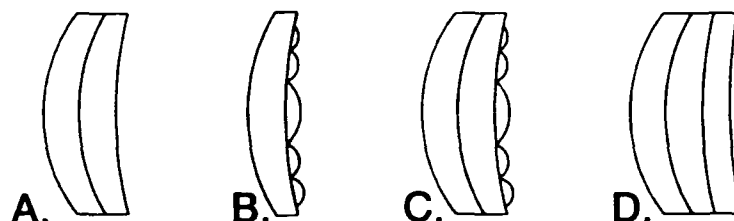6. T. Stone and N. George, "Hybrid diffractive-refractive lenses and achromats," Appl. Opt. 27, (1988) pp. 2960-2971.

Figure 1. Four Achromatic Solutions
A.) Achromatic Doublet B.) Hybrid Achromat
C.) Two Material Hybrid D.)Achromatic Triplet

Material	n(8um)	n(10um)	n(12um)	$x_{1,1}$	$x_{1,d}$
ZnS	2.2228	2.2002	2.1700	-33.81	15.70
ZnSe	2.4173	2.4065	2.3930	-27.70	15.70
Ge	4.0054	4.0032	4.0019	-123.76	12.20

Table 1. Material Properties ($x_{1,1}$ and $x_{1,d}$ in um/m/°C)

Combination	ϕ_1	ϕ_2	ϕ_3	S. S.	$x_{1,1}$
ZnSe/ZnS	1.6467	-0.6467	----	-0.0005	-23.75
Ge/ZnSe	1.0723	-0.0723	----	-0.0002	-130.71
Ge/ZnS	1.0272	-0.0272	----	-0.0002	-126.21
ZnSe/Diff	0.9586	0.0414	----	0.0009	-25.90
Ge/Diff	0.9970	0.0030	----	-0.0001	-123.37
ZnS/Diff	0.9010	0.0990	----	0.0029	-28.90
ZnS/ZnSe/Diff	-7.7760	9.2319	-0.4559	0.0155	0
ZnSe/Ge/Diff	1.2152	-0.2669	0.0517	-0.0012	0
ZnS/Ge/Diff	1.1810	-0.3099	0.1289	-0.0038	0
ZnS/ZnSe/Ge	-0.7903	2.0284	-0.2381	-0.0005	0

Table 2. Possible Achromatic Solutions, Focal Length
Normalized to One ($x_{1,1}$ in um/m/°C)

Solution	Materials	Volume	Mass
Achromatic Doublet	Ge/ZnSe	4985	0.0264
Hybrid Achromat	ZnSe/Diff	2768	0.0146
2-Mat'l Hybrid	ZnSe/Ge/Diff	5228	0.0277
Achromatic Triplet	ZnS/ZnSe/Ge	9214	0.0462

Table 3. Volume and Mass of Optimized Solutions (mm^3 and kg)

PHASE GRATING OPTIMIZATION USING
GENETIC ALGORITHMS

Eric G. Johnson
Teledyne Brown Engineering, Huntsville AL 35807
(205)726-3807
Mustafa A.G. Abushagar
University of Alabama in Huntsville, Huntsville AL 35899
(205)895-6215 ext 408
Alan Kathman
Teledyne Brown Engineering, Huntsville AL 35807
(205)726-2542

INTRODUCTION

With the advancement of computer technology, it has become necessary to interconnect processors using optical connections rather than wires. Considering passive technologies, free space propagation approaches are implemented to act as fanout devices forming a 1:N interconnect, see Figure 1. Quite often this is achieved through the use of a grating with a periodic unit cell phase function. It is this phase function which must be optimized for a desired array configuration using a global optimization approach. Moreover, a robust optimization technique is required so that complex 1 and 2D arrays can be designed without apriori knowledge.

In this paper, a Genetic Algorithm is proposed as an optimization strategy for fanout phase gratings and other diffractive optic components. Moreover, results are presented to confirm the usefulness and adaptability of the algorithm to arbitrary design problems.

APPROACH

Global optimization strategies can be classified into two categories: deterministic methods that rely on functional gradients, and probability based methods which iteratively solve the problem using distribution functions. Since deterministic methods often become trapped in local minima, the probability based methods are becoming a standard design approach. The most popular is simulated annealing[1] , where the algorithm iterates with a finite probability that a poor estimate will be accepted to prevent premature convergence. However, more recently Genetic Algorithms (GA) are gaining a great deal of interest in design problems[2,3]. In this algorithm, optimization is performed on a population of estimates rather than a single one. Additionally, the best estimates are combined to form a new population and a probability for mutation is included to eliminate premature convergence. Figure 2 illustrates a simple GA for function optimization.

In fanout grating design, a unit cell is represented as a phase function which is subdivided into MXM subcells. Each subcell has a variable phase value and a constant amplitude. Fourier Transforming this function results in the diffraction pattern which can be used to determine the diffraction efficiencies in each diffracted order. Since the subcell phase values are discrete and represented by an array of length MxM, they are easily coded into a "gene" for each diffraction estimate in a given population. The cost function for minimization is the mean squared error as follows:

$$cost = \sum_{n=-k}^{+k} |I_{actual}(n) - I_{desired}(n)|^2$$

where, $I_{desired}$ is the desired intensity in the nth diffracted order and the I_{actual} is the calculated estimate. Initially, the population is filled with random phase estimates and then the best estimates are allowed to breed to form a new generation. As can be expected, numerous trades must be performed to arrive at the optimum crossover and mutation rates which are a function of both the string lengths and population sizes.

NUMERICAL RESULTS

An example 2D fanout was designed using the GA algorithm outlined previously. The unit cell was subdivided into 256 pixels corresponding to a 16 X 16 cell size. Each subcell was allowed to vary in phase from 0 to 2 pi. Figure 3 illustrates the resulting phase function for 8 phase levels after 500 generations with a population size of 80 "genes". The corresponding diffraction pattern for 10 periods is given in Figure 4. As can be observed, the resulting phase is a nonseparable function which demonstrates a need for a robust method to optimize nonintuitive spot arrays.

REFERENCES

1. Clark C.Guest,"Annealing Binary Fresnel Holograms for Shaped Beam Generation,"in Diffractive Optics:Design, Fabrication, and Applications Digest. 1992 (OSA) Vol. 9, pp154-156.
2. Mustafa Abushagar and Eric Johnson,"Reconfigurable Adaptable Optical Interconnects,"in OSA Annual Meeting Technical Digest,1992 (OSA) Vol. 23, pp 173.
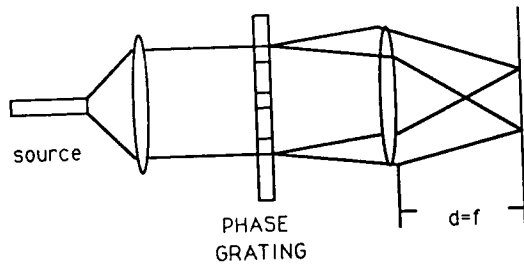3. Lawrence Davis, Handbook of Genetic Algorithms, (Van Nostrand Reinhold, 1991).

Initialize Population
(Random Initialization)

For i=1 to Max Generation {

    Evaluate Fitness (Cost)

    Regenerate Population

        Select Parents
        Crossover Parents

    Mutate Population

}

Fig. 1. Spot array generation using a phase grating.
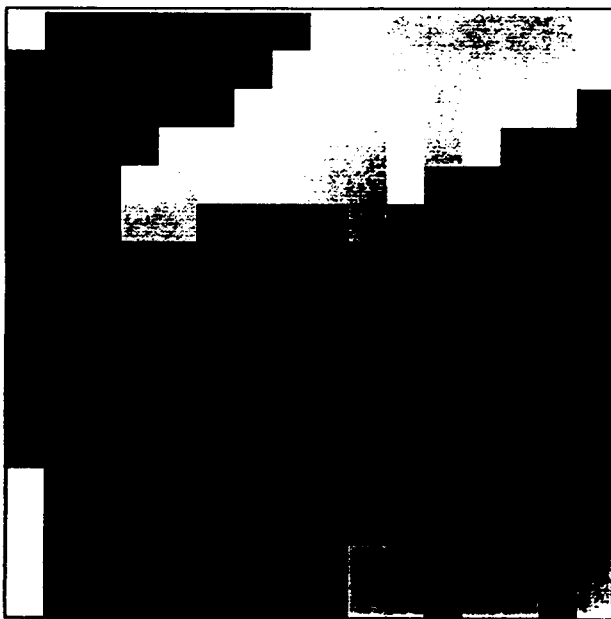
Fig. 2. Genetic Algorithm

Fig.3. Resulting phase function for the unit cell of a 2D periodic grating. Problem size was 16X16 with 8 quantized phase levels.
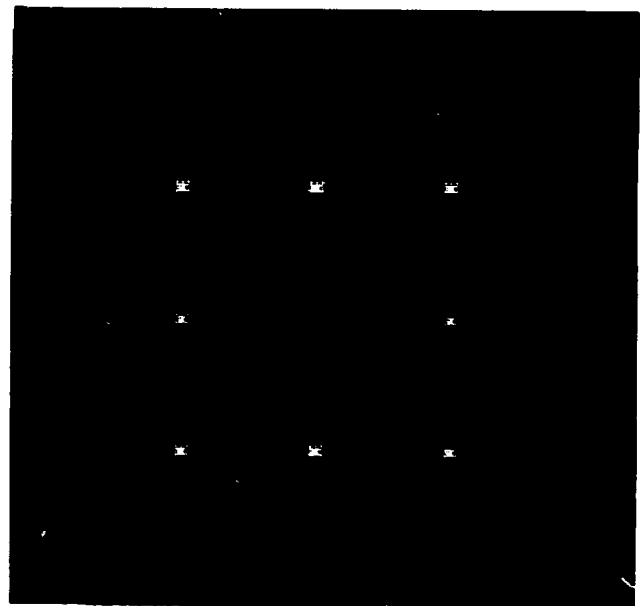
Fig. 4. Corresponding spot array for a square phase plate consisting of 10 periods on a side.

Optical optimization of binary phase diffractive optical elements

K.J. Weible and H.P. Herzig
Institute of Microtechnology, University of Neuchâtel
CH-2000 Neuchâtel, Switzerland
Tel: +41.38.205.275; Fax: +41.38.254.276
E-Mail: Weible@imt.unine.ch

Introduction

The application of simulated annealing to the optimization of phase diffractive optical elements has been investigated using large mainframe computers to perform the time consuming iterations.[1,2] In our work we are applying an optical parallel processor to optimize the design of a binary phase element. A liquid crystal television (LCTV) is used to actively modulate the phase of individual points within the base unit cell of the diffractive element and a simulated annealing algorithm has been used in iterating towards an optimum design.

Phase modulation using a LCTV

The spatial light modulator that we are using is one of three LCTV's originally employed in a video projector. The electronics of the projector are still used to control the television, while the video signal is generated by a PC using a frame grabber board. These LCTV's are designed to perform as intensity modulators by effectively providing a 90° rotation of the input polarization. These devices provide both a very high contrast ratio and a good gray scale performance.[3] In our optimization of binary phase elements we desire to modulate the phase of the impinging beam without modifying its polarization. This is possible if the LCTV is operated at a lower voltage range. The phase of each pixel may be independently modulated between 0 and 2π. Over the full 2π phase range the intensity of the beam is only slightly modulated, Fig. 1. Furthermore, since we are simulating binary phase elements, typically we are modulating the phase between 0 and π. The intensity transmission of the LCTV is essentially the same for these phase values.
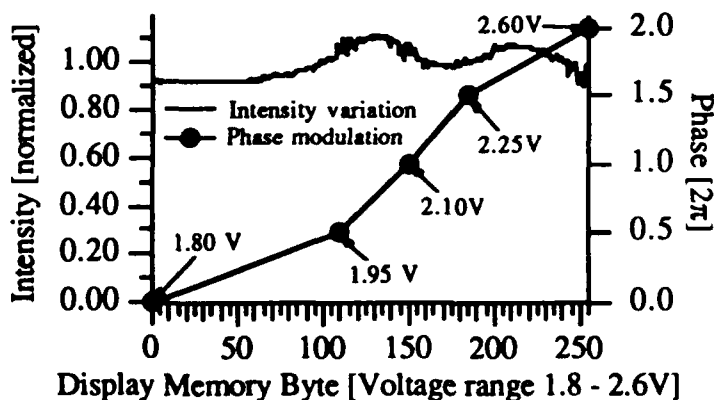

Fig. 1   LCTV intensity variation over 2π phase shift. [Voltage does not vary linearly w.r.t. memory byte.]

For Fig. 2 the LCTV is inserted in one of the arms of a Mach-Zehnder interferometer. A rectangular region of the LCTV is shifted in phase by π. For the simulation of the phase element to be sufficiently precise the uniformity of the LCTV must be of high quality. We have measured a phase variation of approximately 1 fringe across the entire LCTV surface. To make this measurement, the reference beam of the Mach-Zehnder interferometer is adjusted to

compensate the beam transmitted by the LCTV, Fig. 3a. When the LCTV is removed, 1 fringe of phase difference is observed, Fig. 3b. Since we are using only a portion of the screen, the phase variation across our unit cell is even less than 2π. The phase variation has an effect on the intensity of the zero diffraction order which can be ignored during optimization.

Fig. 2   0 – π phase modulation.

(a)   (b)

Fig. 3   Phase quality of LCTV.

Optical processor optimization (OPO)

The optical processing system used in the optimization of the unit cell of a DOE consists of only a few components, Fig. 4. The most important element is the LCTV which has been discussed in detail above. In a similar application these LCTV's have been demonstrated as efficient programmable phase kinoforms.[4] The Fourier transform of the phase information encoded within the television is achieved by traversing the LCTV with a collimated laser source and measuring the intensity in the focal plane of a simple lens. The Fourier plane is imaged onto a photodetector array for 2 reasons: (1) the diffraction pattern resulting from the LCTV pixel structure can be spatially filtered, and (2) the lateral magnification of the Fourier transform can be adjusted to correctly scale the transform w.r.t. the array of photodetectors. Since we are only measuring the intensity of the Fourier transform, the phase information is lost, but for our fan-out purposes we are not interested in the phase of the individual diffraction orders.
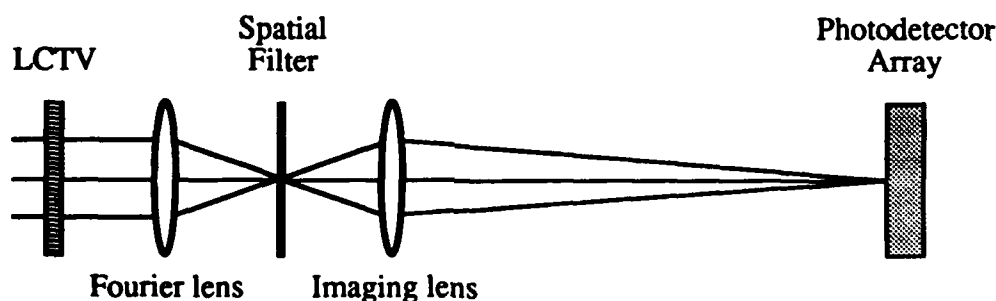

Fig. 4   Schematic of optical processor.

To begin the design process, each pixel of the phase structure is randomly initialized. The phase of a pixel or a group of pixels within the phase structure is modified. The decision whether to accept the modification or not is based on the simulated annealing Metropole algorithm.[5] The cost function is based on both the desired distribution of intensity and the overall efficiency of the element. This can be achieved by either minimizing the loss in the unused diffraction orders, or by maximizing the intensity in the desired orders. The optimization process is complete when the cost function reaches a minimum value and shows no further signs of decreasing.

It is critical that the lateral dimension of the transform be correctly scaled w.r.t. the photodetector array so that 1 photodetector corresponds to 1 diffraction order. Thus, to optimize the intensity within a certain diffraction order, the intensity measured by the corresponding photodetector is incorporated into the cost function of the simulated annealing algorithm. It was noticed that in the early stages of the optimization that the modulation of only 1 pixel of the LCTV produced too small of a change in the cost function. Given the amount of noise present, it was necessary to modulate a block of 3 x 3 LCTV pixels. Towards the end of the optimization, when the cost function had already been considerably reduced, it was possible to measure the effects of modulating 1 LCTV pixel. Therefore, at the end of each optimization a further optimization was effected with the phase of only 1 LCTV pixel being modulated at a time.

Experimental results and analysis

At the beginning of the optimization procedure the Fourier transform of the randomly initialized phase pattern results in a randomly varying intensity profile, Fig. 5a. The zero order is abnormally bright due to light passing the LCTV outside of the modulated region. The intensity at the photodetector array can be optimized to yield a specific pattern by selectively modifying the television while observing the effects at the detector plane. In Fig. 5b, a uniform variation of the intensity within a square area corresponding to 13 x 13 diffraction orders was sought. In Fig. 5c, the cost function was modified to stress the perimeter of the square region. As already observed, the zero order is still abnormally bright.

(a)   (b)   (c)
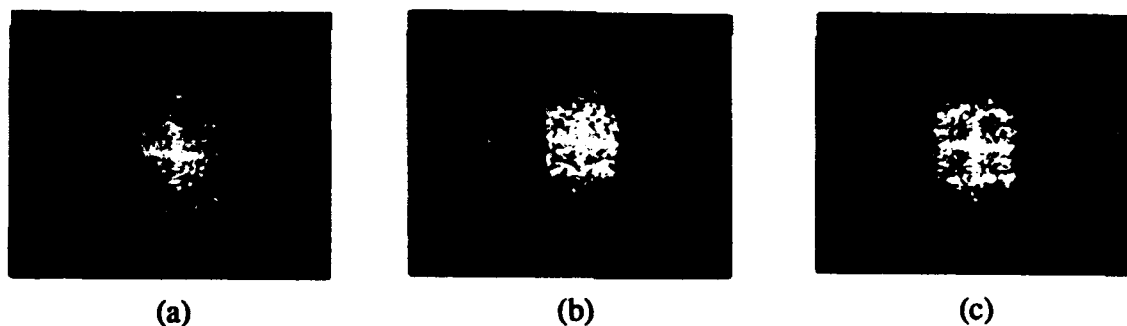
Fig. 5   *Intensity distribution in Fourier transform for (a) random initialization, (b) uniform square region, and (c) perimeter of square region.*

When the optimization is complete the final phase pattern still needs to be fine tuned to compensate for the noise introduced due to the optical variations of the beam and also the electronic noise of our photodetector array. Figure 6a contains the optimized design for a uniform intensity distribution in the central 7 x 7 diffraction orders. The design clearly contains a lot of noise. When analyzed using a fast Fourier transform algorithm on a mainframe computer the design yields an average of 0.7% intensity in each of the 7 x 7 central orders, corresponding to a total efficiency of only 33%. The uniformity of the data is extremely poor with a standard deviation of 92%. After fine tuning on the mainframe computer with an optimization algorithm equivalent to our optical implementation, the performance of the design, Fig. 6b, is improved to yield a total efficiency of 72% with a standard deviation of 2%.

(a)   (b)

*Fig. 6   An optimized phase distribution resulting from the OPO (a). The same phase
distribution after fine tuning on the computer (b).*

System limitations and conclusions

Although the principle of the OPO approach is simple, its performance is greatly deteriorated by the noise within the system. The scattered intensity distribution in the Fourier plane, as seen in Fig. 5, is source of systematic noise. This random variation is due to the interference of each pixel of the unit cell with all the other pixels. When many unit cells are illuminated, the phase of the interference effects are essentially washed out and only correspond to background illumination. However, as we are only illuminating one unit cell, the intensity variation is very visible. The pattern observed is stationary, i.e. it does not vary with time. It does however vary as the phase of the individual pixels of the LCTV are modulated. Yet as we are varying either 1 pixel or a small group of pixels at a time, the effect is negligible. This intensity variation still poses some problems for the intensity detection. For its effects to be removed it is necessary that the size of variation be small w.r.t. to the separation of the diffraction orders. In this case the intensity variation would be integrated by each photodetector and would not inhibit the measurements.

A more problematic source of noise comes from the readout of the photodetector array. The detector signal is very noisy, thus greatly inhibiting the ability of the optimization to correct the individual pixels that was finally done on the mainframe computer. With a better signal-to-noise ratio the capability of the OPO should be greatly improved.

References

1.   M.P. Dames, etal., "Efficient optical elements to generate intensity weighted spot arrays: design and fabrication", Appl. Opt. 30, 2685 (1991).

2.   A. Vasara, etal., "Binary surface-relief gratings for array illumination in digital optics", Appl. Opt. 31, 3320 (1992).

3.   K.J. Weible, N. Collings, and A.R. Pourzand, "Initial results of a fully interconnected neural network with modifiable interconnects", Optical Memory and Neural Networks 1, No. 2 (1992).

4.   J. Amako and T. Sonehara, "Kinoform using an electrically controlled birefringent liquid-crystal spatial light modulator", Appl. Opt. 30, 4622 (1991).

5.   S. Kirkpatrick, C.D. Gelatt, Jr., M.P. Vecchi, "Optimization by simulated annealing", Science 220, 671 (1983).

Binary Optic Beam Steering Techniques

Michael W. Farn

MIT/Lincoln Laboratory, HW45-108

244 Wood St., Lexington, MA 02173-9108

617-981-3798, 617-981-5200 (fax)

1. Introduction

The steering of a collimated laser beam is a fundamental building block for many optical systems. Common examples include bar code scanners, laser radars, laser machining applications and laser printers. Traditionally, this function has been limited to systematic scanning (e.g., raster scans) and is accomplished by mirrors or holographic scanners.

However, the recent development of microoptics in general and binary optics in particular has led to the possibility of quick non-systematic scanning since binary optics technology is capable of manufacturing large arrays of optically coherent microoptics. In a previous paper, Goltsos and Holz used a complementary pair of binary optics microlens arrays to achieve agile steering of a laser beam [1]. In this paper, we present a second design, which is an opto-mechanical implementation of a phased array, to solve the same problem. The goal of this paper is to compare and contrast the two approaches.

2. Basic Principles

The problem is shown in figure 1. A collimated beam of wavelength λ is incident on a pair of periodic binary optics elements. The elements have period d and therefore produce diffracted orders with an angular separation of

$$\Delta\theta = \lambda/d. \tag{1}$$

We want to design the two elements such that the beam is steered to the 0 order when the elements are aligned with each other, as shown in figure 1a, to the +1 order when the elements are translated by amount Δx with respect to each other, and to the nth order when translated by amount $n\Delta x$, as shown in figure 1b.
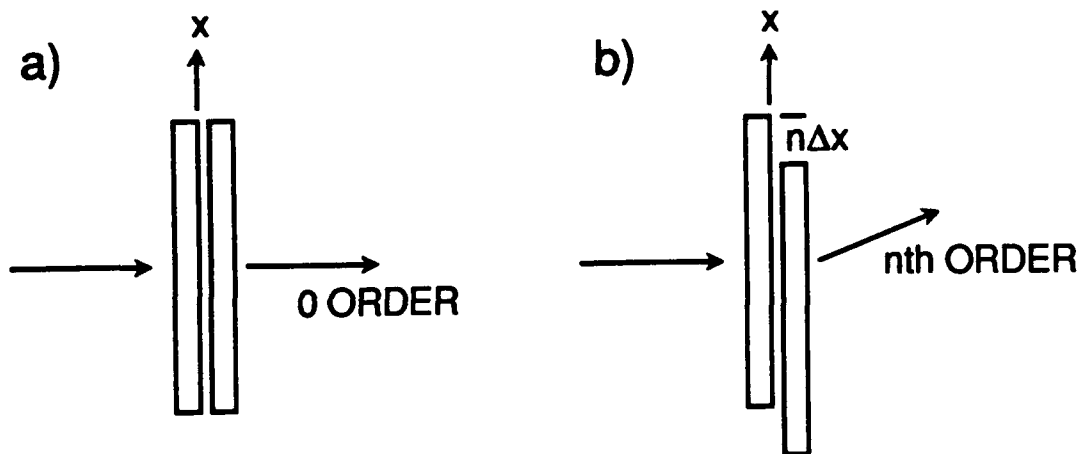
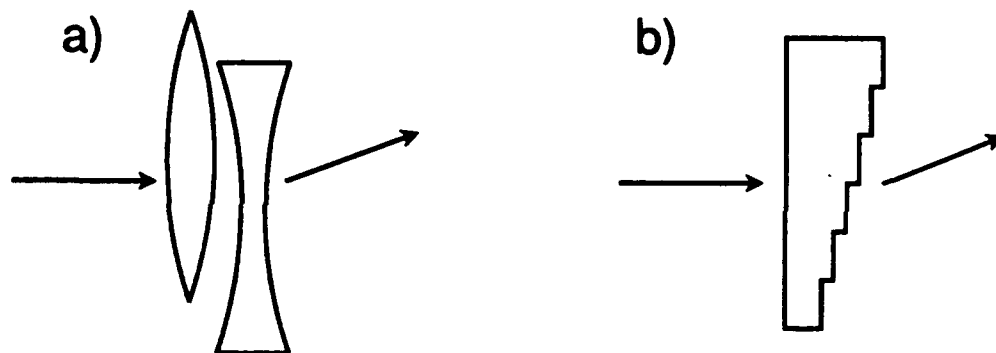Figure 1: Beam steering via binary optics arrays a) Steering to 0 order b) Steering to nth order

Figure 2: Beam steering principles a) Translated lenses b) Phased array

The problem, then, is the following. Given λ, d and Δx, design the two elements to accomplish the desired steering. To date, we are aware of two solutions to this problem. The first is based on the principle illustrated in figure 2a. If two complementary lenses are translated with respect to each other, the incident beam will be steered to a new direction. Since we are interested in small translations, we consider the microoptic version of this approach, previously described by Goltsos and Holz [1]. The second solution is based on the phased array principle shown in figure 2b. If each part of the beam receives a phase delay which varies linearly across the aperture, then the entire beam will be steered to a new direction. Again, we consider the microoptic version of this technique.

3. Experimental Results

Our test elements were designed to the specifications shown in table 1. They were fabricated on 2 inch diameter, 1 mm thick quartz, and consisted of two regions: one for the phased array design and one for the microlens design. Both of these regions were contained on the same substrate and were fabricated simultaneously in order to allow a direct comparison of the two designs. We used the standard binary optics process based on contact lithography and reactive ion etching to fabricate the pieces [2]. The resulting pieces had alignment errors of approximately 0.2 μm and etch errors of 2%.

Table 1: Optical Specifications for Beam Steerers

Specification	Value
Wavelength λ	0.543μm
Period d	320μm
Addressable angle $\Delta\theta$	1.7 mrad
Step size Δx	5μm
Full field of view	109 mrad
Aperture size	24 mm x 16 mm

In beam steering applications, the usual performance measures are pointing accuracy, wavefront quality and efficiency. Since our approach is diffractive, the beam is essentially steered by a variable grating, with pointing errors being the result of systematic variations in the grating period. However, our grating period is lithographically defined, so the pointing errors are very small (less than 1 part in 10000) and are usually not a factor. Similarly, as a result of the VLSI-based fabrication, wavefront errors are determined by the substrate flatness (typically less than $\lambda/20$) and are also usually not a factor. This leaves efficiency as the measure of interest. In our tests, we measured the steering efficiency of both devices, with the results shown in figure 3. The figure plots the efficiency with which each device can steer a beam into the given diffraction order. The solid line is the theoretical prediction and the +'s are the measured results. Some of the measurements are above the theoretical prediction because the efficiencies have been normalized to 100% for the 0 order in order to facilitate comparison with the theoretical predictions. The measurements and
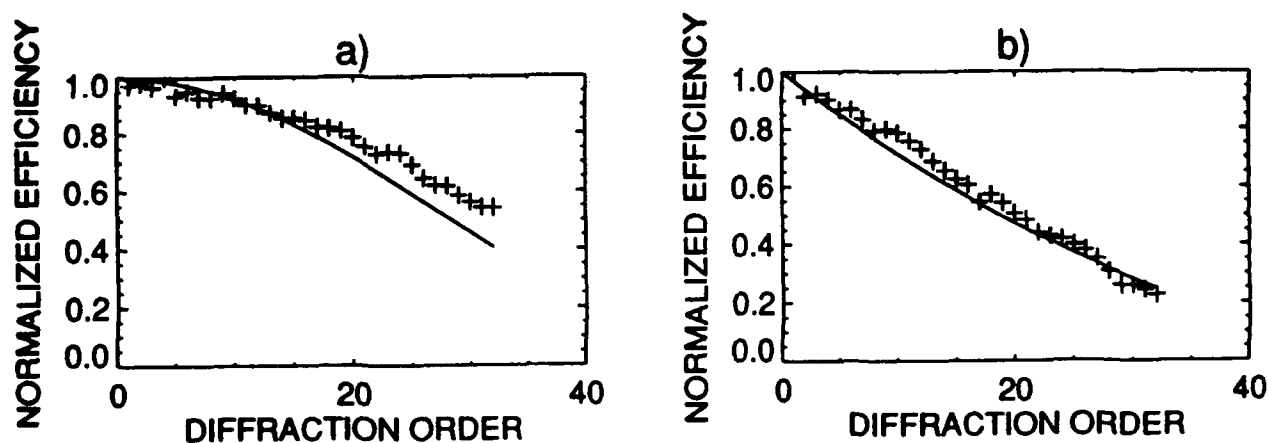
Figure 3: Normalized Beam Steering Efficiency a) Phased Array b) Microlens Array

theoretical predictions agree quite well, declining quickly at first for the microlens case and rolling off gradually at first for the phased array case. In particular, as predicted by theory, there is a dramatic difference in the efficiencies when steering to the extreme orders (over 100% increase in steering to order +32).

4. References

[1] W. Goltsos and M. Holz, "Agile Beam Steering using Binary Optic Microlens Arrays," *Opt. Eng.* 29, 1392-1397 (1990).

[2] M. B. Stern, et. al., "Fabricating binary optics: process variables critical to optical efficiency," *J. Vac. Sci. Tech.* B 9, 3117-3121 (1991).

Multi-Beam Grating Structures

A. D. Kathman, E. G. Johnson and M. L. Scott
Teledyne Brown Engineering
Huntsville, Alabama

Abstract

New systems are being developed around innovative diffractive optical components. Applications in optical interconnects, signal switching and interferometry have created a need for two-dimensional optical fanout gratings with unusual geometries. The increasingly complex gratings being designed for such optical fanout devices require specialized optimization algorithms to achieve desired performance. In this paper, we demonstrate optimization of a fanout grating in an n-dimensional solution space using a simulated annealing algorithm. The algorithm provides a successful first-order design which is further optimized using wave optics design software. A three beam grating is fabricated and tested; diffraction efficiencies will be reported. By means of the example below, we present a design algorithm for fanout grating of arbitrary geometry.

Summary

The growth of optics in commercial fabrication and signal processing has produced a significant opportunity for innovation and the development of new optical devices.[1] Fanout gratings, designed to redirect light into specific diffraction orders, are finding many applications in optical interconnects, signal switching and interferometry. As the complexity of the fanout increases, particularly if the weighting of the orders is asymmetric, the conventional design process becomes untenable. To overcome these limitations, a non-deterministic optimization algorithm must be utilized.

A fanout device has been designed which produces three diffracted beams with equal power in each diffracted order, (see figure 1). The grating operates in transmission under normal incidence, directing light into three non-planar orders. The triangular geometry requires suppression of symmetric orders, increasing the mathematical complexity of the design effort. An attempt was made to design the grating in a deterministic manner using standard scalar diffraction theory, but yielded no solution. To over come the limitations of our initial approach, a simulated annealing algorithm was used to produce a solution. A grating unit cell was defined as a 64 x 64 two-dimensional array of discrete phase values, thus the dimension of the problem was n = 4096. The algorithm converged well for grating patterns of four or phase levels. Optimization by simulated annealing was stopped after 10,000 iterations. The resulting grating structure was counter-intuitive, but showed a simple repeated pattern (see figure 2).

The solution was verified by simulation using a proprietary wave optics design package. Removing the high spatial frequency structure at the boundaries showed a slight increase in the predicted signal to noise(SNR) and diffraction efficiency. Intuitively, the triangular diffraction pattern would best benefit from 60° edges in the grating pattern. To investigate this, as well as to simplify the lithographic masks required to produce the optic, the pattern was re-rendered as a series of hexagons. The hexagonal pattern was adjusted using the simulation code to suppress higher order scatter. This both increased the SNR and improved the diffraction efficiency of the grating. Also, the secondary optimization dramatically reduced the complexity of the masks required to produce the element.

Two reticles were produced on a MANN 3600 pattern generator and the patterns were transferred onto chrome masks using a step and repeat system. The reticle patterns are shown in figure 3. The three-beam grating is being fabricated at Teledyne Brown Engineering as this summary is being written, and experimental results verifying performance will be presented.

Conclusions

A design technique utilizing simulated annealing has been developed to design grating structures for two dimensional fanout devices with unusual geometries. The technique has been demonstrated for an asymmetric three-beam grating and can be expanded to larger, more complex applications. The authors wish to acknowledge K. Baker for his contributions in formulating the problem and A. Cook for his aid in interpreting the results.

1. Alan Kathman and Eric Johnson,"Binary Optics: New Diffractive Elements for the Designer's Tool Kit". *Photonics Spectra*, pp. 125-132, September 1992.
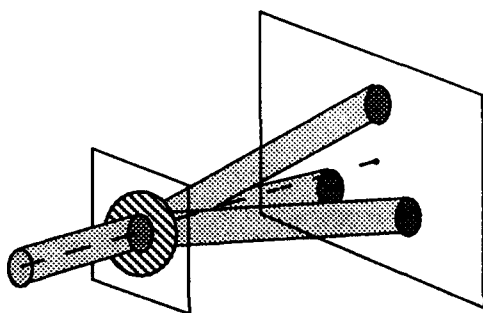

Figure 1. Functional performance of an asymmetric three-beam fanout grating

Phase Depth

0.0

$\lambda/4$
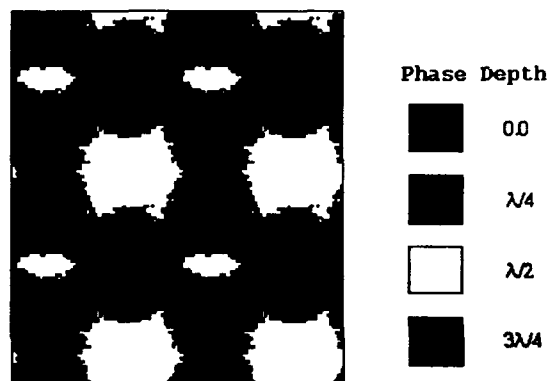
$\lambda/2$

$3\lambda/4$

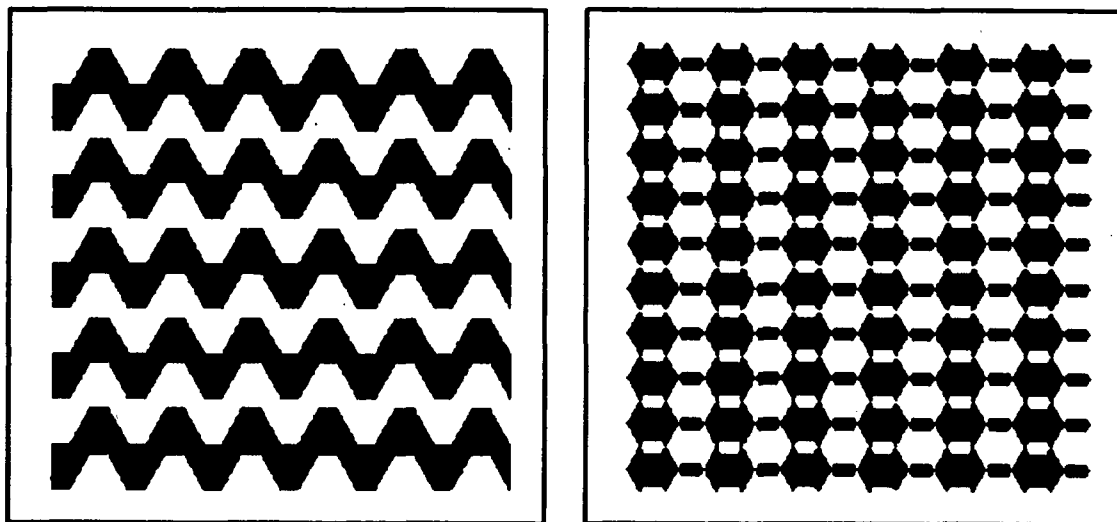Figure 2. Simulated annealing results for the four phase level grating design.

Figure 3. First and second level mask reticles for three-beam fanout grating fabrication.

Multiplexed Substrate-Mode Holographic Interconnects

Y. Amitai

Weizmann Institute of Science
Department of Electronics
Rehovot 76100, Israel
Tel: 972 8 342032

Recently there have been several proposals for fan-in or fan-out optical interconnect architectures with wavelength division multiplexing. One approach to transmit information from several sources onto a single target (or vise versa) relies on multiplexed holographic optical elements (HOEs), where each channel is associated with a separate HOE. Two requirements must be met for successful implementation of this method. On the one hand, the diffraction efficiency of each HOE must be very high for a particular wavelength to ensure a low insertion loss for each channel. On the other hand, each HOE must be transparent to all other wavelengths to prevent cross-talk between the channels. In addition, to achieve low insertion loss, all the HOEs must focus the light waves of the various channels to near-diffraction-limited spot sizes.

In this paper, a method based on multiplexed substrate-mode HOEs is presented. The building block of the system (Fig. 1) comprises two identical HOEs recorded on the same substrate[1]. The first HOE, $\mathcal{H}^s$, collimates the source's light into a plane wave which is trapped inside the substrate by total internal reflection. The second HOE, $\mathcal{H}^d$, focuses the collimated wave onto a target. Since the holographic substrate can be located very close to the source and the target, and since the light is guided by the substrate, this system can be very compact and simple to implement. Furthermore, the double HOE arrangement permits compensation of lateral and longitudinal chromatic effects. The former is accomplished selecting antisymmetric dispersion for the two HOEs. The latter is effected by introducing a deliberate aberration, which is associated with the axilens effect[2]. Therefore the system's performance, and in particular the output spot size, is not sensitive to source wavelength uncertainty.
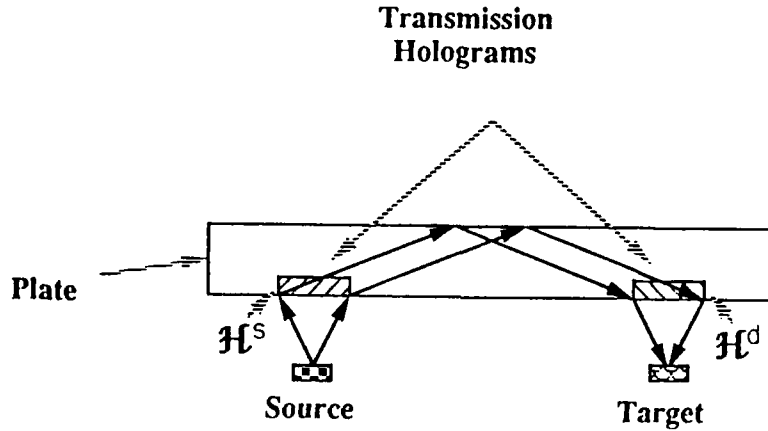
**Transmission
Holograms**

*Figure 1: A building-block for the holographic fan-out system. The source
and target can be fibers or surface-mounted laser and detector, respectively.*

When there are n communication channels, $C_1 \ldots C_n$, with wavelengths $\lambda_1 \ldots \lambda_n$, respectively, a number of building blocks can be superimposed to fabricate the desired fan-out system. The result is one hologram comprising n different multiplexed HOEs, $\mathcal{H}_1^s \ldots \mathcal{H}_n^s$. Each of these HOEs collimates one incoming channel, and diffracts it in a specific direction. Each channel, C_i, is focused by one of the second set of n HOEs, $\mathcal{H}_i^d$, onto its respective target. Naturally, the system can readily be inverted to fan-in n input sources onto one output target.

In order to achieve high efficiency and negligible cross-talk between the channels, each $\mathcal{H}_i^s$ must be Bragg matched at its respective wavelength λ_i, and be far-off-Bragg for all other wavelengths λ_j, $j \neq i$. For this purpose, a sufficiently large spectral separation, $\Delta\lambda_i$, between the channels must be chosen. In this paper, the spectral separation and, N_{ch}, the maximum number of channels are calculated as function of the operating waveband, the emulsion thickness and maximum depth of modulation, and the diffracted angle inside the glass plate, denoted as λ_{av}, T_e, η_{max}, and β_i, respectively. For example, the calculations show that for the following parameters $\lambda_{av} = 780$ nm, $T_e = 40$ μm, $\eta_{max} = 0.08$, and $\beta_i = 60°$, the maximum number of channels is $N_{ch} = 15$ and the spectral separation is $\Delta\lambda_i = 12$ nm.

The design procedure is illustrated experimentally with a two-channel system (Figure 2) where $\lambda_1 = 633$ nm and $\lambda_2 = 595$ nm. The four HOEs: $\mathcal{H}_1^s$, $\mathcal{H}_2^s$ (which were multiplexed together), $\mathcal{H}_1^d$, and $\mathcal{H}_2^d$, were recorded with the aid of recursive procedure[3]. The recording wavelength was $\lambda_{rec} = 458$ nm. It is apparent that $\mathcal{H}_1^s$ and $\mathcal{H}_1^r$ can be identical but oriented antisymmetrically. That is their respective reconstruction and the image waves are interchanged. Therefore, both holograms can be recorded with the same

recording procedure. Since the recording wavelength is different from the readout wavelength, the holographic elements must be recorded with pre-distorted wavefronts, in order to assure high diffraction efficiencies and low aberrations. The pre-distorted wavefronts are derived from interim holograms whose readout geometries differ from those used during recording.
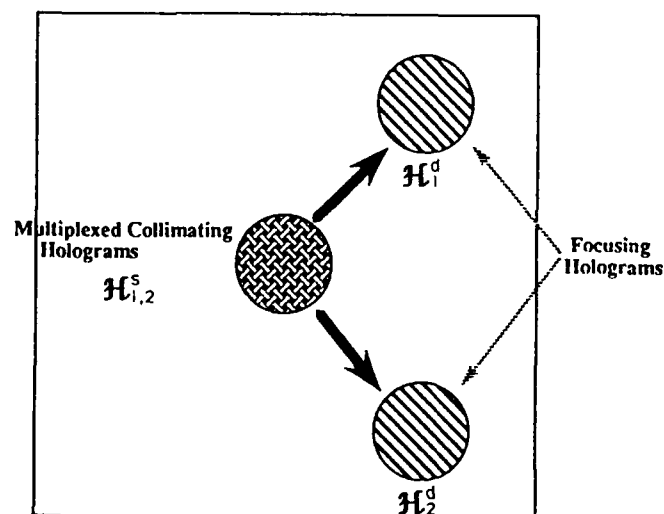
(a) Top View
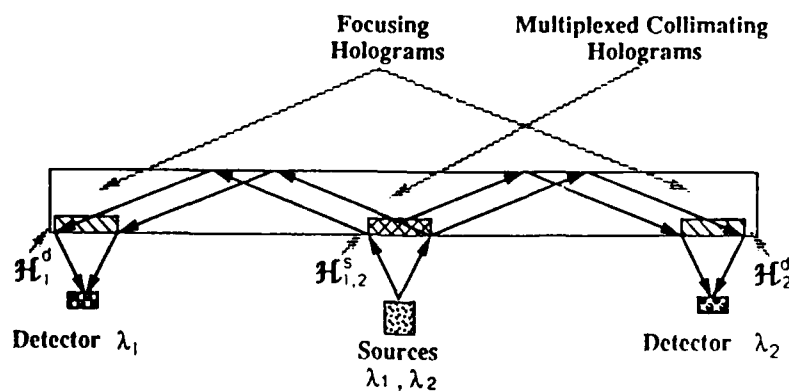
(b) Side View

Figure 2: A system composed of two building-blocks.

Table 1 lists the efficiencies of the various HOEs for λ_1 and λ_2. It is apparent that

each HOE is diffracts efficiently at its design wavelength and is essentially transparent to the other wavelength. The experimental insertion loss of either channel was less than 50%, and the cross-talk between the channels, is practically zero. Our system achieved near-diffraction-limited spot sizes ($\simeq 7~\mu m$) for both channels.

	λ_1	λ_2
$\mathcal{H}_1^s$	68%	0.5%
$\mathcal{H}_2^s$	0.1%	65%
$\mathcal{H}_1^r$	82%	0.9%
$\mathcal{H}_2^r$	1.5%	79%

Table 1: The diffraction efficiencies of the four HOEs.

To conclude, a method for designing and recording a multi-channel system based on substrate-mode HOEs, which can be used for wavelength-division-multiplexing or optical interconnects has been demonstrated. This system can potentially accommodate a large number of channels with a small spectral separation, high efficiency and a negligible cross-talk between the channels. Both the design and the recording procedures are fairly straight-forward, and the system is potentially very compact and easy to use.

References

1. Y. Amitai and J.W. Goodman, "Design of substrate-mode holographic interconnects with different recording and readout wavelengths", Appl. Opt. 30, 2376-2381 (1991).
2. A. Aharoni, J.W. Goodman, and Y. Amitai, "A Beam-correcting holographic doublet for focusing multimode laser diodes", Opt. Lett. in press.
3. Y. Amitai and A.A. Friesem, "Design of holographic optical elements by using recursive techniques", J. Opt. Soc. Am. A 5, 702-712 (1988).

Efficient, broad-band holographic axilens doublets for IR sources

Y. Amitai

Weizmann Institute of Science
Department of Electronics
Rehovot 76100, Israel
Tel: 972 8 342032

A. Aharoni and J.W. Goodman

Department of Electrical Engineering
Stanford University
Stanford, CA 94305
Tel: 415 723 0470

Recently, there has been rapid progress in developing semiconductor lasers as low-cost and compact monochromatic light sources for many applications. Despite their many advantages these devices suffer an inherent deficiency in output beam quality. A typical problem is the significant astigmatism found in gain-guided diodes. This astigmatism is a major disadvantage in many applications, and must be corrected in order to achieve diffraction limited performance. With conventional refractive optical elements, many practical applications require a difficult compromise between poor beam quality, and expensive and bulky corrective optics.

An alternative solution is a holographic correcting and collimating element for its low cost and small dimensions. Unfortunately, semiconductor lasers emit light at wavelengths in the near infra-red, where suitable recording materials are not available; by and large, high quality recording materials are sensitive only to visible light. To overcome this limitation holographic elements can be recorded in the visible for operation in the IR. Nevertheless such recording-to-readout wavelength shift introduces large aberrations

and, for high-efficiency thick media, can compromise the diffraction efficiency. Even if the above difficulties can be overcome the performance parameters of the resulting holographic elements are inherently very sensitive to chromatic variations of the source. This is a major drawback for laser diode sources for which the output frequency depends strongly on temperature and other operating conditions.
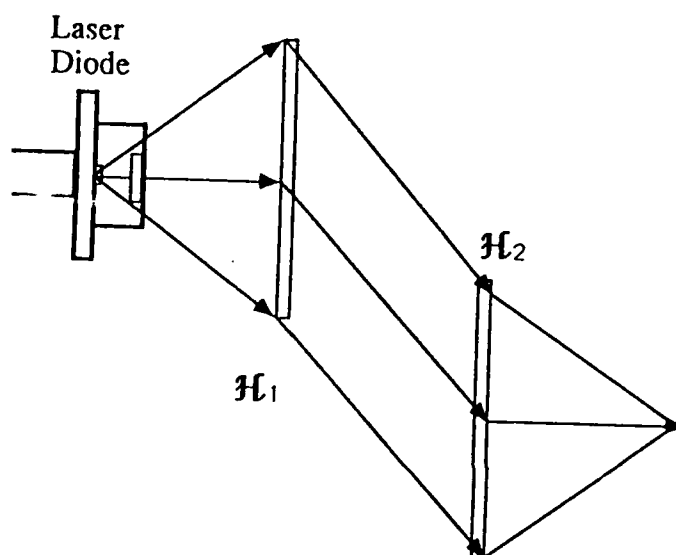

Figure 1. *Schematic layout of the holographic focusing doublet.*

We demonstrate a holographic focusing doublet (Figure 1) which is composed of a collimator, $\mathcal{H}_1$, and a focusing element, $\mathcal{H}_2$. The two elements are fabricated with the recursive design technique[1], namely, they are recorded with predistorted wavefronts which are generated by reading out simple spherical interim holograms with geometries that differ from those used during recording. A proper choice of the recording and the readout parameters of the interim holograms[2] enabled us to record $\mathcal{H}_1$ and $\mathcal{H}_2$ with the following properties:

- The Bragg condition is met over a wide field of view and high diffraction efficiencies (>70%) are achieved for both elements.

- The severe aberrations caused by the wavelength shift are compensated by the deliberate distortions of the interim holograms.

- The astigmatism of the source is corrected by inserting an opposite astigmatism during the recording procedure of $\mathcal{H}_1$.

- The lateral chromatic dispersion is corrected by the doublet anti-symmetric geometry.

- The longitudinal chromatic variation is compensated for by a deliberate spherical aberrations that broadens the spectral range over which the focal spot width is essentially fixed. These aberrations, which are associated with axicon elements, increase the focal depth of field, and reduce the effects of the longitudinal chromatic dispersion by relaxing the tolerance on the focal distance.

Our design is illustrated experimentally with a doublet having high efficiency and a diffraction limited performance over a spectral width of 5 nm that successfully corrects for laser-diode astigmatism and the recording-readout wavelength shift. The device is recorded at 488 nm for operation with an infra-red diode at 820 nm. Figure 2 shows the experimental laser-diode beam focal spot as focused by the holographic doublet. The size of this spot remains essentially constant over the spectral range of 818 nm to 823 nm.

$\longleftrightarrow$

10 μm
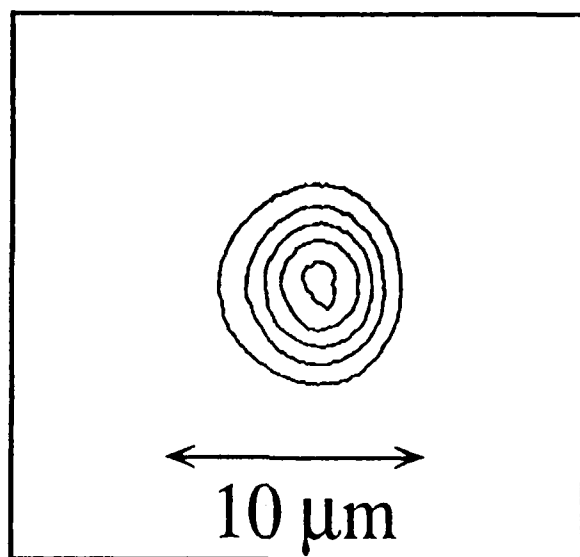
Figure 2. *Experimental focal spot obtained with the holographic doublet as captured by an eight-bit CCD camera. Intensity contours are shown at 10, 30, 50, 70 and 90% of the peak.*

To demonstrate the applicability of the proposed device, we present two applications in which the doublet design is beneficial:

- Low divergence pencil illumination for bar-code scanners in automated checkpoints. The main difficulty with this application is the broad variation in the operating distance of the scanner which is required to accommodate objects of widely varying dimensions. We design a converging doublet with a very long focal depth to address this constraint.

- A focusing lens with a very high resolution. Many application, such as optical disk read-write heads, require maximal possible lateral resolution. Conventional focusing grating lenses suffer from high sensitivity to the operating wavelength: even minute wavelength shifts defocus the spot and can move it laterally to increases the spot size and introduce misalignment, respectively. We design a focusing doublet with an f-number=1 which maintains a focal spot smaller than 1.5 μm over a 4 nm bandwidth (a spectral range which accommodates even low-performance laser-diodes).

To conclude, the proposed design offers highly efficient, low aberrated and compact device. The design and recording procedures are straightforward and require no specialized equipment. The design has several promising potential applications.

References

1. Y. Amitai and J.W. Goodman, "Design of substrate-mode holographic interconnects with different recording and readout wavelengths," *Appl. Opt.* **30**, 2376-2381 (1991).
2. A. Aharoni, J.W. Goodman, and Y. Amitai, "A Beam-correcting holographic doublet for focusing multimode laser diodes," *Opt. Lett.* in press.

Designing Continuous Contour Phase Plates for Beam Smoothing

S. N. Dixit, J. K. Lawson, K. Manes and H. T. Powell

Lawrence Livermore National Laboratory
P. O. Box 5508, L - 493
Livermore, CA 94551
(510) 423 - 7321

and

K. A. Nugent

The University of Melbourne, Parkville, VIC 3105, Australia

Spatial and temporal beam smoothing has now become an integral part of laser driven inertial confinement fusion (ICF) worldwide. Spatial smoothing is often achieved by using random phase plates (RPP) [1] or lenslet arrays [2]. Temporal smoothing is accomplished using smoothing by spectral dispersion (SSD) [3] or induced spatial incoherence (ISI) [4]. All the RPP's used so far have consisted of random layouts of square, rectangular or hexagonal phase plate elements that impose either 0 or π phase shift on the beam. The far-field intensity pattern of such RPP's consists of an envelope characteristic of the phase plate element and a superimposed speckle pattern resulting from the interference among the various phase plate element contributions. The far-field envelope for square and hexagonal shapes is qualitatively similar to an Airy pattern and it contains roughly 81 to 84% of the incident energy within the central maximum [5]. Even though such regular element, binary phase plates are easy to fabricate and are widely used, they offer little flexibility in our ability to tailor the far-field profile and to increase the energy content in the central maximum beyond the 84% predicted for a circular aperture.

In order to overcome these limitations for the binary RPP's, we have designed new phase screens for tailoring the far-field intensity distribution and increasing the energy content therein. These phase screens consist of

smooth, continuous variation of the phase across the aperture and, as such, relax the binary phase and the regular phase plate element assumptions. The design question for such continuous contour (or kinoform) phase plates can be posed as follows: is it possible to construct a phase screen in the input plane which, for a given input intensity distribution, produces a desired far-field intensity distribution? Since we are not interested in the phase in the far-field, we leave it arbitrary. This problem is very similar to the phase recovery problem [6] that has been investigated since the 1970's. It seems that no general mathematical proof exists of the existence and/or uniqueness of the solution to this problem. However, iterative algorithms have been developed to construct solutions for a very wide range of problems - image recovery and synthesis, speckle interferometry, beam profile manipulation for microwave plasma heating, designing diffractive optical elements etc.

We have implemented such an iterative algorithm for generating phase screens which produce desired far-field intensity profiles. The algorithm begins by choosing a prescribed near-field amplitude and a random phase screen. Fourier transform of this complex amplitude leads to amplitude and phase modulated far-field distribution. At this point, the far-field amplitude is replaced by the desired far-field amplitude leaving the phase unchanged. Inverse Fourier transforming this complex field gives the near-field distribution which has both amplitude and phase modulations. Now, the near-field constraint is applied by replacing the amplitude with the desired near-field amplitude but leaving the phase unchanged. The procedure is repeated again by Fourier transforming to the far-field ...etc. The iteration loop is exited after a satisfactory convergence is reached.

Numerical simulations have been carried out for constructing phase screens that produce supergaussian far-field intensity profiles from supergaussian near-field profiles. We find that the dominant part of the convergence is achieved after the first few (5 or so) iterations beyond which point the convergence improves extremely slowly. Nevertheless, after about 50 iterations, greater than 95% of the incident energy is contained within the desired spot in the far-field. This is a significant improvement over the 84% energy content for regular element, binary random phase plates where the

element size is chosen such that the size of the central maximum (to the first zero) is equal to the size of the supergaussian profile in the far-field.

The near-field phase screen obtained after the iterative optimization shows a fairly smooth ripply structure resembling waves on a lake surface. Due to the range of the numerical arctangent function, the calculated phase is always in the range $(-\pi, \pi)$. This compression of the real phase by modulo 2π introduces sharp jumps approximately 2π in size. Except for these jumps, the phase screen appears fairly smooth. A careful 2-d unwrapping of these jumps is currently underway.

In the presentation, we will outline the iterative algorithm and present simulations of phase screens for producing variety of far-field intensity profiles. Finally, we will discuss the consequences of using such phase screens on aberrated beams such as Nova.

ACKNOWLEDGEMENT

REFERENCES

[1]   Y. Kato et al, Phys. Rev. Lett. **53**, 1057 (1984).

[2]   X. Deng et al, Appl. Opt. **25**, 377 (1986).

[3]   S. Skupsky et al, J. Appl. Phys. **66**, 3456 (1989).

[4]   R. Lehmberg and S. P. Obenschain, Opt. Comm. **46**, 27 (1983).

[5]   See, for example, M. Born and E. Wolf, *Principles of Optics* 6th edition (Pergamon, New York, 1980) p. 393.

[6]   See, for example, J. R. Feinup, Appl. Optics **21**, 2758 (1982).

Production of High Damage Threshold Diffractive Optics for Beam Smoothing

J. K. Lawson, S. N. Dixit, A. Morgan, I. M. Thomas, B. W. Woods and H. T. Powell

Lawrence Livermore National Laboratory

P.O. Box 5508, L-490

Livermore, CA 94550

(510)423-2075

Introduction

Diffractive optics based on binary phase patterns have proven valuable in homogenizing the focal plane intensity profiles of high energy laser systems used in Inertial Confinement Fusion (ICF).[1-4] These binary phase plates, by introducing randomly either a 0 or π phase shift to regions of the laser beam, scramble the phase coherence of a laser beam and produce a homogenous focal irradiation spot whose intensity distribution is predictable and well-characterized. These optics are relatively simple to make with good damage resistance by selectively etching away a layer of sol-gel material on a fused silica substate.[3,4] Unfortunately, the high spatial frequencies associated with the binary steps result in a significant portion of the energy (15%) occuring outside of the central focal spot.

One approach to avoiding this type of energy loss is to create random phase patterns whose profiles do not contain abrupt, high spatial frequency steps. Alternate patterns based on continuous phase plates (kinoforms) have been demonstrated on small optics, but do not have the damage resistance required for high energy applications. The technique which we used effectively to create high damage threshold, binary patterns cannot not be applied to this problem partly due the rapid etch rate of the sol-gel. We have developed new relatively low-cost approaches which have the potential for producing high damage resistance kinoforms.

Approach

Previous methods of producing kinoforms generally involve exposure of a photoresist coating applied to a substrate. Development of the photoresist leaves a layer of material whose thickness varies inversely proportional to the exposure fluence. This layer of material either serves as the phase pattern or as a resist for subsequent reactive ion etching into the substrate. Phase patterns based on the developed resist suffer from absorption and subsequent damage when irradiated with high energy, ultraviolet (UV) light. Moreover, phase patterns based on reactive ion etching are costly to produce and difficult to make at large aperture.

We have focussed on two techniques which are designed to give high damage resistance even at UV wavelengths, at a modest cost and with the capability for large aperture optics. The first technique we are attempting involves recording a phase pattern into a polymer coating. Tests of micron thick poly-methyl acrylate (PMA) and poly-methyl methacrylate (PMMA) polymer coating on fused silica have demonstrated damage thresholds of up to 5 J/cm² for 1 ns, 350 nm light. These polymeric materials act as deep-UV photoresists for exposures with $\lambda < 220$nm.[5,6] The phase pattern can be recorded into the polymer coating using either contact printing techniques with UV-transmissive masks or direct writing techniques using excimer lasers. We will present preliminary results based on both of these approaches to deep-UV photolithography.

In the second technique, rather than applying a varying layer to a substrate, we remove a portion of the substrate in order to produce a phase pattern. We have explored this approach using CO_2 radiation to ablate fused silica in a controlled fashion. The 10.6 μm radiation is absorbed on the surface of the substrate, rapidly heating the material above the volatilization point.[7,8] If a small volume of material are removed, recondesation is not a serious problem. The hole left behind is in the characteristic shape of the irradiating spot and is generally free from both surface cracks and contanimants. As a result, the pattern is optically clear and of comparable damage resistance to the rest of the substrate. The depth of the ablation can be controlled by limiting exposure times. Thus, using direct writing techniques, arbitrary phase patterns can be contructed.

Experimental Results

In order to demonstrate deep-UV photolithography, a coating of 1.0 μm optical depth of PMMA was deposited onto a fused silica substrate. Sections of the coating were masked by a metal mask and the optic was exposed to light from a pulsed xenon flashlamp. A significant portion of the light from such a source falls in the 185-250 nm wavelength region. The low power and low repetition rate of the lamp we have currently available required long exposure times. The results, however, were encouraging. After development in a methyl isobuthyl ketone solution, the height of the remaining PMMA was inversely proportional to the exposure fluence. The height was measured by both a phase-stepping interferometer and a contact profilometer.

Currently, we are investigating techniques for contact printing onto the deep-UV photoresists. We are currently developing methods of producing variable density masks which will transmit the deep-UV. Conventional gelatins used in photographic films and plates are not useful due to their strong absorption of wavelengths less than 250 nm. Substitution of a different type of emulsion should result in a useable deep-UV mask.

Experiments using an excimer laser as a direct writing source are ongoing. A pulsed ArF laser ($\lambda = 193$ nm) will be used to expose the polymer coating on a fused silica substrate.

We demonstrated the ablation of a phase pattern on a fused silica substrate by focussing the output of a low-power (5 Watt) CO_2 laser onto the substrate. Focal spot sizes used ranged from 25 to 600 μm. The amount removed was controlled by limiting the exposure time. (Exposures typically on the order of milliseconds). This produced pit depths which varied linearly with exposure. Currently, we are developing procedures for producing complex phase patterns using the ablation technique. We will report on the results obtained.

References

[1] Y. Kato, K. Mima, N. Miyanaga, S. Arinaga, M. Nakatsuke, and C. Yamanaka, Phys. Rev. Lett, Vol. 53, No. 11, pp 1057-64 (1984).

[2] C. N. Danson, R. Bann, D. Pepler, I. Ross, J. Exley, D. Hardie and S. Sails, Rutherford Appleton Laboratory Rep. RAL-91-025 (Rutherford Appleton Laboratory, Didcot, Oxon, UK, 1991), pp.62-65.

[3] S. N. Dixit, B. W. Woods, I. M. Thomas, M. A. Henesian, and H. T. Powell, paper WT2, *OSA Annual Meeting Technical Digest 1990*, Vol. 15 (Optical Society of America, Washington, D.C., 1990) p. 152.

[4] B. W. Woods, I. M. Thomas, S. N. Dixit, M. A. Henesian and H. T. Powell, *SPIE Proceedings, 1410* , 47 (1991).

[5] Yoshiaki Mimura, Takashi Ohkibo, Tatsuo Takeichi and Kyozo Sekikawa, *Japanese Journal of Applied Physics*, Vol. 17, No. 3, pp. 541-550 (1978).

[6] Takao Iwayanagi, Takumi Ueno, Saburo Nonogaki, Hiroshi Ito and C.Grant Wilson, "Materials and Processes for Deep-UV Lithography", *Electronic and Photonic Applications of Polymers*, M.J. Bowden and S.R. Turner, ed.,(American Chemical Society, Washington, D.C., 1988), pp. 109-224.

[7] P. A. Temple, W. H. Lowdermilk and D. Milam, Appl. Opt., Vol. 21, p.3249 (1982).

[8] M. Kubo and M. Hanabusa, Appl. Opt., Vol. 29, pp 2755-2759 (1990).

Optimization of Brightness and Magnification in Holographic Image Combiner Systems

Hirokazu Aritake, Masayuki Kato, Masato Nakashima
Fujitsu Laboratories Ltd.
10-1 Morinosato-Wakamiya, Atsugi 243-01, Japan
Telephone : +81-462-48-3111

1. Introduction

In image combiner systems for mobile applications such as automobiles and trains, magnification is needed as well as bright images for bright environments. To realize an image combiner system, it is useful to apply reflection holograms to the system. Image magnification holograms allow compact systems to be made because of their small optical path lengths. The wavelength selectivity of reflection holograms enables high light use efficiency for both displayed image and background scene.

An effective way to increase image brightness is to use reflection holograms with a broad band reflection spectrum. Unfortunately, if we enlarge optical magnification with broad band reflection, optical aberration is increased. There is an inverse relationship between image size and brightness. For available combiner system, an optimal trade-off must be done between these parameters. Here, we propose a method to produce both bright and large images. We define the permitted levels of aberration in terms of the human eye. In this paper, we describe the hologram limits in magnification and band width for a holographic image combiner systems with a compact optical system and a bright image.

2. Permitted aberration levels

Permitted aberration levels are obtained by information volume (V) as the image clarify parameter. V value of 0.8 designates the boundary between good and bad images. The cut-off line spacing for the optical system is about 7 line/mm at the spacing for distinct vision (250 mm)[1]. Therefore, the permitted aberration is 2 arc min.

In holographic optical systems which use broadband light, chromatic aberration occurs in the images. That image has blurred components in which position and brightness are different for each wavelength (λ). Chromatic aberration is defined by the visual angle for the differences in position for each wavelength. If the images are clear (the image has only chromatic aberration), aberration results only from differences in brightness and position at each wavelength. The permitted levels of chromatic aberration is defined by the visual angle with the maximum different position under these brightness conditions. It should be 2 arc min.

3. Image brightness and FWHM

The system includes two reflection holograms and a display element (Fig. 1). The holograms correct chromatic aberration to some degree. The specification of the optical system is shown in Table.1. High image brightness (for example 1500 cd/m^2) is needed when using the system in bright environments. The image luminance is defined by the integrated product ($\int DHd\lambda$) of the display element luminance spectra ($D(\lambda)$) and the reflection hologram's efficiency ($H(\lambda)$). Display element luminance is the product of

display element radiance and the spectral luminous efficiency. Each of the spectra is shown in Fig. 2. Total system efficiency is the integrated display element luminance divided by the integrated image luminance. Computer simulation result for the relationship between reflection band width (using full-width at half-maximum, FWHM intensities) and the total system efficiency (using a vacuum fluorescent display, VFD) is shown in Fig.3. If the reflection spectrum (FWHM) of the holograms is enlarged, the total system efficiency becomes large, resulting in a bright image.

Investigating reflection holograms with the FWHM varied, if the difference (delta λ) in wavelength (λ) from the spectrum's peak wavelength ($\lambda 0$) increases, intensity goes down (Fig. 4). For example, if we correct chromatic aberration until the wavelength reaches a tenth of the maximum luminance, the delta wavelength (delta $\lambda = \lambda - \lambda 0$) equals 6.2, 12.0, 17.7, and 23.1 nm for FWHM values of 10, 20, 30, and 40 nm.

4. Magnification and FWHM

We calculated the relationship between magnification (m) and chromatic aberration. The relationship is shown in Fig. 5 between chromatic aberration and d1 (with d2 held constant). The aberration is shown in (a) for an FWHM of 10 nm (delta $\lambda = 6.2$ nm) and in (b) for FWHM of 30 nm (delta $\lambda = 17.7$ nm). For low level magnification, chromatic aberration is low. The d1 is large for the position that gives minimum chromatic aberration. To keep chromatic aberration below 2 arc min (that is to say, to get a clear image), magnifica.ions are 2.4 and 1.5 for FWHM value of 10 and 30 nm.

Fig. 6 shows the relationship between the display element luminance and the FWHM to realize a bright image (1500 cd/m^2). If the luminance is strong, the FWHM is small. The FWHM is 30 nm for a VFD luminance of 8000 (cd/m^2). The FWHM is 10 nm for a luminance of 22000 (cd/m^2). The permitted magnifications for these respective levels are 1.5 and 2.4. As it is now possible to get a VFD with a luminance of stronger than 20000 (cd/m^2), we can use holograms with spectra FWHM of 10 nm.

5. Summary

We optimized brightness and magnification in optical systems using two reflection holograms. We described the relationship between VFD luminance and magnification of the optical system for 1500 (cd/m^2) images. We showed that the permitted magnification for a clear image is 2.4 when using the VFD with luminance of 22000 (cd/m^2).

Reference
1. Kazuo Sayanagi, The Journal of the Institute of Television Engineers of Japan, Vol.40, No.4, pp 312-317 (1986).

Table 1 Image combiner system specifications

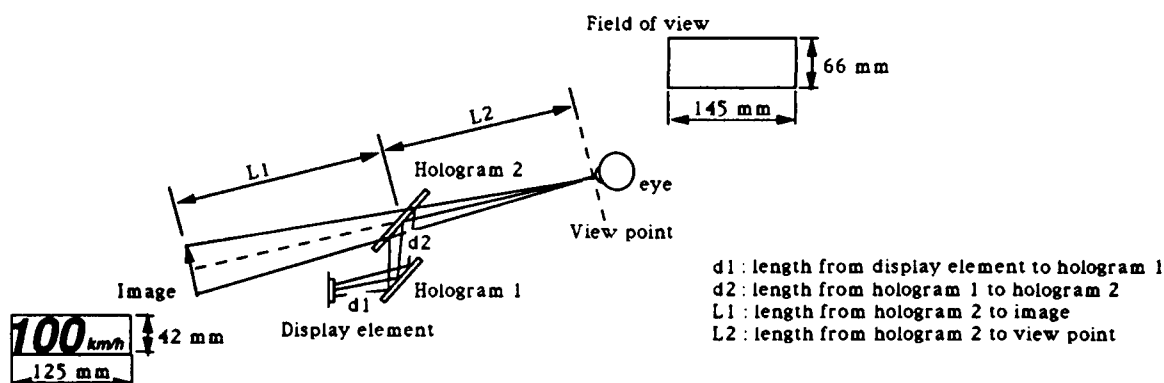| L$_1$ (mm)	1000
L$_2$ (mm)	1000
Field of view (mm)	66 × 145
Image size (mm)	42 × 125
Luminance of image (cd/m^2)	more than 1500
Wavelength at maximum efficiency (nm)	530

Fig.1 The system of holographic image combiner

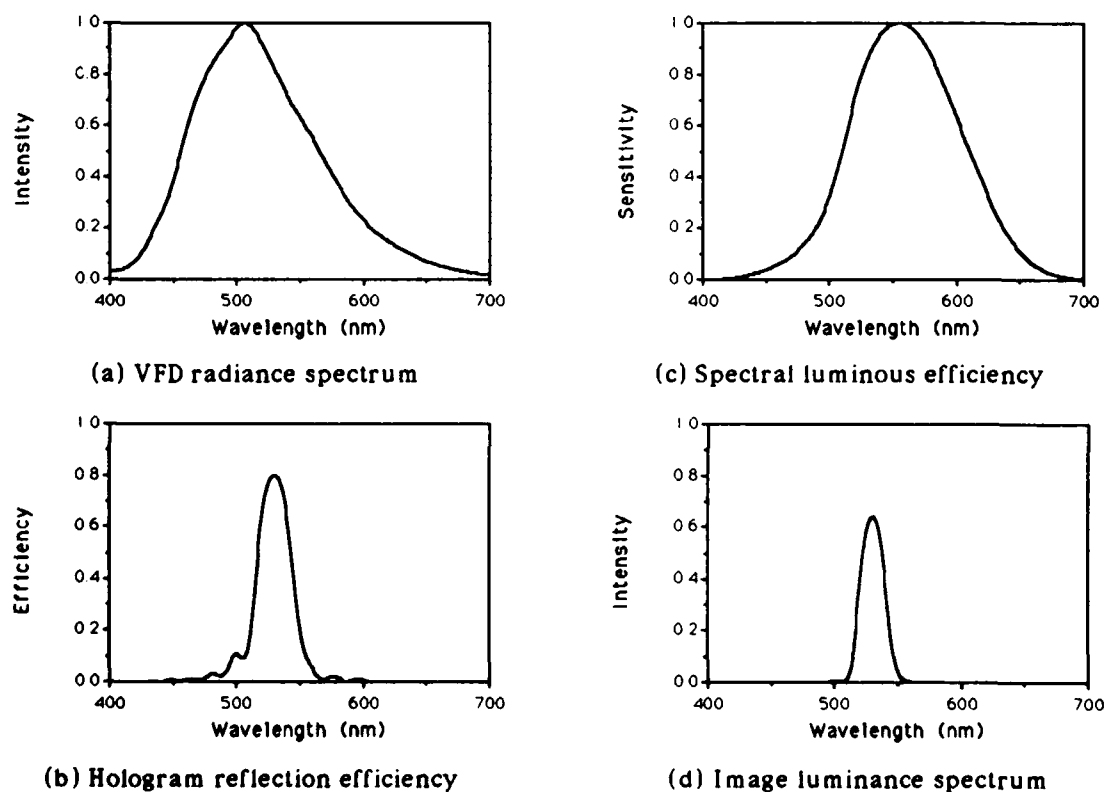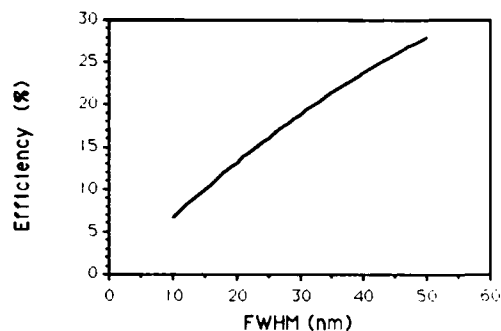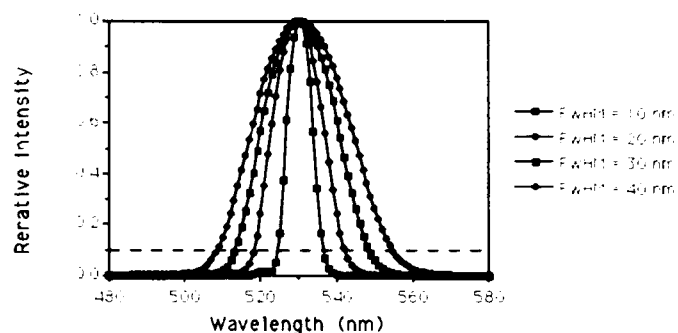(a) VFD radiance spectrum

(c) Spectral luminous efficiency

(b) Hologram reflection efficiency

(d) Image luminance spectrum

Fig.2 spectrums

Fig.3 The relationship between
FWHM and total system efficiency

Fig.4 Image luminance spectra
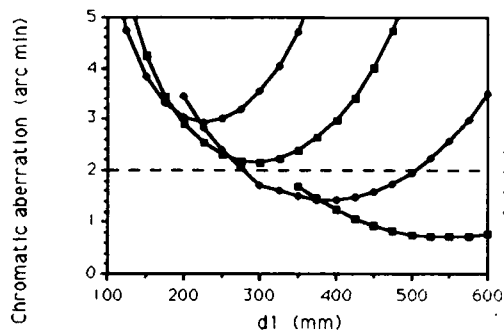
(a) FWHM-10nm
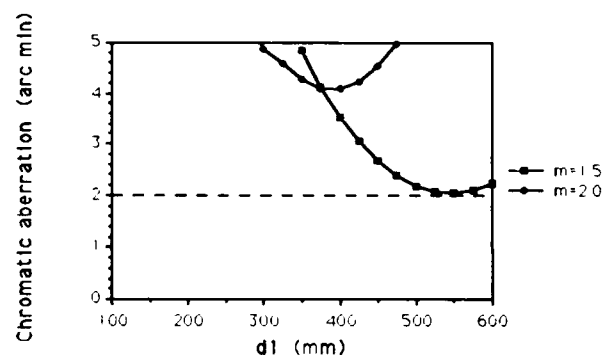
(b) FWHM=30nm

Fig.5   Chromatic aberration against magnification with d2 held constant
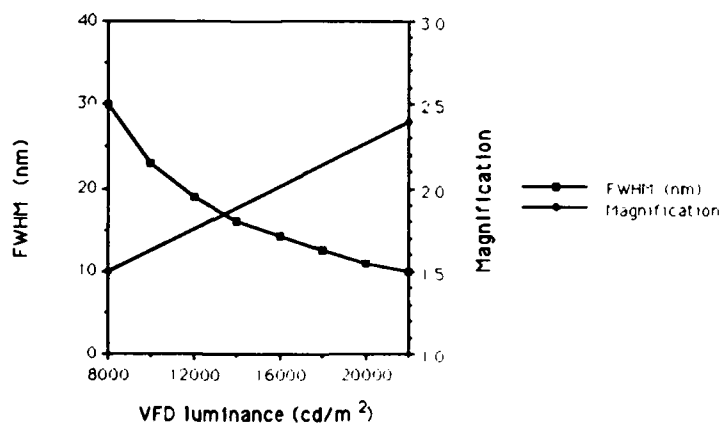
Fig.6 FWHM and magnification against VFD luminance

Diffractive Optics Contributed Papers in Poster Format

(This session includes papers previewed in OTuA.)

OTuB 10:30am-12:00pm
Grand Ballroom

Plenary Session

OTuC 1:30pm-3:00pm
Oleander Room

Susan N. Houde-Walter, *Presider*
University of Rochester

Optical System Design with Diffractive Elements

Professor G. Michael Morris
The Institute of Optics
University of Rochester
Rochester, New York   14627

Diffractive optics provides optical system designers with new and exciting degrees of freedom, which can be used to optimize system performance and create new optical components and systems. Applications include: laser scanners, head-mounted and head-up displays, optical-disk readout heads, aberration-correction for monochromatic and broadband optical systems (XUV to IR), subwavelength structured surfaces, and many others. In this talk we will address three principal topics:

Aberration Correction and Wide Field Imaging using Diffractive Lenses
The performance of wide-field diffractive lenses for monochromatic imaging (infinite and finite conjugates), Fourier transformation, multiple imaging, and broadband imaging using diffractive/refractive hybrids will be described and compared with conventional refractive lens systems. In many cases we find that diffractive lenses provide equal or superior performance to that obtained with refractive lens systems containing many more elements.

Diffractive / refractive components for broadband systems.
Fundamental design principles will be emphasized. Methods to achromatize lenses for optical data storage systems, and achromatization of integrated optical components, including step-index lenses, input/output couplers, and beam-splitters will be described.

Subwavelength Structured Surfaces (SWS)
The design, fabrication and applications of subwavelength surface-relief gratings will also be discussed; these gratings exhibit remarkable anti-reflection properties over a wide range of fields of view and broad wavelength ranges, and can also be used for polarization control and as narrowband filters.

Design Issues in Monolithic Waveguide Integration

R. J. Deri

Bellcore, 331 Newman Springs Rd., Red Bank, New Jersey 07701-7040
currently at Lawrence Livermore National Laboratory, PO Box 808
Livermore, California 94550

Advanced fiber optic systems for communications and sensing are using increasingly sophisticated combinations of optical and optoelectronic devices, with optical functions such as power splitting/switching and wavelength separation. The hardware cost and reliability for such systems can be limited by problems associated with optical packaging, and the strict alignment tolerances for high-efficiency coupling and optical path length control are of particular concern. Interest in monolithic integration of optical and optoelectronic elements on a single substrate has been stimulated by the fact that hybrid packaging of discrete components is intrinsically susceptible to these problems. III-V semiconductor materials provide an extremely flexible approach to such on-chip integration, since they are suitable for both electrooptic waveguide devices as well as optoelectronic functions involving diode lasers, optical amplifiers, and photodetectors operating at $\lambda=0.8$ to $1.6\mu m$. Recently, major progress in III-V optical waveguides[1] and their integration with other optoelectronics to create "photonic integrated circuits"[2] has made this approach increasingly attractive. Nonetheless, key issues must be resolved in order to make this technology viable: by reducing chip size, minimizing fabrication complexity for high yield, and improving the ease of chip packaging (optical coupling to fibers). This talk shows how advanced design techniques have been applied to solve many of these problems in photonic integration.

The yield of device chips from a processed wafer depends on both the ease of fabrication/integration and the overall chip (die) size. The relatively high cost of III-V materials [3] places a premium on satisfactory resolution of these issues. While fabrication concerns tend to be application specific, waveguide circuits generally have strict lithography requirements (eg: linewidths/spaces for directional couplers) which are complicated by the nonplanar topography resulting from integration. Moreover, optical component integration can require order-of-magnitude increases in chip area over discrete optoelectronic devices due to the large size of typical integrated optic devices. While such increases can be avoided by in-line integration of a few devices on a single guide for certain applications,[2] die size remains a concern for advanced devices requiring multiple waveguide input/output ports. Finally, the on-chip interconnection between optical and optoelectronic devices must be accomplished with high-yield integration processes.

This talk will focus on the design techniques required to minimize waveguide circuit size, to realize fabrication-tolerant directional couplers, to efficiently couple waveguided light into easily fabricated photodetectors, and to improve off-chip fiber coupling. It will show how a variety of design tools, ranging in complexity from simple ray optics to planar guide modal analysis [4] to sophisticated modal eigensolvers [5] and propagation codes (such as beam-propagation methods [6] and finite-difference time-domain simulations [7]), are applied to design these components. In particular, the critical influence of optical interference involving both guided and radiation modes on the design of both compact, fabrication-tolerant directional couplers [8,9] and waveguide/photodetectors will be demonstrated. The application of these techniques to the extremely compact (1.3mm length) integration of an optical front-end for coherent lightwave reception (Fig. 1) [10] will be described.

The ease of packaging such device chips is as important to overall hardware cost as the yield in chip fabrication. From the standpoint of optical design, the critical problem is the off-chip optical coupling between external elements (eg: fibers) and waveguides on the chip. Easy packaging demands a large waveguide mode size (or spot size) to improve alignment tolerances and stability requirements. While III-V waveguides with large spot size for easy off-chip coupling have been demonstrated, a larger guided mode degrades most other performance aspects of on-chip devices. Larger modes increase laser threshholds, reduce electrooptic modulator efficiency, and degrade the performance of bending structures needed for compact multi-port devices.[1] These conflicting requirements show the need for on-chip tapers to transform small modes for device performance into large modes near chip edges for easier off-chip coupling.[1,2] Examples of current research in this area [11] will be described.

In summary, difficulties in the fabrication and packaging of waveguide-based photonic integrated circuits can be significantly reduced by using advanced optical designs, which in turn require sophisticated simulation tools which account for optical interference. Further advances in III-V photonic circuits are anticipated with increasing use of these design tools.

REFERENCES

[1] R.J. Deri and E. Kapon, *J. Quantum Electron.* QE-27, p. 626 (1991).

[2] T.L. Koch and U. Koren, *J. Quantum Electron.* QE-27, p. 641 (1991).

[3] A. Podell, S. Moghe, et al., *Microwave J.*, p. 208 (Nov. 1987).

[4] J. Chilwell and I. Hodgkinson, *J. Opt. Soc. Am. A* 1, p. 742 (1984).

[5] M.J. Robertson, S. Ritchie, et al., *Proc. IEE J*, 132, p. 336 (1985).

[6] M.D. Feit and J.A. Fleck, *J. Opt. Soc. Am. A* 7, p. 73 (1990).

[7] R.R. McLeod and R.J. Hawkins, *Tech. Dig. Intgtd. Photonics Research*, p. 38 (New Orleans, 1992).

[8] E.C.M. Pennings, R.J. Deri, et al., *Appl. Phys. Lett.* 59, p. 1926 (1991).

[9] L.B. Soldano, R.B. Veerman, et al., *Proc. European Conf. Opt. Commun.*, paper TuB5-2 (Paris, 1991).

[10] R.J. Deri, E.C.M. Pennings, et al., *Photonics Technol. Lett.* 4, (Nov. 1992).

[11] G.H. Song and W.J. Tomlinson, *J. Opt. Soc. A* 9, p. 1289 (1992).
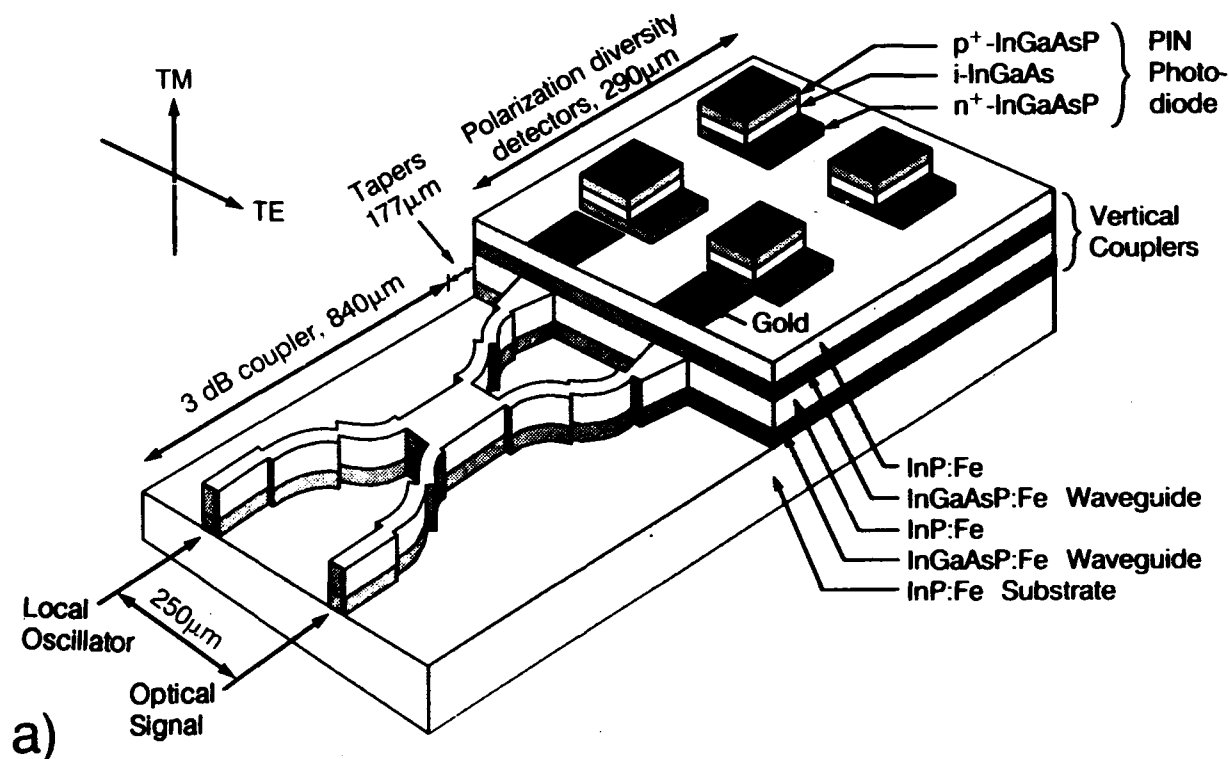
Fig. 1: Coherent receiver front-end on InP using advanced coupler and guide/detector coupling designs. The power-splitting coupler on the left-hand side uses multi-mode-interference to maintain short length (840μm). The right-hand side of the chip features serial integration of detectors and polarization splitting couplers for polarization diversity reception. Vertical definition of the polarizing couplers and detectors allows extremely compact coupling (total length 290μm) while avoiding epitaxial regrowth.

Tutorial Session

OTuD 3:30pm-5:00pm
Oleander Room

Laura A. Weller-Brophy, *Presider*
3M Research Laboratories

Tutorial on
The Applicability of Conventional Design Notions
to Integrated Optics

Lambertus Hesselink
Stanford University
3598 Durand Building
Stanford, CA 94305-4035
Ph: 415-723-4850
Fax: 415-725-3459

The objective of this tutorial is to explore similarities and differences between the design of conventional and integrated optical elements. The approach we take is to briefly review design notions developed for diffractive elements using bulk optics. Particular emphasis is placed on fundamental issues underlying the performance of these devices, usually expressed in terms of aberrations, diffraction efficiency and polarization characteristics computed using raytracing and wavefront analysis. For evaluation of performance in integrated optics, mode characteristics for the various polarization states need to be incorporated into device analysis. We consider examples such as holgraphic optical elements, grating couplers and beam steering elements to illustrate commonly used design strategies and approaches. Throughout the discussion we explore how knowledge of rules developed for the design of conventional diffractive elements can be applied to the area of integrated optics. Notions such as Brewster's angle and k-vector diagrams for thin and thick diffractions grating having equivalent counterparts in the design and evaluation of integrated optical structures will be highlighted and studied.

Design Methods for Photonics Technology Contributed Paper Preview

OWA 9:00am-10:20am
Oleander Room

W.J. Tomlinson, *Presider*
Bellcore

The Use of Fourier Methods To Analyze the Effects of Birefringence in Optical Disk Substrates

Bruce E. Bernacki and M. Mansuripur

Optical Sciences Center
University of Arizona
Tucson, Arizona 85721
(602) 621-8265

1. INTRODUCTION

Current methods of producing optical disk substrates involve injection molding of polycarbonate plastics. The substrates thus produced are birefringent with principal axes of the index ellipsoid both in-plane and perpendicular to the plane of the disk[1-3]. The in-plane, or lateral birefringence is often quoted as having $n_x - n_y \approx 20 \times 10^{-4}$, while perpendicular, or vertical birefringence is substantially greater with $n_z - n_x \approx 500 \times 10^{-4}$.

In-plane birefringence causes polarization ellipticity in the light reflected from the disk surface, and degrades the magneto-optical (MO) signal since differential detection is sensitive to the difference in the phase delay between the original polarization and the orthogonal component that comes about due to the polar Kerr effect[4]. This difference in phase amounts to about 11° for a 1.2mm thick substrate at $\lambda = 800$nm. Fortunately, a $\lambda/4$ plate can be used to equalize the phase shift between the two polarization components and maximize the MO signal.
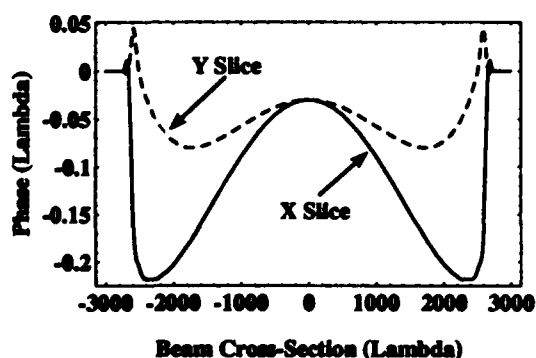

Figure 1. X- and Y-slices for the phase of the beam at the exit pupil of the focusing objective after a double pass through the birefringent substrate. Polarization is along the X-direction. Spatial dimensions are in units of λ.

The effects of vertical birefringence are not so easily remedied. Vertical birefringence also produces a differential phase delay in the focused beam, but as a function of angle of incidence and azimuth. The result is about 0.25λ peak-to-valley of astigmatism (double pass), as can be seen in Fig. 1. This birefringence-induced astigmatism is the cause of the offset in focal position that produces the maximum data readout signal, and the focal position that yields the maximum tracking error signal (TES). This focus offset diminishes optical disk system performance.

2. METHOD OF ANALYSIS

Methods employing ray tracing and Jones calculus are commonly used to analyze the effects of birefringent substrates on the incident polarization of the beam[5,6]. However, the analysis of the optical disk head is complicated, involving moderate numerical aperture focusing objectives (NA ≈ 0.5), optically active (MO) media, phase objects (pre-grooved disk), focusing and tracking methods that rely on diffraction, and differential detection of the data signal that makes use of the polarization state of the reflected beam. Our approach uses Fourier methods and permits an exact treatment of the interaction of light with the birefringent substrate[7].

The Fourier method involves decomposition of the incident beam into plane waves (angular spectrum)[8], diffraction from or interaction with the object/element in the optical path, and propagation to the next object/optical element. The use of optimized Fast Fourier Transform (FFT) codes, especially in conjunction with special computer hardware, make this approach relatively fast and efficient. DIFFRACT[9,10], a modular quasi-vectorial modeling program, was designed using this philosophy, and is used to perform the numerical calculations in this paper.

DIFFRACT contains a general multilayer modeling module that can handle optically active and anisotropic materials, and was used to model the anisotropic plastic substrate. This method is exact as
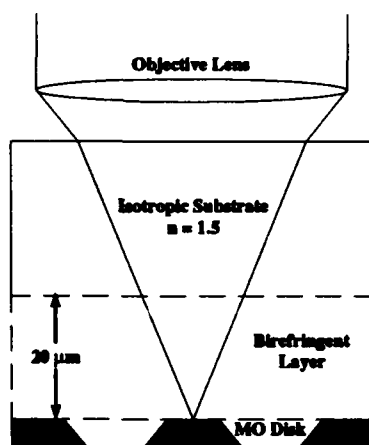
Figure 2. Schematic diagram of model used in the birefringence calculations.

Maxwell's equations are properly solved with regard to boundary conditions at each interface of the substrate.

Figure 2 depicts our model used in this paper. For computational reasons, the birefringence normally found distributed throughout a 1.2mm-thick substrate is lumped into a 20μm-thick layer added to the substrate. This requires a scaling of the birefringence values quoted above by a factor of 60 at λ = 800nm, the wavelength at which the calculations were performed. Also, since the objective is corrected for the 1.2mm substrate thickness, the additional 20μm layer introduces spherical aberration that must be balanced by defocusing. Strehl criterion[1] was used to determine the optimum focus position, and all defocus amounts are referred to this position. For the calculations that follow, spatial dimensions are normalized to the
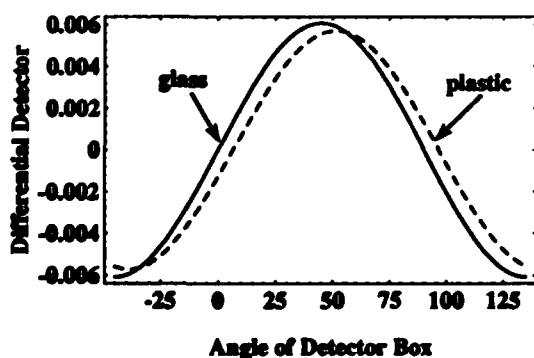

Angle of Detector Box

Figure 3. Detector module angles needed to maximize the MO signal when a $\lambda/4$ plate is employed. The plastic substrate requires that the detector module be placed at 51° to the incident polarization, while 45° is required for glass.

wavelength of light, λ = 800nm.

3. MODELING RESULTS

A $\lambda/4$ plate can be used to equalize the phase delays between the orthogonal polarization components that result due to the polar Kerr effect, and to equalize the additional phase delays due to lateral birefringence. This is accomplished by placing a $\lambda/4$ plate with its fast axis at 45° to the incident polarization direction (parallel to the disk track). The differential detector module is then rotated to produce a balanced signal when reading magnetic domains. Figure 3 shows the differences in detector module angle (with respect to incident polarization) required to produce the maximum MO signal from a uniformly magnetized disk surface for both plastic and glass substrates. Note that the detector box must be rotated by an additional 6° from the balanced position for glass to achieve the maximum differential MO signal and equalize the phase delay caused by the birefringent substrate.

Optimum focus for an optical disk system is obtained in several ways. Two common methods involve maximizing either the TES or data readout signal.
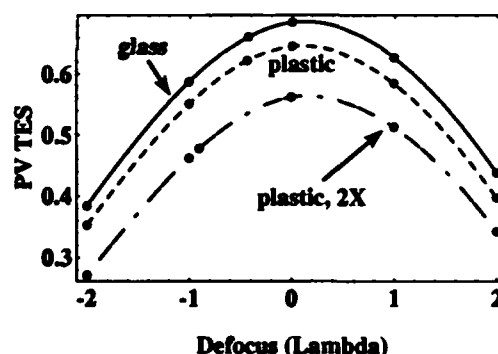

Defocus (Lambda)

Figure 4. Peak-to-valley (PV) TES versus defocus for glass substrate (solid), plastic (dash), and plastic substrate with doubled birefringence values (dash-dot). Note that maximum PV TES occurs at zero defocus with respect to best focus using Strehl criterion.

To obtain optimum focus using tracking data, the optical head is scanned over one or more tracks as a function of focus actuator position while the push-pull TES is monitored, and its peak-to-valley (PV) value recorded. Figure 4 show the results of such through-focus, PV TES calculations. For these calculations, the track pitch was 1.35μm with 1.0μm land width, 0.35μm groove top width, and trapezoidal groove cross-section (0.1μm bottom width). The
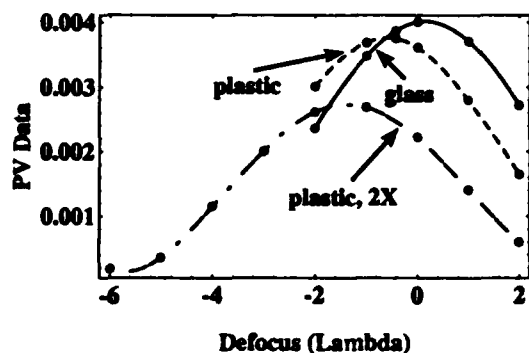
Figure 5. Through-focus, PV data signals for glass (solid), plastic (dash), and doubled birefringence plastic (dash-dot) substrates.

optical depth of the groove is $\lambda/8$. Maximum TES contrast occurs at the best focus position using Strehl criterion.

A second method of determining best focus involves reading a repetitive data pattern, such as a "3T" pattern (repeating 100100100 pattern) as a function of focus, and recording the PV data signal. Figure 5 shows the results of reading three 0.7µm diameter MO marks ($r_1 = 0.7$, $r_\perp = 0.005$, $\phi_1 - \phi_\perp = 0$) with 1.4µm center-to-center spacing for a glass substrate, plastic substrate with nominal birefringence amounts, and a plastic substrate with twice the amount of birefringence typically measured in optical disk

substrates. This calculation is included to emphasize the subtle effects of birefringence-induced astigmatism.

Note that the glass substrate achieves its maximum PV data signal at best focus, Strehl criterion (zero position). However, the plastic substrate with nominal birefringence amounts achieves its maximum PV data signal approximately 0.5λ from best focus. When the birefringence amounts are doubled, maximum PV data takes place about 1.5λ from best focus, and the PV maximum is significantly reduced due to the doubled amounts of birefringence-induced astigmatism from the vertical birefringence.

The cause of the focus offset between maximum PV TES, and maximum PV data signal becomes apparent if the spot shapes at the disk surface are studied for each case. In Fig. 6, the focal position for maximum PV TES (doubled birefringence values) produces an astigmatic spot with its major axis along the direction of polarization, which is parallel to the track direction. By contrast, the focal position for maximum PV data signal also produces an astigmatic spot, but its major axis is now perpendicular to the polarization, and hence, to the track direction, as seen in Fig. 7. The vertical birefringence-induced astigmatism warps the incident spot to favor either TES contrast or MO mark resolution, depending on the amount of defocus.
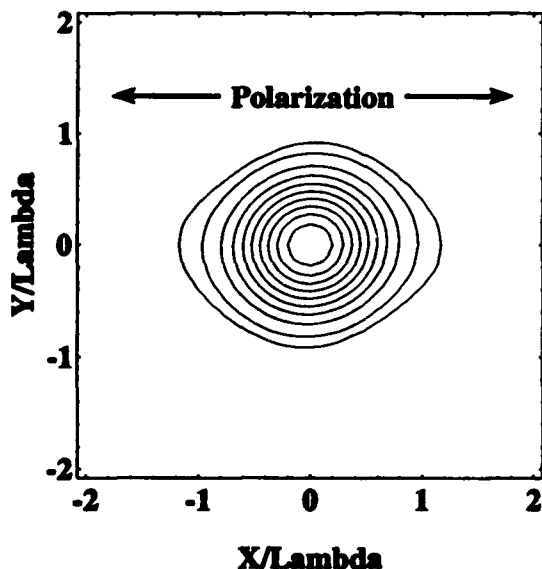
4. SUMMARY

This paper described the use of Fourier

Figure 6. Contour plot of intensity distribution at the disk surface for the focal position that yields the maximum PV TES for doubled birefringence values.
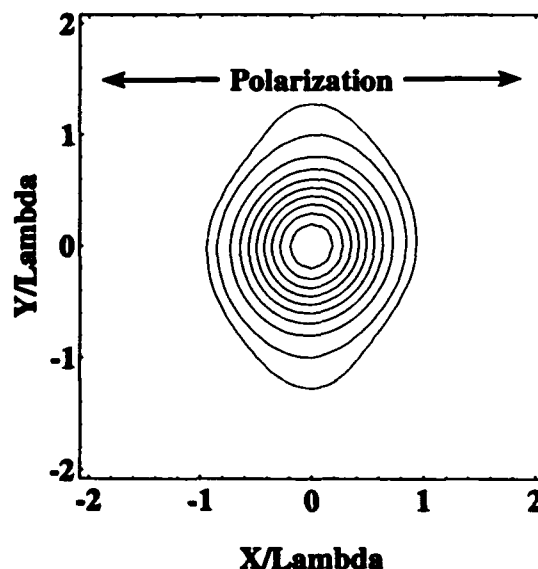

Figure 7. Contour plot of intensity at disk surface for the focal position that yields the maximum PV data signal for doubled birefringence values.

methods to analyze a problem of current interest in optical disk systems: the effects of substrate birefringence on optical disk performance.

Lateral, or in-plane birefringence causes a differential phase delay between the incident polarization component and the orthogonal Kerr component after reflection from an MO disk. Fortunately, this phase delay can be equalized by using a $\lambda/4$ plate with its fast axis at 45° to the incident polarization direction in the return path, and then adjusting the angle of the differential detector assembly to maximize the MO signal.

Vertical birefringence also causes a differential phase delay, but its more serious effect is to induce astigmatism in the incident beam, which was revealed through the Fourier method of analysis. A manifestation of this astigmatism is the existence of two "best focus" positions: the focal position that produces the largest PV TES, and best focus for maximum PV data signal.

Ray tracing and Jones matrix methods for analyzing the interaction of polarized light with optical elements are conceptually simple and attractive when warranted. The interaction of polarized light with birefringent (biaxial) materials, as well as the optically active MO media raises the complexity of the problem sufficiently to recommend a method more amenable to computer calculations.

Whenever the problem at hand can be cast in the form of a Fourier integral, one can take advantage of optimized FFTs, and special computer architectures that accelerate these calculations. Using a plane wave decomposition, or angular spectrum approach, the response of the system to a plane wave input is calculated, and the plane wave solutions added to determine the system response to a complex input distribution. In addition, Fourier methods are used to calculate the diffraction from optical elements found in the read/write path of an optical disk, and the propagation of light between these elements.

By utilizing Fourier methods, the interaction of polarized light with birefringent optical disk substrates was handled exactly, and tracking and data readout performance of an optical disk system was efficiently and accurately modeled. Fourier methods revealed the likely cause of the focus offset between best focus for tracking, and best focus for data detection to be vertical birefringence-induced astigmatism.

5. REFERENCES

1. A.B. Marchant, "Retardation effects in magneto-optic readout," *Proc. SPIE*, **695**, 270 (1986).

2. A. Takahashi, M. Mieda, Y. Murakami, K. Ohta, and H. Yamaoka, "Influence of birefringence on the signal quality of magnetooptic disks using polycarbonate substrates," *Appl.Opt.*, **27** (14), 2863 (1988).

3. S. Shirouzu, S. Sakamoto, K. Shigematsu, T. Nakagawa, and S. Tagami, "Refractive Index Ellipsoids of a Modified Polycarbonate Magneto Optical Memory Disk Substrate," *Jap.J.Appl.Phys.*, **28** (9), 1629 (1989).

4. A.B. Marchant, Optical Recording-A Technical Overview, (Addison-Wesley, Reading, Massachusetts, 1990).

5. J.D. Trolinger,Jr. and R.A. Chipman,"Polarization Ray Tracing in Birefringent Media," *Proc. SPIE*, **891**, 122 (1988).

6. I. Prikryl, "Effect of disk birefringence on a differential magneto-optic readout," *Appl.Opt.*, **31** (11), 1853 (1992).

7. M. Mansuripur, "Analysis of multilayer thin-film structures containing magneto-optic and anisotropic media at oblique incidence using 2×2 matrices," *J.Appl.Phys.*, **67** (10), 6466 (1990).

8. J.W. Goodman, Introduction to Fourier Optics,(McGraw-Hill, New York, 1968).

9. M. Mansuripur, "Certain computational aspects of vector diffraction problems," *J.Opt.Soc.Am.A*, **6** (5), 786 (1989).

10. M. Mansuripur, "Distribution of light at and near the focus of high-numerical-aperture objectives," *J.Opt.Soc.Am. A*, **3** (12), 2086 (1986).

11. M. Born and E. Wolf, Principles of Optics, (Pergamon Press, Oxford, 1980).

# A Technique for Reducing the Spectral Width of an LED

by

Michael M. O'Toole
Optical Communications Div., Hewlett-Packard

Introduction

The spectral width of an LED is an intrinsic property of the LED that depends on the type of material, the peak emission wavelength, dopant, and carrier density[1]. For communication systems using optical fibers and LED sources, the FWHM of the LED interacts with the chromatic dispersion of the fiber to limit the maximum data rate and/or transmission distance[2]. Narrowing the spectral width reduces the effect of chromatic dispersion and reduces the fiber's exit response time to an ideal pulse.

A novel method for reducing the spectral width is to insert a dye with a sharp absorption spectrum into the optical path of the LED. Figure 1 shows a typical fiber communication LED with a ball lens mounted over the junction. A polymer is used to attach the ball to the junction of the LED. Mixing a dye with the polymer is an easy way to insert the dye into the optical path of the light coupled into the fiber from the LED.
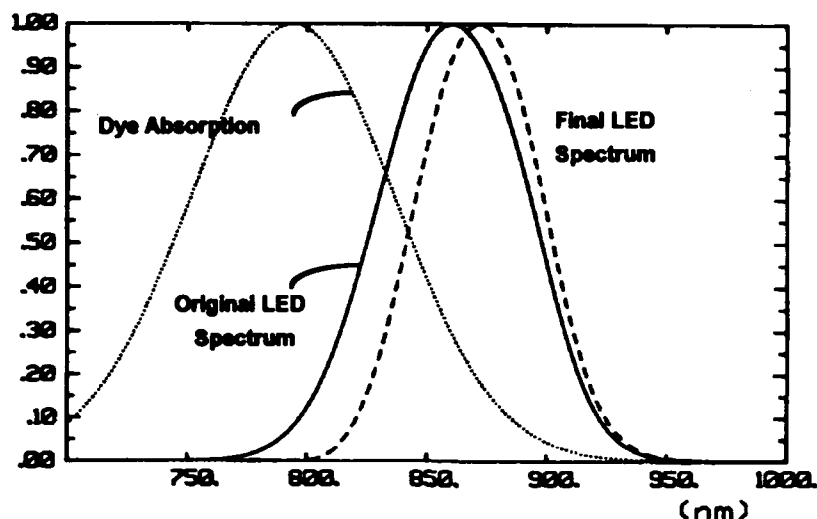
Figure 1
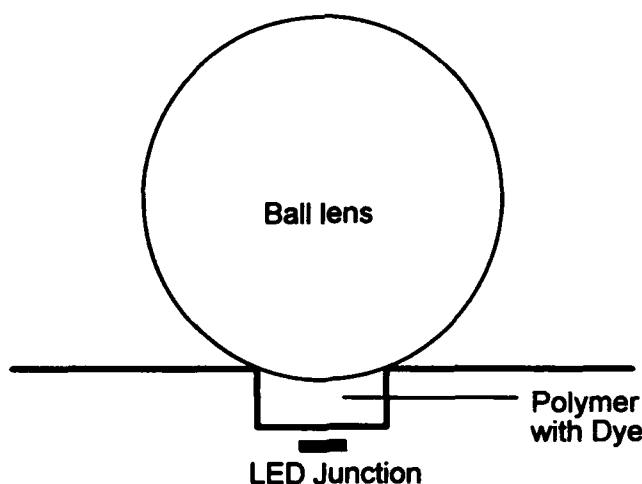
Figure 2

Figure 2 is a computer simulation of the described technique. The solid line of Figure 2 shows the normalized spectral characteristics of a typical optical communication LED centered at 860 nm, marked as "Original LED Spectrum." The full width at half-maximum, or FWHM, of the output spectrum is 73 nm. The dotted line in Figure 2 shows the normalized absorption spectrum of a laser dye chosen for its sharp absorption cutoff. Mixed in the appropriate concentration with the polymer, the dye absorbs energy primarily from the higher energy portion of the LED spectrum. The particular dye shown has a peak absorption wavelength of 794 nm.

The wavelength dependent transmission through the dye/polymer film depends on the concentration of the dye and the thickness of the film. The transmission of the film at the peak absorption wavelength of the dye is given by Beer's law.

$$T_p = 10^{-\varepsilon Cl}$$

where T_p is the relative transmission of the film at the peak absorption wavelength, ε is the absorption coefficient in liters/mole-cm, C is the molar dye concentration, and l is the film thickness in cm. The absorption spectrum of the dye can then be approximated by a Gaussian, or

$$T(\lambda) = T_p \exp\left\{-\frac{(\lambda - 794)^2}{2\sigma^2}\right\}$$

where $\sigma = 0.42*FWHM$ and λ is in nm. Multiplying the original LED spectrum by the transmission spectrum of the dye/polymer film yields the resulting LED spectrum, indicated by the dashed line in Figure 2. If the dye concentration is set such that the transmission at the peak absorption wavelength of the dye is about 4%, the FWHM of the final LED spectrum is 57 nm, and the original spectrum of the LED is narrowed by about 16 nm.

The absorbing dye technique has one disadvantage. Since some of the high energy portion of the original LED spectrum has been absorbed by the dye, the output power of the LED drops. For a peak wavelength transmission of ~4%, the launched optical power, or LOP, of the LED is reduced by about 1.75 dB. In other words, 33% of the available light from the LED was absorbed; and the resulting FWHM narrowed from 73 nm to 57 nm, or about 22%. Increasing the dye concentration or the polymer thickness increases the power loss due to absorption and decreases the FWHM. Figure 3 demonstrates the tradeoff between the reduction in FWHM and the LOP penalty, which are plotted versus the relative transmission at the peak absorption wavelength of 794 nm. The FWHM and LOP penalty are quite non-linear for a film with a peak wavelength transmission below 10%.

Figure 3

FWHM & LOP Penalty vs. Transmission of Dye*

*at the peak absorption wavelength of the dye.   Transmission of 1 is complete transmission.
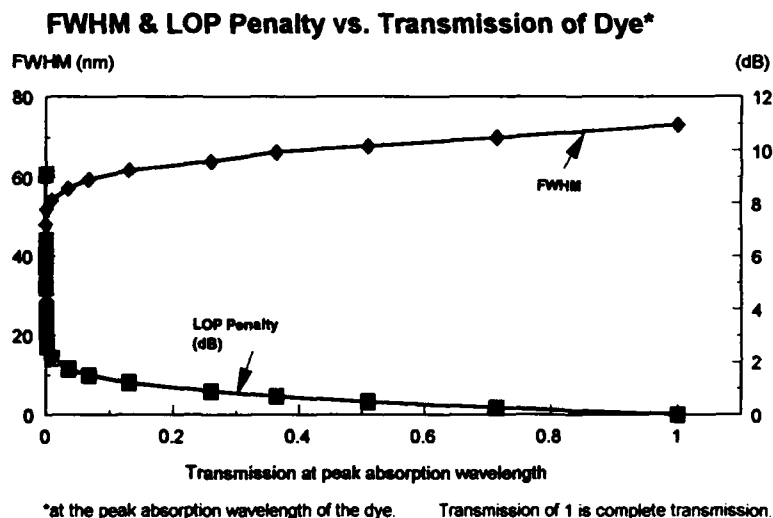
Another effect of this technique is to shift the peak wavelength of the LOP towards higher wavelengths. For a film transmission of about 4%, the peak emission wavelength moves from 860 nm to 870 nm. The shift to a higher peak wavelength is an advantage, since the chromatic dispersion of the fiber is less at higher wavelengths.

Experimental Results:

Figure 4 shows the emission spectra from parts with and without the absorbing dye in the polymer that holds the ball lens to the LED. Figure 4a is the LED spectrum without dye and Figure 4b is the LED with dye. The LED with the dye has a FWHM 16 nm less than the LED without the dye. The power launched into a 62.5/125 um fiber is ~2 dB less for the part with the dye.
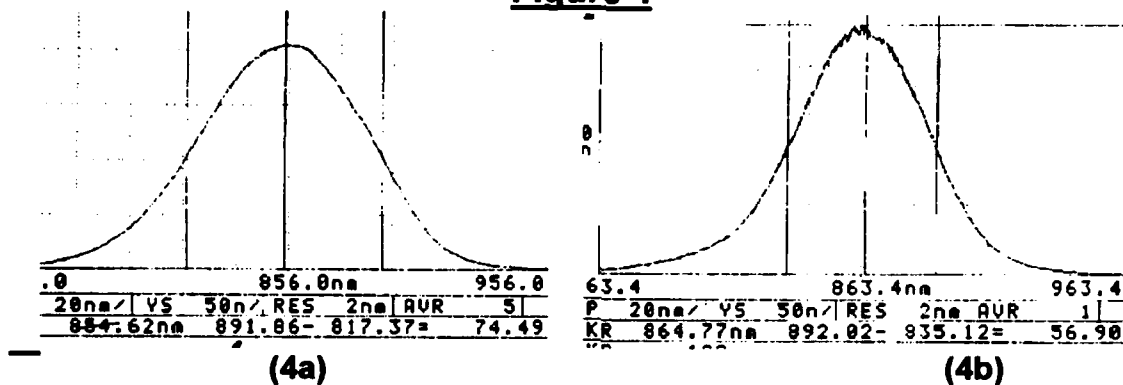
Figure 4

.0	856.0nm	956.0
20nm/ VS 50n/ RES 2nm AVR 5
854.62nm 891.86- 817.37= 74.49

(4a)

63.4	863.4nm	963.4
P 20nm/ VS 50n/ RES 2nm AVR 1
KR 864.77nm 892.02- 835.12= 56.90

(4b)

Figure 5 shows the measured fiber exit response time for the two LEDs in Figure 4 for a 2 km length of 62.5 um and for 50 um fibers. The fiber exit response time is the rise time at the exit point of the fiber due to a step input at the entrance of the fiber. Short exit response times allow faster data rates or longer fiber lengths for the same data rate.

Figure 5
2km Fiber Exit Response Time (25C)

(measured)
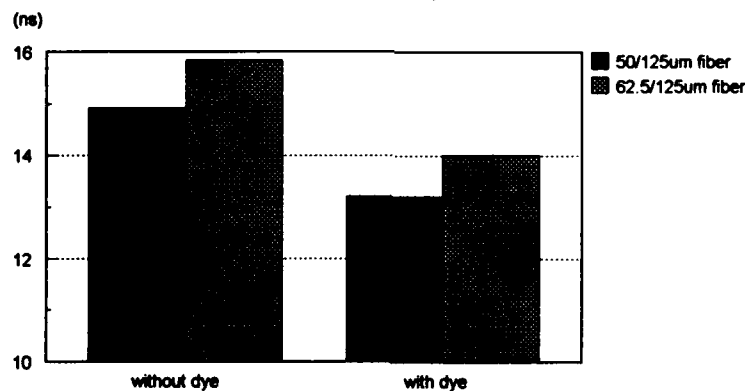
References:
[1] H.C. Casey, Jr., Frank Stern, "Concentration-dependent absorption and spontaneous emission of heavily doped GaAs," *J. Appl. Phys.*, vol. 47, No. 2, Feb. 1976.
[2] Delon C. Hanson, "Progress in Fiber Optic LAN and MAN Standards," *IEEE LCS Magazine*, Vol. 1, No. 2, May 1990.

Design and fabrication of astigmatic GRIN elements for laser diode collimation

K.-H. Brenner, S. Sinzinger, T. Spick, M. Testorf

Universität Erlangen-Nürnberg
Physikalisches Institut, Angewandte Optik
Staudtstr.7\B2
W-8520 Erlangen
Germany

Introduction

Due to advances in semiconductor technology laser diodes found access to more and more applications in hi-tech as well as every day products. Low price, small size and array properties are their most significant advantages. The asymmetric mode profile of such laser diodes, however requires collimating elements as well as elements which compensate for the inherently different divergence angles of the emitted light beams. This job is normally performed by microlenses followed by rather bulky elements like Brewster telescopes consisting of two refractive prisms /like in Ref.1/. Thus some of the most important advantages of the laser diodes, i.e. small size and good packaging, are wasted due to the additionally necessary optical elements. For linear arrays of laser diodes it is especially difficult to keep the collimating and beam shaping elements small and compact.

Therefore in the past efforts have been made to integrate collimation and beam shaping within one single element. In the case of diffractive elements one has to pay credit to high wavelength selectivity /2/. Thus it might be preferable to use refractive elements.

The fabrication of purely refractive elements combining collimation and beam shaping in one single thin glass substrate is possible by the ion exchange technology /3-6/. Such laser diode collimators combine the advantages of refractive optics with the compactness and robustness of the integration in one single element. We investigate the design and fabrication parameters for these GRIN collimators.

Design of the collimating lens array

The design goal for collimating a semiconductor laser array is to achieve both, a symmetrical amplitude distribution and a symmetrical wave curvature, being ideally zero for both lateral directions x_1 and x_2. We model the laser-amplitude distribution by an astimatic Gaussian beam:

$$u(x_1, x_2) = A_0 \, e^{-\pi(x_1^2/\sigma_1^2 + x_2^2/\sigma_2^2)} \tag{1}$$

which is approximatly valid if the emitted light distribution at the laser exit has constant phase and a decreasing amplitude towards the edges. Since the problem is separable with respect to the two lateral directions we introduce the indices 1 and 2.

After Fresnel propagating this beam over a distance z, the beam width changes according to

$$\sigma_m(z) = \sigma_m \sqrt{1 + \frac{\lambda^2 z^2}{\sigma_m^4}} \ , \qquad m=1,2 \qquad \textbf{(2)}$$

If we require the widths in x_1- and x_2-direction to be the same, the distance z is determined uniquely from the initial widths σ_1 and σ_2 of the source:

$$z = \frac{1}{\lambda} \sigma_1 \sigma_2 \qquad \textbf{(3)}$$

For the correction of the different wavefront curvatures, an astigmatic microlens is positioned at this distance z. The phase distribution in this plane is then:

$$\Phi(x_m) = -\pi \ x_m^2 [\frac{1}{\lambda z} (\frac{\lambda^2 z^2}{\lambda^2 z^2 + \sigma_m^4}) + \frac{1}{\lambda f_m}] \ , \qquad m=1,2 \qquad \textbf{(4)}$$

with f_1 and f_2 being the focal lengths of the astigmatic microlens, to be designed. The phase in eq. 4 can be chosen to vanish for a given f_1 or f_2 respectively. This provides a condition for these focal lengths:

$$\begin{aligned} f_1 &= z + \frac{\sigma_1^4}{\lambda^2 z} \\ f_2 &= z + \frac{\sigma_2^4}{\lambda^2 z} \end{aligned} \qquad \textbf{(5)}$$

With this design, the beam diameter behind the microlens is of course depending on the initial beam parameters of the laser. It is however possible to adapt the beam diameter to the given application by using existing techniques for beam collimation with rotationally symmetric standard components.

The fabrication process

For the fabrication of our gradient index microelements we use the Na-Ag ion exchange process. The index distribution is formed during a diffusion process in AgNO$_3$ at about 300°C lasting about 100h. For the fabrication of collimating or imaging elements we use the glass type BGG 35 optimized for the silver sodium ion exchange.

In previous experiments, which aimed at generation of microlens arrays we proved the good characteristics of this glass type /7,8/. In lateral direction the distribution is influenced by a metal mask shielding certain areas of the glass against diffusion
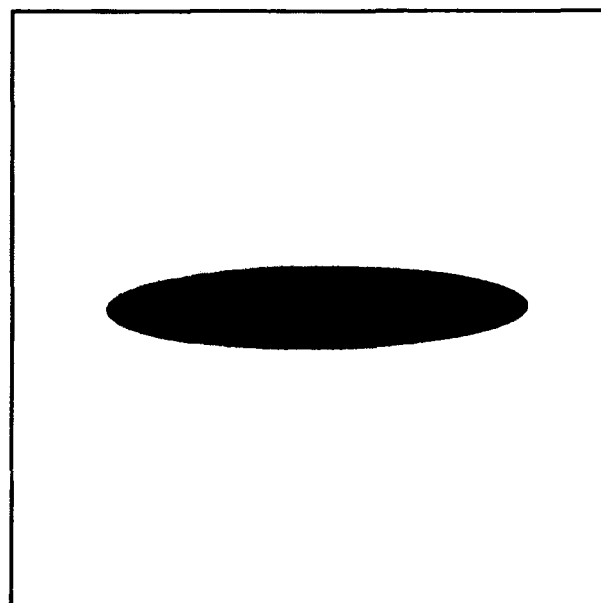

Fig. 1: Elliptic mask fabricated by laser lithography (diameters: 250μm and 50μm)

during the process. Normally, for the fabrication of microlens arrays circular mask apertures are used to get a spherical index distribution. By variation of the mask diameter the lens parameters can be varied within a certain range. Consequently non-spherical (astigmatic) microlenses can be fabricated by using non-circular (elliptic) mask apertures.

Experiments

To investigate the achievable range of lens parameters for these astigmatic microlenses we generated a variety of elliptic apertures with different eccentricities as diffusion masks. Fig. 1 shows an example of such a mask fabricated by laser lithography.

The phase elements resulting from the experiments with these masks are of a similar elliptic shape. The interferogram of an array of such elements is shown in Fig. 2. Evaluation of such interferograms by the phase shift algorithm prove the validity of the previous assumptions. In both lateral directions the phase profile has similar overall shape scaled differently.
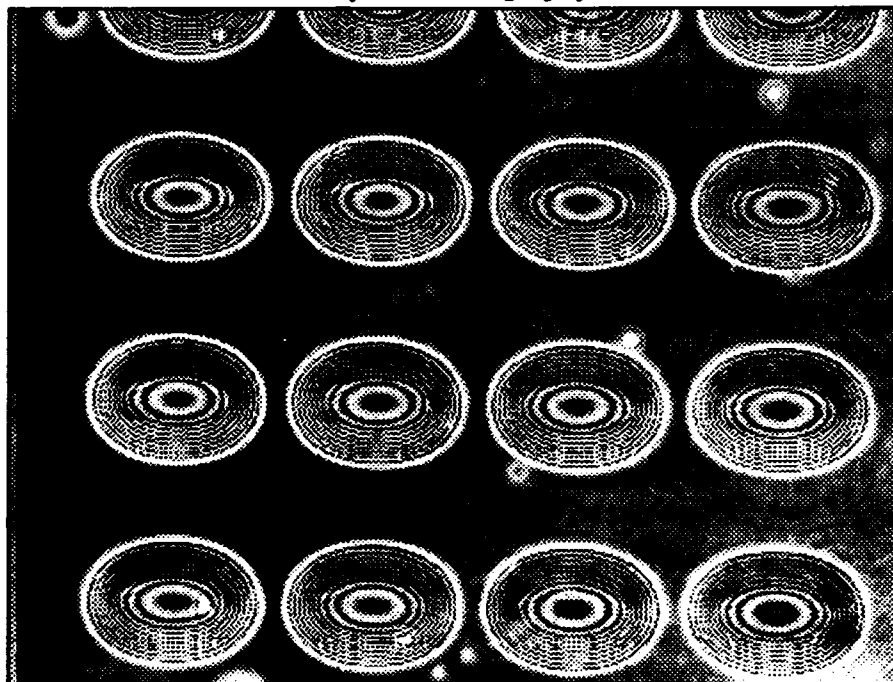

Fig.2: Interferogramm of an array of astigmatic GRIN elements

In Fig. 3 the phase measurement from the transmission interferometer is shown as contour plot. For reasonable mask parameters, e.g. 100 μm and 50 μm diameter in the different lateral directions, the line scans of such a phase profile show in good approximation a parabolic shape for both directions. For collimating elements a parabolic phase profile is desirable.

The difference of the shape of these parabolas in the two directions determines the astigmatic properties of the element. The focal lengths resulting from such measurements are (again for the example of 100 μm and 50 μm mask diameter) 1.036mm in the direction of the bigger mask diameter and 0.688mm in the perpendicular direction which is an astigmatic difference of 0.348mm. The amount of astigmatism of the GRIN element can be varied by different eccentricities of the elliptic mask apertures. So the elements shown in Figs. 2 and 3 have a much higher astigmatism due to the higher difference in mask diameters. The area of reasonable parabolic shape of the index profile however gets smaller in this case.

In this respect, of course the range of lens parameters achievable by mask diameter variation is crucial.

One other important feature of such a collimator consisting of GRIN elements is the possibility to easily fabricate arrays of astigmatic GRIN elements with very goo^d uniformity. Thus laser diode arrays could be collimated into arrays of homogeneous circular laser beams

by arrays of such elements. Fig. 2 shows an array of astigmatic microlenses which however could be packed even more densely. Experience we gathered with the fabrication of microlens arrays prove that the achievable homogeneity within arrays of ion exchanged elements is well within a few percent. To be able to fabricate elements with well determined astigmatism compensating for the difference in the divergence angles of specific laser diodes further parameter studies are necessary.
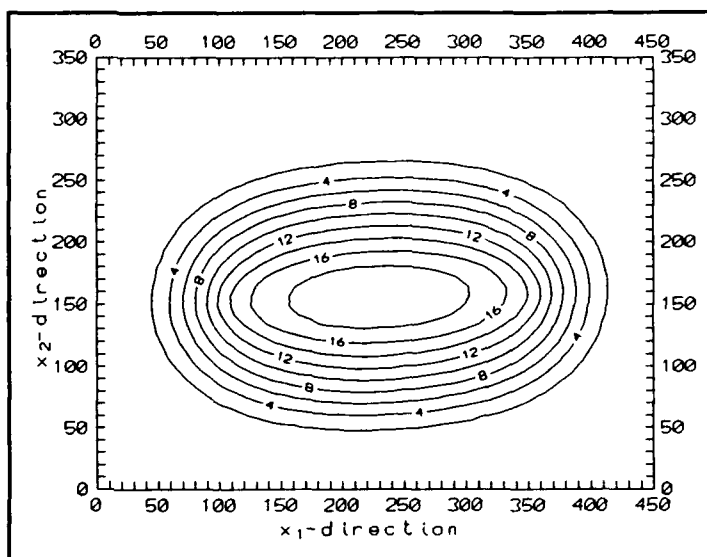

Fig.3: Contour plot of the phase profile (in units of π) of an astigmatic GRIN element

Acknowledgements:

References:

/1/ F.B. McCormick, F.A.P. Tooley, T.J. Cloonan, J.L. Brubaker, A.L. Lentine, R.L. Morrison, S.J. Hinterlong, M.J. Herron, S.L. Walker, J.M. Sasian, "Experimental investigation of a free-space optical switching network by using symmetric self-electro-optic-effect-devices", Appl. Opt. 26 5431 (1992)

/2/ J.R. Leger, M.L.Scott, W.B. Veldkamp, "Coherent addition of AlGaAs lasers using microlenses and diffractive coupling", Appl. Phys. Lett. 52 1771 (1988)

/3/ Y. Asahara, S. Omi, H. Sakai, S. Nakayama, Y. Yoneda," Gradient refractive index type anamorphic planar microlens and method of producing the same", US patent No. 4,805,997 filed 30. May 1986, see also Appl. Opt. 25 2625 (1989)

/4/ K. Iga, Y. Kokubun and M. Oikawa,"Fundamentals of microoptics" Academic Press, Orlando, 1984

/5/ M. Oikawa and K. Iga " Distributed-index planar microlens" Appl. Opt. 21, 1052 (1982)

/6/ D. D'Amato, R. Centamore, "Two applications for microlens arrays: detector fill factor improvement and laser diode collimation",Proc. SPIE Vol. 1544, "Miniature and Micro-Optics: Fabrication and System Applications (1991)", p.166-175

/7/ J. Bähr, K.-H. Brenner, J. Moisel, W. Singer, S. Sinzinger, T. Spick, M. Testorf, "Diffusion elements in glass: comparison and optimization of the diffusion response in different substrates", Tech. digest, OC 92 Topical Meeting, Minsk, Belarus, June, '92

/8/ J. Bähr, K.-H. Brenner, J. Moisel, W. Singer, S. Sinzinger, T. Spick, M. Testorf, "Modifications of the imaging properties of ion-exchange microlenses by mask shaping", Technical digest, GRIN Topical Meeting 1992, Santiago de Compostela, Spain, p. 187-190

Focal plane pixel energy redistribution and concentration using microlens arrays

William H. Southwell
Rockwell International Science Center
1049 Camino dos Rios
Thousand Oaks, California 91360
(805)373-4485

Pixels in focal plane detector arrays are typically square for efficient utilization of light. Microlens arrays with square lensletts the same size as the detector pixels can further concentrate the light. This allows the use of smaller detector areas. This has a number of advantages including more efficiency since the fill factors for microlens arrays can generally be made higher than detector fill factors. Smaller detectors also mean more real estate is available on the focal plane for other electronic functions.

A physical optics calculation has been performed to study the propagation of light from the nominal focal plane of the optical receiver (where the microlens array is located) through the microlens and to the focal plane of the microlens (where the detector array is located). Assuming diffraction-limited optics, ray trace or geometrical optics analysis does not predict Airy pattern focal spreading nor further concentration of these patterns, hence the need to perform the physical optics calculations.
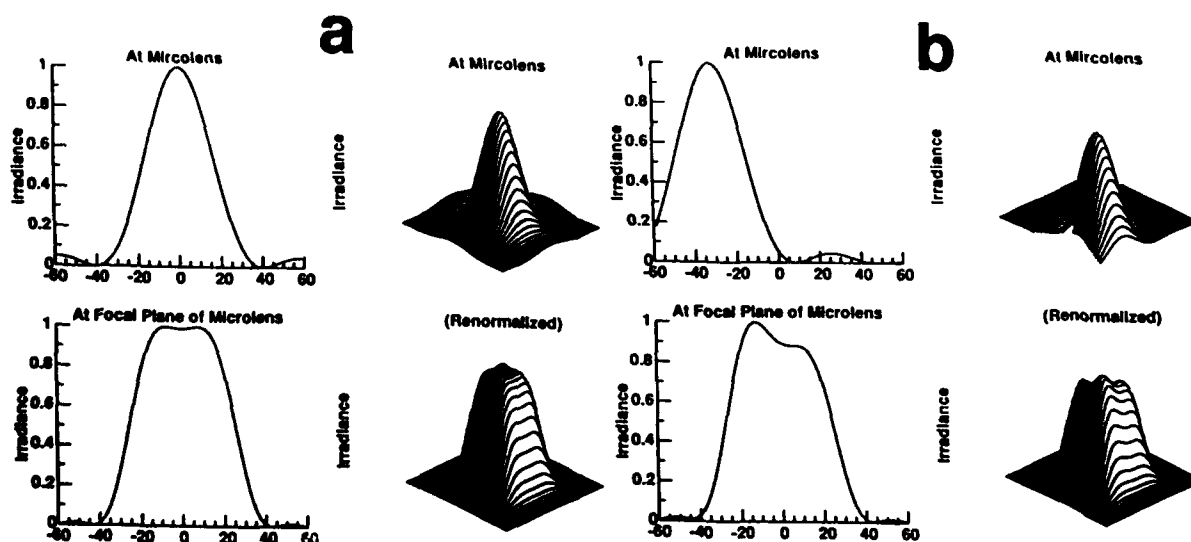
Fig. 1. Receiver optics with f/4 and microlens with f/2. (a) Centered PSF and (b) off-centered PSF incident on the microlens.

All of the examples considered in this paper use incident light at 10µ wavelength and a square pixel 120µ on a side. Shown in the upper left plot of Fig. 1a is the focal plane energy distribution (point spread function PSF) for an f/4 optical receiver. At the right of this plot is a 3-D representation of the PSF within the pixel area. This light is incident on an f/2 lenslett and is then propagaied to the focal plane of the lenslett. The energy distribution in that plane (detector plane) is shown renormalized in the lower left plot of Fig. 1a. One thing that is immediately clear from Fig. 1a is that the pixel microlens converts the PSF to a more square distribution. Another interesting property of the pixel mircrolens is that it transfers light to the center of the detector plane no matter where is falls on the microlens. The upper left plot of Fig. 1b shows the incident PSF off to the side or corner of the pixel, and yet the lower plot shows this light appearing in the center of the detector in the same area as the centered PSF.

A uniform extended object would show a uniform intensity across the top of the microlens, but it would be made up of a superposition of a large number of PFS's uniformly distributed over the pixel. We thus conclude that all light incident on the top of the microlens will be concentrated in the detector plane. This allows dead space on the focal plane while still collecting all the light.
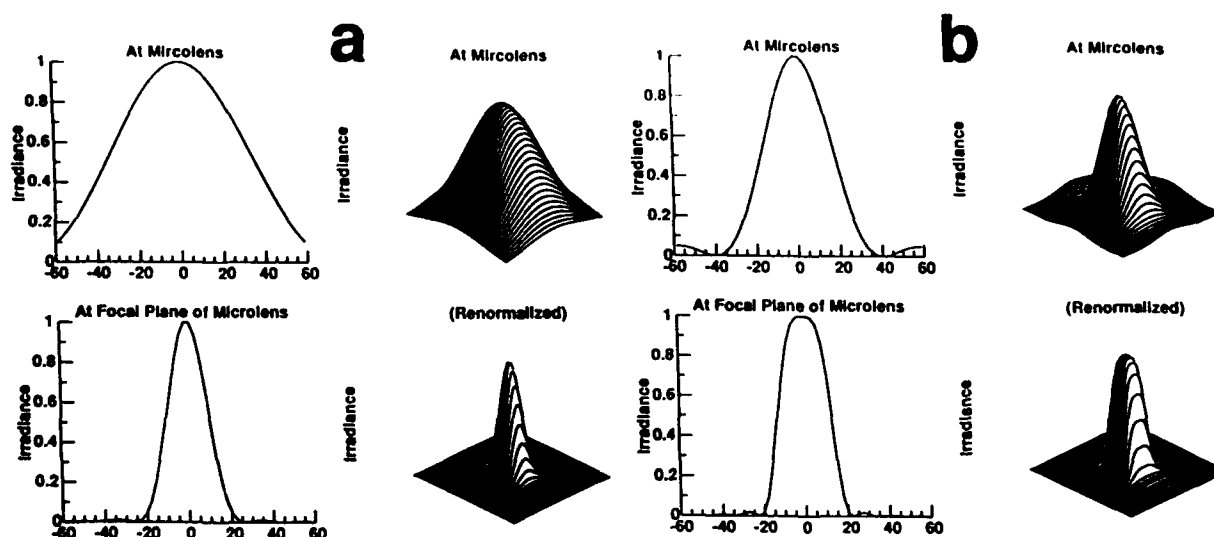
Fig. 2. (a) Receiver optics with f/8 and microlens f/2 and (b) receiver optics with f/4 and microlens f/1. Both have the same concentration.

The linear concentration (one dimensional) depends on the ratio of the f/number of the reciever optics to the f/number of the microlens. Shown in Fig. 2a is an f/8 receiver optics and an f/2 microlens, whereas

Fig. 2b shows an f/4 receiver optics and an f/1 mircolens. Both show about the same amount of linear concentration and they both have the same ratio of f/numbers. Also note that Fig. 2 examples have twice the f/number ratios as those in Fig. 1, and they have twice the linear concentration. The area concentration is the square of the linear concentration, and hence related to the square of the f/number ratio. (In determining the area concentration, it not the ratio of the areas of the PSF before and after the mircolens. It is the ratio of the pixel area to the area of the new PSF in the detector plane.)

This linear concentration being proportional to the f/number ratio does not extend indefinately, as shown in Fig. 3, which shows an f/100 receiver optics and an f/2 microlens. Diffraction effects force a limit on this linear relationship.
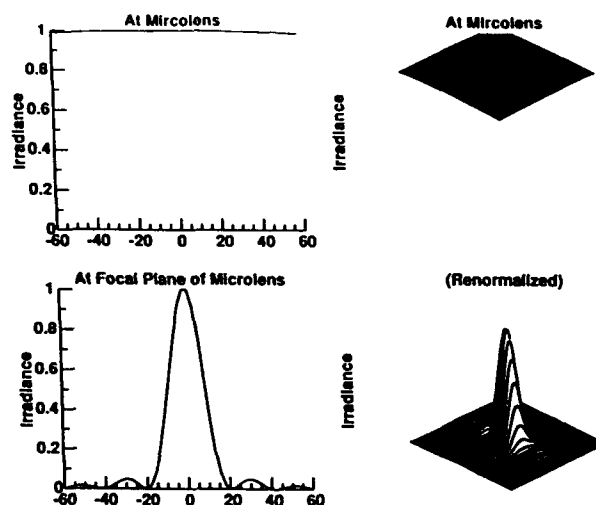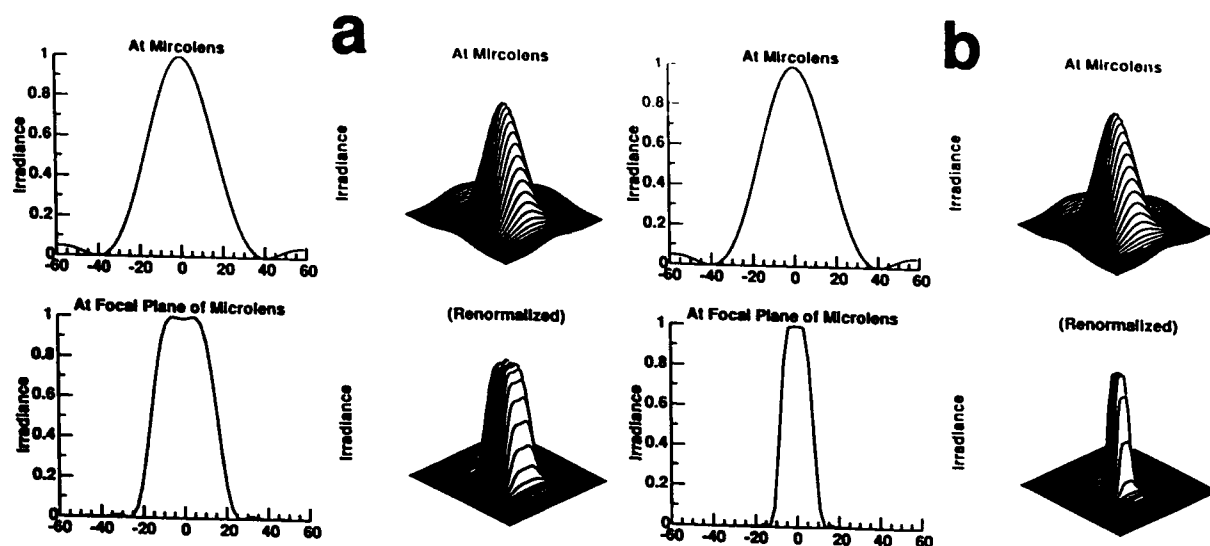

Fig. 3. Receiver optics with f/100 and microlens f/2.

So far we have considered the mircolens focussing in air to the detector plane. Another mechanism producing concentration is to focus not in air but in the substrate of the microlens. This could be realized, for example for a backside illuminated focal plane detector array. Figure 4a shows an f/4 receiver optics and an f/2 microlens focussing into its substrate of refractive index $n_s=1.6$. The f/number in the substrate is defined as the physical distance focal length divided by the microlens width. It should be remembered that the optical power to achieve this f/number in a substrate with index n_s is n_s times higher than that required to focus the same f/number in air. This translates to more rings and finer

feature sizes for diffractive mircolens. The case shown in Fig. 4b has the same f/numbers but a substrate refractive index n_s=3.2. Again we note the linear concentration being proportional to the refractive index, and the area concentration being proportional to the square of the refractive index.

Fig. 4. Receiver optics with f/4 and microlens f/2 and foccusing in the substrate with refractive index n_s = (a) 1.6 and (b) 3.2.

A simple expression for C_{linear} the linear concentration which starts out linear and approaches a constant for large receiver f/numbers is

$$C_{linear} = \frac{Dn_s\{1-\exp(-2\lambda[f\#/receiver]/D)\}}{2\lambda f\#/microlens}, \tag{1}$$

where D is the width of the microlens. The area concentration is the square of this quantity.

Birefringent Polarization Ray Tracing

Stephen C. McClain
Russell A. Chipman

Department of Physics
University of Alabama in Huntsville
Huntsville, AL 35899
205-895-6417

Introduction

The fundamental tool used for design and analysis of optical systems is geometric ray tracing. In isotropic, homogeneous, non-optically active media the procedure is simple -- rays travel in straight lines except at interfaces, where reflection and refraction occur. Application of Snell's law and the Fresnel transmission and reflection coefficients provide all of the information about the progress of the geometric ray: its position, direction, intensity, accumulated phase, and polarization state. The procedure is straightforward because there is a single refractive index for each medium which is independent of the direction of the ray and independent of the polarization state.

Many optical systems contain birefringent materials for use in wave plates, [1] depolarizers, [2][3] optical filters, [4][5] polarizers, [6] or other elements. In order to analyze optical systems containing birefringent elements, ray tracing algorithms which account for the polarization properties of birefringent media are required. Ray tracing in anisotropic or optically active materials is more complicated than in non-optically active isotropic materials because the refractive index depends on the wave direction and polarization state. In general, a ray incident on such a material will bifurcate into two rays with distinct refractive indices and polarization states. This is the phenomenon of double refraction; materials with this property are generally termed birefringent. For example, calcite and quartz are birefringent media. The two polarization states associated with a specified wave direction in a birefringent material are called the ordinary and extraordinary modes. An additional complication of propagation in birefringent media is that the wave direction (the direction normal to surfaces of constant phase) does not generally coincide with the ray direction (the direction of energy flow).

The purpose of this paper is to present a polarization ray tracing procedure which incorporates birefringent media such as crystalline quartz. We have chosen quartz not only because it is a commonly used optical medium, but also because it is both anisotropic and optically active. The ray tracing methods presented here apply to uniaxial optically active materials, and therefore encompass uniaxial non-optically active media, such as calcite and KDP, and isotropic optically active materials, such as sugar water and other organic liquids.

Geometric ray tracing in non-optically active uniaxial crystals has been discussed by several authors. [7]-[11] These references contain formulas to trace the paths of the ordinary and extraordinary rays through these media, but do not derive expressions for the distribution of energy into the ordinary and extraordinary modes. Also, their algorithms do not apply in optically active crystals.

The significance of a polarization ray trace, as opposed to an ordinary geometric ray trace, is that it provides information about the polarization state and intensity of the ray as it travels through the system. [12]-15] Normally a geometric ray trace calculates the ray direction and optical path length, but no polarization or intensity information. Knowledge of the polarization state is often vital in the analysis of optical systems containing birefringent elements, which are chosen for their polarizing effects. Polarization ray tracing is also required for the analysis of polarization critical optical systems composed solely of isotropic elements.

This paper discusses the procedures involved in performing polarization ray tracing in birefringent media. Detailed derivations of algorithms for performing the ray trace in optically active birefringent media are contained in other papers. [16][17]

Birefringent Ray Tracing

Before a ray trace is performed, the optical system is described by a set of input parameters. An optical system is composed of surfaces, which are interfaces between different media. The shape of each surface and the distance between successive surfaces comprise one set of input parameters. Following each surface is an optical medium. In a non-birefringent medium, the refractive index characterizes the optical properties of the medium.

The set of refractive indices describing each medium comprises a second set of input parameters for a system composed of isotropic elements. We use the term "birefringent" to include anisotropic media or optically active media.

In a birefringent medium, the refractive index is a function of the wave direction and polarization state of the light. The refractive index is not an input parameter to the optical system but is calculated on a ray by ray basis. A birefringent medium is characterized by two wavelength dependent tensors, the electric permittivity tensor ϵ and the optical activity tensor $\underline{G}$. The permittivity tensor in any uniaxial crystal can be entered as a diagonal tensor. Likewise, the gyrotropic tensor is also diagonalizable. Values for the elements of these two tensors are obtained from measured values of the refractive indices. In an optical design program, it would be appropriate to store the matrix elements in an extended glass table, just as refractive indices are commonly stored for optical glasses.

The orientation of the crystal is needed to characterize the birefringent optical element in the ray tracing model. The crystal's orientation in the optical system is specified by the direction of the crystal axis $\hat{c}$. Then the tensors $\underline{\epsilon}$ and $\underline{G}$ for the optical element are obtained from the diagonal form of the tensors by the unitary transformations.

Following the standard nomenclature for specifying optical parameters for ray tracing, we label the object surface 0, a general surface with a counter q, and the image surface Q. The input parameters describing the material following surface q are ϵ_{oq}, ϵ_{eq}, g_{oq}, g_{eq}, and $\hat{c}_q$. From these parameters the matrices $\underline{\epsilon}_q$ and $\underline{G}_q$ need only be constructed once per ray trace, not calculated on a ray by ray basis. These input parameters and tensors are needed in the algorithms below to perform refraction and reflection.

The objective of the birefringent polarization ray trace is to calculate the ray direction $\hat{\rho}$, polarization state $\hat{E}$, amplitude a, and optical path length OPL of rays as they propagate from surface to surface through an optical system that incorporates birefringent optical elements. At a birefringent to birefringent interface, an incident ray refracts into ordinary and extraordinary rays with wavevectors $\hat{k}_{to}$ and $\hat{k}_{te}$ and reflects into ordinary and extraordinary rays with wavevectors $\hat{k}_{ro}$ and $\hat{k}_{re}$. Algorithms calculate the refractive index n, wavevector direction $\hat{k}$, electric field polarization $\hat{E}$, magnetic field polarization $\hat{H}$, and ray direction $\hat{\rho}$ for each of the four rays exiting the interface. Simultaneous knowledge of all four exiting rays and their polarization states is required in order to compute the Fresnel coefficients governing the branching of the incident power into each ray.

A ray incident on a birefringent to birefringent interface has a specified wave direction $\hat{k}_i$, refractive index n_i, polarization mode $\hat{E}_i$, and amplitude E_i. It also has a specified polarization mode. The first part of the refraction procedure determines the transmitted and reflected wavevector directions $\hat{k}_{to}$, $\hat{k}_{te}$, $\hat{k}_{ro}$, $\hat{k}_{re}$ and refractive indices n_{to}, n_{te}, n_{ro}, n_{re} for the ordinary and extraordinary modes. The wave directions are not the ray directions $\hat{\rho}$ (which are used in transferring the ray to the next surface); in birefringent media the directions of $\hat{\rho}$ and $\hat{k}$ usually differ. However, $\hat{k}$ and n are needed as an intermediate step in determining $\hat{\rho}$ and the OPL.

The wavevector and refractive index for each exiting ray are determined through solution of Snell's law, taking into account the variation of the refractive index with propagation direction. The iterative solution for quartz, and other uniaxial optically active media, is contained in Reference 17.

With the refractive indices and wavevectors for the four rays calculated, the ray trace proceeds by calculating the polarization states of the rays. These polarization states satisfy a characteristic matrix equation,
$$\underline{M} \cdot \hat{E} = 0.$$
$\underline{M}$ is a matrix containing the tensors $\underline{\epsilon}$ and $\underline{G}$, as well as the ray propagation direction and the refractive index. There is one electric field polarization solution for each mode.

The magnetic fields associated with the modes are also required in order to calculate the distribution of energy into the four modes. The magnetic fields are calculated from the electric field modes using the constitutive relations.

The ray direction $\hat{\rho}$ as opposed to the wave direction $\hat{k}$ is determined from the direction of the Poynting vector:

$$\hat{\rho} = \frac{Re\{\hat{E} \times \hat{H}^*\}}{|Re\{\hat{E} \times \hat{H}^*\}|},$$

After the ray direction following surface q is calculated, the ray is transferred to the next surface and the optical path length is determined. If the ray intersects surface q at the point (x_q, y_q, z_q) and has refracted ray vector $\hat{\rho}$, then the intersection with surface q+1 will occur at the point $(x_{q+1}, y_{q+1}, z_{q+1})$, which is calculated by standard geometric ray tracing formulas for ray-surface intercepts. [18]-[20]

The optical path length OPL is calculated from
$$OPL = nl\hat{k} \cdot \hat{\rho}.$$

Fresnel Coefficients

The distribution of the energy of the incident light into the refracted and reflected modes is governed by generalized Fresnel equations. The amplitude reflection coefficients for the ordinary and extraordinary reflected modes α_{ro} and α_{re} and the amplitude transmission coefficients for the ordinary and extraordinary transmitted modes α_{to} and α_{te} are complex scalars describing the ratio of the complex amplitude of the mode to the incident amplitude. We will refer to $\alpha_{ro}, \alpha_{re}, \alpha_{to},$ and α_{te} as the Fresnel coefficients for this ray at the interface.

The Fresnel coefficients are derived by matching the boundary conditions of the electric and magnetic fields at the interface for the incident ray and four exiting rays. The electric and magnetic polarizations for all four of the rays exiting the interface must first be determined. The boundary conditions then yield a 4 by 4 matrix equation relating the electromagnetic field modes and amplitudes. The solution of the equation requires the inversion of the 4 by 4 complex matrix.

The Fresnel coefficients describe the branching of the amplitude of the incident polarization into reflected and transmitted modes. The energy generally splits into two reflected and two refracted modes. If the coefficient for coupling into one of the refracted modes is zero, then the incident state is said to be in an entrance eigenstate. This incident eigenpolarization refracts into a single mode of the transmitting medium. The amplitude coefficient is then an eigenvalue associated with the eigenpolarization. The amplitude coefficients are not generally eigenvalues.

If the incident medium is isotropic, then two entrance eigenpolarizations always exist, one which couples into the ordinary mode and one which couples into the extraordinary mode. These entrance eigenpolarizations may be generally expressed as superpositions of the s and p polarizations. However, if the incident medium is birefringent, then there may be no entrance eigenpolarization. While it is possible to write down an entrance state $\hat{E}_i$ which yields a zero value for α_{to} or α_{te}, this entrance state is generally in a superposition of ordinary and extraordinary modes in the incident material. Since an ordinary and extraordinary mode sharing the same wave vector $\hat{k}$ do not generally share the same ray direction $\hat{\rho}$, this entrance state would represent two distinct rays incident on the interface, not one.

Determination of the field amplitudes is especially important for birefringent optics. Birefringent elements such as retarders are often introduced for polarization manipulation. The set of Fresnel coefficients when combined with the optical path lengths of the rays describes the final polarization state of the beam. In systems where image doubling is utilized, knowledge of the Fresnel coefficients is needed to determine the distribution of light between the two images.

Conclusion

Polarization ray tracing is a powerful optical design tool. Polarization ray tracing extends geometrical ray tracing because it incorporates the vector nature of the electromagnetic field. It is useful for describing polarization and wavefront effects of birefringent optical elements. The algorithms presented here expand the scope of materials and optical systems which can be analyzed. Birefringent ray trace algorithms allow the optical designer to analyze the non-ideal effects of birefringent elements such as wave plates, polarizers, depolarizers, and birefringent filters in an optical system. If the non-ideal effects of birefringent or isotropic elements are small, they can be documented and safely neglected. If the effects are large, compensation can be introduced. For example, birefringent ray trace algorithms allow the precise determination of aberrations of retarders, such as the astigmatism they introduce in noncollimated light. [21] Also, these algorithms provide a precise means of

analyzing the field of view effects of polarizing elements. Furthermore, a designer can use birefringent polarization ray trace algorithms to improve existing birefringent elements or to design entirely new birefringent devices.

The procedures described here allow the calculation of the amplitude, wavefront aberrations, and polarization aberrations in systems containing birefringent elements. Many related algorithmns are needed by a ray tracing program, such as for polarization dependent point spread functions and modulation transfer functions, for the results of a birefringent ray trace to be fully exploited by an optical designer. The ray trace information obtained by the algorithms in this paper should lead to a better understanding of the performance and ultimate limits of optical systems that contain birefringent elements.

References

1. W.A. Shurcliff, *Polarized Light* (Harvard University Press, Cambridge, Massachusetts, 1966), pp. 71, 87-108.

2. B.H. Billings, "Monochromatic depolarizer," J. Opt. Soc. Am. 38, 819 (1948).

3. J.D. McGuire and R.A. Chipman, "Analysis of spatial pseudodepolarizers in imaging systems," Opt. Eng. 29, 1478-1484 (1990).

4. A.M. Title and W.J. Rosenberg, "Improvements in birefringent filters. 5: Field of view effects," Appl. Opt. 18, 3443-3456 (1979).

5. J.E. Greivenkamp, "Color dependent optical prefilter for suppression of aliasing artifacts," Appl. Opt. 29, 676-684 (1990).

6. J.M. Bennett and H.E. Bennett, "Polarization," in *Handbook of Optics, Sponsored by the Optical Society of America*, W.G. Driscoll, ed. (McGraw-Hill, New York, 1978).

7. O.N. Stavroudis, "Ray tracing formulas for uniaxial crystals," J. Opt. Soc. Am. 52(2), 187-191 (1962).

8. W. Swindell, "Extraordinary -ray and -wave tracing in uniaxial crystals," Appl. Opt. 14(9), 2298-2301 (1975).

9. M. Simon, "Ray tracing formulas for monoaxial optical components," Appl. Opt. 22(2), 354-360 (1983).

10. J.D. Trolinger, Jr., R.A. Chipman, and D.K. Wilson, "Polarization ray tracing in birefringent media," Opt. Eng. 30, 461-466 (1991).

11. Q.-T. Liang, "Simple ray tracing formulas for uniaxial optical crystals," Appl. Opt. 29, 1008-1010 (1990).

12. E. Waluschka, "Polarization ray trace," Opt. Eng. 28, 86-89 (1989).

13. R.A. Chipman, "Polarization analysis of optical systems," Opt. Eng. 28, 90-99 (1989).

14. R.A. Chipman, "Polarization ray tracing," in *Recent Trends in Optical Design; Computer Lens Design Workshop*, C. Londono and R.E. Fischer, eds., Proc. Soc. Photo-Opt. Instrum. Eng. 766, 61-68 (1987).

15. T.J. Bruegge, "Analysis of polarization in optical systems," in *Polarization Considerations for Optical Systems II*, R.A. Chipman, ed., Proc. Soc. Photo-Opt. Instrum. Eng. 1166, 165-176 (1989).

16. S.C. McClain, L.W. Hillman, and R.A. Chipman, "Polarization ray tracing in anisotropic optically active media II. Theory and Physics," submitted to J. Opt. Soc. Am. A.

17. S.C. McClain, L.W. Hillman, and R.A. Chipman, "Polarization ray tracing in anisotropic optically active media I. Algorithms," submitted to J. Opt. Soc. Am. A.

18. W.T. Welford, *Aberrations of Optical Systems* (Adam Hilger, Bristol, 1986), p. 12.

19. W.J. Smith, *Modern Optical Engineering*, 2nd ed. (McGraw-Hill, New York, 1990), pp. 288-297.

20. R. Kingslake, *Lens Design Fundamentals* (Academic Press, New York, 1978), pp. 19-38.

21. S.C. McClain, R.A. Chipman, and L.W. Hillman, "Aberrations of a horizontal-vertical depolarizer," Applied Optics 31, 2326-2331 (1992).

Complexities of image formation through liquid crystal televisions

J. Larry Pezzaniti, Russell A. Chipman
University of Alabama in Huntsville
Physics Department
Huntsville, AL 35899, (205) 895-6417

Introduction

Image formation through spatial light modulators and liquid crystals is not particularly well characterized by the point spread function (PSF) and modulation transfer function of Fourier optics, although these are a suitable first approximation. What actually occurs when wavefronts transmit through SLM's (such as liquid crystal televisions (LCTV) or magneto-optical SLMs) is that the point spread function acquires a spatially varying polarization state due to the polarization characteristics of the SLM. Rather than the image expected from an array of square or rectangular apertures in the pupil, the image acquires additional spatial frequency components in other polarization states. In addition, an unpolarized component due to depolarization in the modulator can also arise. These "polarization aberrations" reduce the information carrying capacity of the wavefront, reducing its resolution. The unpolarized component is useless for further coherent processing. These polarization aberrations introduce additional loss mechanisms when these wavefronts are manipulated by polarizing beam splitters and other polarization elements. Finally, these images are different for different incident polarization states.

These polarization effects need to be considered by optical designers, as they can be one of the limiting factors in resolution, scattered light, and efficiency. Such polarization aberrations in the pupil and image can be measured by imaging polarimetry. Optical design methods are needed to incorporate accurate models of modulators into polarization ray tracing to predict the results of such measurements during the lens design. In the pupil the desired representation is an exit pupil polarization function (Jones vector as a function of pupil coordinates) or a polarization aberration function (a Jones matrix as a function of pupil coordinates). In the image plane, the corresponding Jones vector/matrix functions can be written for the image, but these are difficult to measure in the laboratory.[1,2] The Stokes vector/Mueller matrices of images are much more readily measured and are more desirable since they include the unpolarized fraction of the light and characterize depolarization. In our laboratory we measure the polarization point spread matrix, defined in a Mueller matrix basis, which provides the polarization distribution in an image for an arbitrary incident polarization state. Such measurements produce a wealth of information to assist optical designers understand, model, and possibly compensate for polarization defects in liquid crystal televisions.

Polarization PSF of light focused through a LCTV

To illustrate the effects of the polarization aberrations on images taken through LCTV's, we show an example of spatially varying polarization in a PSF. Figures 1-5 contain measurements made on a Seiko liquid crystal television model LVD-202 at 633nm. The polarizers are removed and the LCTV operated as a phase modulator illuminated with a converging beam of linearly polarized light of numerical aperture 0.15 and beam diameter of 18 mm at the modulator. The light continues to come to focus as it passes through the polarization analyzer section of the polarimeter. The image forms on 14 bit 512 by 512 chilled CCD detector. A series of images are acquired at different settings of the polarization analyzer, and a Stokes vector is measured at each

pixel of the CCD, yielding a Stokes vector image, a set of four images representing image formation with a single incident polarization state. In the following figures, the Stokes vector image is further reduced to illustrate the unusual polarization characteristics of this image.

Figure 1 is an intensity image of the image, photographed on film. This is close to the expected form for the PSF from a rectangular grid of equally spaced rectangular pixels. We will show the measured polarization state across two of the diffraction orders of this image, the central and first diffraction orders (shown enclosed by the rectangular box drawn on the same figure). The remaining images are all from an imaging polarimeter operated at UAH.[3] The intensity of these two orders are shown in Figure 2. Figure 3 plots the orientation of the major axes of the polarization ellipses. This orientation changes abruptly on one side of the first diffraction order. Figure 4 plots the degree of polarization, which varies from 94% to as low as 86%. This represents a loss of coherence of the light in the image, with between 6% and 14% unpolarized light exiting the LCTV. This unpolarized light is useless for further coherent processing because it no longer produces static interference fringes with coherent light. Finally, Figure 5 shows the variation of eccentricity, shown in degrees, (0° represents linearly polarized light, 90° is circularly polarized light). This indicates the light is nearly mainly linearly polarized across this portion of the image. In summary, this example image is linearly polarized with varying orientation, and has a significant unpolarized component.

Summary

Liquid crystal TVs and other modulators can be expected to introduce spatial polarization variation into the wavefront and point spread function. The undesired polarization effects take the form of pixel to pixel variations of the retardance of the modulator, as well as polarization variations within each pixel. The depolarization is due to the bulk scattering in the liquid crystal, as well as possibly edge effects of the pixels. Polarization generalizations of the PSF, MTF, wavefront aberration function and similar imaging measures are necessary to characterize LCTVs and related devices. Incorporating such effects into optical design may well be a challenging endeavor.

References

1. W. Urbanczyk, "Optical transfer functions for imaging systems which change the state of light polarization," Opt. Acta 33, 53-62, (1986).
2. J. P. McGuire, Jr., and R. A. Chipman, "Diffraction image formation in optical systems with polarization aberrations. I: Formulation and example," J. Opt. Soc. Am. A 7, 1614-1626, (1990).
3. J. L. Pezzaniti, R. A. Chipman, "Imaging polarimetry for optical system metrology" Proc. SPIE 1317, pp. 280-293, 1990.
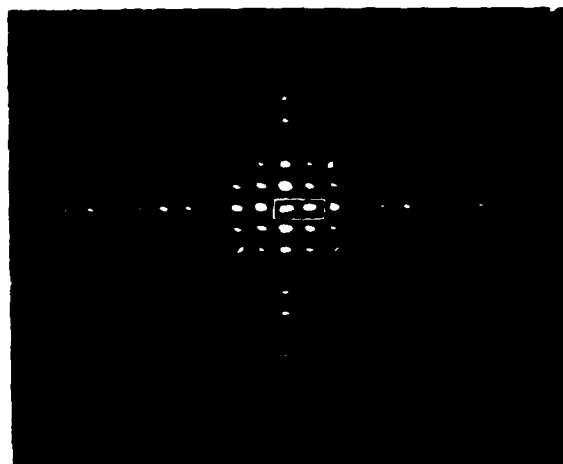
Figure 1   Image of converging beam diffracted by a rectangular array of rectangular pixels (liquid crystal television). Polarization measurements are made across the two diffraction orders highlighted in the rectangular box.
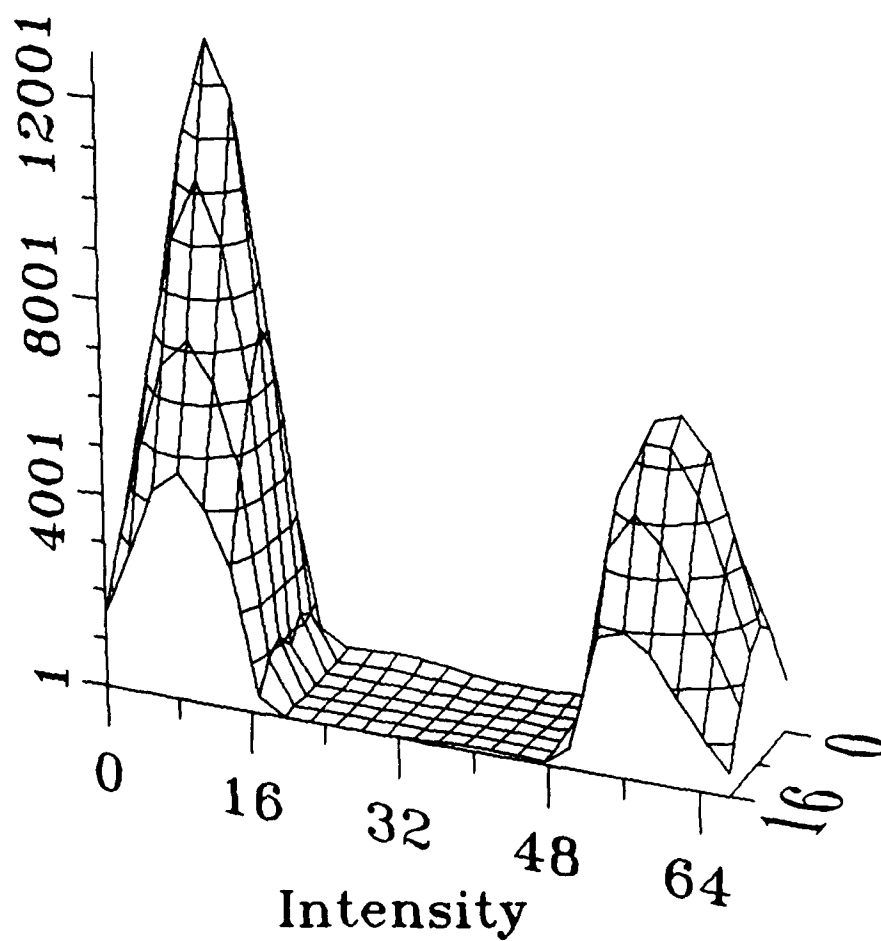

Figure 2   Intensity image across two diffraction orders.
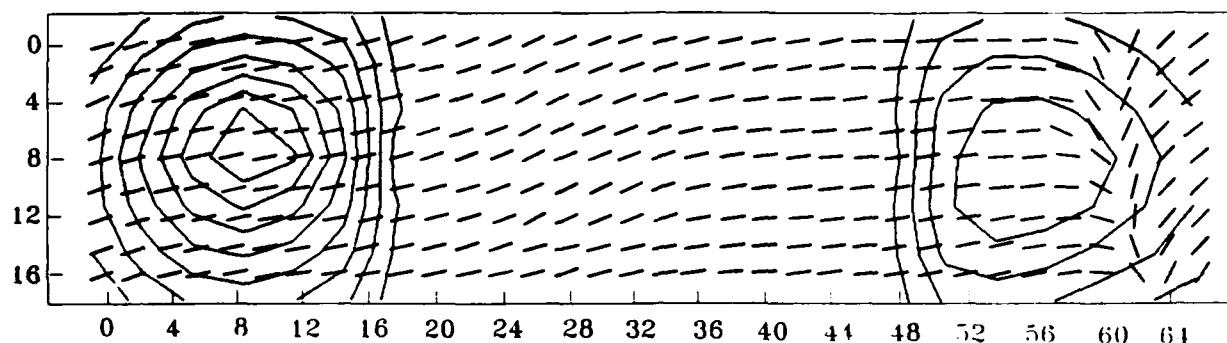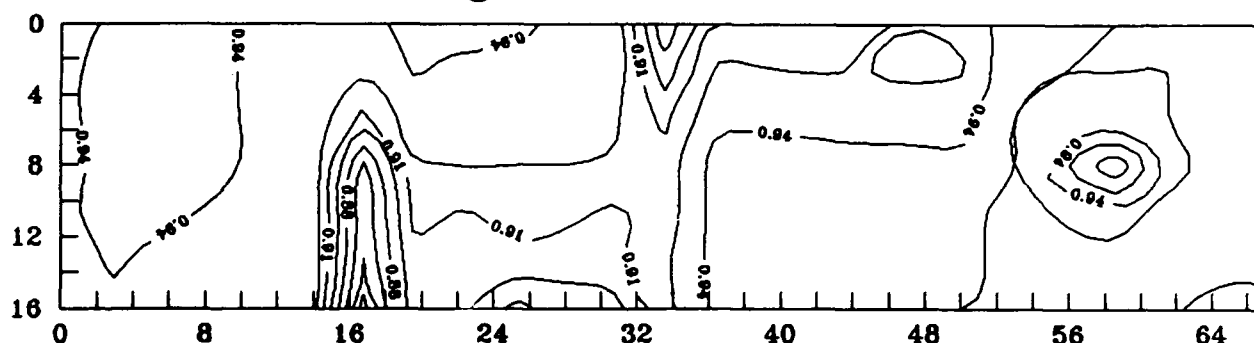
Orientation of Polarization Ellipse

Figure 3 Image of converging beam diffracted by a rectangular array of rectangular pixels (liquid crystal television). Polarization measurements are made across the two diffraction orders highlighted in the rectangular box.

Degree of Polarization

Figure 4 Plot of the degree of polarization across the two diffraction orders.

Eccentricity of Polarization
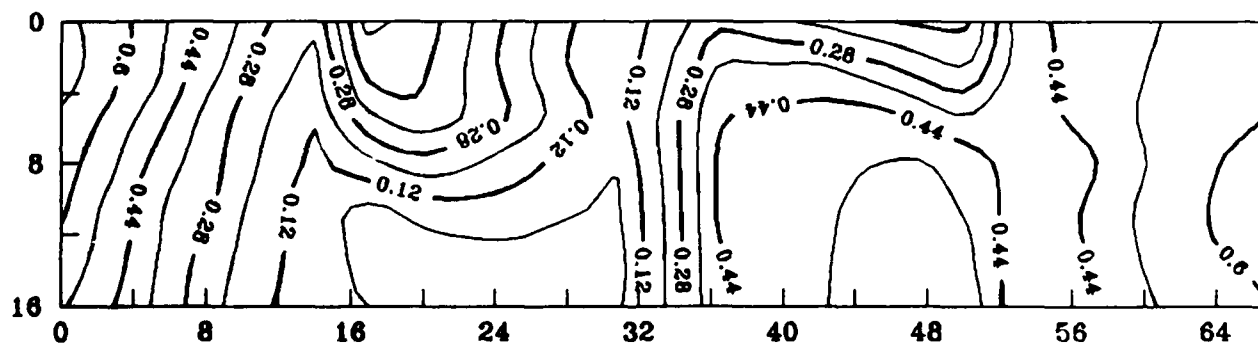
Figure 5 Plot of the eccentricity of the polarization ellipses across the two diffraction orders.

Analysis of coupling efficiency in single-mode
fiber components as an optical design problem

Stanislaw Szapiel
National Optics Institute
369 Franquet
Sainte-Foy (Quebec) G1P 4N8
Canada
Phone: (418) 657-7006
Fax: (418) 657-7009

and

Jasmin Côté
University of Arizona
Optical Sciences Center
Tucson, AZ 85721 U.S.A.
Phone: (602) 621-1263
Fax: (602) 623-9034

A growing number of potential applications of laser diodes and optical fibers has increased the need to design and optimize coupling systems. The evaluation and optimization of coupling efficiency in single-mode (SM) fiber components has already attracted considerable attention[1-7]. Wagner and Tomlinson[1] provided useful compilation of some fundamental expressions and formulated a general theoretical approach to the problem. Since optical aberrations of coupling optics have been recognized as the main source of coupling loss in many practical arrangements, some authors[3,4] have developed analytic expressions to evaluate coupling efficiency in some isolated but experimentally important cases. A complementary approach was put forward by the others[5-7], who also wrote their own computer programs to get some numerical insight into the problem.

In this communication, it is shown that an overlap integral commonly employed to calculate coupling efficiency in SM fiber systems can be formally recast in terms of familiar Strehl ratio and then approximated by using second-order expansion of corresponding pupil integral. As a result, a global approach, which is completely consistent both with optical design practice and related software packages can be developed.

Our starting point is the well-known overlap integral[1]

$$Q\,(V,V_0) = |\iint V(\overline{u})\,V_0^*\,(\overline{u})\,d\overline{u}|^2 \tag{1}$$

where $V(\overline{u})$ describes optical field generated by a coherent laser source and $V_0(\overline{u})$ represents corresponding eigenmode of the SM fiber. Although this is not a mandatory requirement[1], the integration is taken in the exit pupil plane of the coupling optics. Both the optical fields are normalized to carry unity power in the area of integration. Furthermore, let $V(\overline{u}) = |V(\overline{u})|\exp[i\psi(\overline{u})]$, $V_0(\overline{u}) = |V_0(\overline{u})|\exp[i\psi_0(\overline{u})]$ and the effective wavefront aberration

function is

$$kW(\overline{u}) = \psi(\overline{u}) - \psi_0(\overline{u}), \qquad (2)$$

where $k = 2\pi/\lambda$ is the wavenumber. Recall that the function $W(\overline{u})$ includes wavefront errors due to misalignments and decentrations as well. After simple manipulations one obtains the following approximate result for coupling efficiency:

$$Q(V, V_0) \cong Q(\sqrt{I}, \sqrt{I_0}) \cdot exp(-k^2 E_T), \qquad (3)$$

where $I(\overline{u}) = |V(\overline{u})|^2$ and $I_0(\overline{u}) = |V_0(\overline{u})|^2$, respectively.

In the above formula, the first factor, $Q(\sqrt{I}, \sqrt{I_0})$, describes the coupling loss due to mismatch of intensity distributions in the pupil, whereas

$$E_T = <TW^2> - <TW>^2 \qquad (4)$$

denotes the corresponding weighted wavefront variance, i.e.,

$$<TW^n> = \iint T(\overline{u}) W^n(\overline{u}) d\overline{u} / \iint T(\overline{u}) d\overline{u} \qquad (5)$$

and

$$T(\overline{u}) = [I_0(\overline{u}) \cdot I(\overline{u})]^{1/2} \qquad (6)$$

stands for the weighting function. Note that when general decentrations are introduced in the optical system, not only wavefront aberration $W(\overline{u})$ but also the weighting function $T(\overline{u})$ and the factor $Q(\sqrt{I}, \sqrt{I_0})$ will be changed. Following standard arguments known from diffraction theory of aberrations[8,9], the approximate formula (3) should give an accuracy better than a few percent provided that $exp(-k^2 E_T) > 0.3$ and that the factor $Q(\sqrt{I}, \sqrt{I_0})$ is calculated exactly.

It is evident from Eqs. (3-6) that both evaluation and maximization of coupling efficiency can be now treated as examples of application of the generalized Maréchal approach[10,11]. Namely, the formula (3) can be used as:

1° Numerical tool. It is both easier and faster to calculate E_T than the exact form of the overlap integral (1) which involves highly oscillatory integrand and requires special numerical integration schemes to be employed.

2° Analytic tool. Since E_T is a positive-definite quadratic form of wavefront aberration coefficients, appropriate analytic aberration-balancing schemes can be developed, and better understanding of the coupling loss problem can be possibly achieved.

3° <u>Optimization tool</u>. The weighted variance E_T can be used as a target in optical design optimization routines, which, in turn, could lead to the development of optimal coupling geometries.

4° <u>Tolerancing tool</u>. Starting from a tolerance criterion analogous to the Maréchal criterion, a -1dB loss-based tolerance budget can be established.

In the common case when both intensity distributions $I(\overline{u})$ and $I_0(\overline{u})$ are assumed to be close to Gaussian ones, optimization procedure can be further simplified, and it is not absolutely necessary to use the weighted variance E_T as a target. As is well-known[11], for weakly truncated Gaussian beams optimally balanced wavefronts are expressed by appropriate Laguerre polynomials. They should replace orthogonal Zernike polynomials in standard derivations of corresponding targets for a merit function. The procedure is straightforward, but it will vary depending on particular features of an optical design software package selected for design work.

References

1. Wagner, R.E. and Tomlinson, W.J., *Appl. Opt.*, <u>21</u>, 2671-2688 (1982).

2. Sumida, M. and Takemoto, K., J. *Lightwave Tech.*, <u>LT-2</u>, 305-311 (1984).

3. Lu, Y. and Palais, J.C., *Proc. SPIE* <u>839</u>, 79-90 (1987).

4. Senlu, X., Xiaoxin, X., Weizhi, W. and Yonghang, S., *Int. Journ. Optoelectron.*, <u>7</u>, 11-18 (1992).

5. Hillerich, B., *J. Lightwave Tech.*, <u>7</u>, 77-86 (1989).

6. Karstensen, M. and Frankenburger, R., *J. Lightwave Tech.*, <u>7</u>, 244-249 (1989).

7. Karstensen, M. and Drögemüller, K., *J. Lightwave Tech.*, <u>8</u>, 739-747 (1990).

8. Mahajan, V.N., *J. Opt. Soc. Am.*, <u>73</u>, 860-861 (1983).

9. Szapiel, S., *Opt. Acta*, <u>33</u>, 981-999 (1986).

10. Szapiel, S., *Opt. Lett.*, <u>8</u>, 327-329 (1983).

11. Szapiel, S., *J. Opt. Soc. Am.*, <u>72</u>, 947-956 (1982).

Effective Medium Theory Approach to Guided-Mode Resonances

Scott M. Norton, Daniel H. Raguin, G. Michael Morris

The Institute of Optics, University of Rochester, NY 14627, (716) 275-8008

1. Introduction

Guided-mode resonances are a form of Wood's anomaly, which were first properly characterized as a resonance effect by Hessel and Oliner.[1] These anomalies occur because at a specific wavelength λ and incident angle θ, a weakly-bound (leaky) mode of the grating structure is excited. The resonating leaky mode acts as a coupling mechanism between the fields on either side of the grating region. The coupling conditions are quite selective, resulting in sharp changes in the reflection and transmission characteristics of the structure over small detunings in the incident wavelength or incident angle. Because of these narrow bandwidth filter properties, guided-mode resonances have received renewed interest, see for example Refs. 2 and 3.
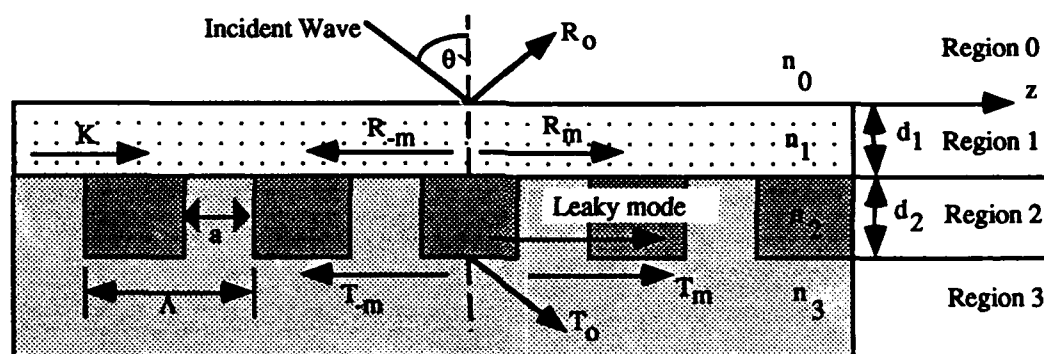
Fig. 1. Embedded grating structure. Period Λ is sufficiently fine compared to the incident wavelength λ that only the zeroth order reflected and transmitted waves (R_0 and T_0, respectively) propagate. All higher diffraction orders are evanescent. To support leaky modes, $n_2 > n_3$ or n_1.

In Fig. 1 we diagram an embedded grating structure in which the index of refraction in the grating region (region 2) n_2 is larger than the index of refraction of either the cover (region 1) n_1 or substrate (region 3) n_3. The condition $n_2 > n_3$ or n_1 must be satisfied in order for the structure to support leaky waveguide modes. The resonance phenomena is strongest when the grating is sufficiently fine that only the zeroth order reflected and transmitted orders are propagating and all higher diffraction orders are evanescent. For this condition to be true, the grating period must always be smaller than the incident wavelength ($\Lambda < \lambda$). In Fig. 2, we illustrate a specific example of the resonance effect on reflectivity. The peak is narrow with a full-width half maximum (FWHM) of about 2 Å. By changing the structure's parameters, the FWHM and resonant wavelength may be modified.
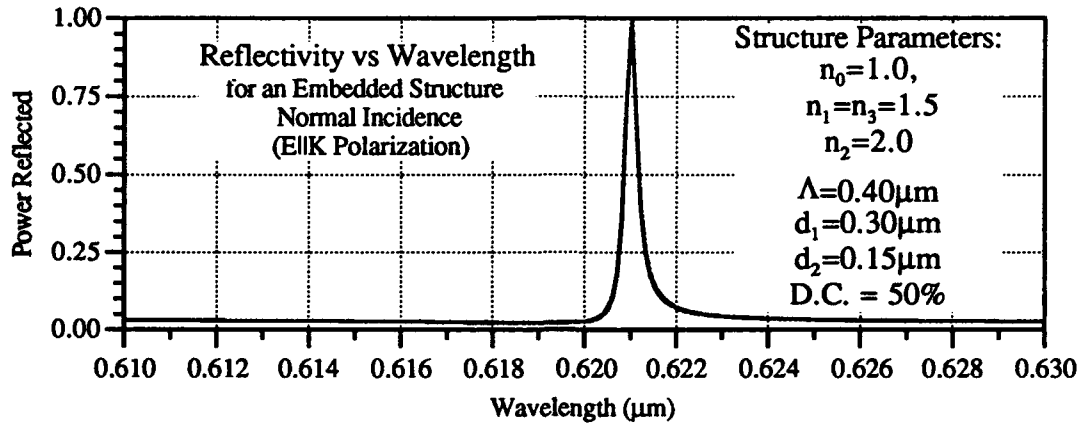
Fig. 2. Reflectivity resonance effect.

Magnusson and Wang[3] used rigorous coupled-wave analysis (RCWA) to analyze similar embedded structures. Rather than discrete modulation of the refractive index in region 2, their grating region had a refractive index equal to $n_2 + \Delta n \cos(Kz)$. They were able to show a connection to the ideal slab waveguide for small modulations Δn; enabling an analytic expression for the location of the resonance to be derived. For large modulations, however, their expression deviated from RCWA data. We will show that by using effective medium theory (EMT)[4] combined with the solution of the dispersion relation for the ideal four-layer waveguide, one can obtain a good estimate for the resonance wavelength.

2. Analytic method of determining the resonance wavelength

To excite modes in an embedded structure, a coupling mechanism is needed to match the tangential phase component of the incoming field to that of the leaky wave.[5] Since these modes are leaky (their propagation constant β is complex), one can only match to the real portion of the propagation constant, $\mathrm{Re}(\beta)$. The periodicity of the structure, through the grating vector, provides the coupling mechanism in the form

$$k_z + K = \mathrm{Re}(\beta) \ , \tag{1}$$

where K is the grating vector equal to $2\pi/\Lambda$ and $\mathrm{Re}(\beta)$ is equal to $2\pi \, \mathrm{Re}(N) \, /\lambda$, where $\mathrm{Re}(N)$ is the real portion of the mode's effective index. When the coupling condition, Eq. (1), is satisfied, the incident field will excite a weakly guided mode. Equation (1) therefore provides an intuitive argument for where resonances will occur. Through rigorous Bloch wave analysis[6] one may obtain propagation constants for leaky modes, but due to the computation time of rigorous methods, it is fruitful to develop faster techniques to predict the wavelength peaks at which resonance phenomena occur. We suggest one possible technique which involves the determination

of the effective index of region 2 using EMT and the subsequent use of the dispersion relation for an ideal four-layer slab waveguide to determine the propagation constant $Re(\beta)$.

Since the propagation constant, β, is wavelength dependent, an iterative algorithm was devised. When the electric field E is polarized parallel to the grating vector K, second-order EMT^4 can be used to find the effective index of refraction of region 2, as follows:

$$n_{E\parallel K}^{(2)} = n_{E\parallel K}^{(o)}\left[1 + \frac{\pi^2}{3\gamma^2}f^2(1-f)^2(\alpha_n - 1)^2\frac{1 + f(\alpha_n^2 - 1)}{\left[\alpha_n^2 - f(\alpha_n^2 - 1)\right]^2}\right]^{1/2}$$

(2)

In Eq. (2), the constant f is the filling factor (defined as a/Λ), $\varepsilon^{(0)}$ is the zeroth-order effective index of refraction defined as

$$\left[\frac{1}{n_{E\parallel K}^{(o)}}\right]^2 = \frac{f}{n_3^2} + \frac{1-f}{n_2^2},$$

(3)

γ is defined as

$$\gamma = \frac{(\lambda/\Lambda)}{n_2 + n_3},$$

(4)

and $\alpha_n = n_3/n_2$. The second-order effective index of region 2, $n_{E\parallel K}^{(2)}$, is initially obtained using an arbitrary wavelength. The effective index, $n_{E\parallel K}^{(2)}$, is then used in the ideal waveguide dispersion relation for a four-level waveguide to determine the effective index N of a guided mode. The coupling relation [see Eq. (1)], was then used to obtain a new wavelength, which is input in the algorithm again until a satisfactory convergence is achieved. This process is illustrated in Fig. 3 as follows:

$$\lambda \xrightarrow{\text{EMT}} n_{eff} \xrightarrow[\text{Dispersion Rel.}]{\text{Waveguide}} N \xrightarrow[\text{Equation.}]{\text{Coupling}} \lambda_{new} \xrightarrow{\text{Converges}} \lambda_{peak}$$
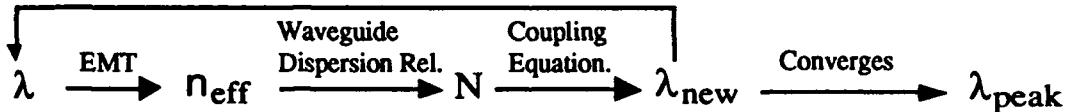
Fig. 3. Iterative algorithm to determine the resonance wavelength of embedded grating structures.

3. Specific Results

With reference to Fig. 1, the structure that we have chosen to examine has the following parameters: $n_1 = n_3 = 1.5$, $n_2 = 2.0$, $\Lambda = 0.4$ μm, $d_1 = 0.30$ μm, and $d_2 = 0.3$ μm. This structure is similar to that discussed by Gale, et. al.[2] The incident external field is assumed to be a normally-incident plane wave with its electric field polarized parallel to the grating vector ($E\parallel K$). We use the algorithm described in Fig. 3 to determine the location of the resonant wavelengths as a function of duty cycle. Note that in this case the duty cycle is equal to the filling factor $f = a/\Lambda$. The results of this algorithm are shown in Fig. 4.
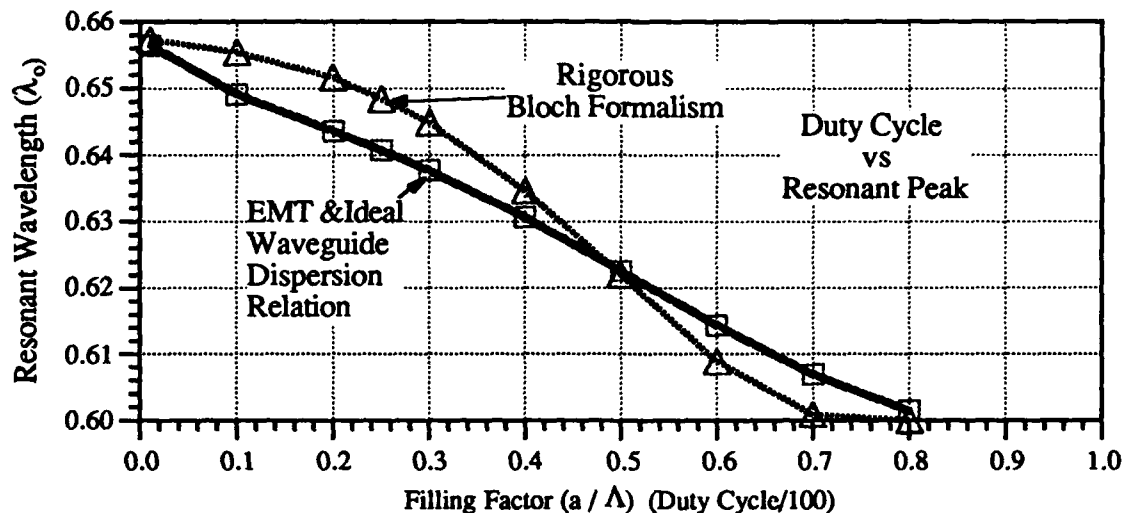
Fig 4. Location of reflection peak vs duty cycle for normally-incident radiation on an embedded grating structure. No data presented for filling factors beyond 0.8 since the structure no longer supports modes (system is beyond cutoff).

In Fig. 4, we also compare the predictions for the resonance wavelength obtained using the EMT approach to that found using a rigorous Bloch wave approach.[6] The Bloch wave approach finds the true field solutions to a certain accuracy, which is dictated by number of mesh points and number of diffraction orders retained. The EMT approach matches the rigorous approach almost exactly at the 50% duty cycle and deviates to a maximum of 1.2% at a 20% duty cycle.

Although computer modeling of the rigorous Bloch wave analysis requires approximately 2.5 minutes on a MicroVAX II to determine a single data point, many data points must be calculated in order to locate the extremely narrow resonant peaks. Consequently, rigorous methods can entail an hour of computation time. On the other hand, using the EMT-based iterative algorithm, a good estimate of the resonance wavelength can typically take less than 10 seconds. While the iterative method is not exact, it does provide a fairly accurate first guess for use with other more rigorous search methods. It also provides an intuitive basis for investigations of coupling mechanisms.

1. A. Hessel and A. A. Oliner, "A new theory of Wood's anomalies on optical gratings," Appl. Opt. 10, 1275-1297 (1965).
2. M. T. Gale, K. Knop, and R. Morf, "Zero-order diffractive microstructures for security applications," SPIE Proc. 1210, 83-89 (1990).
3. S. S. Wang, R. Magnusson, and J. S. Bagby, "Guided-mode resonances in planar dielectric-layer diffraction gratings," J. Opt. Soc. Am. A 7, 1470-1474 (1990).
4. D. Raguin and G. M. Morris, "Antireflection structured surfaces for the infrared spectral region," accepted for publication in Applied Optics, July 1992.
5. T. Tamir, "Inhomogeneous wave types at planar interfaces: III - leaky waves," Optik 37, 204-228 (1973)
6. R. M. Emmons, "Wave guiding and grating coupling phenomena in silicon based integrated optics," Ph.D. Thesis, University of Rochester 1992.

The Migration of Bound and Leaky Solutions to the Waveguide Dispersion Relation

R. E. Smith and S. N. Houde-Walter
The Institute of Optics, University of Rochester
Rochester NY, 14620, 716-275-7629

The eigenmodes of open planar waveguides, like that in Fig. 1, are often determined by finding the solutions to a equation formed by setting a complex function, the *open dispersion function*, equal to zero.[1-3] In the past the study of the migration of these solutions, as waveguide parameters are varied, has been hindered by the form of this function.[1,4,5] When β or β^2 — β being the propagation constant — is used as the independent variable this function is four-valued.[6] When instead, the mode's transverse wavenumber in one of the two outer layers is used, the function is two valued.[1,4,5] Only when the refractive indices of the two outer layers are identical does the function in this form reduce to being single-valued. The function's multivaluedness gives rise to complications, through requiring either migration paths traveling multivalued surfaces, or branchcuts through which solutions can appear and disappear. Recently, a general, single-valued form for the dispersion function that greatly facilitates the study of solution migration, has become available.[7]

A single-valued *open dispersion function*, say $\Phi(Z)$, is obtained by choosing as an independent variable,

$$Z = Ln\left(\frac{\alpha_0 + \alpha_N}{R}\right), \qquad \text{Eq. 1}$$

where, $R = (k_N{}^2 - k_0{}^2)^{1/2}$, $\text{Re}[R] > 0$, k_0 and k_N are the material wave numbers of the substrate and cover, and α_0 and α_N are proportional to a mode's transverse wave numbers in these two outer regions, $\alpha_0{}^2 = \beta^2 - k_0{}^2$ and $\alpha_N{}^2 = \beta^2 - k_N{}^2$.

The domain for this function is shown in Fig. 2 along with the types of solutions found in the various subregions. Notice that unlike the real direction, the function is periodic in the imaginary direction, with period 2π. Only one period is shown. One can imagine joining the top and bottom of the plot in Fig. 2 to form a cylinder on which the function is analytic.

To understand why choosing the independent variable Z results in $\Phi(Z)$ being
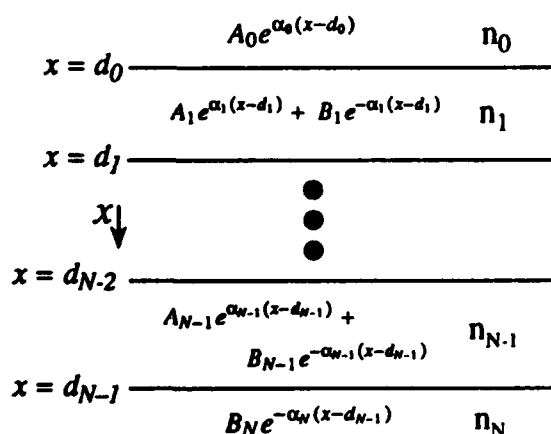

Fig. 1. An open planar waveguide and the forms of the transverse modal amplitudes.

single-valued, considered α_0 and α_N defined in terms of the variable Z,

$$\alpha_0 = R\left(\frac{e^Z + e^{-Z}}{2}\right), \quad \text{Eq. 2}$$

and

$$\alpha_N = R\left(\frac{e^Z - e^{-Z}}{2}\right). \quad \text{Eq. 3}$$

From Eqs. 2 and 3 one sees that for a given value of Z the signs of α_0 and α_N follow unambiguously. It is this sign ambiguity, resulting when α_0 and α_N are defined in terms of β or each other, that is the source of the multivaluedness.

In Fig. 2 one sees that the square-normalizable solutions are contained in the region defined by Re[Z] > 0 and $\pi/2$ > Im[Z] > $-\pi/2$. The bound modes of a transparent waveguide are further constrained to be on the real axis within this same region. All of the solutions found outside this region will be discrete nonnormalizable solutions and as such are nonphysical. However, there are two good reasons to consider the migration of these improper solutions in addition to the migrations of the bound solutions.

1) When a new bound mode is created by varying a physical waveguide parameter, there is a corresponding migration of a solution from the nonphysical to the physical region. The nonphysical solutions are the source for additional physical solutions and as such, the migration of these nonphysical solutions foretells cut-on.

2) For some devices the square-normalizable solutions are insufficient for a complete description of the optical fields. When this is the case, the radiation continuum is necessary to complete the description. It turns out that the nonphysical solutions will provide important clues as to the role that the radiation continuum plays in the device.
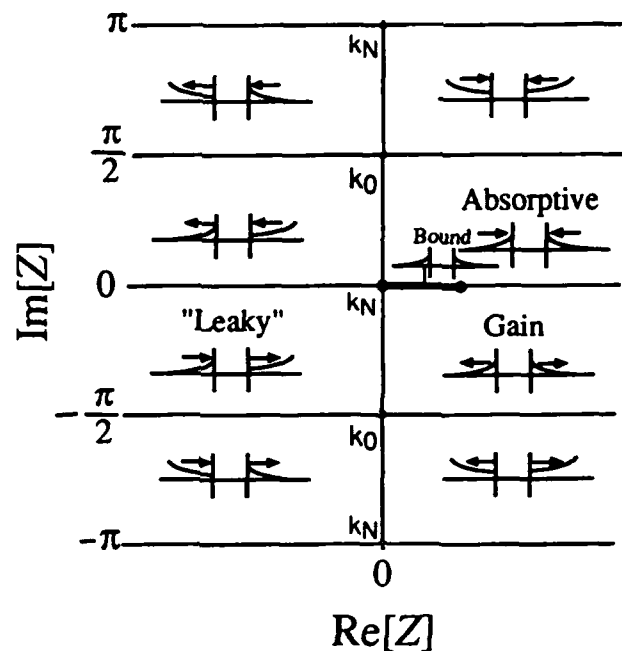
Fig. 2. The domain of $\Phi(Z)$ labeled with the types of solutions found in the various subregions. The arrows represent transverse power flow and the traces represent exponential growth or decay in layers 0 and N respectively.

Knowing how to interpret the migration of these nonphysical solutions can be a very valuable tool for understanding the role of the radiation field. In some structures the role played by the entire continuum can be well described by a single discrete solutions of the dispersion function.[8]

As an example consider the resonant-tunneling waveguide polarizer in Fig. 3.[9] Since the top layer (layer 5) has the same index of refraction as the guiding layer (layer 1), the guiding layer cannot support bound modes. As such, fields excited in the guiding layer will leak into the high index outer region.

The role of the thin semiconductor layer is to amplify the differences between the rates of leakage for the two polarizations. The migration resulting when the width, t, is varied is shown in Figs. 4. The bound solutions
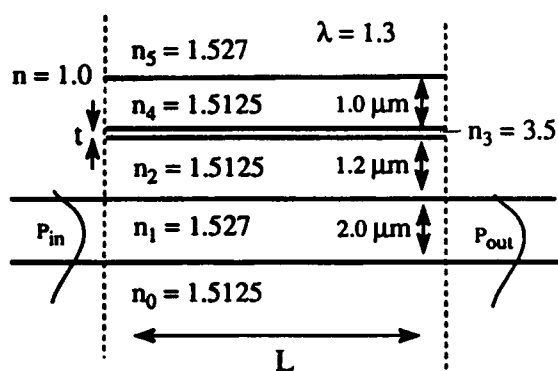
Fig. 3. Waveguide polarizer

shown are all confined to the semiconductor region and the path are those traveled during the cut-on of these bound solutions.

The paths followed during the cut-on of successive modes are quite similar, shown at this scale they are nearly degenerate. In each case, as the width, t, is increased, pairs of solutions migrate in toward the real axis where they coalesce at a point to the left of origin. One then splits right and the other left. When the right going solution passes the origin it becomes a bound mode. This cut-on process is
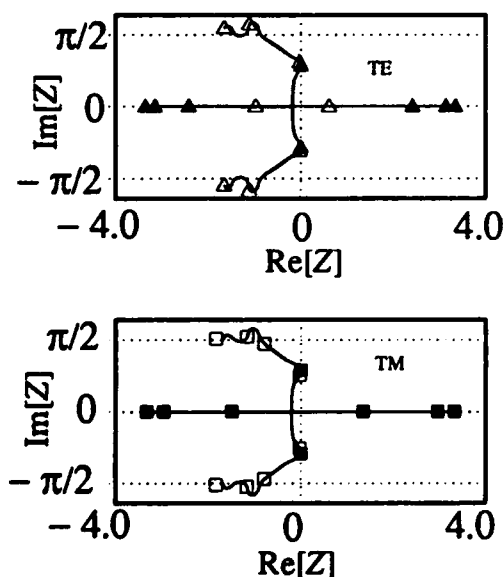
Fig. 4. The migration paths for t varied from 10 nm to 500 nm. The open symbols correspond to 10 nm and the closed symbols correspond to 500 nm.
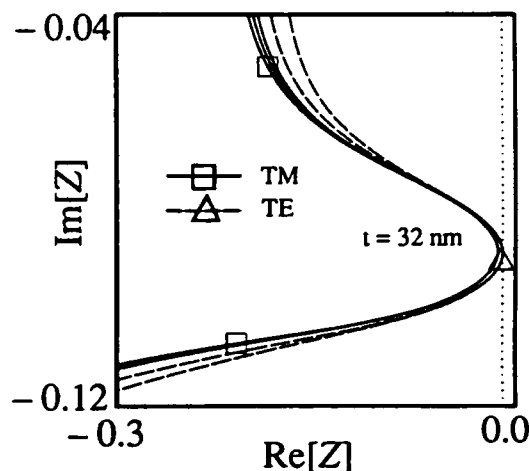
Fig. 5. The improper solutions for the structure in Fig. 3 with t = 32 nm, superimposed on the paths from Fig. 4.

similar to that undergone by the bound modes of all transparent structures. Note that in this case, as with all transparent structures, the migration plots exhibit complex conjugate symmetry.

In this device it is not the semiconductor layer, but rather the guiding layer (layer 1), that is excited by the incoming mode of the 3-layer waveguide. To understand the behavior of such an excitation consider again the paths in Fig. 4. Within the "Leaky" region (see Fig. 2) of theses plots there is an area where the paths dip in close to the imaginary Z-axis. It is this region, close to imaginary Z-axis but far away from the real Z-axis, where improper solutions accurately represent leaky fields.

In Fig. 5 the TE and TM solutions for t = 32 nm are superimposed on the paths from Fig 4. There is a single TE solution very close to the imaginary Z-axis, and a pair of TM solutions further away. Most often, the smaller the value of $Im[\beta]$ is, the tighter the leaky resonance is, and the more accurately the decay is approximated by an exponential. As such, from the information in Fig. 5 we would expect a TE excitation to undergo a slow

longitudinal exponential decay at a rate given by $Im[\beta] \approx 7.03E\text{-}5$. Further, we would expect the TM excitation to decay more rapidly, and though not with an exponential form, we would expect the rate of decay to be approximately given by $Im[\beta]$ of the two solutions that are both about 0.01.

The plot in Fig. 6 compares the decay predicted by these improper solutions to that predicted by a complete sampling of the radiation continuum. As expected the TE solution quite accurately predicts the decay, whereas the TM solutions provide a less accurate approximation. Although, it lacks the exponential form the TM field does decay at a rate that is approximately that predicted by the improper solutions.

From the results seen in Figs. 4 and 5 we see that for both polarizations of leaky modes will undergo either slow or rapid decay depending on the value of t. By choosing thickness for which one polarization undergoes slow decay, and the other does not, one can achieve the a large *differential* leakage. A plot similar to Fig. 5, not shown, demonstrates that absolute leakage can be controlled by varying the thickness of layer 3 as one might expect.

Conclusion: Migration plots like Figs. 4 and 5 are very useful for determining the roles that physical waveguide parameters play in devices. A single-valued *open dispersion function* greatly facilitates the study of these migrations. Owing to the analytic nature of this function, the migration of solutions will often be more clear on the complex plane than when the variation of the real or imaginary parts of β are examined independently. Although the fields associated with the improper solution are nonphysical, the $Im[\beta]$ associated with these solutions provides an estimate of the leakage that is very accurate in the high leakage regime and approximate in the low leakage regime, as is shown in Fig. 6.
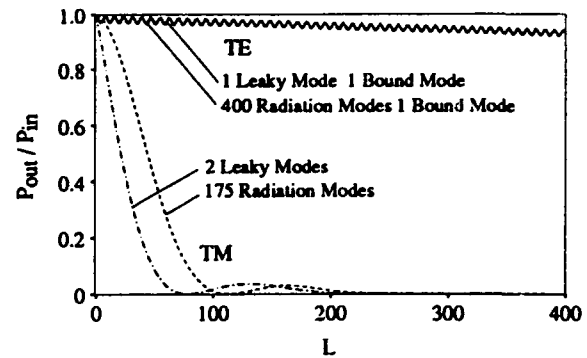

Fig. 6. A comparison of the result of the leaky mode approximation with the more exact sampled radiation mode result.

References
1. R. B. Smith and G. L. Mitchell, EE Technical Report No. 206, Dept. of Electrical Engineering, U. of Washington, (1977).
2. J. Chillwell and I. Hodgkinson, *J. Opt. Soc. Am. A* **1**, pp. 742-753 (1984).
3. A. K. Ghatak, K. Thyagarajan, M. R. Shenoy, *J. of Light. Tech.* **5**, pp. 660-667 (1987).
4. V. V. Shevchenko, *Radio. Phys. Quant. Electron.* **13**, pp. 1176-1178(1970).
5. C. W. Hsue and T. Tamir, *J. Opt. Soc. Am. A* **1**, pp. 923-931(1984).
6. R. E. Smith, S. N. Houde-Walter, and G. W. Forbes, *J. of Quant. Elect.* **28**. *pp* 1520-1526 (1992).
7. R. E. Smith, S. N. Houde-Walter, and G. W. Forbes, accepted for publication in *J. of Quant. Elect.*.
8. A. K. Ghatak, *Opt. and Quant. Electron.* **17**, pp. 311-321(1985).
9. K. Thyagarajan, S. Diggavi, and A. K. Ghatak, *J. of Light. Tech.* **9**, pp. 315-317(1991).

Design of Optical Devices through the
Finite Element Method

M. Zoboli, S. Selleri, F. DiPasquale
Dipartimento di Ingegneria dell'Informazione
University of Parma
Viale delle Scienze I-43100 Parma, Italy
Tel: 00 39 521 905763 Fax: 00 39 521 905758

Recent developments in optical fabrication technology and optoelectronics have provided an abundance of new optical elements whose analysis requires design techniques and powerfull numerical methods. In fact, an analitycal approach of this devices, is possible only with simplifing hypothesis which reduces the original vectorial problem to a scalar one and also in this conditions the mathematical difficulties are not simple, sometime impossible, to overcame. In this work a complete design process based on a full vectorial finite element method (VFEM), applied to the analysis of nonlinear optical fibers, is presented together with graphics based pre-processor and post-processor, necessary tools to characterize optical devices and to describe obtained results. Moreover, an analysis of the refractive index changes induced by the nonlinearity is presented in order to discuss the validity limit of the scalar approach.

The process starts dividing up the domine of interest in second order triangles to form a mesh describing all the geometric and the electromagnetic characteristics of the studied device. The results of this preprocessing is illustrated in Fig.1. The full-vectorial finite-element formulation derives from the curl-curl equations in term of magnetic field vector $\overline{H}$; the application of a standard Galerkin procedure to this equation gives a generalized algebric eigenvalue problem

$$\mathbf{A}[H] - (\beta/k_0)^2 \mathbf{B}[H] = 0, \tag{1}$$

being β and k_0 the phase constant and the wavenumber respectively, and $\mathbf{A}$, $\mathbf{B}$ two sparse matrices depending on the permittivity tensor $\hat{\epsilon}$. In the case of ideal Kerr-low nonlinearity, $\hat{\epsilon}$ is defined as: $\hat{\epsilon}_{lin} + \alpha \mid E \mid^2$, with α related to the Kerr coefficient $\overline{n}_2$ through: $\alpha = c\epsilon_0 n_{lin}^2 \overline{n}_2$, with n_{lin} the linear refractive index. Equation (1) can be solved numerically and iteratively in order to achieve the vectorial field distributions evaluated on the nodes of

the mesh and the effective indices β/k_0 of the guided modes [1]. Finally the post-processor allows to obtain the graphics field distributions of the guided modes and the refractive index profile of the studied structure. The compared scalar approach [2] starts from the nonlinear scalar wave equation in term of the electric field magnitude $\psi(r)$, and allows to compute the effective index β/k_0 for optical waveguides with an ideal Kerr nonlinear behavior, assuming a gaussian trial function for $\psi(r)$. It worths to point out that this approach indicates that nonlinear guided modes do not exist above the critical value $P_c = 2\pi n_{lin}c\epsilon_0/k_0^2\alpha$. On the countrary, the VFEM analysis permits to investigate nonlinear solutions also over the value P_c, as no restrictive hypothesis in power have been introduced.

Applications to nonlinear optical fibers

As first example, in order to verify the validity of the VFEM code, an optical fiber with ideal Kerr nonlinearity in the core has been studied; the fiber parameters are $r_{co} = 2.5\mu m$, $n_{co} = 1.55$, $\Delta n_l = 2.500081 \times 10^{-3}$ (linear index step), $\overline{n}_2 = 3.04 \times 10^{-20}[m^2/W]$. Fig.2 shows the normalized propagation constant $b(\nu) = ((\beta/k_0)^2 - n_{cl}^2)/(n_{co}^2 - n_{cl}^2)$ as a function of the normalized frequency $\nu = r_{co}k_0\sqrt{n_{co}^2 - n_{cl}^2}$ both in linear and in nonlinear case being $P = 200KW$. The VFEM solutions have been compared with the gaussian approximation and with a scalar approach [3] providing good agreement. Moreover an optical fiber with ideal Kerr-law nonlinearity both in the core and in the cladding has been tested. The mesh generated by the pre-processor (Fig.1) consists of 264 triangles and 537 nodes. The step index fiber parameters are $r_{co} = 1\mu m$, $n_{co} = 1.466$, $n_{cl} = 1.45$, $\overline{n}_2 = 3.2 \times 10^{-20}[m^2/W]$. Fig.3 and Fig.4 show respectively, the main component of field distribution in the linear (weak optical intensity) and in the nonlinear case ($P = 1200KW$) for

the foundamental mode, obtained through the post-processor. Noticeable is the changement of the field shape as a consequence of the new refractive index profile induced by the nonlinearity. The same nonlinear optical fiber has been analyzed by varying the input power. Fig.5 shows the nonlinear effective index (left axis) as a fuction of the input power computed both numerically by the VFEM and analytically through the gaussian approximation, with a wavelenght $\lambda = 632$ nm. As already pointed out, the gaussian approximation finds guided modes only over the value $P_c = 1.355 MW$. Furthermore it is forced to work for lower powers in order to verify the weakly guiding condition; in fact growing over $P = 1.3 MW$ the refractive index variation $\Delta n_{nlin} = (n_{nlin} - n_{cl})/n_{cl}$, induced by the nonlinearity, is 5 times greater then the original refractive index step $\Delta n_{lin} = (n_{co} - n_{cl})/n_{cl}$, as shown by the dot line describing $\Delta n_{nlin}/\Delta n_{lin}$ (right axis) in Fig.5.

References

[1] M. Zoboli, F. Di Pasquale, P. Bassi, G. Tartarini, "**Analysis of a Nonlinear Directional Coupler by a Full Vectorial Finite Element Method**", Integrated Photonics Research, 1991 Technical Digest Series Vol.8, April 9-11, 1991, Monterey, California.

[2] R.A. Sammut, C. Pask, "**Gaussian and Equivalent-Step-Index Approximations for Nonlinear Waveguides**", J. Opt. Soc. Am. B, Vol.8, No. 2, February 1991, pp.395-402.

[3] K.Okamoto, A.J.Marcatili,"**Chromatic Dispersion Characteristics of Fiber with Optical Kerr-Effect Nonlinearity**", Journal of Lightwave Technology, Vol. 7, No. 12, December 1989, pp. 1988-1994.
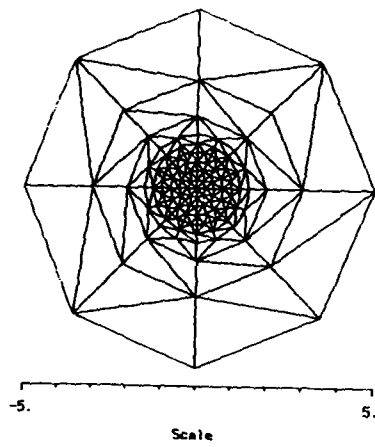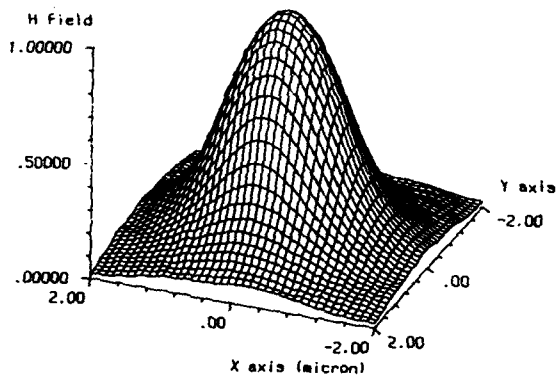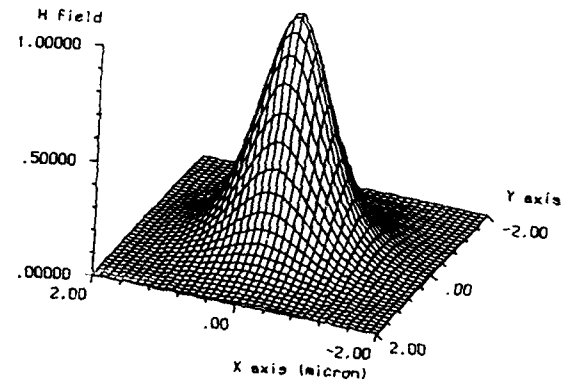
Fig.1
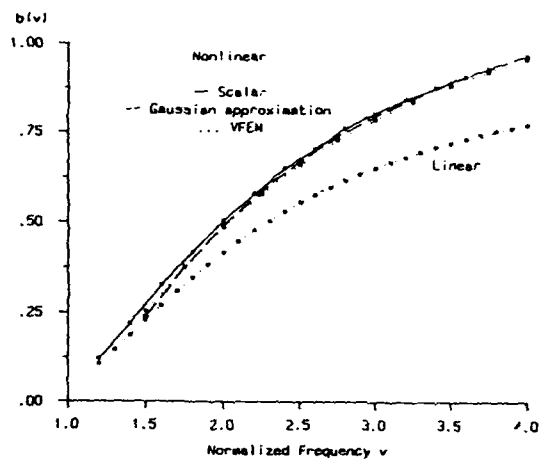
Fig.2

Fig.3

Fig.4
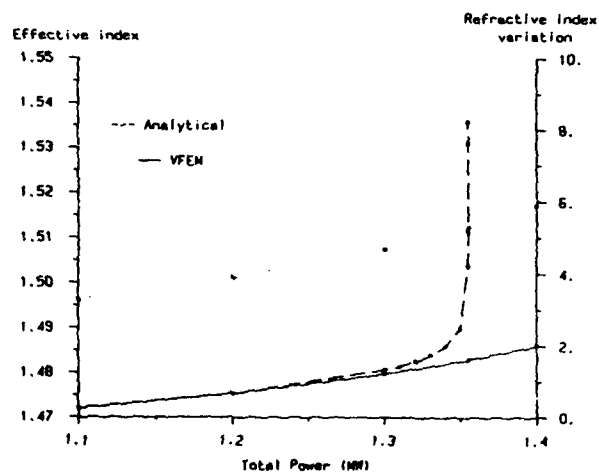

Fig.5

BPM_CAD - Waveguide Optics Modelling Software System

Zdzislaw Jakubczyk

National Optics Institute, 369 Franquet, Sainte-Foy
Quebec, Canada G1P 4N8, tel. (418)657-7006

The BPM_CAD system is a computer software for the modelling of integrated optical devices, planar waveguide structures and fiber optic waveguide problems in a powerful, user-friendly system operating in a mouse- and menu-driven configuration. The core of the package exploits the Beam Propagation Method (BPM), which allows to simulate the propagation of an optical field through any two-dimensional or three-dimensional device. The BPM programs exploit the Finite Difference Method (Crank-Nicolson scheme for 2-D BPM and Baracat-Clark scheme for 3-D BPM) with Transparent Boundary Conditions. Both functional and passive structures can be considered along with loss or gain in the waveguide material.

Examples of the application of the BPM_CAD optical waveguide modelling system encompass most areas of integrated and some of fiber optics. From a simple, planar step index waveguide, for which the propagation constants of the modes of the structure and the modal electric field distributions can be obtained, to complex diffused waveguiding structures with electrodes, or multilayer, semiconductor structures, all can be modelled with no prior expertise. Through a series of mouse-driven pop-up windows, the user is guided through the problems description, definition of input and output files, and to computation. Propagation can be temporarily halted at any time to analyze results using 3-D multiwindow menu-

driven graphics.

2-D BPM_CAD provides programs for the modelling of step index and diffused waveguides, along with programs to characterize an optical waveguide which utilize the 2-D Correlation Function Method, the Transfer Matrix Method and program to calculate the modes of a multilayer planar waveguide. The BPM Diffused Waveguides program can be applied to both passive and functional devices, and for the former, a full treatment included in the application of electrodes and the consideration of the electro-optic properties of the waveguide materials is given. For example, critical parameters required to design a Ti:LiNbO$_3$ modulator, such as waveguide dimensions and the influence of electrode positioning on modulation behaviour can be precisely assessed. The Effective Index Method, which takes into account both lateral and depth diffusions, is built into this program.

3-D BPM_CAD allows modelling of channel or fiber geometries in a full three-dimensional form. The BPM Channel Waveguides program provides the possibility of specifying any 3-D waveguide geometry through multi-layer structure definition, including buried, ridge, loaded and embedded waveguides. Waveguiding primitives along with user-defined files provide the basic building blocks needed to design any structure. In addition to the BPM method, programs for the 3-D Correlation Function Method, Modes of a Channel Waveguide and LP Modes of Fibers are included.

All data generation programs for BPM simulation include a Device Layout Designer where one can construct a device defining regions and entering library waveguide primitives to the regions. The Device Display is continuously updated as new regions

and waveguides are added to the structure. Included in the library are straight waveguides, angled waveguides, various types of tapers, and S-bends. In addition, with both 2-D and 3-D BPM_CAD, the system allows the introduction of user defined files with a complex refractive distribution. These, combined with the library of basic waveguides provided, allows an almost limitless variety of optical waveguide structures to be considered. Furthermore, all designs can be very easily modified by editing one or more parameters of the structure. As an example, Figure 1 shows the computer screen image displaying the Device Layout Designer with Mach - Zehnder modulator on Ti:LiNbO$_3$. This layout is constructed with seven regions and three electrodes are added to the structure. The propagation simulation for a certain voltage is shown in Figure 2.

Any type of field can be propagated through the device under consideration, a user defined field distribution, a Gaussian input field provided by the software library, or a field previously computed using BPM, or modal field obtained from other BPM_CAD programs.

This software system has been utilized to investigate different problems in integrated and fiber optics and to design various waveguide devices. For example in fiber optics the modal noise in short fiber sections was studied and the tapered fiber connector was developed. In integrated optics, we have analyzed the Integrated Laser Doppler Velocimeter, star couplers in polyamide thin films, 1-to-N planar and fiber optical beam splitters, etc. On practical level, BPM_CAD closes the optical waveguide device development loop. Now the performance of a device can be predicted before fabrication, thereby saving development costs.
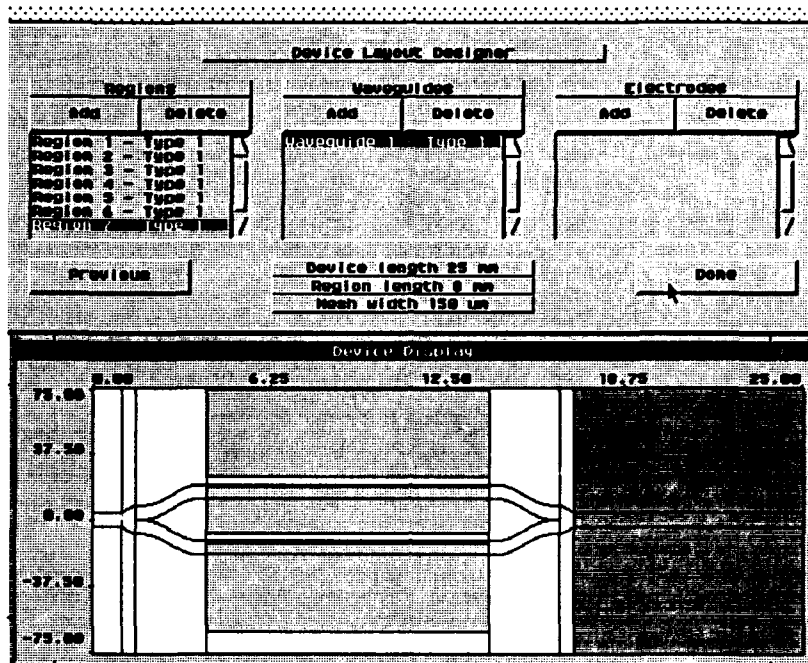
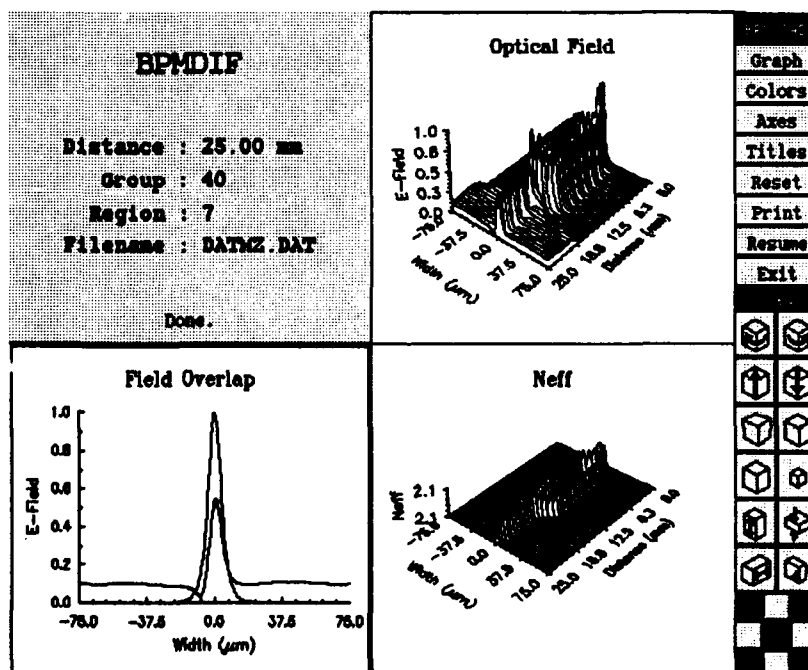Fig.1. Computer screen image of the Device Layout Designer

Fig.2. BPM simulation of the Mach-Zehnder modulator.

Integrated Optical Two-dimensional Time-integrating Correlator

Tristan J. Tayag, Brian M. Sadler, and John M. Pellegrino

Army Research Laboratory
AMSRL-SS-SF, Photonic Processing Branch
2800 Powder Mill Road
Adelphi, Maryland 20783
(301) 394-2520

Two-dimensional (2-D) acousto-optic correlators offer large processing gains for applications in wide-band signal processing systems. A bulk optical implementation of a 2-D correlator which uses surface acoustic waves (SAWs) in LiNbO$_3$ has been demonstrated previously [1]. In this paper, we present an integrated optical architecture that performs a 2-D multi-product correlation. Design specifications are presented for the SAW transducers, waveguide lenses, and vertical outcoupling gratings.

The proposed architecture for an integrated optical (IO) version of a 2-D time-integrating correlator is shown in Figure 1. The unique feature of this architecture is its ability to process 2-D data fields with the planar geometry of integrated optics. This is accomplished by processing each axis of the data field within the waveguide plane, super-imposing the 1-D data fields, and outcoupling the 2-D result from the surface of the waveguide. The integrated nature of this processor offers the inherent advantages of small size, light weight, power efficiency, insensitivity to environmental effects, and the potential for low cost batch fabrication.

The proposed IO processor performs a 2-D three- or four-product correlation through Bragg diffraction, interferometric combination, and time-integration. The signals to be correlated, $A(t)$ through $D(t)$, are imposed on SAW carrier frequencies, ω_1 through ω_4; e.g.,

$$S_1 = A(t)\cos\omega_1 t. \tag{1}$$

Signals S_1 and S_2 are applied to interdigital transducers (IDTs) which produce a pair of counter-propagating, tilted wavefront SAWs. If the IDTs are tilted at the appropriate angles with respect to each other and to the incident guided optical wave (see Figure 2), a doubly Bragg-diffracted component is produced [2],

$$L_{1,2}(t,z) = A(t - \frac{z}{v})B(t + \frac{z}{v})\cos[(\omega_l + \omega_1 + \omega_2)t]. \tag{2}$$

where v is the SAW velocity and ω_l is the angular frequency of the guided optical light. The SAW carrier frequencies, ω_1 and ω_2, are chosen to be unequal so the doubly diffracted wave may be spatially filtered from the undiffracted waves.
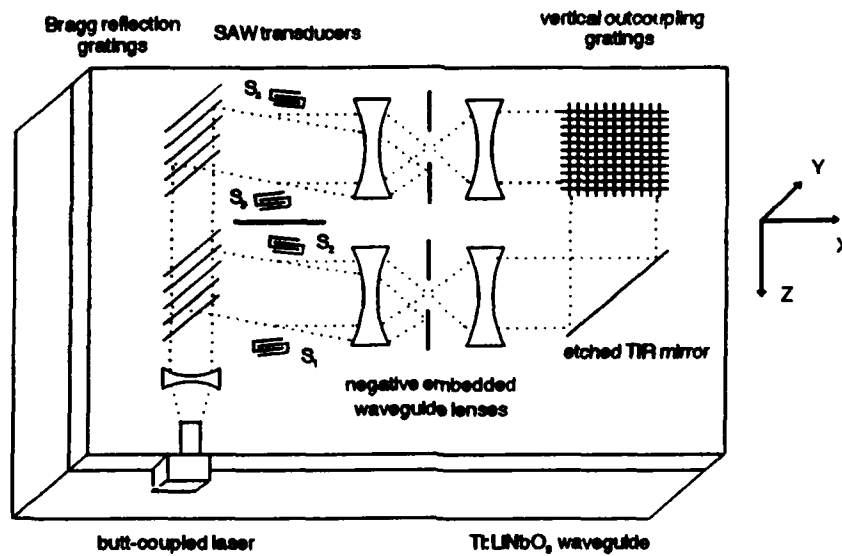
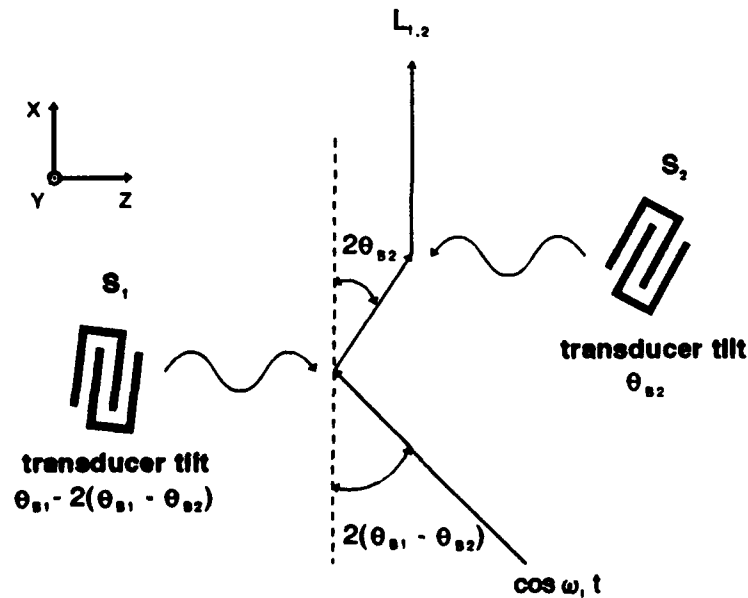Figure 1: Integrated optical 2-D time-integrating correlator.

Figure 2: Acousto-optic interactions producing a doubly Bragg-diffracted wave. Θ_{B1} and Θ_{B2} are the Bragg angles which correspond to the SAWs from S_1 and S_2, respectively.

The doubly diffracted and spatially filtered guided wave, $L_{1,2}$, then encounters a fixed photorefractive waveguide phase grating. This grating uniformly diffracts the guided wave vertically out of the waveguide over the entire interaction length of the grating.

Similarly, input signals S_3 and S_4 produce the following doubly Bragg-diffracted wave, which can be spatially filtered from the undiffracted waves:

$$L_{3,4}(t,x) = C(t - \frac{z}{v})D(t + \frac{z}{v})\cos[(\omega_l + \omega_3 + \omega_4)t]. \tag{3}$$

This field encounters a second waveguide phase grating which is super-imposed and orthogonal to the first phase grating. Thus, $L_{3,4}$ is also diffracted vertically out of the waveguide. The 2-D vertically outcoupled waves are coherently added and detected by a square law detector array. Time integration occurs over a period, T, and the relevant output voltage is given by

$$V(T,x,z) = \int_T A(t - \frac{z}{v})B(t + \frac{z}{v})C(t - \frac{z}{v})D(t + \frac{z}{v})\, dt. \tag{4}$$

In this way, the IO processor forms a 2-D multi-product correlation.

As an example, a wideband radar signal processing application calls for transducers with center frequencies of 80 and 100 MHz and bandwidths of 30 MHz [3]. A 4 μs SAW time aperture enables this IO architecture to be accommodated by a standard 3 inch diameter LiNbO$_3$ substrate. The double diffraction bandwidth and SAW time aperture result in 240×240 resolvable cells within the 1.5×1.5 cm^2 output aperture.

Large aperture (1.5 cm diameter), low f-number (f/1) waveguide lenses are required to maintain the compact system size without sacrificing processing power. Given the IDT bandwidth, the waveguide lenses must be diffraction limited over a ± 1 degree field-of-view. Further desirable waveguide lens characteristics include <2 dB optical power loss, minimum lens footprint, and manufacturable fabrication processes. Low index embedded waveguide lenses [4] have the potential for providing index changes large enough to produce large aperture, low f-number lenses. This lensing technique also has the flexibility to utilize available lens design software packages to design aberration-corrected waveguide lenses. Difficulties with embedded waveguide lenses arise in minimizing optical loss and scattering at the lens/waveguide boundaries.

The IDTs, which generate a doubly diffracted wave from $\pm Z$-propagating SAWs in a Y-cut LiNbO$_3$ crystal, have a dynamic range of 40 dB when the guided wave is TE polarized [5]. The TE$_o$ guided mode therefore is input to each of the two transducer sets. However, in order to achieve coherent interference at the waveguide outcoupling grating, the polarization states of the outcoupled waves must be colinear. This requires that orthogonally polarized waves be input to the orthogonally multiplexed gratings. One means of accomplishing this is to design IDTs 1, 2, and 3 to perform isotropic Bragg diffraction (i.e., TE$_o$ to TE$_o$), while IDT 4 performs anisotropic Bragg diffraction (TE$_o$ to TM$_o$). Therefore, a guided TE$_o$ mode enters the multiplexed outcoupling gratings from the $-Z$-direction and a guided TM$_o$ mode enters the gratings from the X-direction as shown in Figure 2.

The broad area multiplexed outcoupling gratings are the most novel feature of this integrated optical 2-D processor. It is this component that permits the generation of a 2-D data field with the planar geometry of integrated optics. The fixed photorefractive phase gratings allow waveguide outcoupling diffraction within the Bragg regime [6]. Thus, low cross talk among the multiplexed gratings is possible when there is an appreciable separation between Bragg angles.

The photorefractive sensitivity in the Ti-indiffused LiNbO$_3$ waveguide can be enhanced by locally doping the grating region with Cu or Fe. By controlling the phase index modulation over the interaction length of the waveguide, a uniformly outcoupled wave is possible.

Coherent interference and square law detection of the outcoupled waves produces the multi-product correlation. To improve the visibility of the correlation spot, we typically

impose a spatial carrier on the 2-D signal. For this design, the wavevectors of the vertically outcoupled fields should be about 0.8 degrees from the waveguide normal.

We have presented a novel architecture for a 2-D time-integrating correlator which is integrated on a LiNbO$_3$ planar optical waveguide. Optical integration of the processor offers compact size, low weight, power efficiency, robustness, and potentially low cost. Design specifications for the critical waveguide components have been presented. These components are the SAW transducers, the waveguide lenses, and the waveguide outcoupling gratings. Our current experimental research efforts have concentrated on the design and fabrication of aberration-corrected embedded waveguide lenses and on the polarization characteristics of the outcoupling gratings.

References

[1] I. J. Abramovitz, N. J. Berg, and M. W. Casseday. Interferometric surface-wave acousto-optic time- integrating correlators. In *1980 Ultrasonics Symposium Proceedings*, pages 483–487. IEEE, 1980.

[2] J. N. Lee, N. J. Berg, and M. W. Casseday. Multichannel surface acoustic wave correlation and convolution with acousto-optic processors. In *1979 Ultrasonics Symposium Proceedings*, pages 34–39. IEEE, 1979.

[3] E. A. Viveiros, L. J. Harrison, M. S. Patterson, R. J. Berinato, K. W. Williams, V. R. Riasati, and R. A. Durrett. Acousto-optic range-doppler processor design for radar insertion. In *Advances in Optical Information V*, pages 19–30. SPIE, 1992.

[4] M. M. Minot and C. C. Lee. A new guided-wave lens structure. *J. Lightwave Tech.*, 8(12):1856–1865, 1990.

[5] N. J. Berg, M. W. Casseday, and C. Garvin. A new single AO element two-dimensional signal processor. In *1983 Ultrasonics Symposium Proceedings*, pages 482–486. IEEE, 1983.

[6] S. I. Bozhevol'nyi, E. M. Zolotov, V. A. Kiselev, and E. A. Shcherbakov. Investigation of diffraction gratings induced in LiNbO$_3$ for integrated-optics applications. *Sov. J. Quantum Electron.*, 9(2):216–218, 1979.

ALIGNABILITY VERSUS SIGNAL DENSITY IN INTEGRATED PLANAR-OPTICAL INTERCONNECT PACKAGES

Anjan K. Ghosh and Russell S. Beech

Department of Electrical and Computer Engineering
The University of Iowa, Iowa City, Iowa 52242, USA

Free space optical interconnects are well suited to complex, 3-D interconnect patterns and high density parallel interconnections because of their low cross-talk and the ability of beams to pass through one another with minimal interference [1]. To align all of the optical elements in an optical interconnect package so that the interconnect operates correctly, efficiently and reliably is a difficult task than that of simply connecting a wire between two points [2-4]. One method of reducing the alignment problem and producing a better package for optical interconnect systems is to use integrated, planar-optics (IPO) [5,6]. The IPO approach utilizes a glass slab which has all the necessary optical elements fabricated on one of its sides (usually, the opposite side is mirrored). Side, top, and end views of this integrated, planar-optics substrate (IPOS) are shown, schematically, in Fig. 1. Because the optical elements are fabricated on a single substrate the package is compact and manufacturing of the optical system is simpler than an assembly of discrete components. The slabs can be designed as modules to be connected together as needed for a complex optical system [5].

In this paper, we analyze the alignment and determine design guidelines for fabrication of IPO interconnects. Signal density and crosstalk are primary considerations in this analysis. As our case-study we use the popular IPO idea of making a holographic optical backplane (HOB) for board-to-board interconnections [7-11]. We study the design of a basic multi-channel IPO device interconnecting two electronic boards as depicted in Fig. 2. The light beams from optical transmitters on one board are directed by the input holograms and guided by the IPOS, through a series of reflections, to the receiver holograms. At the receiver holograms, the beams are redirected to optical receivers on the other board. This idea of an optical backplane with IPO can be easily extended to the interconnection of multiple electronic boards with multiple parallel channels [9].

We calculate the efficiency of power transfer and alignability of a basic HOB device as a function of the lateral separation between the adjacent channels, the amount of tolerable crosstalk and other parameters of an IPOS design, such as, the lateral and angular offsets in the input, the error in the spatial frequencies of the hologram, the distance between the two boards, the thickness of the substrate, the beam divergence, and the sizes of the holograms and the beam spot. From these calculations, guidelines on choosing the lateral separation of adjacent optical channels and the amount of allowable crosstalk as a function of the substrate thickness, reflection angle, and board-to-board separation are developed. We show that for a given substrate thickness, channel separation and board-to-board separation, the angle of reflection can be chosen to maximize the alignability of the system. A design with a high alignability is more suitable for manufacturing because that design can tolerate more offsets. Thus, the design with an optimum alignability will produce the highest manufacturing or assembly yield.

The alignability of an optical interconnect is a measure of the degree of difficulty of aligning the devices and light beams of the interconnect in the presence of random offsets. The alignability is related to other performance measures of the interconnect system such as the power transfer efficiency, signal-to-noise ratio, bit-error-rate, and the spatial and temporal bandwidths. Knowledge of the alignability of an interconnect system helps in the estimation of the cost of the

development and deployment of the system [10].

For one channel of the IPOS, there are four independent offsets: Δx, Δy, $\Delta\theta$, and γ, where Δx and Δy denote the lateral offsets in positioning the input beam, $\Delta\theta$ is the angular offset along the x direction as a result of hologram error, and γ is the angular offset in the y direction. As a result of these offsets the efficiency of power transfer to the output hologram port of each channel decreases and the crosstalk in the output port of the adjacent channel increases. We assume that the basic probability distribution function (pdf) of each offset is known. These pdfs are integrated to find the total probabilities of achieving an efficiency of η in one channel and a crosstalk efficiency of η_c on the adjacent channel. From these probabilities we obtain the overall alignability as a function of the size of the output ports (d), the separation between adjacent output ports (D), the spot size at the input beam (s), the thickness of the IPOS substrate (t), the total distance between the circuit boards (x_T), the nominal angle of deflection from the holograms (θ_0), the reflectivity of the IPOS surface and the amount of optical crosstalk that we can tolerate.

Preliminary results of our analysis and simulations are shown in Figs. 3 and 4. Values for the various IPOS parameters, used to generate these plots, are given in Table 1. In Fig. 3, we see the effects of varying the separation between adjacent channels, D, while keeping the other parameters constant. As this separation increases, the tolerable alignment offsets, from a crosstalk standpoint, also increase. This eases the alignment task and results in an increase in alignability; as shown in the plots.

Figure 4 shows the effects of changing the crosstalk tolerance, c, and the board-to-board separation, x_T, while keeping the channel separation and the other IPOS parameters fixed. The value of c depends on the required SNR and BER of the interconnect.[11] Similar to the effect of changing the channel separation, increasing the crosstalk tolerance leads to an increase in the system's alignability. If x_T is changed, this general effect remains the same. However, decreasing x_T leads to higher alignability and a shift of the alignability peak to a lower reflection angle. The increase in alignability is due, primarily, to a decrease in reflection losses.

From these calculations, guidelines for designing IPO interconnects and improving the alignment of IPO packages can be developed. For example, for our case study of a simple HOB, we can say that for a good alignment we need the following conditions: (a) Keep the angle of reflection, θ_0, large, about 50°-60°, preferably greater than the critical angle of the glass substrate-air interface. With such values of θ_0 we have total internal reflection at the top and bottom surfaces and the IPOS fabrication can be simplified. (b) The channel separation, D, needs to be about twice the diameter of the output holograms. (c) The choice of the board-to-board separation is a function of c, D, and the reflection angle θ_0. We are continuing such analyses of alignability with more complex IPO interconnects. We have shown that it is possible to design an IPO structure with an optimum alignability. Selection of design parameters to produce the maximum alignability would ensure a low-cost, robust, and efficient IPO interconnect system.

REFERENCES:
[1]   J. W. Goodman, F. J. Leonberger, S. Kung, and R. A. Athale, *Proceedings of the IEEE*
       72, 850 (1984).
[2]   D. Z. Tsang, *Applied Optics* **29**, 2034 (1990).
[3]   A.K. Ghosh, *Applied Optics* **29**, 5253-5261 (1990).
[4]   A.K. Ghosh and R.S. Beech, *Proc. SPIE* **1389**, 630-642 (1990).
[5]   J. Jahns and A. Huang, *Applied Optics* **28**, 1602 (1989).
[6]   J. Jahns and B.A. Brumback, *Optics Communications* **76**, 318 (1990).
[7]   R.C. Kim, E. Chen and F. Lin, *J. of Lightwave Tech.* **9**, 1650-1656 (1991), see also
       K. Rastani and W.M. Hubbard, , *Applied Optics* **31**, 4863 (1992).
[8]   H. J. Haumann, H. Kobolla, F. Sauer, J. Schmidt, J. Schwider, W. Stork, N. Streibl,
       and R. Volkel, *Optical Engineering* **30**, 1620-1623 (1991).
[9]   J.W.Parker, *J. of Lightwave Technology* **9**, 1764-1773 (1991).
[10]   R. S. Beech and A. K. Ghosh, *Proc. of the 2nd IEEE International Workshop on Photonic
       Networks, Components, and Applications*, 1.18.1-1.18.10 (1992).
[11]   R. K. Kostuk, *Applied Optics* **31**, 2438 (1992).

Table 1. Data for IPO Backplane Alignability Plots					
(s=0.75 mm, d/s=2, σ=0.01, β=0.0013 rad, t=3.175 mm)					
PLOT	**θ (deg)**	**N**	**x_T (mm)**	**D (mm)**	**c (%)**
3a	10.03 to 79.21	89 to 3	100	3.0	5
3b	10.03 to 79.21	89 to 3	100	3.25	5
3c	10.03 to 79.21	89 to 3	100	3.5	5
3d	10.03 to 79.21	89 to 3	100	6.0	5
4a	10.03 to 79.21	89 to 3	100	3.0	5
4b	10.03 to 79.21	89 to 3	100	3.0	1
4c	9.93 to 82.76	45 to 1	50	3.0	5
4d	9.93 to 82.76	45 to 1	50	3.0	1
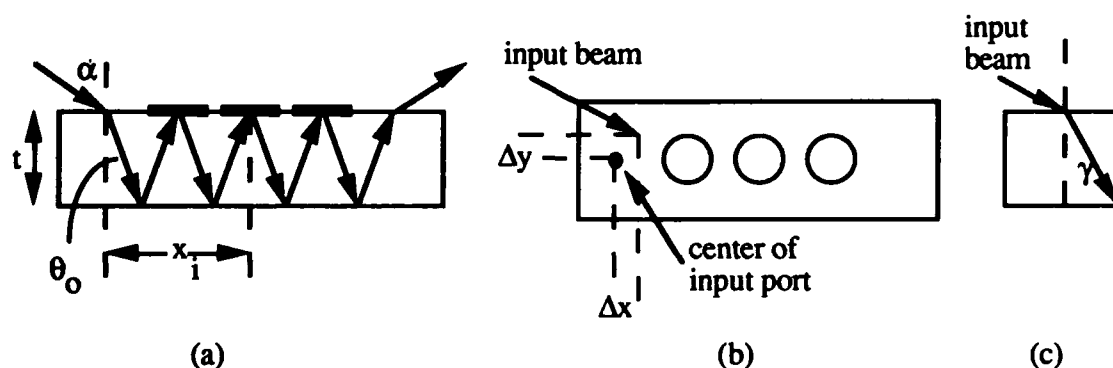
Figure 1. Side view (a), top view (b), and end view(c) of an IPOS.
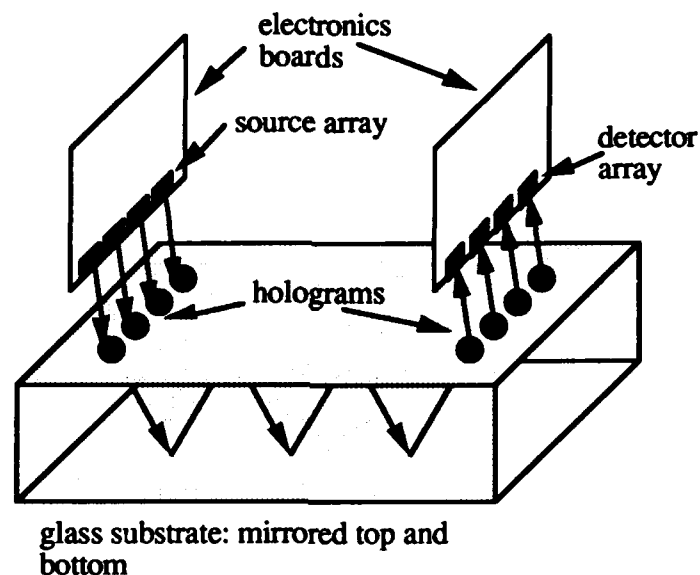
Figure 2. Schematic of the IPOS backplane concept for board-to-board interconnects.
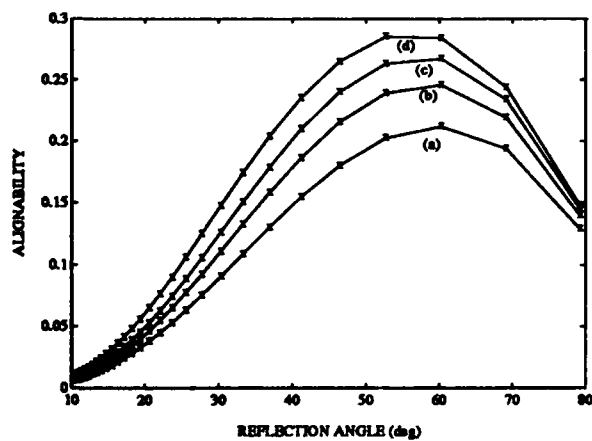

Figure 3. Plots of alignability vs θ. Curves a, b, c, and d represent channel separations of 3, 3.25, 3.5 and 6 mm respectively

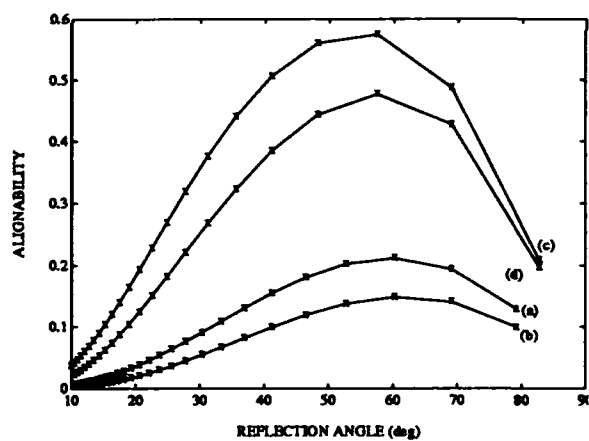Figure 4. Plots of alignability vs θ. Effects of changing crosstalk tolerance and board separation are shown (see Table 1).

Frequency Control, Modulation, and Packaging of an SDL (100 mW) Laser Diode for a Free-Space Photonic Switching Fabric

Jose M. Sasian, Rick L. Morrison, Thomas J. Cloonan, Martin G. Beckman
Michael J. Wojcik, and Stephen J. Hinterlong

AT&T Bell Laboratories
263 Shuman Blvd.
Naperville, IL 60566

1. INTRODUCTION

Free-space optical switching and computing systems utilize macroscopic optical elements such as diode lasers, holograms, gratings, lenses, and mirrors as their basic hardware building blocks. In these systems information is carried by arrays of beams of light that are collimated, manipulated, and focused onto spatial light modulators in a stage by stage fashion. The photonics switching work at AT&T Bell Laboratories has involved the fabrication of several prototype systems[1] [2] with increased complexity and functionality. The motivation in developing free-space optical switching systems is the opportunity offered by optics to interconnect a large number of communication channels at a high bit rate. There are various engineering issues involved in a practical optical system for switching and computing. In this paper we discuss the frequency control, modulation, and packaging of a laser diode for a free-space multistage optical switching system. The laser system is built around a 5400 series (100 mW) laser diode from Spectra Diode Labs. The lasing wavelength could be tuned and controlled by means of an external grating cavity.

2. REQUIREMENTS

To better understand the light source requirements it is appropriate to discuss the basic elements of a free-space photonic switching stage as illustrated in Fig. 1. The optical path starts at the laser source and associated optics (called laser pen) that generate a collimated beam of light. Following the laser pen an array of beams is generated by a multi-level phase grating. The array of collimated beams is transmitted through an optical isolator formed by a polarizing beam splitter and a quarter wave plate that serves as a two-way door for input and output. Then a lens objective creates an array of focused spots on a spatial light modulator such as a Symmetric Self Electro-optical Effect Device[3] (S-SEED) array. The modulated array of spots is reflected, collimated by the lens, reflected by the beam splitter, manipulated by the interconnection hologram, and finally transferred to the next stage.

The spatial light modulator used in our application is an array of uniformly spaced S-SEEDs. These multiple quantum well devices have a switching speed inversely proportional to their active window area so that to maximize the system speed it is crucial to minimize the window size. This in turn implies a minimization of the F-number of the objective lens and to require diffraction limited laser beam quality. In addition, because the phase grating may be required to split several thousands times the single beam from the laser pen and because of light losses in the optical system, it is necessary to require a high power beam from the laser pen. The size of the spot array created by the lens is proportional to the wavelength of light used. To keep the spot array size in our system to within 0.001 mm it is necessary to maintain the wavelength at 850 ± 1 nm. For optimum operation the S-SEED array requires this center wavelength and about the same bandwidth. In addition to these optical requirements it is necessary to provide beam alignment mechanisms, modulate the laser source to a bit rate of 155 MHz, and integrate the optics, mechanics, and electronics in a small package in the order of a few centimeters in size. The main laser pen requirements are:

Power	50 mW	Beam positioning	± 0.050 mm
Wavelength	850 nm ± 1	Beam pointing	± 3 arc-seconds
Beam quality	Diffraction limited	Modulability	DC to 155 MHz

3. OPTICS

The core of our laser pen is a 5400 series GaAlAs laser diode from Spectra Diode Labs. This type of laser can be frequency controlled by means of an external grating as illustrated in the laser pen design presented in Fig. 2. The laser pen optical components are: the laser diode, the collimating lens, the grating, and the anamorphic prism pair. The laser is specified as a single mode device but an external grating cavity had to be implemented to control mode instability and center the wavelength at 850 nm. The grating used is manufactured by Milton Roy (part # 35-33-12-080) and it is used in transmission at Littrow's angle (approximately 14 degrees). The grating has 600 groves per millimeter and is blazed for 400 nm. This grating is not optimized for our application but it was used because it provided a light transmission of 79%, could control the laser diode wavelength with a bandwidth of approximately ± 10 nm, and could be obtained as an off-the-shelf item. The grating was designed to be used on reflection so the reflecting coating was etched off to operate in transmission. The amount of feedback provided to the laser is approximately 1% of the incident light.

The light from the laser is collimated by a lens from Optima Precision (part # 336-1027-001) that has a focal length of 4.5 mm and that works at a speed of f/1. This lens compensates for the spherical aberration generated at the laser sapphire window and provides a diffraction limited field of view of 2 degrees or 0.16 mm at the focal plane. After the beam passes through the grating its aspect ratio is corrected by expanding the beam three times with two prisms from Optima Precision Inc. (part # 420-1212-830) arranged to displace the beam without deviation.

4. OPTO-MECHANICS

The laser diode is factory mounted in a TO-3 window package containing a thermo-electric cooler and a photodiode. This package in turn is held by two machine screws on a stainless steel block pedestal as illustrated in Fig. 3. The screws allow the laser to be moved laterally ± 1.0 mm and to center the laser with respect to the optical axis of the lens. The lens is mounted on a bored brass cylinder that can be threaded (40 tpi) in the laser block which has also a threaded bore. This permits placing the lens at the appropriate distance from the laser to collimate the laser beam. The lens is glued with UV curing cement form Norland Products, Inc. in the brass cylinder which has a recess that centers the lens. A set screw at the top of the block pedestal locks the position of the brass barrel.

An MM-1 mount from Newport Corporation is used to hold the grating. The central hole in the MM-1 plates are made larger to accommodate a beam of up to 10 mm in diameter. The grating from Milton Roy is cut to 15X15 mm squares which are glued on the MM-1 mount plates. Another steel pedestal holds the MM-1 mount at 14 degrees with respect to the vertical. The two anamorphic prisms are glued on a third pedestal that provides the correct prism height. The gluing of the grating and prisms is done with the help of simple jigs to insure proper component alignment. The laser and lens, grating, and prism unit are screwed on a stainless steel plate (laser pen plate) to form the laser pen. An area of 25 X 38 mm of this plate and behind the laser is allocated to mount the electronics. The complete laser pen measures 28 mm in width, 54 mm in height, and 161 mm in length.

5. ELECTRONICS

The electronics necessary to supply laser current (both CW and pulsed) and the connector platform for both electronic power and thermal control lines are provided by an electronics card at the rear of the laser pen mount. In order to meet the power requirements noted earlier, it is necessary to provide from about 100 mA to 140 mA of current during the on (high power state). During the low power off state, the laser must be supplied with less current than the nominal 20 mA threshold current. The current driver circuit must also allow modulation from DC up to 150MHz. Instead of designing a circuit constructed from discrete components, we investigated purchasing IC's designed specifically for laser diode current control. We were unable to locate a single suitable driver chip that matched all requirements, but upon experimentation we found that we could combine two laser driver chips (GigaBit Logic 16G075) in parallel to successfully meet our requirements.

The driver provides an adjustable bias current when an ECL-like differentially driven input is in the off state. When the ECL inputs are switched to the on state, an additional modulation current (also adjustable) is added to

the bias current. The laser driver is capable of accepting ECL signals directly from other system components; however, it was desirable to provide an interface that allowed independent operation of the laser. Therefore an ECL multiplexer chip was included in the design between the input and laser driver. Using two switches, the user can choose modulation via an ECL input signal, or select from two CW states: a bias state or a high power state. Finally, an RJ-45 connector similar to a typical telephone jack provides connectivity for the circuit power supplies and for the thermal controls. The thermal connections (two for a thermistor and two for thermo-electric cooler control) are routed to a second set of pins from which they are individually wired to the appropriate pins of the laser diode package.

6. ALIGNMENT

The components of the laser pen must be aligned with respect to the laser pen plate and in turn the laser pen beam must be aligned with respect to the main plate of our photonic switching system. This main plate is the foundation to assemble the switching stages mentioned above. The surface of the system plate defines the XZ plane. The system plate has several slots running along the Z-axis to mount the optical components. The laser pen beam must be positioned at the front plane of the corresponding beam-splitter. The lateral positioning error of the beam at this plane is required to be no larger than 0.050 mm and the angular error less than 15 arc-minutes.

The lateral and angular positioning of the beam in the X direction are accomplished by displacing or rotating the anamorphic prism pedestal. The attachment holes in this pedestal are oversized to allow a small movement and align the beam ± 1.5 mm along the X-axis and ± 2 degrees in the X angular position. There is no provision to align the beam along the lateral and angular position in the Y direction. However, the vertical position of the beam at the plane of interest can be adjusted by displacing the laser can in the Y direction. This can be done as long as the laser stripe remains within the useful field of the lens. The alignment freedom that this provides is the allowed vertical angular error (15 arc-minutes) times the distance from the laser to the beam-splitter (approximately 200 mm) or about 0.9 mm. The angular positioning error is about one eighth the useful field of view of the lens (2 degrees) so that no significant wavefront deformation should be introduced in the beam. In addition, the tolerance (.025 mm) specified in the mechanical parts contributes to a good prealignment of the laser pen. The fine angular (0 to 15 arc-minutes) alignment of the beam in both directions can be done optically with Risley steering wedges located at the beam-splitter. This fine optical tuning allows steering the beam to within the required 3.3 arc-seconds.

As mentioned before, the laser beam must not be degraded in quality by mispositioning the laser stripe outside the field of view of the collimating lens. The grating must also be aligned so that the reflected beam from the grating returns to the laser. This requires aligning the grating with an angular error less than 20 arc-seconds which is within the angular resolution of the MM-1 mount (5 arc-seconds). In addition, the beam must not be truncated in its passage through the anamorphic prism pair.

We made an alignment jig plate to simplify and make uniform the assembly and alignment of 17 laser pens that are required. This jig partially simulates the system main plate and provides two slots to align the laser pen beam. The first slot has two positions for the laser pen; these positions are provided because the anamorphic prism pair displaces the laser beam 6.4 mm. In the first position the laser beam is centered with respect to the slot when the anamorphic prisms are not mounted on the laser pen. In the second position the beam is again centered with respect to the slot but the anamorphic prism pair is mounted in the laser pen. In the second slot the laser beam is displaced 3 mm from the slot center in the X direction to exactly simulate the mounting on the system main plate. To check the position of the beam with respect to the slots a CCD camera is mounted on a cylinder that can be slid along the slots. A precision made cylinder with a central pinhole permits finding the ideal beam XY coordinates on the CCD plane and also permits determining the beam position with respect to the slots. This measuring scheme allows one to define the beam position to 0.05 mm in the x and y directions and determine the beam angular position to within 1 arc-minute.

7. TESTING

Several tests are required to characterize the performance of the laser pen. The main tests are: beam interferometry, spectral analysis, and modulation. Figures 4, 5, and 6 show results from these tests.

8. SUMMARY

We have frequency controlled, modulated, and packaged a laser diode for a photonic switching system. In this laser system the laser diode, the optical elements, the electronic components, and the grating mount were obtained as off-the-shelf items. This was an important feature because the production cost was decreased. The successful completion of the laser system not only required good optical, mechanical, and electronic designs but a number of tests to verify the laser pen performance. The process of the overall optimization of the laser system required approximately one and a half iterations for the optics, two iterations for the opto-mechanics, and two for the electronics.

Basic photonic switching stage
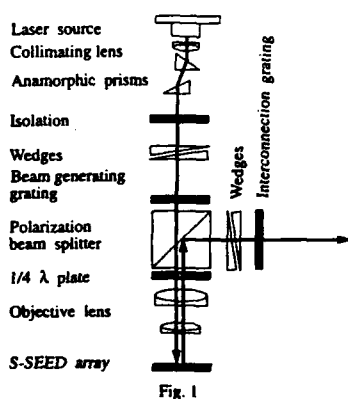
Laser pen optical design

Fig. 1
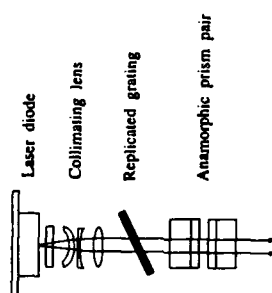
Fig. 2

Laser pen opto-mechanics
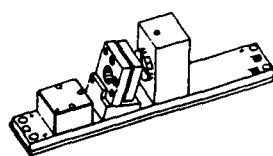
Fig. 3

Fig. 4 Beam interferogram

Fig. 5 Spectra

nanometers

nanoseconds
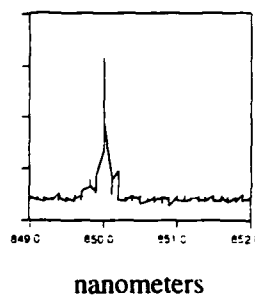
Fig. 6 Waveform

REFERENCES

1. F. B. McCormick, F. A. P. Tooley, T. J. Cloonan, J. L. Brubaker, A. L. Lentine, R. L. Morrison, S. J. Hinterlong, M. J. Herron, S. L. Walker, and J. M. Sasian, "S-SEED-based Photonic Switching Network Demonstration," in *OSA Proceedings on Photonic Switching*, H. Scott Hinton and Joseph W. Goodman, eds. (Optical society of America, Washington, DC 1991), Vol. 8, pp. 48-55.

2. F. B. McCormick, F. A. P. Tooley, J. L. Brubaker, J. M. Sasian, T. J. Cloonan, A. L. Lentine, S. J. Hinterlong, and M. J. Herron, "Optomechanics of a free-space photonic switching fabric: the system", *Optomechanics and Dimensional Stability*, Proceedings of SPIE, 1533, 97-114, (1991).

3. A. L. Lentine, H. S. Hinton, D. A. B. Miller, J. E. Henry, J. E. Cunningham and L. M. F. Chirovsky, "Symmetric Self Electro-optic effect Device: optical set-reset latch, differential logic gate and differential modulator/detector", *IEEE Journal of Quantum Electronics*, QE-25, 1928-1936 (1989).

Multiple-Plane Optical Interconnections Using Through-Wafer Hollow Dielectric Waveguide Vias

A. D. Norte, A. E. Willner, W. Shieh, and A. R. Tanguay, Jr.
Dept. of EE and Center for Photonic Tech., USC, LA, CA 90089-2565, (213)740-4664, FAX:(213)740-8729

Introduction: It is of critical importance for future data communications to connect multiple high-speed processors simultaneously in a local environment. Currently, two-dimensional (2-D) optical planes can achieve this function in a manner not limited by the bottlenecks of size, speed, and power consumption inherent in electronic switches [1-2] as well as the difficulties inherent in fabricating densely-packed vertical electrically-conductive through-wafer vias. However, it is highly desirable for a given plane to communicate simultaneously with several other planes without data being detected and then retransmitted at each plane. In addition, the various substrates may be opaque to the light emitted by a given surface-emitting laser. One solution for multiple-plane optical processing utilizes large non-guiding via-hole windows and integrated lenses for its implementation [2]. Alternatively, we propose using through-wafer hollow-dielectric-waveguide vias such as those fabricated using laser-assisted photochemical etching [3-4]. Furthermore, we establish the critical performance parameters for such hollow-waveguide vias.

We analyze a 2-D optical interconnection configuration that depends solely on the guiding properties of hollow dielectric waveguides to establish simultaneous multiple-plane communications in order to specify guidelines establishing their usefulness. This scheme is well-suited for systems in which the laser light is absorbed by the substrate or in which integrated lenses and anti-reflection (AR) coatings may be impractical or undesirable. This paper addresses critical system design guidelines such as waveguide packing density, optical plane separation distance, and hole radius issues. The 2-D analysis considers the wavelength range of 0.5 to 1.6 μm for which surface-emitting semiconductor lasers are available. We find that this system's utility depends strongly on the preferential excitation of the fundamental EH_{11} mode, resulting in a high waveguide packing density, small separation distance between planes, and reasonable hole radii. Additionally, we derive analytical expressions for adequately modeling all guided and unguided aspects of beam propagation and loss for this interconnection architecture.

Generic Multiple-Plane Hollow Waveguide Interconnection Configuration Modeling: The generic 2-D multiple-plane optical interconnection configuration is shown in Fig. 1. This interconnection consists of N 2-D optical planes, each of wafer thickness L_p and separated by a distance L_s. Each plane consists of a 2-D array of pixels, each containing either: (1) a source and hollow waveguide, or (2) a detector, or (3) a hollow waveguide only. A vertical-cavity source is fabricated on the substrate, in this paper GaAs, and its signal field is guided to another plane by a combination of hollow waveguides and free-space. The plane separation distance, wafer thickness, source wavelength, λ, adjacent hole separation distance, D, and hole radius, a, constitute the interconnection system parameters. The source and detector radii are considered to be the same as the hole radius.

The various optical fields associated with a hollow dielectric waveguide interconnection system are shown in Fig. 2. The field quantities are partitioned into four regimes: (1) the guided signal field; (2) the leaky field out of the via-hole; (3) the transmitted Gaussian field tails and; (4) the output signal field to be coupled into the following via. The guided signal field is that part of the incident field that excites propagating modes in the via cavity. As the guided signal field propagates through the hole, the lossy nature associated with hollow waveguides causes part of the guided signal power to leak into the surrounding semiconductor material, constituting the leaky field. A ray model is used to characterize this leaky field for wavelengths not absorbed by the semiconductor material.

In the non-absorption region within the semiconductor, the waveguide modes are characterized by a transverse propagation vector [5] that results in the leaky field of all the lower order modes exiting from the via walls at approximately an angle of 73°, as shown in Fig. 2, at a source wavelength of 1.6 μm. At this wavelength, the semiconductor-air interface critical angle is 17°. This small critical angle results in the total internal reflection of the leaky field when it is incident at both the front and back plane facets, resulting in the non-intuitive confinement of the leaky field to the substrate in which it originates; hence, the leaky field will not couple energy into the hollow waveguides located beyond this substrate. We find that the totally internally reflected leaky-field rays impinge upon other via walls at the critical angle, resulting in minimal crosstalk between other waveguides in the same plane. Furthermore, the totally internally reflected leaky rays result in a small leakage flux along the front and back substrate facets causing minimal crosstalk to any detectors located on these surfaces. In the wavelength region for which the semiconductor is opaque to the signal, the semiconductor is highly lossy and prevents the leaky field from propagating into the material, resulting again in negligible crosstalk among guides.

The transmitted Gaussian field tails of the incident free-space signal field impinge on the front facet of the substrate outside the via area. These field tails decay in the radial direction, so that when the plane separation distance is small, we find that the tails will not couple significant energy into adjacent guides and are negligible. The remaining

field component, the output signal field, emanates from a given via, diverges, and acts as the incident signal field on the following optical plane. In order to optimize the various optical fields, several optical interconnection parameters, such as the separation distance between optical planes L_s, must be considered. For the transmitted Gaussian field tails to be considered negligible, the separation distance between planes must be such that the preferential excitation of the waveguide fundamental EH_{11} mode is established.

EH_{11} Modal Coupling Efficiency: When the separation distance between planes is small and the laser emits in the TEM_{00} mode, the waveguide fundamental EH_{11} mode exhibits the best coupling ratio into the via. We find the EH_{11} modal plane-to-plane coupling efficiency, K_{11}, due to diffraction losses and without intermediate lenses to be

$$K_{11} = \frac{\frac{4}{w^2(L_s)}\left|\int_0^a \exp(-r^2/w^2(L_s))\exp\left(-jK_or^2/(2R(L_s))\right)J_0(k_ir)rdr\right|^2}{\int_0^a J_0^2(k_ir)rdr} \qquad (1)$$

in which J_0 is the zero-order Bessel function, $K_0 = 2\pi/\lambda$, $k_i = 2.405/a$ and $w(L_s)$ and $R(L_s)$ are the beam spot size and radius of curvature, respectively, at the inter-planar separation distance L_s. The dependence of K_{11} on hole radii is shown in Fig. 3 for $\lambda = 1.6$ and $0.5\ \mu m$. For $a = 12\ \mu m$ and $K_{11} > 95\%$, the separation distance between planes must not exceed 50 and 150 μm for $\lambda = 1.6$ and $0.5\ \mu m$, respectively. The coupling efficiency increases with decreasing wavelength, thereby allowing greater separation distances at shorter wavelengths. Note that the separation distances between planes can be practically made to be $< 50\ \mu m$ by appropriate chip bonding.

Signal Attenuation: An important design consideration when using waveguide via interconnections is determining a low-loss hole radius, which is established by considering the signal attenuation through N identical planes. The guided modal field attenuation through one plane [5] shows that the EH_{11} mode has, for all hole radii and wavelengths, an attenuation constant that is approximately an order of magnitude smaller than that of the next higher-order mode.

When the separation distance between planes results in the preferential guiding of the EH_{11} mode, we determine the net guided-signal attenuation through N identical optical planes, α_g, to be given by

$$\alpha_g = N(10\log(\exp(2\alpha_{11}L_p)) + (1-N)((10\log(K_{11}) - 83.3 \times 10^{-3})) \qquad (2)$$

where α_{11} is the EH_{11} modal attenuation constant. The losses in Eq. (2) represent waveguide losses (first expression) and divergence losses (second expression). We compare the guided attenuation to the case in which the signal field is completely unguided. The unguided attenuation, α_u, results from the diverging signal field impinging on a detector of fixed area and is given by

$$\alpha_u = 0.7011 - 10\log\left(\exp\left(\frac{(L/Z_0)^2}{1 + (L/Z_0)^2}\right)\sinh\left(\frac{Z_0^2}{L^2 + Z_0^2}\right)\right) \qquad (3)$$

in which $Z_0 = (\pi a^2/\lambda)$ and $L = (NL_p + (N-1)L_s)$. The net guided and unguided signal attenuation through four planes as a function of hole radii is shown in Fig. 4; for both the guided and unguided cases, the total propagation distance is 950 μm with $L_p = 200\ \mu m$ and $L_s = 50\ \mu m$. As a design guideline, there exists a range of hole radii for which the guided signal attenuation through four identical planes is less than that due to unguided propagation, where the maximum difference between the guided and unguided attenuation, α_Δ, for $0.5\ \mu m < \lambda < 1.6\ \mu m$ is shown in Fig. 5. It is within this range of radii that the use of vias to guide light between many planes is quite beneficial. Furthermore, for $a = 12\ \mu m$, the net guided signal attenuations through 4 planes are only 3 and 1 dB at $\lambda = 1.6$ and $0.5\ \mu m$, respectively. In general, the range of appropriate radii increases with wavelength.

Power Penalty: Another important design consideration is the separation distance, D, between adjacent vias within the same plane, as the power penalty due to crosstalk determines the allowable interconnection packing density. The guided-signal power penalty dependence on D for $\lambda = 1.6\ \mu m$ is shown in Figs. 6a and 6b for $L_s = 50$ and 200 μm, respectively, resulting in EH_{11} coupling efficiencies of 95% and 56%; note that the penalty is governed here by the waveguide losses and not by the divergence losses. These cases are compared with the completely unguided case. The

guided and unguided power penalties result from considering the detector crosstalk due to the 8 most adjacent signal fields. For wavelengths that are not absorbed by the material, the unguided power penalty approaches zero with increasing separation, while the guided power penalty approaches a constant non-zero value because the leakage flux density is independent of D. The holes can be spaced arbitrarily close together because the leakage flux crosstalk power is small compared with the desired signal power incident on the detector. This results in the efficient utilization of the semiconductor wafer area. For wavelengths that are absorbed by the semiconductor, the leakage flux is negligible and results in power penalties similar to those shown in Figs. 6a and 6b except that the guided power penalty now approaches zero.

Summary: Using derived analytical expressions, we have determined the system guidelines of using hollow dielectric waveguide vias in an optical interconnection configuration. It was shown that vias provide the desirable leaky-field properties of total internal reflection at the front and back plane facets, and negligible crosstalk between adjacent guides. The net signal attenuation through N identical planes results in a range of hole radii for which the guided attenuation is significantly less than the unguided attenuation. The preferential excitation of the EH$_{11}$ mode results in minimal signal attenuation and negligible energy coupling between adjacent guides. Therefore, optical interconnections incorporating hollow waveguides can be low-loss, thereby removing the need for integrated lenses and AR coatings and circumventing any signal absorption by the substrate.

References
1) M. R. Feldman, S. C. Esener, C. C. Guest, and S. H. Lee, Appl. Opt., **27**, p. 1742, 1988.
2) A. Dickinson and M. E. Prise, Appl. Optics, **29**, p. 2001, 1990.
3) D. V. Podlesnik, H. H. Gilgen, A. E. Willner, and R. M. Osgood, Jr., J. Opt. Soc. of Am. B, **3**, p. 775, 1986.
4) R. M. Osgood, Jr., A. Sanchez-Rubio, D. J. Ehrlich, and V. Daneu, Appl. Phys. Lett., **40**, p.391, 1982.
5) E. A. J. Marcatilli and R. A. Schmeltzer, Bell Syst. Tech. J., p. 1783, 1964.
6) D. E. Aspnes and A. A. Studna, Physical Rev. B, **27**, p. 985, 1983.
7) R. L. Abrams, IEEE J. of Quant. Elect., **QE-8**, p. 838, 1972.
8) F. W. Ostermayer, Jr., P. A. Kohl, and R. H. Burton, Appl. Phys. Lett., **43**, p. 642, 1983.
9) A. Hongo, K. Morosawa, K. Matsumoto, T. Shiota, and T. Hashimoto, Appl. Opt., **31**, p. 5114, 1992.
10) R. M. Jenkins and R. W. J. Devereux, Appl. Opt., **31**, p. 5086, 1992.
11) A. Yariv, Optical Electronics, 3rd ed., Holt, Rinehart and Winston Publishing, New York, 1985.
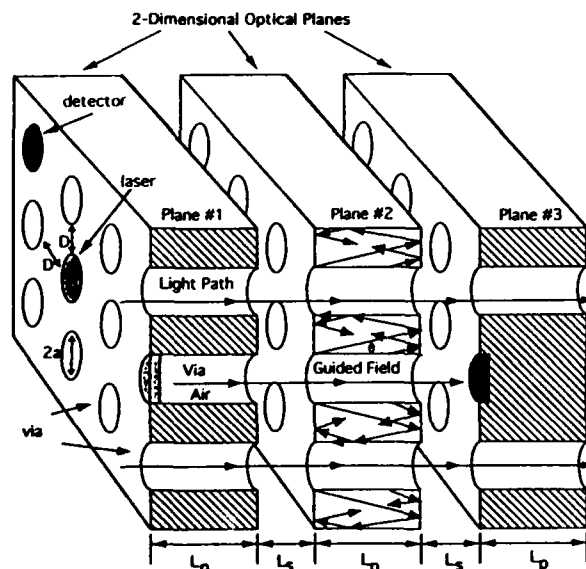
Fig. 1. Generic 2-D optical interconnection using through-wafer hollow dielectric waveguide vias.
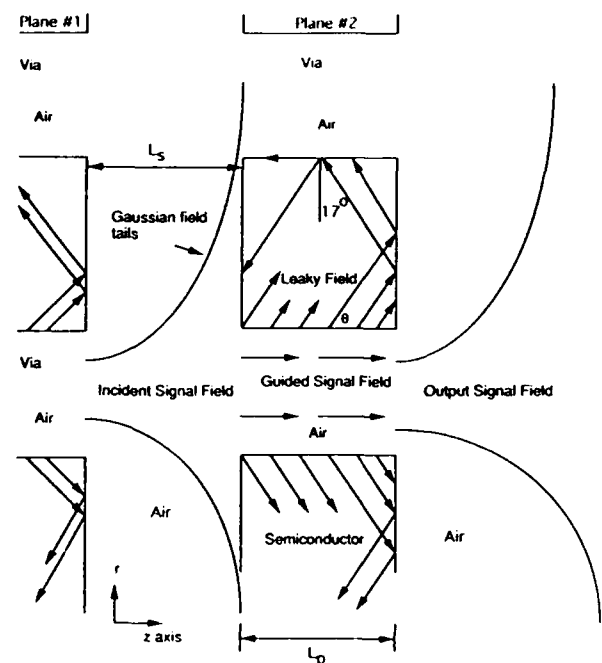
Fig. 2. Cross-sectional view of the various optical fields associated with a hollow dielectric waveguide interconnection.
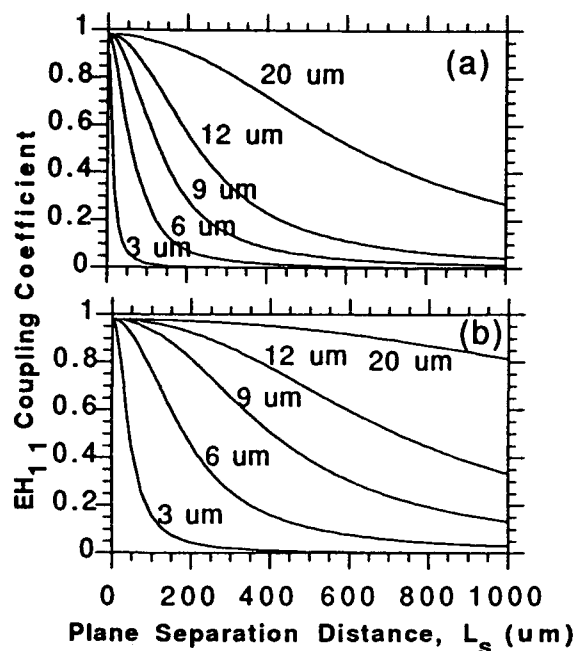
Fig. 3. EH_{11} modal coupling coefficient dependence on hole radius and plane separation distance, L_s, for λ of (a) 1.6 um and (b) 0.5 um.

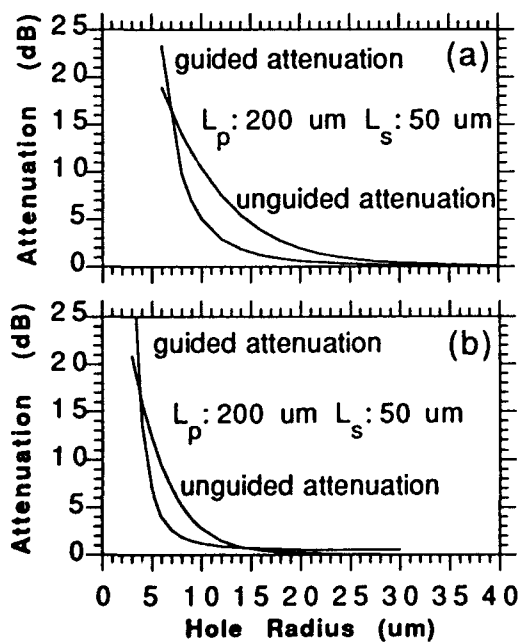Fig. 5. Maximum attenuation difference between unguided and guided attenuation for λ between 0.5 um and 1.6 um.

Fig. 4. Attenuation curves showing hole radii for which guided attenuation is less than unguided attenuation for λ of (a) 1.6 um and (b) 0.5 um.
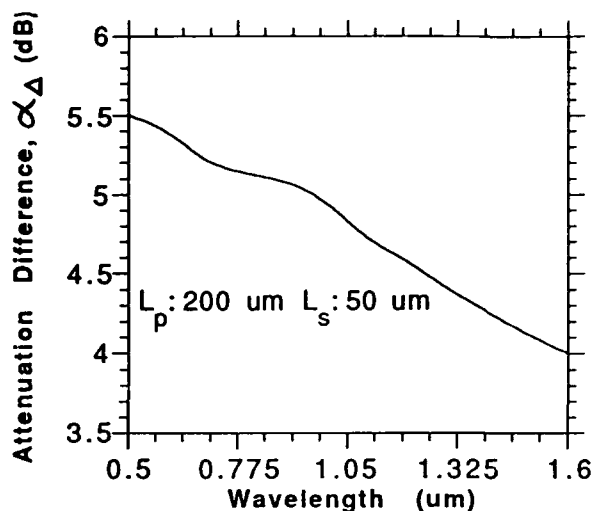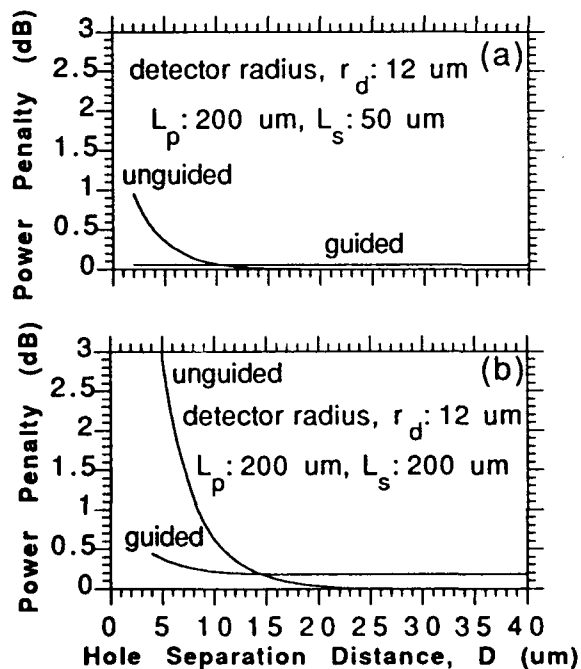

Fig. 6. Guided vs. unguided power penalty indicating an arbitrarily small planar hole separation distance, D, for λ = 1.6 um and (a) L_s = 50 um; (b) L_s = 200 um.

Design Methods for Photonics Technology Contributed Papers in Poster Format

(This session includes papers previewed in OWA.)

OWB 10:20am-12:00pm
Grand Ballroom

Optoelectronic Packaging Design

OWC 1:30pm-3:00pm
Oleander Room

Bulent Nihat Kurdi, *Presider*
IBM

OEIC Packaging for Fiber Optic Computer Interconnects

Kenneth P. Jackson
IBM Applications Business Systems
3605 Hwy. 52 North
Rochester, MN 55901
(507) 253-6949
FAX (507) 253-1438

The challenges facing optoelectronic packaging for fiber-optic computer interconnects will be discussed with emphasis on parallel array implementations.

Photonic Subsystem Design Based on Hybrid Optoelectronic Integration on Silicon Substrates

Craig A. Armiento

GTE Laboratories, 40 Sylvan Road, Waltham, MA 02254
(617) 466-2806

Photonics is envisioned as a means for alleviating some of the performance bottlenecks in present-day electronic systems. Emerging applications include local loop telecommunications (fiber-to-the-home, fiber-to-the curb), computer interconnects (optical backplanes, optical computing) and avionics (fly-by-light, smart skins). These applications have different requirements than long-haul telecommunications, which historically has driven photonic hardware development. Unlike long-haul fiber systems these new systems will require many parallel optical channels each requiring optoelectronic, electronic and optical components. The component density required in such systems invokes new challenges in controlling the cost, reliability and physical size of photonic hardware. These requirements will not be satisfied by using the conventional approach of mounting individually-packaged components (such as lasers, photodetectors, integrated circuits etc.) on a printed circuit board. New approaches to component integration and packaging are required that are capable of accommodating the diverse physical, electrical, thermal and optical characteristics of these devices in a cost-effective and size-effective manner.

This paper reviews a hybrid integration approach called Silicon Waferboard which seeks to break through the cost and size barriers of conventional optoelectronic component technology. This approach uses silicon as a platform for integration of electronic, optoelectronic, and optical components and, as depicted in Figure 1, may ultimately lead towards the development of optical multichip modules (OMCM). A hybrid (rather than monolithic) integration approach allows the choice of components that are best suited to realize a particular subsystem function. Development of an integration approach that is compatible with electronic packaging technology could provide an impetus for incorporation of optoelectronic and optical components in electronic systems. Initial efforts to develop silicon waferboard technology have focused on demonstration of transmitter and receiver arrays which are essential elements for parallel, fiber-based interconnections. These transmitter and receiver arrays are shown on the optical front end of the OMCM depicted in Figure 1.
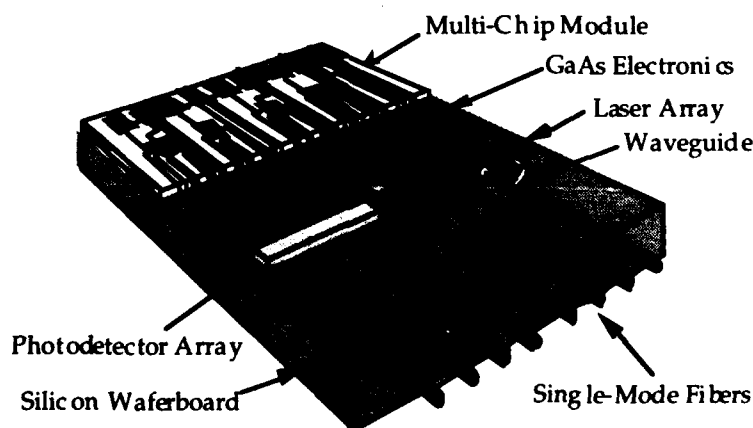

Figure 1. Optical Multichip Module based on hybrid integration on silicon.

The cost of optoelectronic components such as diode lasers is dominated by packaging. Optoelectronic device packaging has typically been accomplished using a labor-intensive, hand-crafted approach. For example, pigtailed diode lasers are assembled by manipulation of an optical fiber with respect to a active (powered) laser to achieve maximum optical coupling. A key feature of the Silicon Waferboard approach that this active alignment procedure is replaced with a passive technique. Passive alignment, which does not require laser powering or fiber manipulation, is realized by precise relative placement of the components on the silicon waferboard. This precision is accomplished through the use of mechanical alignment features that are fabricated on the surface of a silicon waferboard and on the component chips.

The approach used for passive alignment of a laser array and single mode optical fibers on is shown in Figure 2. A four-element, individually-addressable laser array is flip-chip bonded (active-layer-down) onto a solder metallization on the waferboard surface. Accurate ($\pm$ 1 μm) placement of the laser array is achieved through the use of three alignment pedestals and two standoffs fabricated on the waferboard surface. The 1.3 μm InGaAsP/InP laser array, based on a ridge waveguide structure, has a laser-to-laser spacing of 350 μm and threshold currents of 22 $\pm$ 1 mA across the array. The laser array is fabricated with a notched edge that is mated with a side alignment pedestal to control the positions of the four lasers in the y direction. The two front alignment pedestals are used to position the array in the x direction. The height of the four emitting regions above the waferboard surface (z direction) is controlled by the standoff thickness and laser dimensions and is designed to coincide with the location of the fiber cores (controlled by the v-groove dimensions). This approach has been used to achieve the first demonstration of passive optical coupling between lasers and single mode fibers.[1] Coupling efficiencies of 8% have been achieved which compare favorably with efficiencies obtained with actively-aligned, butt-coupled single mode fibers.
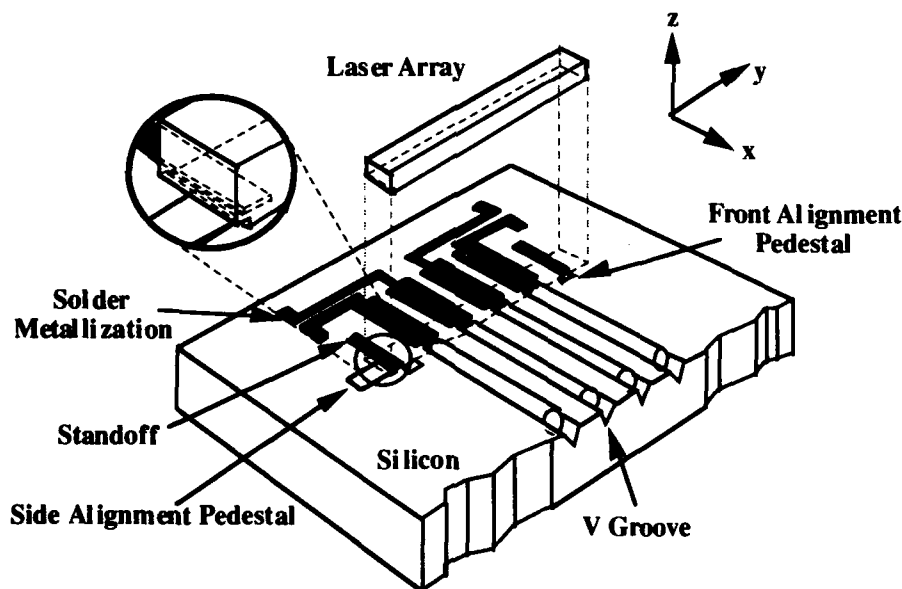

Figure 2. Waferboard design for passive laser/fiber array alignment

Development of a four-channel transmitter array required the addition of electronic driver circuits to provide the bias and modulated drive currents to the individual lasers.[2] The transmitter array waferboard was designed to accommodate a laser array, GaAs driver array IC and four single-mode optical fibers. The transmitter array waferboard design uses a single metallization layer to route power and ground. The driver array chip was based on GaAs MESFET process and consisted of four circuits laid out on 350-μm centers. Wire bonds, which were kept to less than 1 mm in length in critical high-speed sections of the transmitter array, were used to provide

interconnections between the various components. A SEM photomicrograph of a portion of a completed transmitter array is shown in Figure 3. A package was developed to house the array which utilizes four SMA connectors and controlled-impedance striplines to provide high-speed connections to the input pads of the laser driver array. A thermoelectric cooler was bonded directly to the silicon waferboard for efficient heat sinking and temperature control of the laser array. All of the four channels could be toggled with a voltage of 0.8 V and operated at data rates of 1 Gb/s. Figure 4 shows an eye diagram of a transmitter channel operating at 1.1 Gb/s. Preliminary crosstalk measurements, which were made by monitoring the light output from a single unmodulated channel (laser biased at threshold) with a high-speed photodetector, show crosstalk between adjacent transmitters at 1 GHz to be –29 dB.
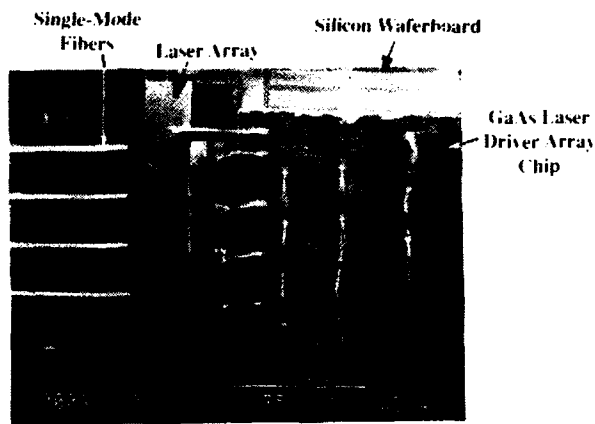
Figure 3.   Photomicrograph of a four-channel array on silicon waferboard
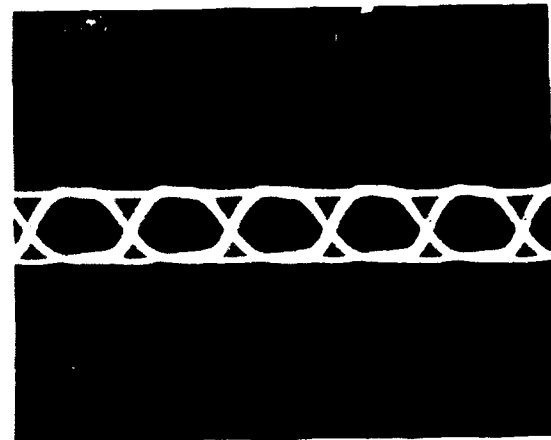
Figure 4.   Eye diagram of one channel on transmitter array operating at 1.1 Gb/s.

Silicon Waferboard technology has been demonstrated as an approach for hybrid integration of components required in optical subsystems. Passive alignment of lasers and single-mode fibers has been demonstrated for the first time, with coupling efficiencies approaching those achieved with active alignment. The incorporation of arrays of electronic components provides the electronic functionality required for many high-speed systems, as demonstrated by the development of transmitter arrays operating at Gb/s data rates. Although not described here, receiver arrays have also been realized using a waferboard approach.[3] Silicon Waferboard offers the potential for realization of low-cost, high-density optical subsystems that are particularly attractive for short-haul, highly parallel applications.

References:

1.   "Passive Coupling of an InGaAsP/InP Laser Array and Single Mode Fibers Using Silicon Waferboard", C.A. Armiento, M. Tabasky, C. Jagannath, T. Fitzgerald, C.L. Shieh, V. Barry, M. Rothman, A. Negri, P.O. Haugsjaa, and H. Lockwood, Elect. Lett. 27, No. 12, 1109 (1991)

2.   Gigabit Transmitter Array Modules on Silicon Waferboard", C.A. Armiento, A.J. Negri, M.J. Tabasky, R.A. Boudreau, M.A. Rothman, T.W. Fitzgerald, and P.O. Haugsjaa, to be published in December issue of IEEE Transactions on Components, Hybrids and Manufacturing , (1992)

3.   "Four Channel Hybrid Receiver Utilizing a Silicon Substrate For Packaging," M.J. Tabasky, J. Chirravuri, A.N.M.M. Choudhury, A.J. Budman, P.O. Haugsjaa, and A.J. Negri, SPIE Conference No. 1582, pp. 152–157, 1992.

Design and fabrication/packaging of low-loss passive optical devices

Hirochika Nakajima
Communication & Space Division
Fujitsu Laboratories Ltd.
1015 Kamikodanaka, Nakahara-Ku
Kawasaki 211, Japan

Low-loss microoptic/guide-wave passive optical devices, such as magneto-optical switch, in-line isolator, LN switch/modulator, and polymeric spot-size converter etc., are reviewed accompanied with design and fabrication/packaging methods.

Packaging Techniques for
Guided Wave Optical Systems

OWD 3:30pm-5:00pm
Oleander Room

Joseph W. Goodman, *Presider*
Stanford University

NEW PACKAGING TECHNOLOGY

Current packaging technology has been developed for long distance telecommunication systems. Performance is the most important issue for these applications. However, in 1990s, short-haul applications, such as subscriber loops, computer interconnections, become more important. For these applications, cost is the most important issue.

Recently, studies on SMF-LD array modules for computer interconnection have been increased. Some of these uses active alignment techniques [5,6], however, there are some reports proposing novel passive alignment techniques [7,8]. From the view point of packaging cost, active alignment has disadvantage because of time for alignment and necessary worker's skill. Though automated manufacturing system can be a solution to this problem, passive alignment seems more attractive. Passive alignment techniques can minimize module size, and may open the way to hybrid integration of optical devices.

REFERENCES

[1] H.Kuwahara et al, Appl. Opt.19,2578-2583(1980)
[2] M.Saruwatari et al,IEEE J.Quantum Electron.,17,1021-1027(1981)
[3] H.Honmou et al,Nat.conv.Rec.of IECE Jpn. C-454(1988) (in Japanese)
[4] H.Onaka et al,Nat.conv.Rec.of IECE Jpn. C-541(1989) (in Japanese)
[5] A.Takai et al,IEICE Tech. Rep. OCS92-30(1992) (in Japanese)
[6] K.Moriya et al,Nat.conv.Rec.of IECE Jpn. C-269(1992) (in Japanese)
[7] C.A.Armiento et al, Electron.Lett.,27,1109-1111(1991)
[8] M.S.Cohen et al, IEEE Trans.Photo.Tech.Lett.,3,985-987(1991)

Holographic Optical Module Integrated with Chip Elements for Optical Disk Pickups

Yuzo Ono

Opto-Electronics Research Laboratories, NEC Corporation
1-1, Miyazaki 4-chome, Miyamae-ku, Kawasaki 216, Japan
Phone:+81-44-856-2106

Optical disk memories, especially CD-ROMs, have begun to be equipped commonly in desk-top personal computers as a key device for mass memories in the recent multimedia circumstances. A demand for equipping them into notebook PCs will be a matter before long. To use in notebook PCs by reducing their optical pickup thickness, the authors have already developed an optical pickup integrated with bear laser diode and photodiode chips and a holographic optical element[1].

This paper will discuss optical design, packaging and assembly for the pickup developed. A new concept thin optical pickup, utilizing a photodiode substrate as an opto-base on which chip optical elements are hybrid-integrated, and applying flip-chip bonding technique for the substrate packaging[2], will also be previewed. The following three features will be emphasized.

1. Structural design: Conventional optical pickups have difficulties twofold for thin design. First, they have two-floor construction consisting of an opto-base on which an objective lens actuator is mounted. Secondly, package size for a laser diode and a photodiode has prevented to make the opto-base thin. To conquer these problems, a micro optical module integrated with chip optical elements has been developed. In the optical pickup design, the module is put into the actuator to make the structure one-floor.

2. Optical design: An HOE is used to reduce optical element number. Other elements except the HOE are assembled within ordinary mechanical accuracy and adjustment is done only for the HOE at the final stage of assembly. Optics was optimized to maximize the assembly tolerances. For this purpose, a very small negative lens power is given to the HOE. This results in increase in the position tolerance of HOE in the direction of its optical axis and decrease in the offset magnitude in the focusing error signal due to chromatic aberration of the HOE. In the final adjustment, the offset magnitudes in focusing and tracking error signals are made null by adjusting the HOE position in its plane and also the offset magnitude in the focusing error signal due to position error in the other element assembly is compensated by rotating the HOE around its optical axis.

3. Packaging: To make the pickup thinner and make its assembly easier, the flip-chip bonding is used for electrical connection between the package and the photodiode. On the photodiode substrate, a laser diode with a heat sink and a micro prism for beam reflecting, with a beam splitter function for the laser diode output monitoring, are hybrid-integrated, and a preamplifier chip for readout signal is also mounted using a flip-chip bonding.

References
1) R. Katayama, T. Nagano, S. Sugama and Y. Ono, "Compact Optical Head Integrated with Chip Elements for CD-ROM Drives," *Proc. of Optical Data Storage Topical Meeting, San Jose, CA., 1992*, Proc. SPIE **1663**, 37-45 (1992).
2) T. Nagano, R. Katayama and Y. Ono, will be presented at Joint Int. Symp. on Optical Memory and Optical Data Storage 1993, July 5-9, 1993, Maui, Hawaii.

Modeling and Design of Integrated Micro-optical Systems

Jürgen Jahns

AT&T Bell Laboratories
Rm. 4G-524
101 Crawfords Corner Road
Holmdel, NJ 07733
Tel.: 908-949-4093

The use of lithographic fabrication techniques offers the potential to build compact, robust and alignment-free micro-optic systems. In the planar optics approach [1], micro-optical elements are etched on the surfaces of an optical substrate at well-defined postions. Light bounces between the two surfaces of the substrate along a zigzag path. The light interacts with a lens or a beamsplitter or simply a mirror at every surface along its path. Lenses and beamsplitters can be implemented either as refractive or diffractive micro-optical elements. An optical system may comprise both types of elements for optimized performance.

One potential application of planar optics are parallel interconnections between VLSI chips. For an interconnection scheme, several design goals must be achieved such as a high interconnection density and the possibility for implementing arbitrary interconnections. For planar optical interconnects, the particular zigzag propagation imposes geometrical constraints that require special designs of the lenses and limit the system performance. We consider three generic optical systems to implement parallel interconnections: (1) a conventional imaging system using a pair (or triplet) of large lenses, (2) a system based on microlens arrays, and (3) a hybrid imaging system [2] that combines (1) and (2). System (1) yields a high interconnection density and (2) a large amount of flexibility. The hybrid system is attractive in particular for a planar optical implementation. By combining refractive and diffractive optical elements and by splitting the imaging task in a favorable way, it is possible to optimize the system performance. For the analysis and the design of the optical system, simulation models based on raytracing and Gaussian beam propagation are used.

[1] Jahns, J. and Huang, A., "Planar integration of free-space optical components," *Appl. Opt.* **28** (1989) 1602-1605.
[2] Lohmann, A. W., "Image formation of dilute arrays for optical information processing," *Opt. Comm.* **86** (1991) 365-370.

KEY TO AUTHORS, PRESIDERS AND PAPERS

Abe, Yuji — OWD1
Abushagar, Mustafa A. G. — OTuA10
Aharoni, A. — OTuA7, OTuA15
Amitai, Y. — OTuA7, OTuA14, OTuA15
Aritake, Hirokazu — OTuA18
Armiento, Craig A. — OWC2

Battiato, James M. — OTuA1
Beckman, Martin G. — OWA14
Beech, Russell S. — OWA13
Behrmann, Gregory P. — OTuA9
Bernacki, Bruce E.- OWA1
Blair, P. — OTuA2
Brenner, K.-H. — OWA3

Campbell, Gene — OTuA1
Chipman, Russell A. — OWA5, OWA6
Clark, Peter — OMA2
Cloonan, Thomas J. — OWA14
Cote, Jasmin — OWA7

Deri, Robert J. — OTuC2, ITuC5
Di Pasquale, F. — OWA10
Dixit, S. N. — OTuA16, OTuA17
Dorsch, Rainer G. — OTuA5

Fabricius, Norbert — OMC2
Farn, Michael W. — OTuA12
Forbes, G. W. — OMB2

Ghosh, Anjan K. — OWA13
Goodman, Joseph W. — OTuA7, OTuA15,
   OWD

Haggans, Charles W. — OTuA1
Haruna, M. — OMD2
Herzig, H. P. — OTuA11
Hesselink, Lambertus — OMB1, OTuD1
Heydenburg, T. — OMA3
Hinterlong, Stephen J. — OWA14
Hinton, H. S. — OMD3
Houde-Walter, Susan N. — OTuC, OWA9

Ih, Charles S. — OTuA4

Jackson, Kenneth P. — OWC1
Jahns, Jurgen — OWD3
Jakubczyk, Zdzislaw J. — OMC, OWA11
Johnson, Eric G. — OTuA10, OTuA13

Kathman, Alan D. — OTuA10, OTuA13
Kato, Masayuki — OTuA18
Knoesen, Andre — OTuA6
Kokubun, Yasuo — OMC3
Kostuk, Raymond K. — OTuA1
Kurdi, Bulent Nihat — OWC

Lawrence, George N. — OMB3
Lawson, J. K. — OTuA16, OTuA17
Leger, J. R. — OMA1
Lohmann, Adolf W. — OTuA5
Londono, Carmina — OMA2

Manes, K. — OTuA16
Mansuripur, M. — OWA1
McClain, Stephen C. — OWA5
Morgan, A. — OTuA17
Morris, G. Michael — OMA, OTuC1, OWA8
Morrison, Rick L. — OWA14

Nakajima, Hirochika — OWC3
Nakashima, Masato — OTuA18
Noll, Robert J. — OTuA3
Norte, A. D. — OWA15
Norton, Scott M.- OWA8
Nugent, K. A. — OTuA16

O'Shea, Donald C. — OTuA8
O'Toole, Michael M. — OWA2
Ono, Yuzo — OWD2

Pellegrino, John M. — OWA12
Pezzaniti, J. Larry — OWA6
Plummer, William T. — OMA2
Powell, H. T. — OTuA16, OTuA17
Presby, Herman M. — OMD1

Raguin, Daniel H. — OWA8
Robertson, B. — OTuA2

Sadler, Brian M. — OWA12
Sasian, Jose M. — OWA14
Scott, M. L. — OTuA13
Selleri, S. — OWA10
Shieh, W. — OWA15
Sidick, Erkin — OTuA6
Sinclair, Douglas C. — OTuA
Sinzinger, Stefan — OTuA5, OWA3
Smith, R. E. — OWA9
Southwell, William H. — OWA4
Spick, T. — OWA3
Suleski, Thomas J. — OTuA8
Szapiel, Stanislaw — OWA7

Taghizadeh, M. R. — OTuA2
Tanquay, Jr., A. R. — OWA15
Tayag, Tristan J. — OWA12
Testorf, M. — OWA3
Thomas, I. M. — OTuA17
Tian, Rongsheng — OTuA4
Tomlinson, W. J. — OWA
Turunen, J. — OTuA2

Weible, K. J. — OTuA11
Weller-Brophy, Laura A. — OMD, OTuD
Willner, A. E. — OWA15
Wojcik, Michael J. — OWA14
Woods, B. W. — OTuA17

Xia, Xiaoqing — OTuA4

Young, Terry P. — OMC1

Zavislan, James M. — OMB
Zhou, Haixian — OTuA4
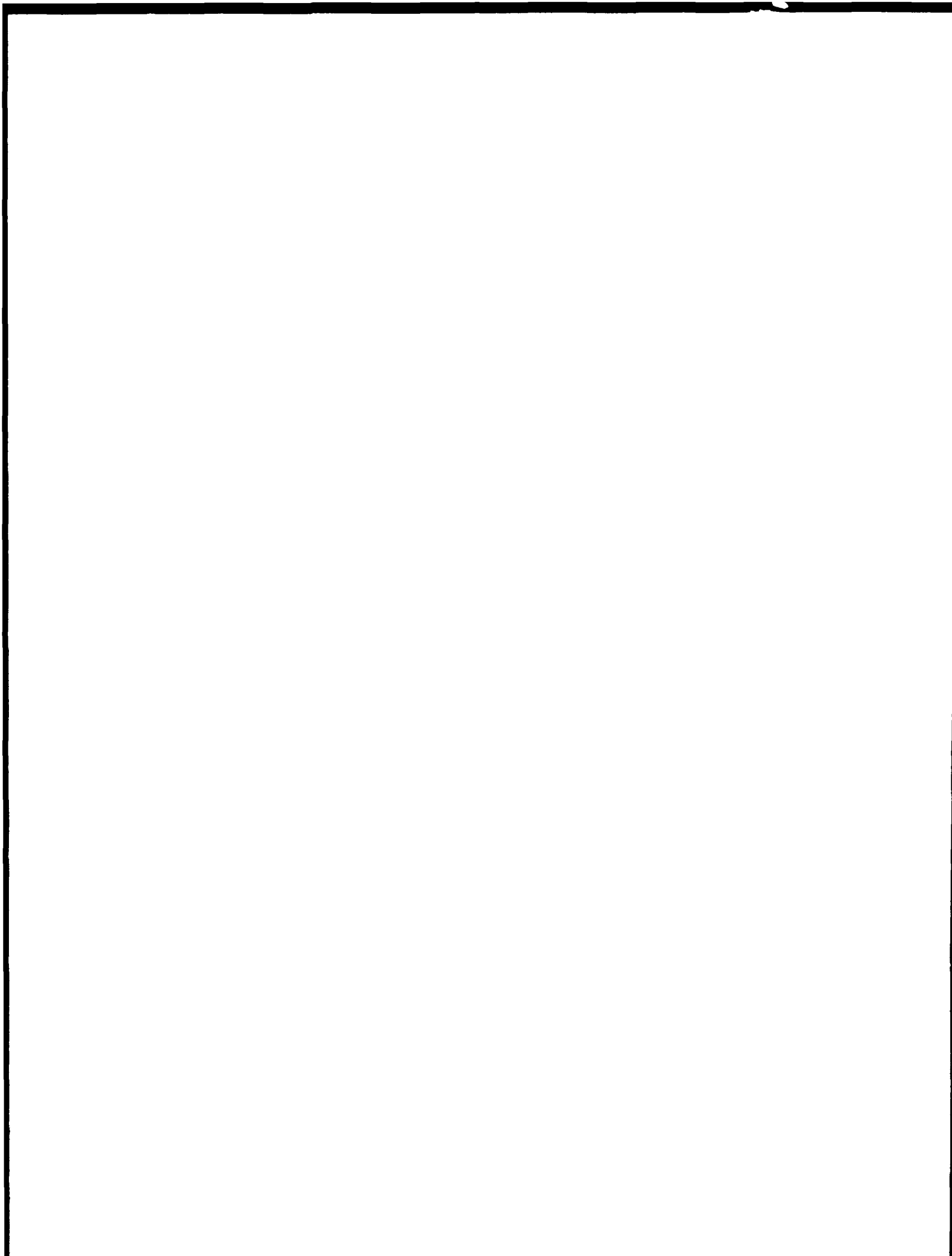Zoboli, M. — OWA10
Zweig, David A.- OMA3

OPTICAL DESIGN FOR PHOTONICS

POSTDEADLINE PAPERS

MARCH 22–24, 1993
PALM SPRINGS,
CALIFORNIA

OPTICAL DESIGN FOR PHOTONICS
POSTDEADLINE PAPERS

OPTICAL DESIGN ISSUES FOR SOFT-X-RAY PROJECTION LITHOGRAPHY

W.C. Sweatt, D.A. Tichenor, G.D. Kubiak,
W.W. Chow, P.D. Rockett, and R.E. Olson
Sandia National Laboratories

T.E. Jewell
Consultant

O.R. Wood Jr, D.L. Windt, J.E. Bjorkholm
M.D. Himel, and A.A. MacDowell
AT&T Bell Laboratories

ABSTRACT: A projection lithography tool is being developed to make 100-nm features using 14-nm radiation. Multilayer coatings allow near-normal reflections in this large-field, diffraction-limited system.

SUMMARY: Sandia and AT&T are jointly developing a projection lithography tool that will make microchips with 100-nm features. It images a reflective mask onto photoresist using 14-nm photons from a laser plasma source. Our systems are all-reflective, using multilayer coatings which have reflectivities up to 63%. We are now performing imaging experiments and photoresist studies with a very simple lithographic camera. It consists of two spherical mirrors, and has a magnification of 10x. The resolution is good over a small field, and we regularly make 100-nm features.

A 5x lithographic camera for the manufacture of large wafers is under development; it creates a 25-mm-long ring-field image that can be scanned across the chip. The camera's numerical aperture is only $n.a. = 0.08$, so the camera will have to be nearly diffraction-limited to give 100-nm resolution. This image quality requires mild aspheric surfaces in the camera and a cumulative wavefront error <1 nm rms.

The brightness of the laser plasma source is being maximized. If the plasma ball is small, ~150 μm, the condenser should be able to collect and relay >10% of the light from the source to the camera. In addition, the illumination along the length of the ring field must be uniform to within 1%, and the system must provide a reasonable degree of partial coherence. We have an optical design that appears to meet these goals.

This system requires optical fabrication and metrology beyond the state of the art; we are vigorously pursuing both areas. Multilayer coatings are another major research thrust. Many of the coatings in our 5x camera need to be tapered to accommodate variations in the angle of incidence. In the 5x condenser, tapered coatings need to be applied to steeply curved aspheric surfaces.

Correspond with: W. C. Sweatt,   Dept. 9225,   (505) 845-8566
              Sandia National Laboratories,   FAX 844-8711
              Albuquerque, NM 87185-5800

Simulat'on of Highly Multimode Star Couplers in Polymers

Igor Ilić, Robert Scarmozzino, and Richard M. Osgood, Jr.

Microelectronics Sciences Laboratory

Columbia University

New York, NY 10027

Phone: (212) 854-8980

Fax: (212) 932-9421

James T. Yardley, Karl W. Beeson, Michael J. McFarland

AlliedSignal

Research & Technology

Morristown, NJ 07962

Introduction

Optical star couplers are widely used in lightwave local-area networks for even distribution of signals among several users. Configuration of a star coupler consists of an input and output array of waveguides connected by a wide slab waveguide. Star couplers with single-mode waveguiding arrays are widely used and studied.[1,2,3,4] However, due to limitations of multimode waveguiding in communication networks,[5] multimode star couplers have been persistently neglected. Multimode star couplers are important for lightwave division in local subscriber systems for distributive services, star-based local area networks,[6] and high-power splitting. In addition, multimode star couplers can be readily fabricated in polymers with the aid of various processing techniques.[7]

In this paper we present the first numerical study of multimode star couplers suitable for fabrication in polymer materials. Two arrays of multimode channel waveguides separated by a wide interaction region make the basic structure of the device. We have examined operational characteristics including intensity profiles as a function of device geometry, refractive index difference (or numerical aperture) and input profile. These calculations form the basis for constructing effective polymer waveguide devices and they extend the viability of finite difference beam propagation computational techniques into the realm of multimode structures.

Method

The analysis of the devices was performed by utilizing the finite-difference beam propagation technique as described in Ref. 8, with boundary conditions described in Ref. 9. To perform the simulations, we define multimode star coupler structures in a layout with N input and output waveguides having a symmetric step-index profile of width W. They are connected by an interaction region which is a waveguide of width N·W; input and output waveguides enter that region at various angles. Through the effective index method, channel waveguiding structures are represented in the simulation as slab waveguides. We launch a field distribution into one of the waveguides in the input array. The launched field distribution is comprised of a sum of all the modes supported by the input waveguide. The total signal power is equally split among the modes and the initial phase is chosen randomly. These conditions simulate the lightwave output of the previous device serving as a source for the star coupler, as each mode propagates with different characteristic phase velocity.

The beam is propagated along the structure as described in Ref. 8. The field distribution in the input waveguide, the interaction region, and the output waveguides is observed and the field intensity determined at the end of each output waveguide. Note that the resulting power distribution should ideally be uniform across the output array. Finally, the influence of several different parameters of device geometry, as well as the refractive index difference of the material, on the uniformity of the output intensity distribution is investigated.

Results

Our simulation considers the operation of a multimode star coupler made in polymer material on a PMMA substrate. The widths of the waveguides in the arrays were varied between 50 and 200 μm and their refractive index was varied in the range from 1.50 - 1.581. The device was simulated for the wavelength of λ=838 nm. The behavior of the device was studied as a function of the length of the interaction region for different number of modes supported by the input waveguide, keeping all other parameters fixed.

The number of modes was varied between 30 and 120 by first selecting different width of the input waveguides with the refractive index difference fixed and later changing the index difference with the width fixed. While in the most of the parametric studies, we examined the simplest case of the 2x2 star coupler first, in orde_r to gain better understanding of the fundamental dependencies, our subsequent work considered 4x4 star couplers as well.

Figure 1 shows the computed field distribution in a 60-mode 4x4 star coupler. Note that the high spatial frequency present in the field distribution represent the large number of modes and their differing propagation velocities and random phases. The lightwave signal is launched in the left outermost input waveguide and it spreads in the structure establishing a particular field intensity profile in all the four output waveguides. The relation between the power in output waveguides and length of the interaction region shown in Fig. 2 exhibits two different types of behavior, as seen on the graph. The first effect is a decay of power in the input waveguide and a rise of power being transferred into remaining waveguides. Later, power division among output waveguides fluctuates, reaching different values over the limited interval. The length of the interaction region necessary for the first uniform distribution is found to be inversely dependent on the insertion angle of the input waveguide. In addition, the level of fluctuations is observed to become narrower when a larger number of modes is supported by the structure. Thus we can determine the number of modes and required interaction length to achieve a certain level of output uniformity.

Conclusion

We have described the first simulation of the operation of multimode star couplers using beam propagation techniques. By varying several design parameters we obtained uniform power distribution among output waveguides. The required length of the interaction region of the device and the intensity difference among output waveguides can be controlled by adjusting the geometry of the input waveguides and increasing the number of modes supported.

References

1. C. Dragone et al, IEEE Photon. Technol. Lett. 1, 241 (1989)
2. M. Tabiani and M. Kavehrad, J. Lightwave Technol. 9, 448 (1991)
3. K. Okamoto et al, IEEE Photon. Technol. Lett. 4, 1032 (1992)
4. C. Dragone, J. Lightwave Technol. 7, 479 (1989)
5. R. Ulrich and T. Kamiya, J. Opt. Soc. Am. 68, 583 (1978)
6. J. Sharony et al, Proc. of Globecom'92, Orlando, 1301 (1992)
7. K.W. Beeson et al, American Chemical Society, 303 (1991)
8. R. Scarmozzino and R.M. Osgood, Jr, J. Opt. Soc. Am. A 8, 724 (1991)
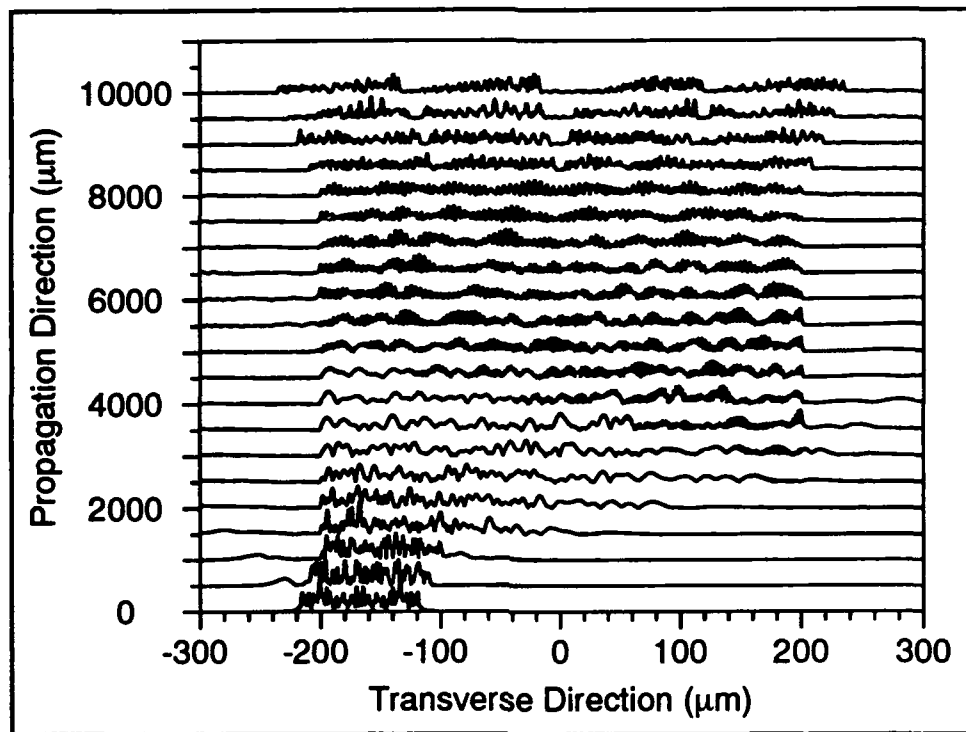9. G.R. Hadley, IEEE J. Quantum Electronics 28, 363 (1992)

Figure 1 Optical wave propagation in 60-mode star coupler.
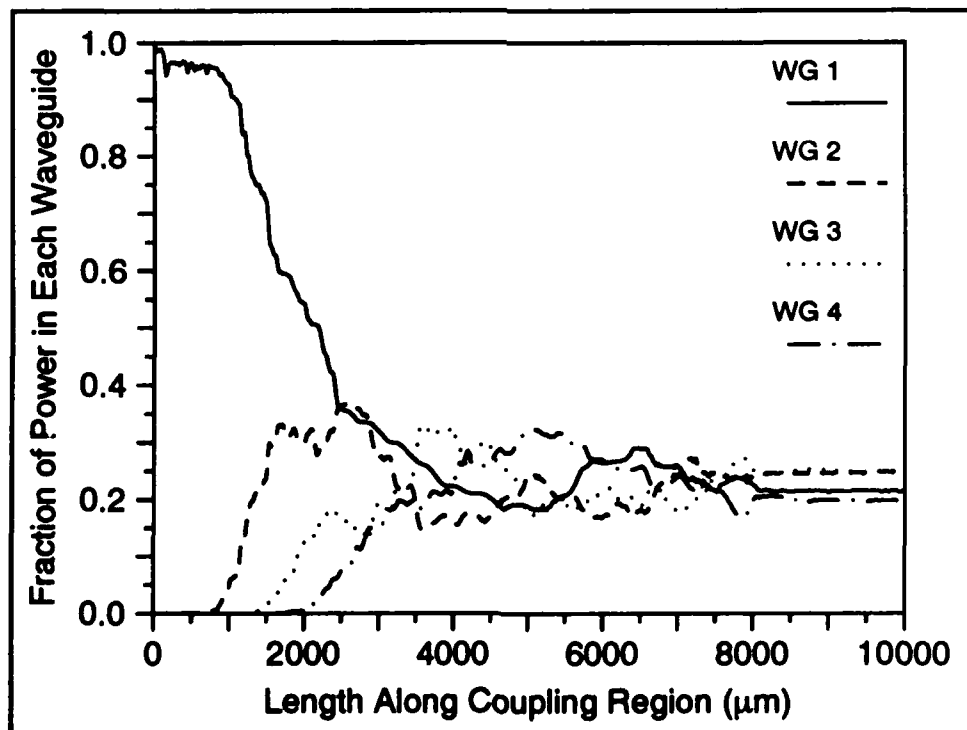

Figure 2 Optical power transfer in 60-mode star coupler.

Finite Difference Beam Propagation Method Modeling for High Power Semiconductor Fanned-Out Amplifier Lasers

Joseph H. Abeles, Robert Amantea, Rafael Rios, and Donald J. Channin

David Sarnoff Research Center
201 Washington Rd.
Princeton, NJ 08543-5300
Tel: (609) 734-2571

High power single-mode semiconductor lasers are needed for applications such as optical computing, sensing, and data writing. But for 10 years, increases in maximum power from single-spatial mode semiconductor lasers had stalled: Narrow-stripe, index-guided, edge-emitting lasers are limited to a few hundred mW by series resistance and propagation loss. A search began for devices exempt from this limit. Semiconductor master oscillator power amplifiers (MOPA's), first published at 77° K by Kosonocky and Cornely in 1968,[1] were revisited[2,3] in 1989. After significant development they are now emerging as practical sources for single-wavelength, single-spatial mode light exceeding 1 watt.

The fanned-out amplifier laser (FOAL) is one MOPA which exploits diffractive spreading of a single spatial mode beam from a narrow-guide DFB-type oscillator (Figure 1). A typical InGaAs/AlGaAs material structure consists of an SCH waveguide and InGaAs QW active layer, and a GaAs grating layer in which corrugations are patterned.[4] As surface-emitters, resonant gratings (~2800 Å period) provide oscillator feedback, while off-resonant gratings (~3050 Å period) out-couple amplifier light at a 14° angle. Alternatively, FOAL edge-emitters have emitted up to 3 W of diffraction limited power.[5]

Unless designed properly, various effects combine to deteriorate single lateral mode shape, which reduces radiance and increases spot size of the emitted beam. As discussed below, material nonuniformity interferes with broad-area amplification. In contrast with a traditional narrow-guide design approach based on modal analysis, we adopt a beam-propagation approach. Our method utilizes a finite difference predictor-corrector approach to stepping rather than Fourier transforms, resulting in faster convergence in the presence of nonlinearities. Physical effects such as diffraction, interference, optical gain, gain saturation, optical nonlinearity, carrier diffusion, and current spreading are included implicitly or explicitly at each step.

Intensity and carrier distributions within a 2 mm long FOAL amplifier at 4.9×10^3 A/cm^2 for perfectly uniform material (Figure 2) show characteristics of strong gain saturation: approximately linear increase of intensity with longitudinal position. The diversion of carriers from spontaneous to stimulated emission is necessary for high efficiency. The accompanying reduction in carrier density is greatest in regions of highest intensity. (Parameters, see Table 1.)

Streaks observed experimentally in the near fields of the FOAL output gratings were initially conjectured to result from localized carrier traps. But simulation indicates they are scattering defects within the guide, based on the great absorption strength (2000 cm^{-1}) required to reproduce them qualitatively.

Figure 1: Schematic of Fanned-Out Amplifier Laser.

Figure 3 shows the comparison between model calculation and experiment.

Antiguiding nonlinearity has the potential to cause filamentation, degrading beam quality. However, simulations in uniform material reveal that for the range of parameters here antiguiding must substantially exceed $R = 2.0$, a value characteristic of quantum well material, for a filament to form (Figure 4).

Investigation of random refractive index nonuniformity for $R = 2.0$ reveals that filamentary behavior is highly sensitive to the RMS amplitude. The correlation length of simulated nonuniformities was taken as 10 μm, based on measurements by laser interferometry of thickness fluctuations. For $\Delta n_{RMS} = 0.00012$, which corresponds to tiny thickness variations of less than 10 Å for a typical 3000 Å thick waveguide, the near-field on the left of Figure 5 is relatively uniform. However, for $\Delta n_{RMS} = 0.00120$, strong filamentary behavior is observed. Optical tests were performed to compare this novel aspect of material quality among numerous OMCVD reactors and institutions. They reveal substantial variation in uniformity, suggesting the extreme importance of obtaining the highest quality material for FOAL devices.

Table 1: FOAL Beam Propagation Parameters for 1 mm length device at low-to-moderate drive currents. (case BPM.in.p16)

Wavelength (λ)	0.94 μm
Amp. Input power (P_{in})	50 mW
Fan-out angle (θ)	2°
Loss (α)	5 cm^{-1}
Refractive index (n_r)	3.4
Index guide (Δn)	0.01
Gain coefficient (g_0)	1 × 10^{-16} cm^2
Transparency density (n_0)	1.8 × 10^{18} cm^{-3}
Antiguiding factor (R)	2.0
Carrier recomb time (τ)	5.0 nsec
Carrier recomb coeff (B)	2.6 × 10^{-11} cm^2/sec
Carrier diffusion coeff (D)	10 cm^2/sec

Other subjects to be addressed include simulation of highest power structures and multimode gain properties explained by model.
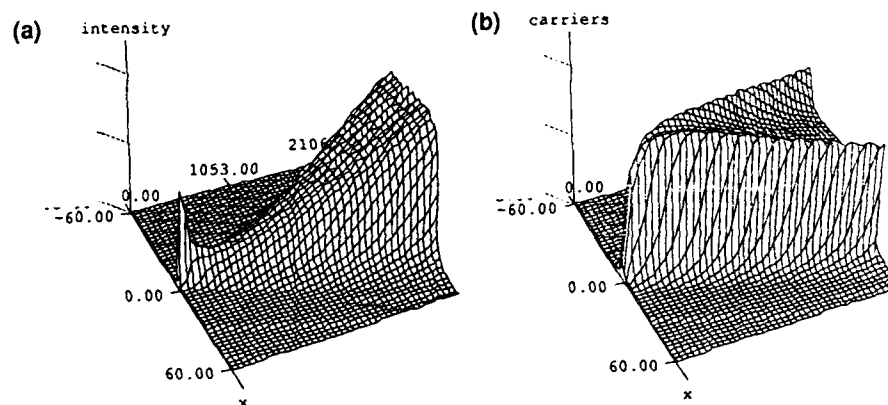
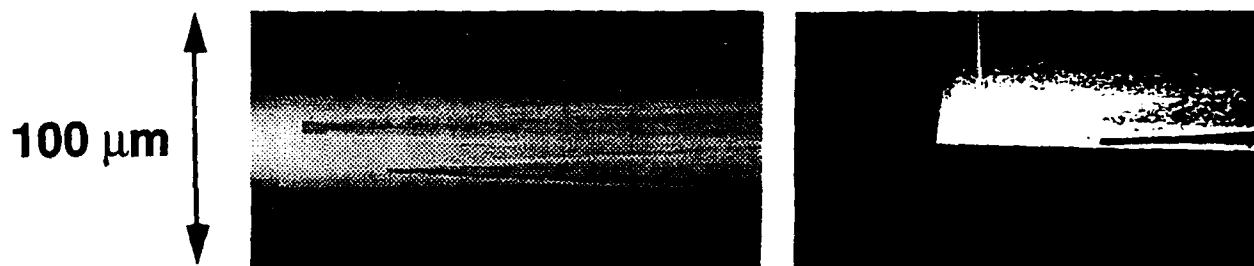Figure 2: Simulation of FOAL (ideal uniformity). (a) Intensity and (b) carrier distributions.

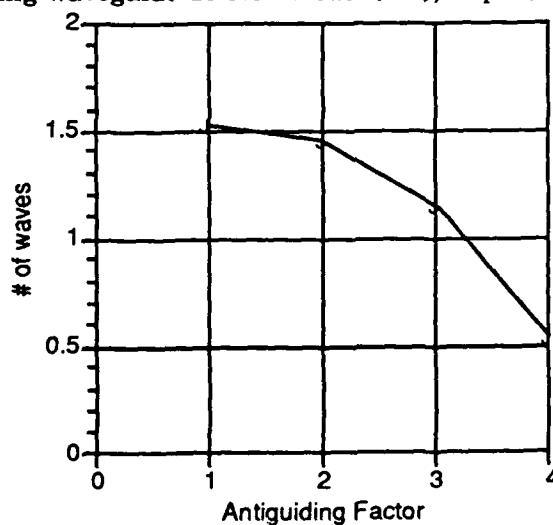Figure 3: Strongly-absorbing waveguide defect: Model (left); Expt. (right).

Figure 4: Number of waves of phase front curvature vs. antiguiding factor R. Phase front curvature arises from circular expansion of wave front is measured from $1/e^2$ power points.
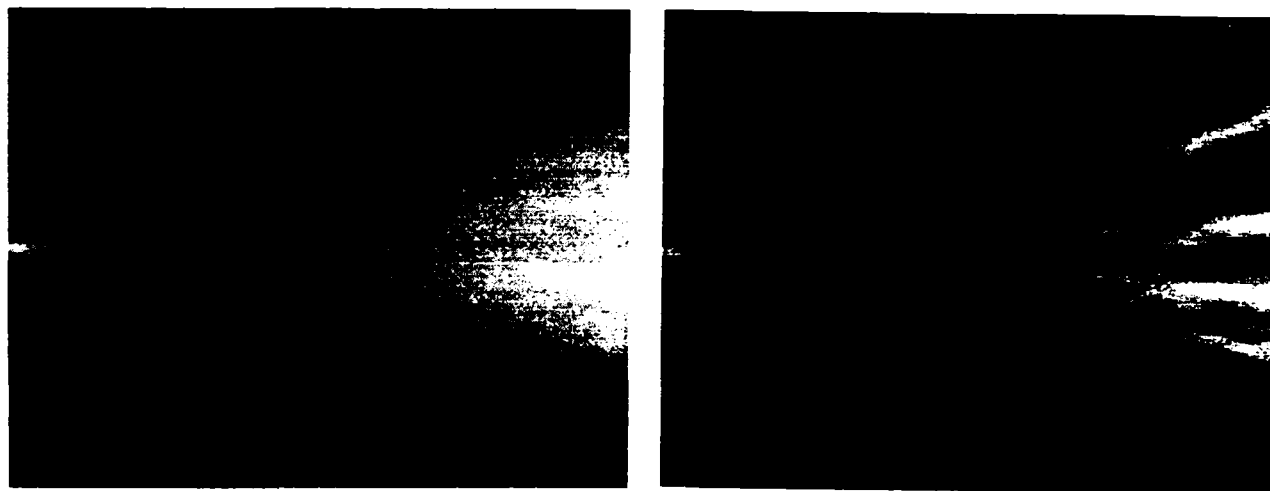
Figure 5: Calculated near fields for material having $\Delta n_{RMS} = 0.00012$ (left) and 0.00120 (right).

ACKNOWLEDGEMENTS

REFERENCES

[1] W. F. Kosonocky and R. H. Cornely, *GaAs Laser Amplifiers*, IEEE Journal of Quantum Electronics QE-4, 125 (1968).

[2] N. W. Carlson, J. H. Abeles, D. P. Bour, S. K. Liew, W. F. Reichert, P. S. D. Lin, and A. S. Gozdz, *Demonstration of a Monolithic, Grating-Surface-Emitting Laser Master Oscillator-Cascaded Power Amplifier Array*, Photonics Technology Letts. 2, 708 (1990).

[3] D. F. Welch, D. Mehuys, R. Parke, R. Waarts, D. Scifres, and W. Streifer, *Coherent Operation of Monolithically Integrated Master Oscillator Amplifiers*, Electronics Letters 26, 1327 (1990).

[4] J. H. Abeles, R. Amantea, N. W. Carlson, J. T. Andrews, P. K. York, W. F. Reichert, J. B. Kirk, N. A. Hughes, S. K. Liew, J. C. Connolly, and G. A. Evans, *Monolithic High Power InGaAs/AlGaAs Grating Surface Emitting Fanned-Out Amplifier Lasers Emitting Monochromatic High-Quality Beams*, IEEE LEOS Annual Meeting (Boston, Nov. 16-19, 1992).

[5] R. Parke, D. F. Welch, D. G. Mehuys, A. Hardy, R. Lang, D. R. Scifres, *One-watt cw diffraction-limited operation of a monolithically integrated master oscillator power amplifier*, SPIE OE/Lase'93, Paper 1850-34 (Los Angeles, 1993).

Design and Characterization of a Novel Fiber Optic Coupling Device for Data Communication Applications

A. J. Heiney, C.-L. Jiang, and W. H. Reysen
AMP Incorporated, Lytel Division
Somerville, NJ 08876

Abstract:

Many of the functions necessary for fiber optic coupling in data link applications have been incorporated into one opto-mechanical device called a lens/receptacle. The lens enables assembly of data links with reduced parts count, simplified assembly, lower cost, and streamlined testing with many performance advantages. The packaging consistent with this lens can accommodate data rates up to 600 Mb/s.

This paper outlines the design of the lens/receptacle while highlighting the performance benefits of the package as a whole. Performance results presented are on pre-production prototypes operating at 125 Mb/s in the long wavelength region centered around 1330 nm.

Introduction:

The availability of inexpensive fiber optic data communication equipment will enable the realization of wide area, shared resource, computer networks. The adoption of the Fiber Distributed Data Interface (FDDI) standard [1], including recent work toward a Low Cost FDDI standard, guides the path to the data communication superhighways of the future. Data link packaging efforts to date [2,3], including so called "low cost" packaging, have concentrated primarily on integrated circuit packaging and consolidation. The trusty "TO" header has been consistently relied upon to house active devices and mate with expensive optical coupling elements such as GRIN lenses and split sleeves. The header has also seen increased integration by housing preamplifier circuits. While this approach is technically sound, it shifts the cost from the drive/receive electronics to the active device mount (ADM).

An approach to manufacturing cost reduction has been taken which involves optical solutions to the ADM problem. The introduction of an integrally molded lens/receptacle element which performs fiber-receiving, light-coupling, and light-bending functions eliminates the need for headers by allowing tight integration of all electronics and active devices on a pre-tested board assembly. The multifunction precision molding further reduces cost by reducing parts count, allowing modular connector assemblies, and improving yield by improving performance. Design and packaging considerations will be described and compared with current data links.

Packaging Comparison:

The construction of the current 16 pin data link is shown in the exploded view of Figure 1. It follows current industry trends in that an electronic assembly and an optical subassembly are separately built and mated. The electronic assembly consists of integrated circuit(s) and passive components mounted on a cofired ceramic substrate. A Kovar subframe is brazed to the bottom of the ceramic for attachment of the case frame. The optical subassembly consists of a stainless steel fiber receptacle which accepts a "TO" lensed assembly. The optoelectronic device is die bonded to a ceramic submount which is attached to, but electrically isolated from, the header. The device and the top of the submount are then wire bonded to the header leads. A sapphire lens cap provides focusing and is welded to the header, hermetically sealing the opto device, as shown in the cross section of Figure 2. The header assembly is then actively aligned into the receptacle and fixed with epoxy. The tested optical subassembly is then mated to the case frame using a clip and the leads are soldered to the board. Finally a lid is attached for bubble tight sealing. A listing of process steps is shown in Table 1. This package provides a very rigid and stable environment for the data link.

TABLE 1: Assembly Operations for Standard and New Design Data Links

Current Design	New Design
▶ Electronics Board Assembly ▶ Case Wall Attach ▶ Attach Submount to Header ▶ Die & Wire Bond Device to Submount ▶ Purge Device & Test ▶ Cap Weld Lens ▶ Active Align to Receptacle & Backfill ▶ Cut & Form Leads ▶ Attach Receptacle to Case ▶ Solder Leads to Board ▶ Lid Attach ▶ Burn-in & Test	▶ Electronics Board Assembly ▶ Die & Wire Bond Device to Board ▶ Purge/Burn-in Board & Test ▶ Attach Fiber Stop to Lens ▶ Attach Lens to Case ▶ Active Align & Backfill

The construction of the new data link is shown in Figs. 3 & 4. The lens/receptacle provides the seat for the fiber and the board while conducting the light to/from the optoelectronic device. The 6 layer printed wiring board is assembled with the same circuit and components as the current design using chip-on-board. The PIN/LED is then die & wire bonded onto special low capacitance/high thermal conductivity traces. With this configuration, the opto device can be purged while the populated board can be simultaneously burned in. The advantages of the complete electrical subassembly are:

- Simpler testing earlier in the integration path;
- Reduced parasitic capacitance leading to higher gain;
- Reduced radiation from long exposed leads;
- Easier gripping for active alignment compared with headers.

The lens/receptacle is then attached to a case and the board is actively aligned in the case. Table 1 shows the large reduction in process steps of the new design. To reduce cost some sacrifices in the specifications had to be made. The fiber receptacle had to be changed from stainless steel to plastic. This turns out to be a relatively small penalty due to the availability of high performance plastics. In moving away from welded metal housings, hermeticity was not feasible. In order to evaluate the elimination of hermeticity of the opto device, extensive 85°C/85% RH testing was performed on bare devices and no degradation was observed. This opened the door for the new design.

Opto-mechanical Design of The Lens/Receptacle:

The key to cost reduction in the new design is the integration of functions into the lens/receptacle. The bore is designed for standard 2.5 mm ferrules. The tolerance on the bore is a total range of 0.3 mil. This range provides adequate resistance to fiber movement within the bore so that optical coupling is not compromised. The outer diameter of the bore nose is designed to match the Japan Industrial Standard (JIS) and Low Cost FDDI (LCF - PMD) specifications for the protrusion between the ears of the SC connector. In this way the lens/receptacle can be used for at least three connector types. A fiber stop must be inserted into the bore to provide repeatable optical spacing. This step is performed before the lens is mated to the case. For repeatable optical spacing of the board (and hence device) to the lens, a shelf was incorporated which runs the width of the board. The board thus rests on the case in the rear and the lens in the front. The shelf portion of the mold was made steel safe so that the optical design could be verified and adjusted after prototype testing. The bore and the first lens surface are molded using the same tightly toleranced core pin. This assures that the optical axis of the lens surface is highly concentric with the bore and eliminates the off axis performance concerns with

using aspheric surfaces. The second lens surface is designed to be smaller in diameter than the first since the beam is expanding inside the lens when travelling from surface 2 to surface 1. The 45° prism for folding the light path is a total internally reflecting surface. This was assured by choosing a material with a relatively high index of refraction. Other criteria for the lens material were high temperature resistance, chemical resistance, resistance to galling and wear, high transmittance at 1.3 μm, and low scattering. None of the traditional optical plastics had adequate temperature resistance so several materials were evaluated before final selection. Finally, an anti-rotation key is molded into the bottom front of the case mating surface for repeatability of assembly.

Optical Design:

A ray tracing program developed in-house was used to design the lens/receptacle. It was realized that there would be a performance penalty in going with this lens right from the start since antireflection coating was not possible on the surface inside the bore. The lens was therefore designed to optimize LED coupling since this parameter had the highest margin for improvement. The on axis coupling was optimized first and then the lateral coupling was evaluated, by simulation and experiment. PIN coupling was experimentally verified to be in the expected range without AR coating, approximately 80%. Losses due to aberrations were verified to be low by using another PIN with larger active area.

The ray tracing program used for this work was derived from a previous model [4] with the addition of a 45° prism and aspheric surfaces. As shown in Figure 5, ray/surface intersection points and direction cosines are calculated for each surface. The ray tracing algorithm follows the flow chart. The program generates 160,000 rays emanating from the LED active area with a Lambertian distribution. Refracted or reflected angle and surface reflection losses are then calculated for each surface progressively. Intersection misses are accounted for at each surface for loss evaluation. The fiber is modeled as a gradient index lens and the guided rays are ratioed to the starting number. Coupled power is then calculated considering the surface reflection losses. The steps are repeated for each off axis position of the LED to obtain the lateral coupling curves.

The optical model and experimental results are in very good agreement. The geometry for measurements of the LED is shown in the schematic ray path diagram of Figure 6. Dimension Z is the distance from the board stop shelf to the substrate surface that the LED is bonded to. Dimension X shows the lateral displacements that the device is subjected to for off axis coupling analysis. A 62.5 μm fiber is placed into the lens/receptacle and the device is scanned using a one micron precision micropositioner. Figure 7 shows the coupling schematic

for the PIN in a receiver. The on axis coupling variation with Z is shown in Figure 8. The zero Z point corresponds to the seating of an LED mounted substrate to the initial lens shelf. The curve peaks at Z = 200 μm for both the calculated and measured curves. However, the lateral coupling curves in Figure 9 show that for any non-zero X value both the calculated and measured coupling is greater for the Z = 150 μm curve. This dimension will give the most resistance to lateral offset in either the opto device or the fiber ferrule in the bore. This latitude is useful when actively aligning LEDs during final package assembly. The tolerance to X movement of the PIN detector is greater than for the LED. This is due to the fact that the reduced capacitance afforded by having the PIN on the board was partially traded for a larger active diameter. A similar tradeoff may also be able to make for the LED since the edge speeds obtained are faster in the new design - see the performance comparison summary in Table 2. Ultimately, opto device placement accuracy can be improved and the lateral width of the optical coupling can be widened to the point where no active alignment is necessary and the board and lens can be snapped into place in the case. Right now the LED coupling limits are ± 40 μm for all tolerances.

TABLE 2: Comparison of Data Link Performance

Performance Property	Units	Device Type	Standard Data Link	New Design Data Link
Effective Capacitance	pf	PIN	1.6	1.1
Rise/Fall Time	ns	LED	1.7/1.8	1.4/1.7
Spectral Width	nm	LED	148	140
Fiber Coupled Power *	dBm	LED	-15.5	-14.8
Coupling Efficiency	%	PIN	90	80 **
Relative Cost	-	Rx & Tx	1.0	.55
- Material	% of total	Rx & Tx	55	75
- Labor	% of total	Rx & Tx	45	25

* - Ambient reading; less than ±0.5 dB variation 0 - 70°C
** - Below Standard due to lack of antireflection coating

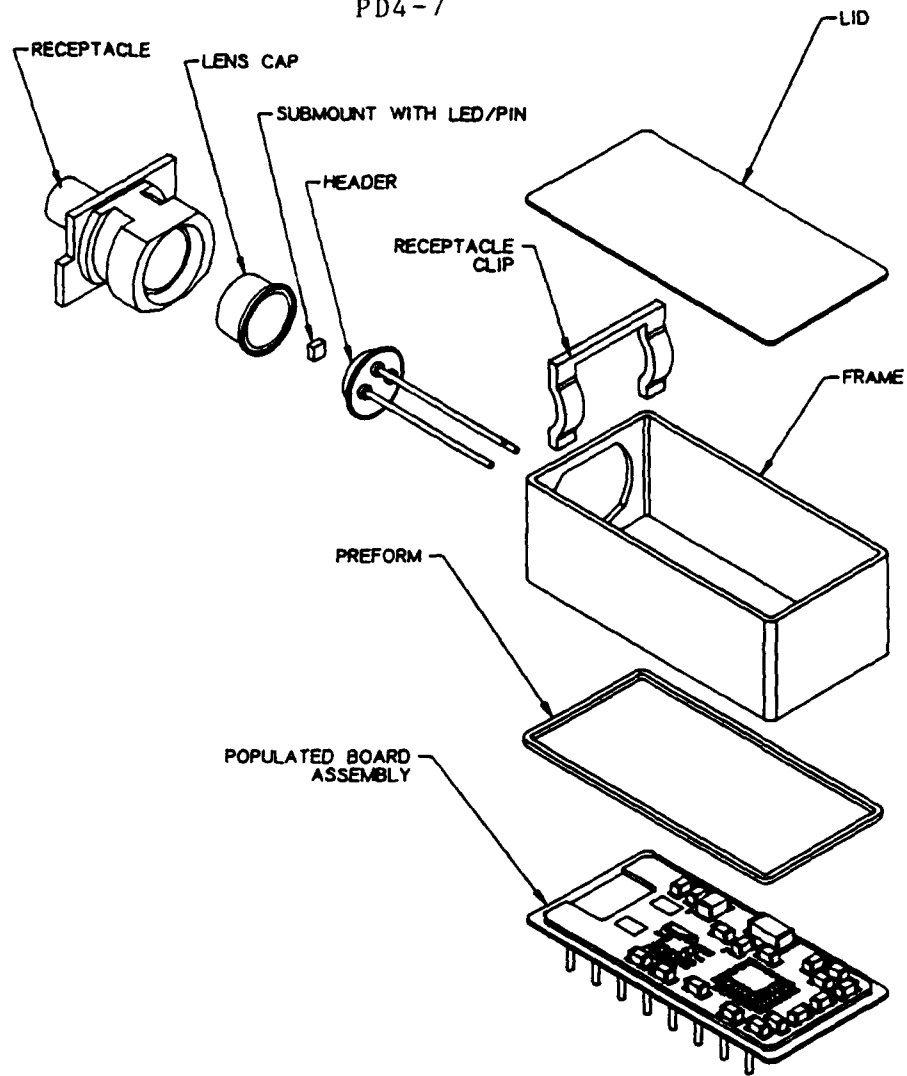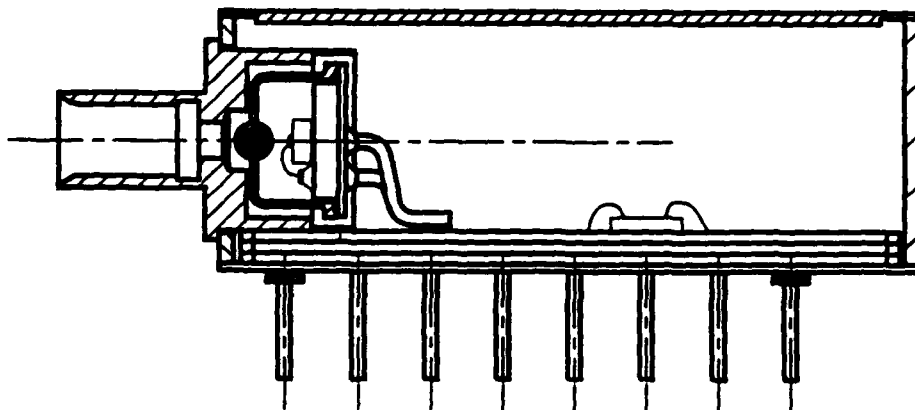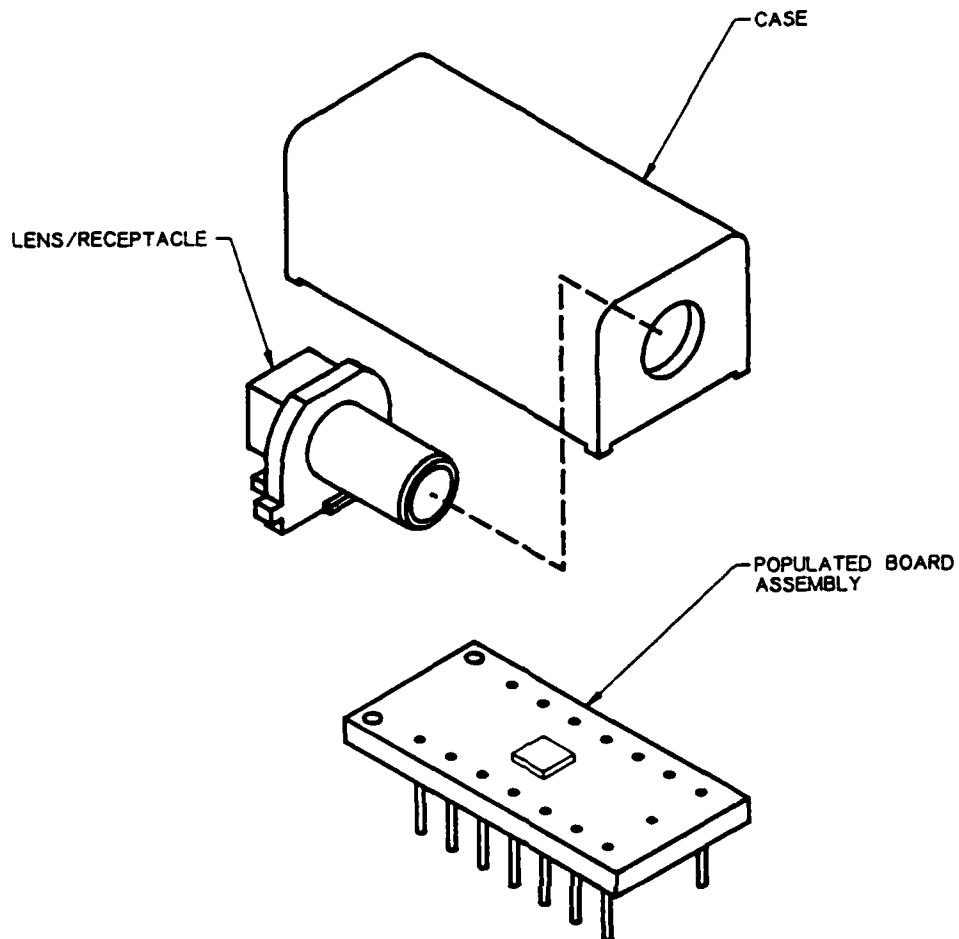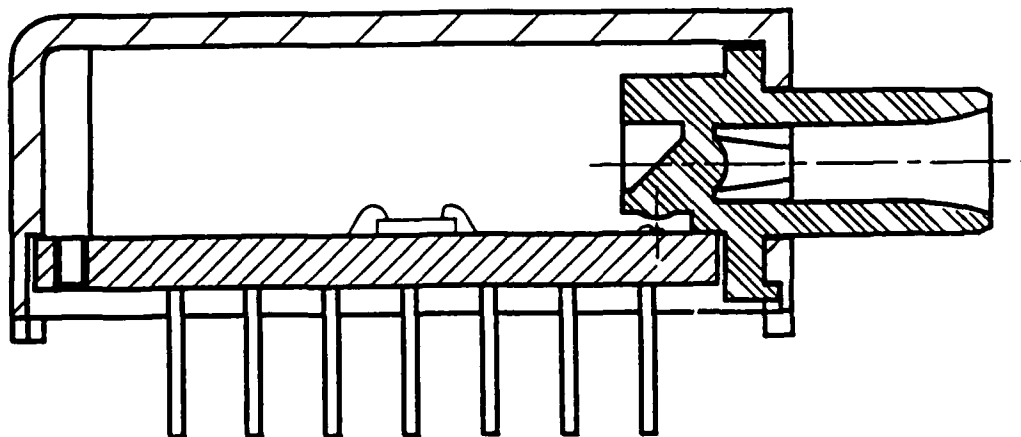## Conclusions:

It has been demonstrated that a new version of our standard data link can be built with fewer parts and less labor content while at the same time improving performance in many areas. These performance improvements are summarized in Table 2. Preamp input capacitance has been reduced which can be used to improve sensitivity through increased gain or to increase active area for increased lateral optical coupling tolerance. Edge speeds have been *improved while staying within the same overshoot guidelines as the standard* product. Spectral width has been reduced at room temperature which increases center wavelength tolerance, improving yields for compliance with FDDI standards. More importantly, since the electrical design is temperature compensated, increasing drive current with temperature, the spectral width differential at 70 °C is expected to be approximately 25 nm. There has been a nominal increase in peak LED coupling which may allow decreasing drive current. The major fallout encountered has been PIN coupling efficiency. Some of the losses can be recovered by improving lens surface finish and antireflection coating lens surface #2.

References:

[1]   FDDI Physical Layer Medium Dependent (PMD) standards:
             - US: ANSI Standard X3.166 - 1990
             - International: ISO Standard IEC 9314 - 3; 1990(E)

[2]   M. S. Acarlar, S. L. Moyer, and S. D. Robinson, "Use of Low Cost DIPs and Injection Molded Parts in Packaging of Optical Data Links", ECTC Conference Proceedings, 1992, San Diego, CA, pp.661 - 666.

[3]   D. Chown, R. Musk, D. Manton, C. Sparkes, M. Birch, M. Benton, J. Somerville, R. Hooley, L. Krauss, "Integrated Transceiver for FDDI", ECTC Conference Proceedings, 1989, Houston, TX, pp. 378 - 383.

[4]   C.-L., Jiang, "Ray Tracing Model for Efficient Coupling of LEDs Using a 'TO' Package", AMP Journal of Technology, 1993.

RECEPTACLE

LENS CAP

SUBMOUNT WITH LED/PIN

HEADER

LID

RECEPTACLE CLIP

FRAME

PREFORM

POPULATED BOARD ASSEMBLY

FIGURE 1

FIGURE 2

CASE

LENS/RECEPTACLE

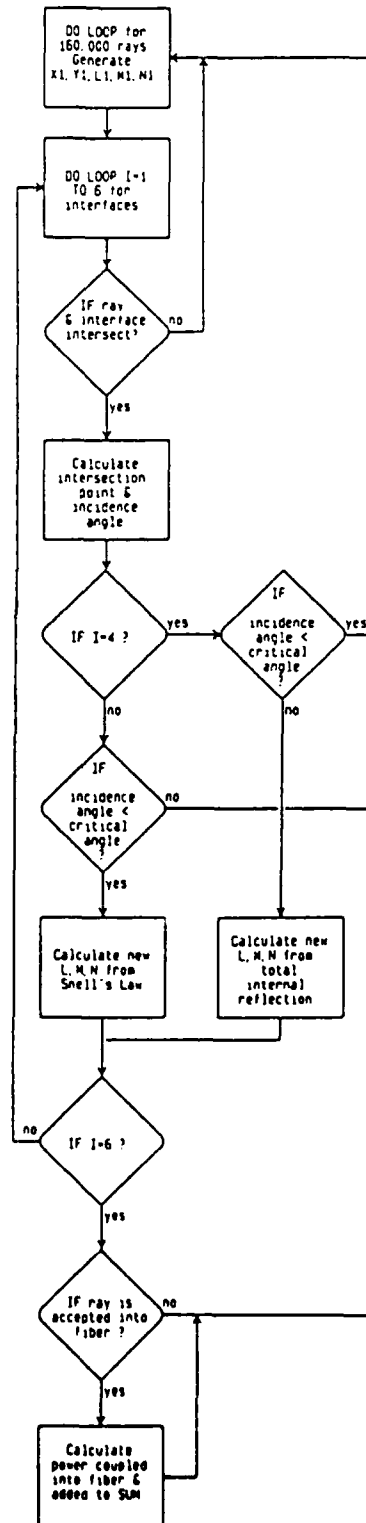POPULATED BOARD
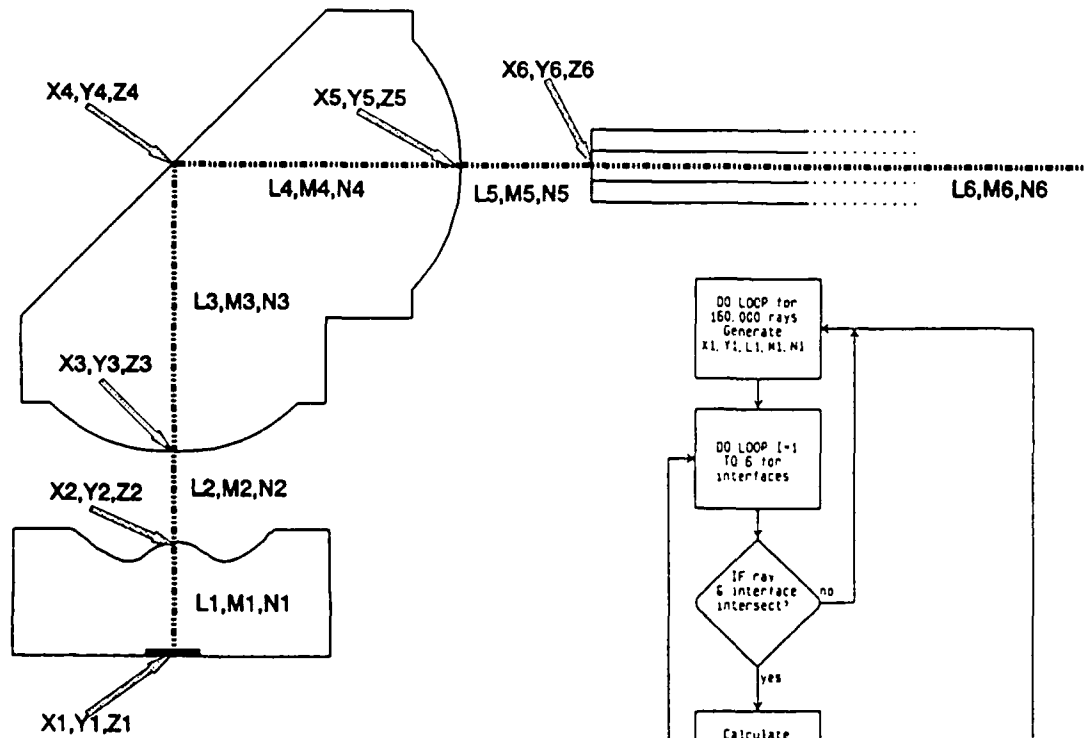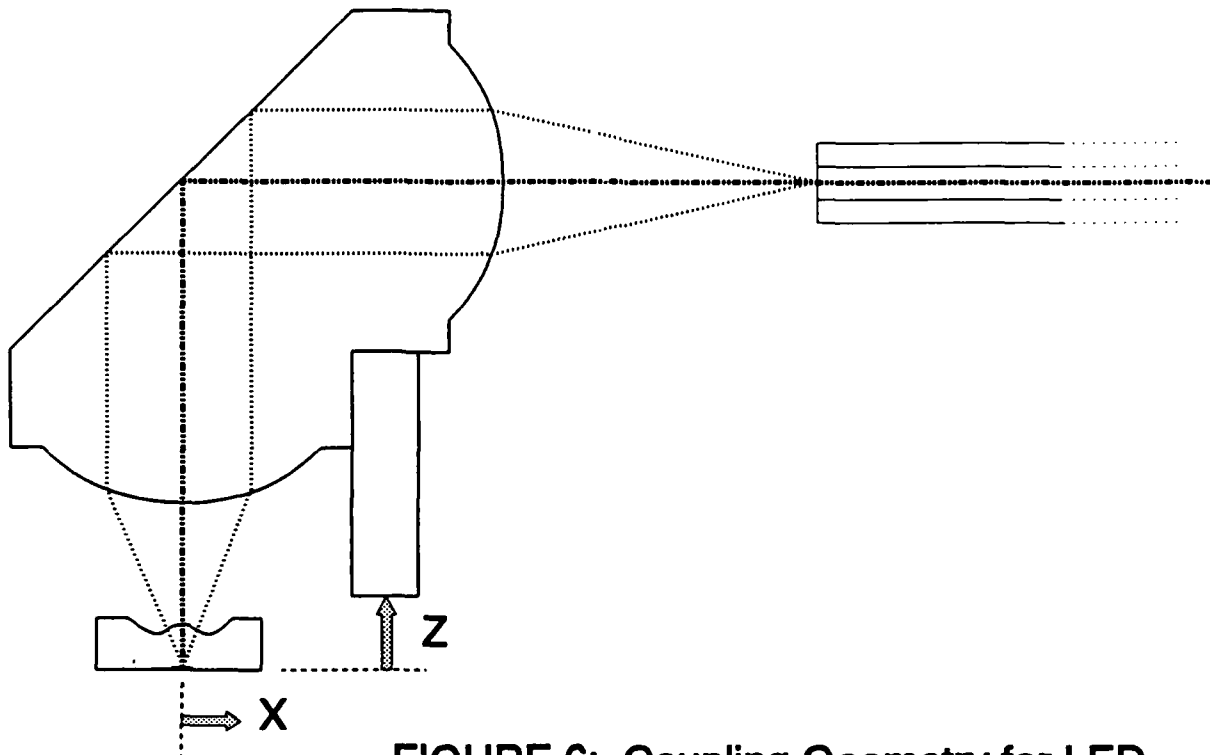ASSEMBLY

FIGURE 3

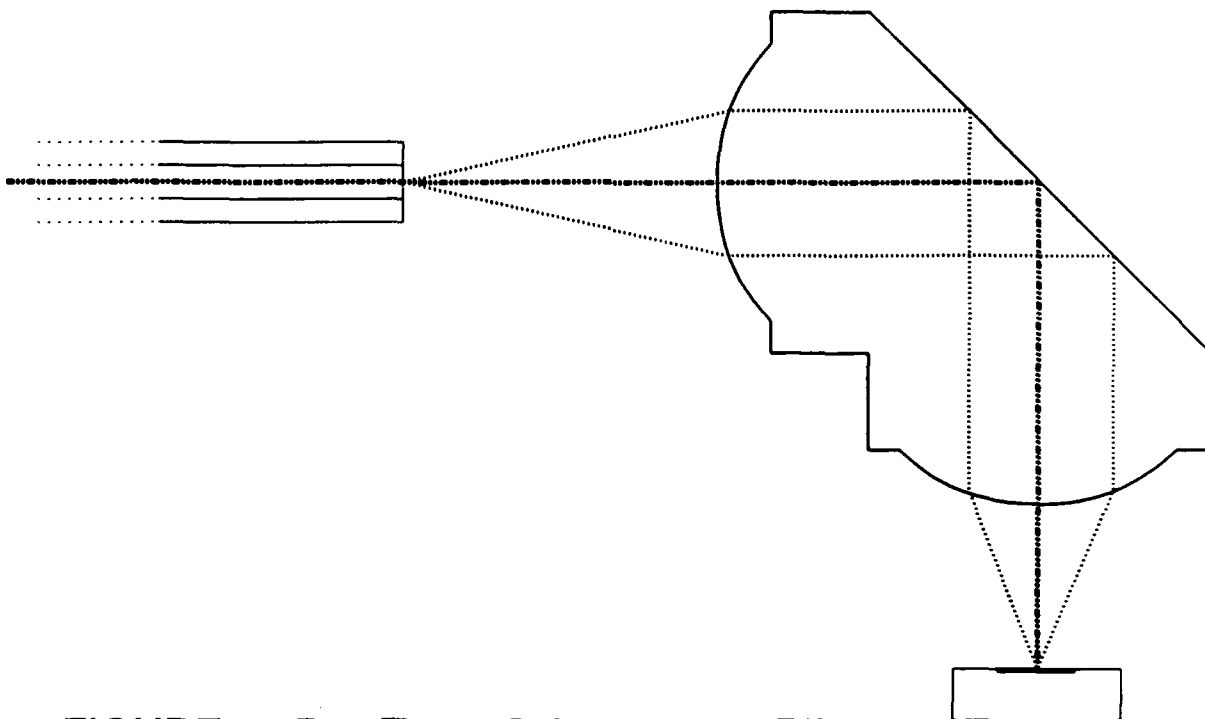**FIGURE 4**

Figure 5

FIGURE 6: Coupling Geometry for LED

FIGURE 7: Ray Trace Schematic for PIN

Variation of On-Axis Coupling with Z
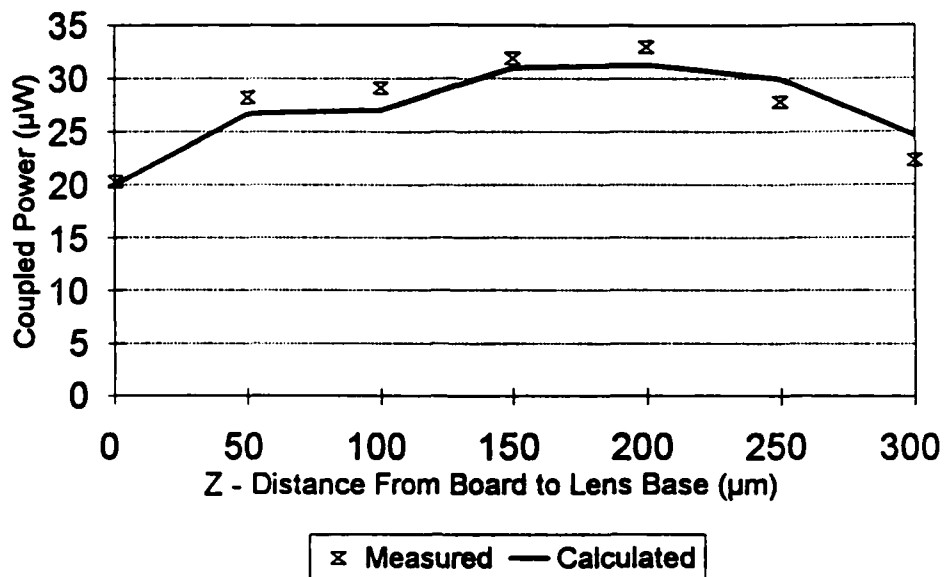### Experiment & Theory into 62.5 μm MMF

FIGURE 8

LED Lateral Coupling Curves
Experiment & Theory @ Two Z's
(Z is Distance from Board to Lens Base)

FIGURE 9